Synthesis, Characterization and Optimization of New Thermoelectric Materials

Petr Levinský

Czech Technical University in Prague
Faculty of Nuclear Sciences
and Physical Engineering

jointly with

Université de Lorraine
Doctoral school C2MP
Institut Jean Lamour (Nancy)

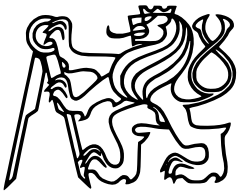

PHD THESIS

under joint supervision

Synthesis, Characterization and Optimization of New Thermoelectric Materials

11 October 2018

Membres of the jury:

Ms Sylvie HÉBERT	reviewer	Research supervisor in the CRISMAT laboratory, Caen
Mr Čestmír DRAŠAR	reviewer	Professor at the University of Pardubice
Mr David SEDMIDUBSKÝ	examiner	Professor at the University of Chemistry and Technology Prague
Mr Peter BALÁŽ	examiner	Research supervisor at the Institute of Geotechnics of the Slovak Academy of Sciences
Mr Stanislav VRATISLAV	examiner	Professor at the Czech Technical University
Mr Christophe CANDOLFI	examiner	Maître de conférences at the Université de Lorraine
Mr Ladislav TICHÝ	examiner	Professor at the University of Pardubice
Ms Věra CIMROVÁ	examiner	Research fellow at the Institute of Macromolecular Chemistry of the Czech Academy of Sciences

Petr Levinský

Prague 2018

Declaration

As the head of the research team in the laboratory at Institut Jean Lamour, I confirm that Petr Levinsky is the key author of the work which was carried out in this laboratory and is presented in this thesis. The exceptions are stated in the text.

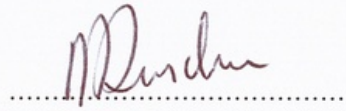

Dr Anne Dauscher

I hereby declare that I wrote this thesis independently and used the resources mentioned throughout the work or in the attached list. Work presented in the thesis is my own work unless otherwise stated.

In Prague ....

Petr Levinský

Acknowledgements

I would like to thank all those who took part in my supervision, Dr Anne Dauscher, Prof Bertrand Lenoir, Dr Jiří Hejtmánek and Assoc Prof Ladislav Kalvoda, for their supervision and guidance which made this thesis possible. They deserve my gratitude for the countless remarks, comments, observations, motivation, advice and help in general, which they have patiently and open-mindedly provided me over the years.

Another big thanks goes to Fumiki Ono, a motivated and polite intern who synthesized and prepared several samples and who was a delight to work with. Further thanks go to the colleagues from the French and the Czech laboratories.

A very special thanks belongs to all the members of my family, who have kindly and graciously supported me throughout my whole life. Without them, this thesis would never have existed.

This work was supported by the French Ministry of Foreign Affairs, the Czech Science Foundation (projects No. 13-17538S and 14-36566G), and the Grant Agency of the Czech Technical University in Prague (grants No. SGS13/219/OHK4/3T/14 and SGS16/245/OHK4/3T/14).

Petr Levinský

Contents

Chapter 1

Introduction and Motivation

This thesis focuses on thermoelectric (TE) materials, or thermoelectrics for short, which provide direct conversion between heat and electricity and vice versa. This allows us to take the shortest conversion route between the two and eliminate the need for a working gas, turbine and alternator used in traditional electricity generation or a compressor in traditional cooling. In this way, devices without any moving parts can be constructed which provides superior reliability as well as silent operation and no need for maintenance.

However, the efficiency of these devices is rather low, of the order of 5 %, which has restricted their use to niche applications, along with the high cost and certain toxicity of the constituent materials. Traditionally, the most important use for thermoelectrics was in space applications in the so-called radioisotope thermoelectric generators (RTG) which use a radioisotope as a source of heat which is converted by TE materials into electricity, effectively providing a stable, continuous and autonomous source of electricity for decades. Another use was simple and small-scale cooling using the so-called Peltier modules. In the past twenty years, TE research was boosted by two impulses. One of them was the society's increased concern about the environment, giving TE a new purpose in energy recovery from waste heat which comprises a large part of the humanity's energy budget. The other boost came from the development of new concepts coupled with the synthesis of new materials, broadening the thermoelectric field and showing new ways for its exploration.

While various efforts to push back the drawbacks of thermoelectrics are under way, the process of improving known TE materials or searching for new ones is rather strenuous. The main conditions for a good thermoelectric material are rather straightforward – high Seebeck coefficient and, at the same time, low electrical resistivity and thermal conductivity. These parameters are, however, interdependent so the task of finding and optimizing a good thermoelectric material is strenuous and requires various approaches, leading to a large variety of different families of materials. [1–10]

This experimental thesis is named rather clearly: Synthesis, Characterization and Optimization of New Thermoelectric Materials. As the title suggests, one part is the synthesis of samples of TE materials, generally from pure elements or simple

precursor compounds. Another part is the characterization of sample properties, either synthetic or not. We characterize thermoelectric properties of the samples (the Seebeck coefficient, electrical resistivity and thermal conductivity) in a wide range of temperatures. This is supplemented by characterizations of the crystal structure, microstructure or chemical composition. The measured properties are analysed in the hope for a better understanding and providing suggestions on how to optimize the material properties. Regarding the new materials, the main focus of this thesis is on tetrahedrites, a sulfosalt-mineral based family of materials whose promising TE properties were discovered only 6 years ago. [11] Two more families are studied: oxides and polymers.

The main goal of this thesis is to study the properties of tetrahedrites. This is a loose follow up on a previous thesis [12] done in the laboratory at Institut Jean Lamour. Our study begins with an investigation of TE properties of natural tetrahedrites. Next, we will further develop the idea of fabricating TE materials from mixtures of natural and synthetic tetrahedrites [13] by investigating the mixing process in more detail. Furthermore, we will prepare and study synthetic tetrahedrites to determine the influence of substitution by As as well as by other elements (e.g. Mg, Ca, Al, In, Sn, Ag). In the case of oxides, we will try to better understand the thermal conductivity of $CaMnO_3$ with light doping from the window where these materials are commonly investigated for their TE properties. In the case of polymers, we will measure the properties of conductive polymers supplied by a partner laboratory. This is mainly to gain experience with a new, specific family of materials and possibly open the way towards future collaboration.

This PhD work was done jointly between the Czech Technical University in Prague, Czech Republic, and the Université de Lorraine in Nancy, France, under the joint supervision (a.k.a. co-tutelle) scheme. The general and special supervisors for the Czech part are Assoc. Prof. Ladislav Kalvoda of the Czech Technical University in Prague and Dr. Jiří Hejtmánek of the Institute of Physics of the Czech Academy of Sciences. For the French part, Dr. Anne Dauscher of the Institut Jean Lamour and Prof. Bertrand Lenoir of the Université de Lorraine assume the roles.

Chapter 2

Fundamentals

This chapter will begin by introducing the thermoelectric effects, followed by a description of a TE module which makes use of them. Then we shall review their applications in electricity generation and cooling. Next, we will focus on electric and thermal transport, followed by considerations for improving TE materials. In the second part, we will present a short overview of various TE material families. For thorough and comprehensive information on this topic the reader is invited to consult some of the numerous available texts which have served as an inspiration for this chapter. These include classical books on solid state physics [14–17], books and reviews on thermoelectrics [1–10], as well as theses [12, 18–22].

2.1 Thermoelectricity

2.1.1 Thermoelectric Effects

In 1821, Thomas Johann Seebeck discovered that when two dissimilar metals are joined together and their two junctions are kept at a different temperature, electric current will flow through this circuit. That is due to the fact that when a material is subject to a temperature gradient ΔT, a proportional voltage gradient ΔV also develops:

$$\Delta T = S\Delta V \,. \tag{2.1}$$

The proportionality coefficient S, named after its discoverer, is expressed in the units of $\mathrm{V.K^{-1}}$. Its magnitude is of the order of $\mu\mathrm{V.K^{-1}}$ for metals and 100 $\mu\mathrm{V.K^{-1}}$ for semiconductors. The sign can be both negative and positive, depending on the charge of the majority carriers.

One decade later, an effect inverse to the Seebeck effect was discovered by Jean Charles Athanase Peltier. When a voltage is applied to a conducting material, it is not only electric flux $\vec{j}$ that we observe but thermal flux $\vec{q}$ as well:

$$\vec{q} = \Pi\vec{j} \,. \tag{2.2}$$

The Peltier coefficient Π varies between different materials. Therefore when electric current I is passing through their junction, a discontinuity in the heat flux will form

there. The Peltier heat per unit of time dQ/dt generated or extracted at such a junction will be

$$\frac{dQ}{dt} = (\Pi_A - \Pi_B)I \tag{2.3}$$

where Π_A and Π_B are the Peltier coefficients of the two materials. The units of Π are V or, put more intuitively, $\mathrm{W.A^{-1}}$.

There is in fact a third effect predicted and discovered William Thomson, also known as Lord Kelvin. The Thomson effect describes heat exchange with the surrounding environment when electric current is passed through a conductor which is subject to a temperature gradient $\vec{\nabla}T$. The heat generation/absorption rate is described as

$$\frac{dQ}{dt} = -\tau \vec{j} \cdot \vec{\nabla}T \tag{2.4}$$

where τ is the Thomson coefficient. Thomson showed that the three coefficients governing the effects described above are related:

$$\Pi = ST \tag{2.5}$$

$$\tau = T\frac{dS}{dT}\,. \tag{2.6}$$

These so-called Thomson relations show that the knowledge of any one of the three coefficients tells us the value of the two others. Most often the choice falls to the Seebeck coefficient S because it is the easiest to determine experimentally. More importantly, we see that there is one physical mechanism behind the three effects which are sometimes grouped under the common name thermoelectric effects .

2.1.2 Modules

We have seen that the thermoelectric effects allow for conversion between heat and electricity, directly and in both ways. That paves the way for the thermoelectric module, a device converting heat to electric energy and vice versa. Figure 2.1 shows a basic principle of such a module. It consists of two legs of thermoelectric materials which are marked n and p depending on whether their majority carriers are electrons or holes, respectively. These are connected in series with metal interconnects on top and bottom and attached to an external source/load through metal leads and wires. Heat then flows parallel to the two legs.

If we drive current through the module, then, depending on the direction of the current, one side will cool down while the other one will heat up, effectively pumping heat. If, however, we maintain a temperature gradient over the module by continuously heating one side while cooling the other one, the heat flow through the module will be converted to electricity flow through the attached load. For both modes of operation we use the exact same module, only its name changes from a *Peltier cooler* to a *thermoelectric generator (TEG).*

In reality, the current is rather large, in the order of amperes, while the voltage on one leg is on the order of only 10 $\mathrm{mV.K^{-1}}$. For practical applications, the modules

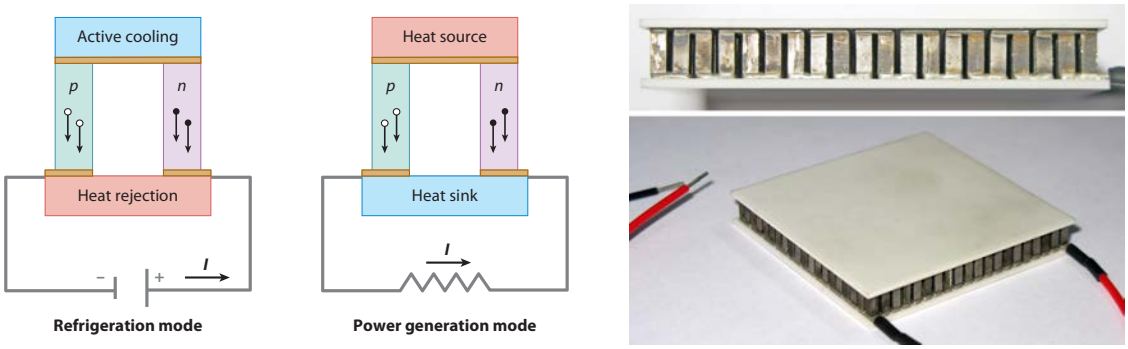

Figure 2.1: Schematic depiction of a thermoelectric module [8] which can be used in a refrigeration mode (and called a Peltier cooler) or a power generation mode (and called a thermoelectric generator). To the right, a photo of a commercial module ($40 \times 40 \times 6$ mm) with a detail of its legs.

thus contain a chain of tens or even hundreds of legs connected electrically in series in order to rise the operating voltage to usable levels.

The maximum efficiency η of a thermoelectric generator with its hot and cold sides maintained at temperatures T_H and T_C is

$$\eta = \frac{T_H - T_C}{T_H} \frac{\sqrt{1+ZT}-1}{\sqrt{1+ZT}+\frac{T_C}{T_H}}\,. \tag{2.7}$$

Here, the first fraction represents the Carnot efficiency, a hard thermodynamic limit. The second fraction depends on ZT, a key material parameter in thermoelectric materials research:

$$ZT = \frac{S^2}{\rho\kappa}T \tag{2.8}$$

where S represents the Seebeck coefficient in $\mathrm{V.K^{-1}}$, ρ the electrical resistivity in Ω.m and κ the thermal conductivity in $\mathrm{W.m^{-1}.K^{-1}}$. Electrical resistivity is often used interchangeably with its reciprocal value, the electrical conductivity $\sigma = 1/\rho$ expressed in $\mathrm{S.m^{-1}}$. This is especially popular among chemists who also often refer to S as the thermopower.

As we can see, the thermoelectric figure of merit ZT quite elegantly groups the three material parameters in one dimensionless unit. However, this elegance is spoiled by the fact that the average efficiency of a TEG is around 5 %, hardly above 10 % for the very best experimental materials and designs, and the process of improving is surprisingly difficult. Sometimes, a quantity called the power factor $PF = S^2/\rho$ is also used to judge a material instead of ZT. It does not take into account the thermal conductivity and therefore can be useful when thermal conductivity data are not available or when the efficiency of conversion is not of concern (for example in heat exchangers where the main priority is the efficient transfer of heat).

2.1.3 Applications

As has been said, the efficiency of thermoelectric devices is low, roughly an order of magnitude bellow that of the state-of-the-art more conventional heat engines. Another disadvantage is the low abundance (implying high cost) and relative toxicity of the elements used in their fabrication. There are however several advantages which have made thermoelectrics a perfectly viable, albeit not mainstream, technology:

- Absence of any moving parts
- Absence of a working fluid
- Reliability: even tens of years of reliable service
- Vibration-free operation: for mechanically sensitive environments
- Noise free operation: for higher comfort or stealth applications
- Maintenance-free: reduces running costs and allows deploy-and-forget usage
- Non-stop operation poses no problem
- Simple scalability: from microchip cooling to 20kW train air conditioning
- Dual operation mode: trivial switching between refrigeration and heating
- Direct conversion between heat and electricity: less space for problems

Generaly, we may group the application of thermoelectric effects into the following four categories:

- Electricity generation off the grid
- Electricity generation from waste heat
- Cooling
- Temperature sensing

Electricity generation using thermoelectric materials can be either active or passive. In the former, historically more important, case we actively generate the heat to be converted to electricity. Simply because in certain situations this is the most suitable method of generating electricity. In the latter case, the heat is already being produced as a by-product of some other process, we are only tapping into this source to extract some extra energy which would otherwise be lost.

Heat is the lowest form of energy and it is dissipated in the environment with every irreversible process taking place. Put in layman's terms: everything we do produces, to some extent, waste in the form of heat. Its sources are thus plentiful and with the whole world going greener people have started to look into the means of its recuperation and thermoelectrics represent one approach. While power plants can be optimized to work at a specific regime and obtain high efficiency, the same cannot be said for a car. It is expected to work in a wide range of regimes, ranging from rush hour city driving to strong acceleration to highway cruising. Furthermore, the manufacturers are constrained by a reasonable weight and size of the engine.

During a steady cruise at a highway speed, a car can do with some 10–15 kW of mechanical power. However, to generate this power burning petrol, another 15 kW are dumped into the cooling water and 15 more kW escape as hot exhaust gases. Extraction of some energy from the latter part using an exhaust-pipe mounted TEG has been investigated by every major car maker. The electrical power obtained with

current TE materials, generally around 200 W, is not enough for economic viability. Thermoelectric generators are also investigated as means for improving the total efficiency of solar panels by converting the low-energy infrared part of the spectrum otherwise lost as heat. [1]

There are certain situations where we have to generate electricity on the spot and in some of them, thermoelectricity is the most suitable way to do so. The most prominent example is in space too far from the Sun to use solar panels. The supply of raw power is a radioisotope, usually plutonium, continuously delivering great amounts of heat for decades. Because of their long-term reliability TE are the method of choice for the heat-electricity conversion step. Radioisotope thermoelectric generators (RTG) with an electrical output of up to several 100 W have been powering space probes for decades; Voyager 1, already outside the solar system, has recently celebrated its 40^{th} anniversary.

On a different size scale, RTGs have been used to power cardiac pacemakers. Gas pipelines in remote locations such as Alaska use burners and TEG to convert oil to heat to electricity. [9]

There are several applications for cooling. Without doubt, TE cannot compete with household or industrial refrigerators. But as we scale the cooling system down, the price, size and weight of a compressor/heat exchanger does not significantly decrease with the size. Unlike for a Peltier cooler which in the case of a small car-powered fridge already becomes more cost effective than a classical system. Partly due to their compactness, TE modules are used to cool various opto-electronic components, let it be to simply remove heat (e.g. lasers, laser diodes) or to cool the components way below room temperature (various detectors etc.) The fact that they operate silently makes Peltier coolers interesting for military stealth applications, let it be for rifle-mounted IR scopes or submarines. [1, 9]

Hand in hand with cooling go temperature control applications. The basic rule of regulation is that for effective regulation one needs forces pulling both ways, in this case both cooling and heating power. Only being able to pull one way and letting relaxation pull the other way is enough in some cases. However, precise control of the magnitude and direction of pumped power in Peltier coolers makes them suitable for this task with superior speed and accuracy. Among other uses of temperature control we will mention thermal cyclers for polymerase chain reaction (PCR), a major method for multiplying a strand of DNA by several orders of magnitude. That is done by cycling the sample mixed with enzymes through different temperatures to sequentially activate specific processes.

Last but not least we have to mention temperature sensing. A mature and well-established technology allows us to use thermocouples to routinely measure temperatures between absolute zero and 2000 °C and in special cases up to 3000 °C. As the measured value refers to the point of contact between the two lead wires, their suitable choice allows us to reduce this area to well bellow one millimetre, improving spatial resolution, and by reducing the heat capacity of the sensor we limit its influence on the measured system. Even in this area there is progress with attempts to print thermocouple arrays on plastic sheets to be able to obtain a temperature map of a 2D surface.

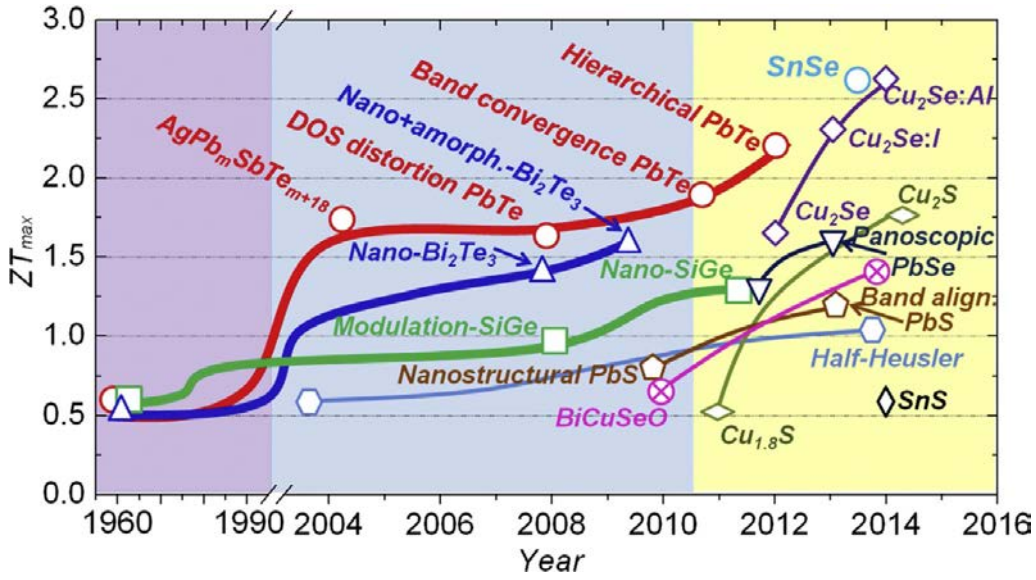

Figure 2.2: Evolution of the figure of merit ZT of different bulk materials in time. Note the different time scale at the beginning. *After [10].*

2.1.4 Thermoelectric Research Throughout Time

Equation (2.8) introduced ZT, a temperature dependent figure of merit most often used to judge the suitability of a given material for thermoelectric applications. Higher ZT means higher efficiency which means better material. As a general rule we can say that a good one should have a value $ZT \approx 1$ or above. Getting there, however, is far from straightforward.

Figure 2.2 shows the evolution of ZT of the best materials in time. We see that it is after the second world war, one century after the discovery of the underlying TE effects, that first materials suitable for TE applications emerged – namely Bi_2Te_3, PbTe and $Si_{1-x}Ge_x$ which still play a major role today. After the first wave, progress in thermoelectrics was slow for quite some time. A new impetus came some 20 years ago with the development of new concepts (e.g. nanostructuring), synthesis of new materials and elevated interest in the environment and greener energy production.

2.1.5 Electrical Transport

Using the Boltzmann transport theory, we can derive the following general expression for electrical conductivity σ: [2]

$$1/\rho = \sigma = ne\mu\,, \tag{2.9}$$

where n is the charge carrier concentration (either negative electrons or positive holes), e the elementary charge and μ the charge carrier mobility for which

$$\mu = \frac{e\tau}{m^\star}\,. \tag{2.10}$$

Here τ is the average time between collisions and $m^\star$ is the carrier effective mass.

In metals, which have a partially filled conduction band, n does not vary much with temperature. However, τ decreases with increasing temperature, generally as T^{-1}, because of electron-phonon collisions becoming more frequent. Overall, conductivity of metals decreases with increasing temperature. In semiconductors, increasing temperature excites carriers into the conduction band where their population n increases exponentially. This increase dominates the temperature dependence of σ which increases exponentially with temperature. This picture is generally valid but in reality, the temperature dependence of all the factors is extremely complex and depends on a myriad of aspects.

The classical notion of a semiconductor has carriers excited into the conduction band where they are delocalized and can move somehow freely and participate in conduction. A more specific mechanism of conduction is the so-called hopping. In this case, the carriers have not been excited and are localized. Nevertheless, it is still possible for them to move –hop– to another site with the assistance of a phonon and this results in charge flow. Unless the electron is strongly localized, the probability of such a hop is a function of the hopping distance as well as the energy difference between the two states. [23] The conductivity associated with this so-called variable range hopping (VRH) process depends on the number of dimensions d in which it takes place:

$$\sigma = \sigma_0 e^{(-T_0/T)^{1/(d+1)}}, \tag{2.11}$$

where T_0 is a characteristic temperature. If the electron is strongly localized, it will only jump to the nearest state in space, resulting in nearest-neighbour (NN) hopping with the $\sigma \sim e^{-E_h/(k_B T)}$ temperature dependence, E_h being the hopping energy.

The Seebeck coefficient may be qualitatively understood as the entropy per charge carrier. It is in fact the measure of heat which is carried along with a unit charge, linking the thermal and electrical currents. With a rigorous treatment [2,23], S can be expressed with the Mott formula:

$$S = \frac{\pi^2 k_B^2}{3e} T \left(\frac{\mathrm{d} \ln(\sigma(E))}{\mathrm{d}E} \right)_{E=E_F}, \tag{2.12}$$

where $\sigma(E)$ is the energy dependent conductivity. For the case of metals or degenerate semiconductors (parabolic band, energy-independent scattering approximation), we obtain: [7]

$$S = \frac{8\pi^2 k_B^2}{3eh^2} m^\star T \left(\frac{\pi}{3n} \right)^{2/3}. \tag{2.13}$$

The Seebeck coefficient can provide us with useful information about the charge carriers and mechanisms of conduction. First of all, the sign reflects the polarity of majority charge carriers; in the case of electrons, S is negative. Furthermore, we may investigate its magnitude and temperature dependence. Some typical cases, see e.g. [23, 24], are schematically illustrated in Figure 2.3.

When more than one conduction channel is active, the contribution of the individual channels will be weighted by their conductances. For two channels we have

$$S = \frac{S_1 \sigma_1 + S_2 \sigma_2}{\sigma_1 + \sigma_2}. \tag{2.14}$$

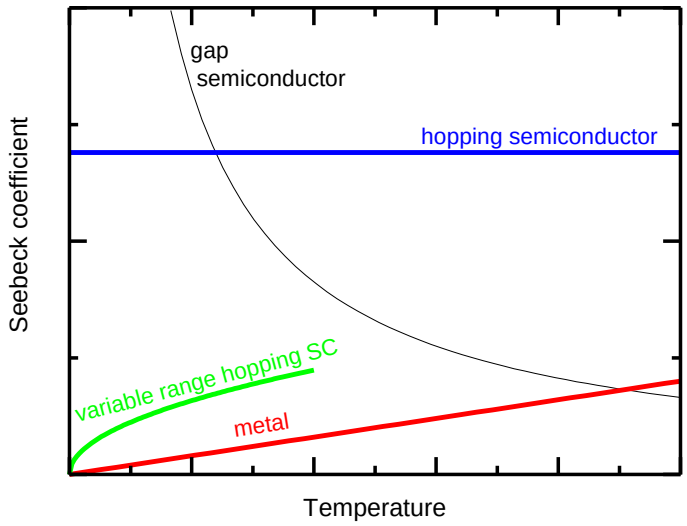

Figure 2.3: Schematic illustration of the temperature dependence of the Seebeck coefficient for various conduction mechanisms. Adapted from [26, 27].

2.1.6 Heat Transfer

Heat transfer occurs by three main mechanisms: conduction, convection and radiation. Conduction is the exchange of thermal energy by means of excitations on the atomic scale. Convection is characterized by the flow of mass in addition to the flow of energy. A typical example is the warm air with lower density rising above hot surfaces while the denser colder air sinks in its place. Radiation is mediated through photons and the Stefan-Boltzmann law states that the amount of radiated energy per unit area is proportional to T^4.

Conduction, described by the physical quantity thermal conductivity κ, is by far the most important mechanism in solids and we will therefore describe it in more detail. It may be further split into different contributions based on which excitations take part in the heat transport: κ_l for phonons (lattice waves), κ_e for electrons and, in some materials, even κ_m for magnons (spin waves). Neglecting the last component which is negligible in most cases, we can write

$$\kappa = \kappa_l + \kappa_e \,. \tag{2.15}$$

From the kinetic theory we may obtain the following equation for thermal conductivity:

$$\kappa = \frac{1}{3} C_v v l \,, \tag{2.16}$$

where C_v is the volumetric heat capacity associated with the excitation, v is the velocity with which it propagates, and l is its mean free path. It is often useful to write the last factor as $l = v\tau$, where τ is the mean time it takes for the excitation to get scattered.

We will now focus on the lattice part of the thermal conductivity. Let us examine some characteristics of its temperature dependence. The speed of sound, i.e. the

phonon velocity v, generally does not vary much with temperature. For temperatures above the Debye temperature Θ_D, the heat capacity of solids is nearing the Dulong-Petit limit ($3R$ per mole of substance, R is the universal gas constant) and shows little temperature dependence. The phonon mean free path l will therefore have the main influence on $\kappa_l(T)$. The dominant scattering mechanism at high temperatures are phonon-phonon interactions in the so-called Umklapp process which occurs when the resulting wave vector of two colliding phonons exceeds the first Brillouin zone, effectively reflecting the resulting phonon. The phonon number is proportional to T and the phonon-phonon collisions cause l and therefore κ_l to vary as T^{-1}. [15]

At low temperatures, the phonon wave vectors are not large enough for Umklapp processes to occur and impede the heat flow. Phonon mean free path will be determined by scattering at the grain boundaries and so may be considered constant. The temperature dependence of κ_l will mimic that of the heat capacity which follows the T^3 law. The absolute value will reflect the grain size.

In a more rigorous treatment, we have to consider all components of (2.16) as dependent on the wave frequency ω and integrate over all possible frequencies in addition to summing over all modes to get κ_l. Table 2.1 summarizes some scattering mechanisms, their frequency dependence and their influence on the temperature dependence of lattice thermal conductivity.

Table 2.1: Phonon scattering mechanisms and their influence on scattering probability and thermal conductivity. *After [29].*

Scattering mechanism	$1/l(\omega)$	$\kappa_l(T)$
Low temperature $T < \Theta_D$		
External boundaries	ω^0	T^3
Grain boundaries	ω^0	T^3
Stacking faults	ω^2	T^1
Conduction electrons in metals	ω^1	T^2
Point defects	ω^4	T^{-1}
Umklapp processes	ω^0	$T^3 e^{-\Theta_D/\alpha T}$
High temperature $T > \Theta_D$		
Umklapp processes	...	T^{-1}
All imperfections	...	T^0

If we make use of the Debye model of specific heat and plug it into (2.16), we obtain an expression for thermal conductivity through acoustic phonons [31, 32]

$$\kappa_{l,ac} = \frac{k_B}{2\pi^2 v}\left(\frac{k_B T}{\hbar}\right)^3 \int_0^{\Theta_D/T} \tau(x)\frac{x^4 e^x}{(e^x-1)^2}dx\,, \tag{2.17}$$

where k_B is the Boltzmann constant, $\hbar$ the reduced Planck constant, and $x = \hbar\omega/k_B T$.

Different scattering mechanisms are implemented through the relaxation time τ by summing the relaxation rates according to the Matthiessen's rule: $\tau^{-1} = \tau_1^{-1} + \tau_2^{-1} + \tau_3^{-1} + \ldots$

As an illustrative case we may write [31, 32]

$$\tau^{-1} = \frac{v}{L} + A\omega^4 + B\omega^2 T e^{-\Theta_D/3T} + \frac{C\omega^2}{(\omega_0^2 - \omega^2)^2}\,, \tag{2.18}$$

where L is the grain size, ω_0 the resonance frequency and A, B and C are adjustable scaling factors for individual scattering mechanisms. From left to right, these mechanisms are: grain boundary scattering, scattering by point impurities (Rayleigh type scattering), Umklapp scattering, and resonant scattering.

If we make use of the Einstein model of specific heat and plug it into (2.16), we obtain an expression for thermal conductivity through optical phonons [33]

$$\kappa_{l,opt} = n v_{opt}^2 R \left(\frac{\Theta_E}{T}\right)^2 \frac{e^{\Theta_E/T}}{(e^{\Theta_E/T} - 1)^2} \tau_{opt}\,, \tag{2.19}$$

where n is the number of optical branches, R the gas constant, and Θ_E the Einstein temperature corresponding to the frequency at which the optical phonons oscillate. Note that due to the rather flat dispersion of optical modes, v_{opt} will be much lower than v for acoustical phonons.

For the best thermoelectric performance, thermal conductivity has to be as low as possible. It is therefore convenient to introduce the concept of minimum thermal conductivity to assess how low a value we may get in a crystal. Cahill et al. [30] based their model on Einstein's theory of thermal conduction in solids which was an extension of his famous theory of specific heat. They borrowed from Debye's theory and divided the sample into regions sized half the wavelength λ, whose oscillation frequencies were based on the low-frequency speed of sound $\omega = 2\pi v/\lambda$, and set $\tau = \pi/\omega$. This model treats thermal transport as a random walk of energy in a network localized quantum mechanical oscillators with the bulk of the transport of energy occurring only between the nearest neighbours. For the temperature dependent value of minimum thermal conductivity, the authors present the following equation:

$$\kappa_{min} = \left(\frac{\pi}{6}\right)^{1/3} k_B n^{2/3} \sum_i v_i \left(\frac{T}{\Theta_{D,i}}\right)^2 \int_0^{\Theta_{D,i}/T} \frac{x^3 e^x}{(e^x - 1)^2} dx\,, \tag{2.20}$$

where n is the number density of atoms and the sum is taken over all modes i (two transverse, one longitudinal) with speed of sound v_i and Debye temperature $\Theta_{D,i} = v_i(\hbar/k_B)(6\pi^2 n)^{1/3}$. The authors confronted the model with experimental data for different highly disordered crystals as well as amorphous solids and concluded that their lattice vibrations were essentially the same. [30]

The second contribution to thermal conductivity is the electronic part κ_e. Unlike the lattice part, it only contributes when the material conducts electricity. It is the main mechanism of heat transfer in metals and plays an important role when optimizing thermoelectric properties of materials. To quantify it, we once again start with the general equation (2.16). For the sake of simplicity, we perform the analysis for a free electron gas. When we plug in its heat capacity and put v equal

to the Fermi velocity v_F, as it is only the electrons close to the Fermi level which take part in the transport, we obtain [15]

$$\kappa_e = \frac{\pi^2 n k_B^2 T \tau}{3 m_e} \,. \tag{2.21}$$

By further combining this equation with (2.9) and (2.10) we arrive to

$$\kappa_e = \frac{\pi^2}{3} \left(\frac{k_B}{e} \right)^2 \sigma T = L_0 \sigma T \,, \tag{2.22}$$

This is the Wiedemann-Franz law which links the electronic part of thermal conductivity κ_e and the electrical conductivity σ via the absolute temperature and the Lorenz number L. Its value for free electrons is $L_0 = 2.44 \times 10^{-8}$ W.Ω.K^{-2}. A useful value to remember is that at room temperature, $\sigma = 10^{-5}$ Ω.m corresponds to $\kappa_e \approx 0.7$ W.m^{-1}.K^{-1}.

For electrons in a crystal, the value of L can and does vary with temperature as well as for different materials, namely depending on the scattering mechanisms. [7] Kim et al. [28] proposed to correlate the value of L used with the Seebeck coefficient:

$$L(S) = 1.5 + \exp\left(-\frac{|S|}{116} \right) , \tag{2.23}$$

where L is in 10^{-8} W.Ω.K^{-2} and S in µV.K^{-1}. For low values of $|S|$, it approaches the degenerate limit L_0 valid for free electrons and heavily doped degenerate semiconductors. With increasing values of $|S|$, it drops and converges to $L = 1.5 \times 10^{-8}$ W.Ω.K^{-2}, a value valid for acoustic phonon scattering in non-degenerate semiconductors.

2.1.7 Choice of Materials

Apart from the obvious general requirements for materials, such as good thermal, temporal and mechanical stability, the main requirement for good thermoelectric materials revolves around the equation (2.8): get the value of $ZT = \frac{S^2 T}{\rho \kappa}$ as high as possible by tuning its three constituting material parameters, the Seebeck coefficient S, electrical resistivity ρ and thermal conductivity κ. These are, however, interdependent and improving one usually degrades the others.

As we saw from (2.9), (2.13) and (2.22), both S and ρ (and κ_e as a consequence) depend on the carrier concentration n. Figure 2.4 qualitatively illustrates how the three parameters depend on the carrier concentration and what is the influence on overall ZT.

For the case of insulators with low n, the electrical resistivity is too high to allow significant current to pass through the TE material. In the case of metals with high values of n, the Seebeck coefficient degrades too much, along with thermal short circuiting. Depending on the material, a compromise can be found around $n \approx 10^{19}$ cm^3 ±an order of magnitude, in the realm of heavily doped semiconductors.

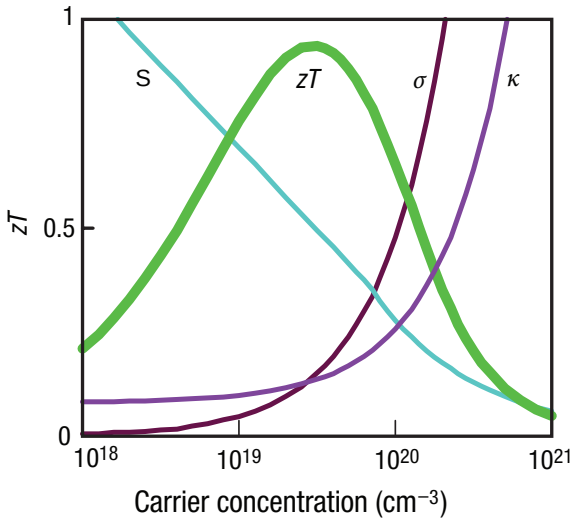

Figure 2.4: Qualitative influence of carrier concentration n on the key material parameters: Seebeck coefficient S, electrical conductivity σ, thermal conductivity κ, and $ZT = \frac{S^2\sigma}{\kappa}T$. *After [7].*

Carrier concentration is only one of several conflicting parameters. Take for example the effective mass: increased $m^\star$ leads to increased S (2.13), which is good. On the other hand, heavy carriers have lower mobility (2.10) and therefore lead to increased resistivity (2.9), which is bad.

Based on the above facts, as well as some more rigorous analyses, several classical guidelines for the choice of suitable materials have been formulated: [9]

- Materials composed of different, rather heavier elements in large unit cells to favour phonon scattering and reduction of κ_l
- Lower electronegativity difference of constituent elements to reduce ionicity of bonds and favour carrier mobility
- Sharp variation of the density of states at the Fermi level
- Energy band gap adjusted according to working temperature to be between roughly 5 and 10 kT
- Single type of charge carrier; otherwise they work against each other lowering the overall TE performance
- Do not adhere strictly to the above stated rules as there are many exceptions

2.2 State of the Art

There is a surprising variety of different materials which possess interesting thermoelectric properties. In the following paragraphs, we will introduce the three material families studied in this thesis (tetrahedrites, oxides and polymers), followed by a short summary of other families. Order-of-magnitude values of the main parameters of a good TE material should be $S \gtrsim 100$ µV.K^{-1}, $\rho \approx 10^{-5}$ Ω.m and $\kappa \approx 1$ W.m^{-1}.K^{-1}.

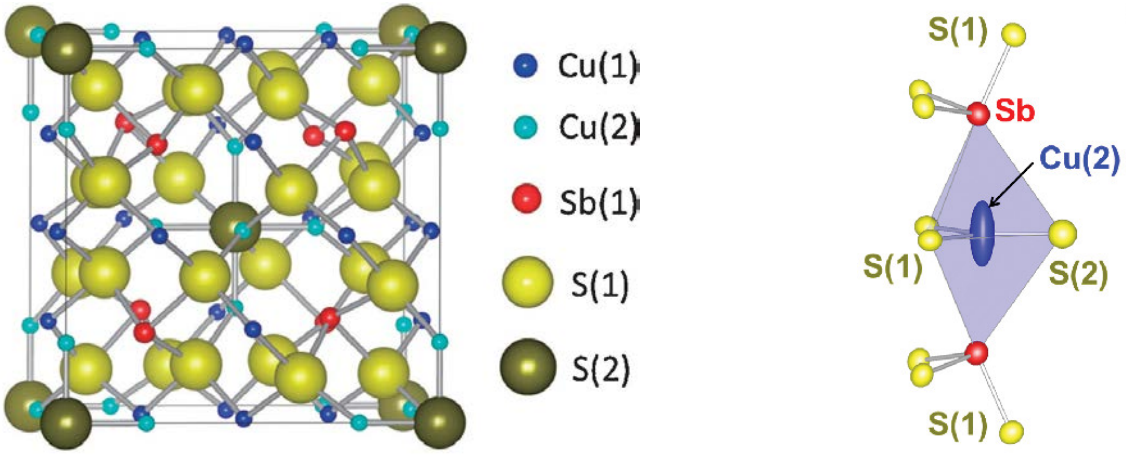

Figure 2.5: Tetrahedrite crystal structure. Thermal ellipsoids highlight vibrations of Cu atoms with large atomic displacement parameters. *After [11, 48].*

Generally speaking, we can adopt two different strategies in the quest for better thermoelectrics: (i) the search for new materials in a form of crystallographic phases and (ii) exploitation of size effects on the nano scale for known phases and composites. As was mentioned above, S is enhanced when E_F falls close to a sharp variation in the electronic density of states. By reducing one or more dimensions of the material to values comparable with the electron wavelength, such variations will appear. And indeed values of $ZT \approx 2$ have been reported for PbTe/PbTeSe nanowires. [8] In a different approach, nanoinclusions or nanostructuring of the material are used to impede the propagation of phonons without influencing electrons.

2.2.1 Tetrahedrites

Tetrahedrite is a sulfosalt mineral with the following general chemical formula: $Cu_{10}Me_2Sb_4S_{13}$ where Me is a metal. It gets its name from the tetrahedral shape of its crystals. While its crystal structure and rich chemistry have been studied extensively for many decades [55–57, 59], it was not until 2012 when its interesting thermoelectric properties have been discovered. [11]

Tetrahedrite is characterized by a cubic crystal structure (see Fig. 2.5). Regarding its chemistry, a wide variety of elements can substitute into tetrahedrite without changing its crystal structure, apart from the cell parameter, to form a solid solution. In fact, some of the substituted minerals have acquired their own name throughout the course of history. For example, tennantite is a form with all Sb atoms replaced by As. Goldfieldite is a mineral with Te substitutions on the Sb site and freibergite is another name for a silver-rich tetrahedrite. Since tetrahedrite is the most common and well known form, we will resort to certain inaccuracy and, for the sake of clarity and simplicity, refer to all these minerals as tetrahedrites.

The elements known to enter (and known to not enter) into the tetrahedrite structure are marked in the periodic table of elements on page 25. Some of these elements can substitute only partially. For example, up to three S atoms may be

replaced by Se. Regarding the Sb atoms, they can be replaced by up to four As atoms, up to two Te atoms (or up to four if we substitute two Cu atoms by vacancies) or up to 0.16 Bi atoms. For the two Me atoms, there are reports about substitution by Cu itself as well as by the following elements: Zn, Fe, Co, Ni, Mn, Cd, Hg, Sn, Ge. Makovicky, Karup-Møller and their team have done a truly formidable task in investigating tetrahedrite substitutions. They synthesised hundreds of samples to determine which elements substitute to what extent on which sites. [63–68]

The crystal structure of tetrahedrite, shown in Figure 2.5, is illustrated on $Cu_{12}Sb_4S_{13}$ which is often taken as the prototypical composition. Tetrahedrite crystallizes in the body-centred cubic structure (space group $I\bar{4}3m$) and its cell parameter is around 10.3 Å. Its large unit cell contains 58 atoms on 5 distinct crystallographic sites. One half of the copper atoms occupies the Cu(1) sites, while the other half occupies the Cu(2) site. When Me atoms substitute for copper, they go exclusively on the tetrahedrally coordinated Cu(1) site. The only exception is Ag which may replace any Cu atom. [60] It is, however, the Cu(2) atoms which make tetrahedrites especially interesting. They are in a planar triangular coordination between three sulfur atoms but they also weakly interact with active lone pairs of two Sb atoms, each located on one side of the plane, see Fig. 2.5 right. This produces strong anharmonic out-of-plane vibrations of Cu(2) which strongly scatter acoustic phonons, greatly reducing thermal conductivity. [76, 90]

Figure 2.6 shows the electronic band structure of tetrahedrite obtained from density functional theory (DFT) simulations. [69] Tetrahedrite is an indirect semiconductor with a gap size around 1.4 eV. For the case of $Cu_{10}Zn_2Sb_4S_{13}$, the Fermi level falls inside the band gap rendering this composition insulating. Up to two Cu atoms can replace Zn but they supply one electron less, creating holes in the valence band, decreasing the resistivity to 10^{-5} Ω.m and pushing the Fermi level onto a sharp edge in the density of states at the top of the valence band. This results in a relatively large value of the Seebeck coefficient $S \approx 85$ μV.K^{-1} for the fully substituted $Cu_{12}Sb_4S_{13}$. We can tune the electrical properties by adjusting the ratio of Cu to Zn or to other metals which function in a similar was as zinc.

A more correct way to treat this matter is to use the Brilluoin-zone model, counting the electrons supplied by each atom to fill the Brilluoin zones. The $Cu_{10}Zn_2Sb_4S_{13}$ composition has 208 electrons per unit cell, resulting in the 52$^{\text{nd}}$ Brilluoin zone being filled and rendering this compound insulating. Zinc provides two electrons and copper only one, so the Cu substitution leads to the Brillouin zone being only partially filled, rendering the system less stable but metallic and conductive. [58]

An alternative and more simple way to think about the doping issue is by considering the pristine $Cu_{12}Sb_4S_{13}$ composition as $Cu^{1+}_{12}h^{+}_{2}Sb^{3+}_{4}S^{2-}_{13}$ where h^+ represents a hole. Most metals substituting for Cu are divalent, so substituting e.g. one metal Me atom per formula unit results in $Cu^{1+}_{11}h^{+}_{1}Me^{2+}_{1}Sb^{3+}_{4}S^{2-}_{13}$ which still has one hole per f.u. which can take part in electrical transport. Iron in tetrahedrite can occur both as Fe^{2+} and Fe^{3+}. When a composition would result in holes being left in the valence band, e.g. in $Cu^{1+}_{11.5}h^{+}_{1}Fe^{3+}_{0.5}Sb^{3+}_{4}S^{2-}_{13}$, iron will be in the Fe^{3+} and supply two extra electrons per atom, instead of just one as is the usual case with other elements.

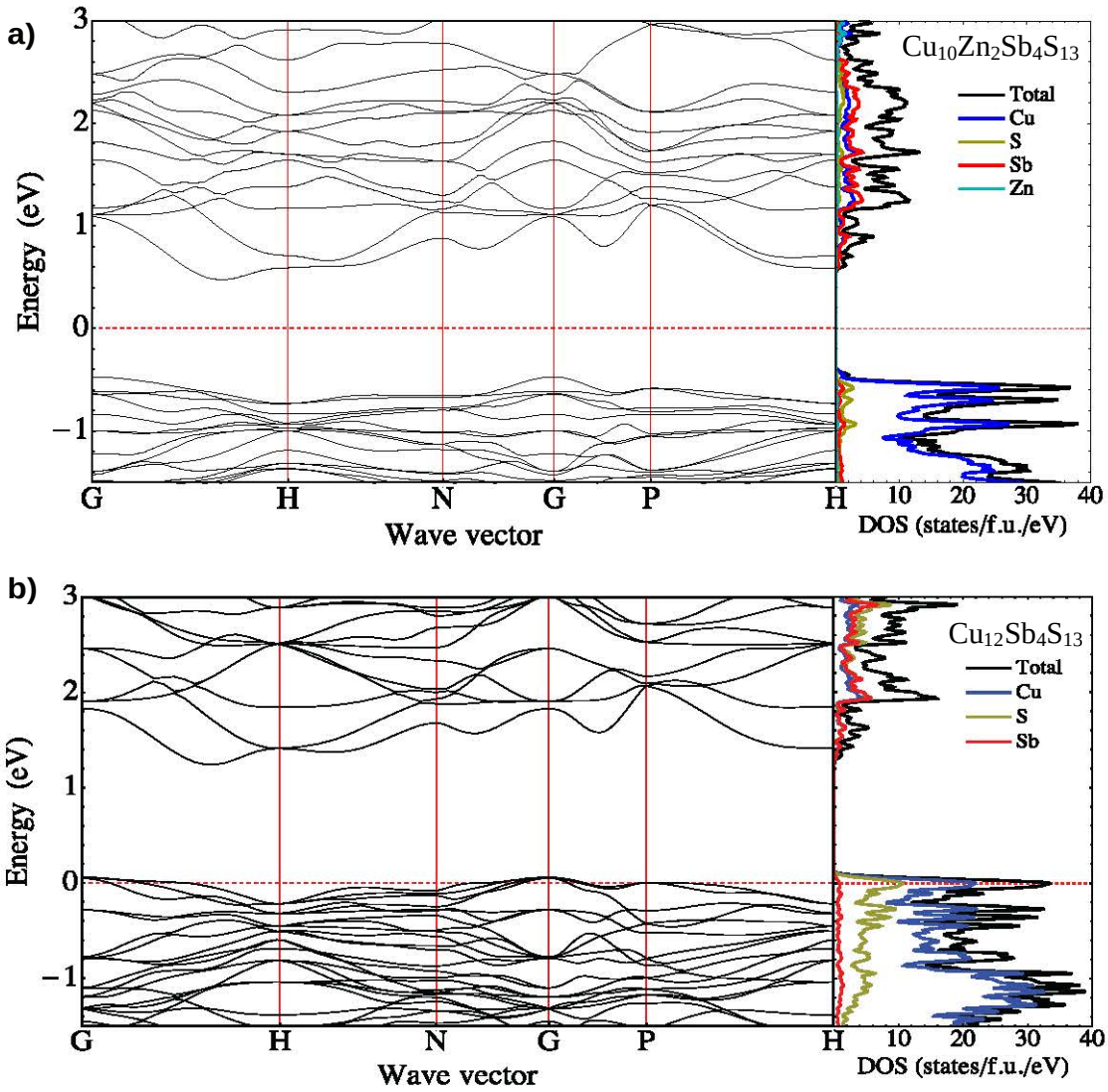

Figure 2.6: Calculated electronic band structure and density of states for $Cu_{10}Zn_2Sb_4S_{13}$ and $Cu_{12}Sb_4S_{13}$. The Fermi level is marked with a dashed red line. *After [69].*

When not needed, e.g. in $Cu_{10}Fe_2Sb_4S_{13}$, iron will be in the Fe^{2+} oxidation state, supplying only extra one electron. [62] Atoms such as Sn or Ge enter tetrahedrite in the 4+ oxidation state and have an effect analogous to three times the amount of Zn atoms. [53] Substitutions which modify the carrier density are possible at the Sb site as well, e.g. $Cu_{12}^{1+}h_1^{+}Sb_3^{3+}Te_1^{4+}S_{13}^{2-}$. [73]

When substituting $Cu_{12}Sb_4S_{13}$ with Fe, Co, Ni or Mn, a qualitatively same concept as for Zn holds but we have to take into account the modification of electronic band structure due to spin-split states, see Fig. 2.7. [50] In general, the majority spin states are fully occupied, lying well below the Fermi level, while the minority spin states fall inside the band gap where they can influence transport properties. [6] This is especially evident in the case of Ni where these states partially merge with the top of the valence band. Because of these extra states, the valence band effectively opens at the top which prevents it from being filled, as is the case with other substituting elements. $Cu_{10}Ni_2Sb_4S_{13}$ therefore remains conducting even at full substitution. [51]

Lattice thermal conductivity of tetrahedrites, $\kappa_l \approx 0.4$ W.m^{-1}.K^{-1}, is exceptionally low for a crystalline material and is even lower than for several amorphous ones (e.g. $\kappa_{\mathrm{glass}} \approx 1$ W.m^{-1}.K^{-1}). As explained before, it originates from the peculiar environment of some of the Cu atoms giving rise to strong anharmonicity of the associated lattice vibrations.

An interesting trait of the $Cu_{12}Sb_4S_{13}$ tetrahedrite is the metal–semiconductor transition (MST) at 85 K whose exact mechanism remains elusive. Below the transition, the electrical resistivity increases by an order of magnitude, the Seebeck coefficient increases four-fold to 100 µV.K^{-1} and the system undergoes a structural transformation. [52] The MST can be suppressed by pressure above 1 GPa [77], substitutions for Cu reducing the carrier concentration, as well as isoelectronic substitution of As for Sb [52] or Se for S [75].

In pristine $Cu_{12}Sb_4S_{13}$, the peak ZT value reaches around 0.5 at 700 K. Various substitutions result in a decreased hole concentration and therefore reduced

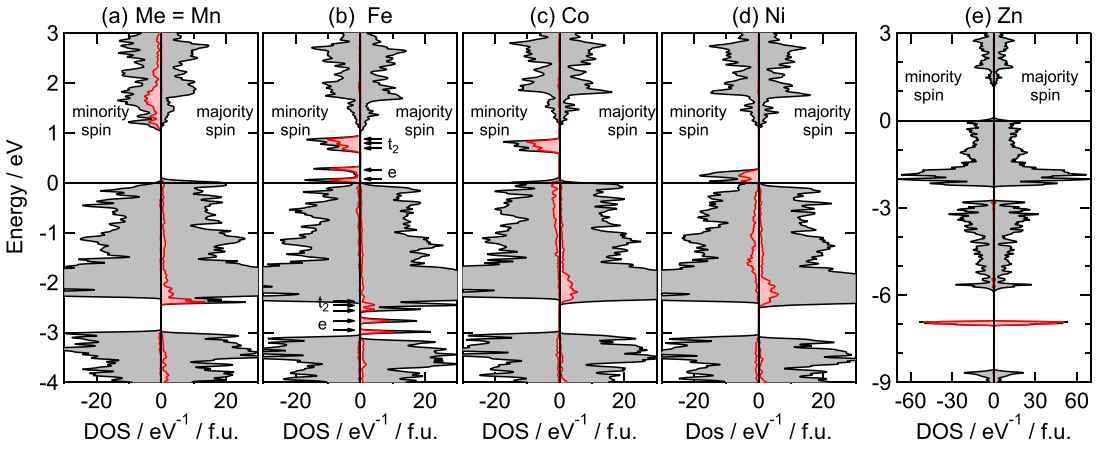

Figure 2.7: Spin-resolved electronic DoS of $Cu_{11}Me_1Sb_4S_{13}$. The red area describes partial DoS for the Me element. *After [50].*

electronic part of the thermal conductivity. This usually leads to an improvement in ZT between 0 and 40 % and credible values approaching unity have been achieved. [48,49] The periodic table on page 25 summarizes the best values achieved for different elements. It is, however, important to note that these values should be treated with care, especially when comparing one to another, as the uncertainty in measuring ZT is around 20 %. [43] In addition to single-element doping, there are reports on co-doping, e.g. with Co and Te [12], or with Ni and Zn [71]. Again, this leads to an improvement of ZT.

Tetrahedrites are typically synthesised using the classical solid state synthesis which generally requires days of annealing at high temperatures. This method costs time, energy and labour. Many other methods for synthesis have been shown to produce good quality tetrahedrites. In some cases, this significantly reduced the production costs, in other cases that was not a priority. Among the methods there is solvothermal synthesis [91], synthesis from a hydrazine solution [92], by a modified polyol process [93], nanocrystal synthesis from solution [94], melt spinning [95], reactive sintering [96] or ball milling [97].

As we mentioned earlier, tetrahedrite occurs in nature and is in fact a rather abundant ore. [13] For this reason, the mineral, already synthesised by nature, has been proposed for direct use in manufacturing thermoelectric devices. All naturally occurring tetrahedrites, however, contain two divalent atoms on the Cu site, rendering the natural material electrically insulating; the $Cu_{12}Sb_4S_{13}$ composition does not occur in nature. Tuning the chemical composition by mixing the mineral with an appropriate amount of synthetic $Cu_{12}Sb_4S_{13}$ significantly improves the thermoelectric properties of the resulting material. Lu and Morelli [13] did exactly that and used ball milling to perform the mixing. They achieved values of ZT over 0.8 using 25 % or 50 % of the natural mineral.

The same authors then showed that the synthetic $Cu_{12}Sb_4S_{13}$ is not in fact needed. [70] They ball milled the mineral with pure Cu, Sb and S elements in the 12:4:13 ratio and after several hours they obtained a single tetrahedrite phase with averaged composition and ZT around 0.8. Milling only the pure elements without the mineral did not lead to the formation of a tetrahedrite phase in this case. In another study, however, Barbier et al. [97] also ball milled only the pure elements and succeeded in synthesizing a single tetrahedrite phase after several hours. The authors suggested that the conditions used by the other team were probably too energetic. In any case, they emphasised the need to carefully study the experimental conditions.

Possible substitutions into tetrahedrite: $Cu_{10}Me_2Sb_4S_{13}$.
Elements substituting for Sb or S are bordered. All others substitute for Me.
Green: element substitutes fully. Light green: substitutes partially. Red: does not enter tetrahedrite.

Z	weight
Cu	
ZT	[ref]

Z = atomic number;
weight = standard atomic weight;
ZT = peak ZT;
[ref] = reference ([this] denotes this thesis)

1 1.008 **H** Hydrogen																	2 4.0026 **He** Helium
3 6.938 **Li** **0.65**	4 9.012 **Be** Beryllium											5 10.806 **B** Boron	6 12.011 **C** Carbon	7 14.006 **N** Nitrogen	8 15.999 **O** Oxygen	9 18.998 **F** Fluorine	10 20.180 **Ne** Neon
11 22.990 **Na** Sodium	12 24.304 **Mg** **0.55** [this]											13 26.982 **Al** Aluminium	14 28.084 **Si** Silicon	15 30.974 **P** Phosphorus	16 32.059 **S** Sulfur	17 35.446 **Cl** Chlorine	18 39.948 **Ar** Argon
19 39.098 **K** Potassium	20 40.078 **Ca** Calcium	21 44.956 **Sc** Scandium	22 47.867 **Ti** Titanium	23 50.942 **V** [63]	24 51.996 **Cr** [63]	25 54.938 **Mn** **0.89** [80]	26 55.845 **Fe** **0.8** [82]	27 58.933 **Co** **0.98** [83]	28 58.693 **Ni** **0.7** [51]	29 63.546 **Cu** **0.5–0.6**	30 65.38 **Zn** **0.95** [82]	31 69.723 **Ga** Gallium	32 72.630 **Ge** **0.65** [53]	33 74.922 **As** **0.68** [this]	34 78.971 **Se** **0.86** [86]	35 79.901 **Br** Bromine	36 83.798 **Kr** Krypton
37 85.468 **Rb** Rubidium	38 87.62 **Sr** Strontium	39 88.906 **Y** Yttrium	40 91.224 **Zr** Zirconium	41 92.906 **Nb** Niobium	42 95.95 **Mo** Molybdenum	43 (98) **Tc** Technetium	44 101.07 **Ru** Ruthenium	45 102.906 **Rh** Rhodium	46 106.42 **Pd** Palladium	47 107.868 **Ag** Silver	48 112.414 **Cd** **0.9** [84]	49 114.818 **In** **0.6** [this]	50 118.710 **Sn** **0.65** [53]	51 121.760 **Sb** Antimony	52 127.60 **Te** **0.92** [72]	53 126.904 **I** Iodine	54 131.293 **Xe** Xenon
55 132.905 **Cs** Cesium	56 137.327 **Ba** Barium	57-71 * Lanthanides	72 178.49 **Hf** Hafnium	73 180.948 **Ta** Tantalum	74 183.84 **W** Tungsten	75 186.207 **Re** Rhenium	76 190.23 **Os** Osmium	77 192.217 **Ir** Iridium	78 195.084 **Pt** Platinum	79 196.967 **Au** Gold	80 200.592 **Hg** [67]	81 204.382 **Tl** Thallium	82 207.2 **Pb** [63]	83 208.980 **Bi** **0.84** [85]	84 (209) **Po** Polonium	85 (210) **At** Astatine	86 (222) **Rn** Radon
87 (223) **Fr** Francium	88 (226) **Ra** Radium	89-103 ** Actinides	104 (261) **Rf** Rutherfordium	105 (268) **Db** Dubnium	106 (269) **Sg** Seaborgium	107 (270) **Bh** Bohrium	108 (269) **Hs** Hassium	109 (278) **Mt** Meitnerium	110 (281) **Ds** Darmstadtium	111 (282) **Rg** Roentgenium	112 (285) **Cn** Copernicium	113 (286) **Nh** Nihonium	114 (289) **Fl** Flerovium	115 (289) **Mc** Moscovium	116 (293) **Lv** Livermorium	117 (294) **Ts** Tennessine	118 (294) **Og** Oganesson

*	57 138.905 **La** Lanthanum	58 140.116 **Ce** Cerium	59 140.908 **Pr** Praseodymium	60 144.242 **Nd** Neodymium	61 (145) **Pm** Promethium	62 150.36 **Sm** Samarium	63 151.964 **Eu** Europium	64 157.25 **Gd** Gadolinium	65 158.926 **Tb** Terbium	66 162.500 **Dy** Dysprosium	67 164.930 **Ho** Holmium	68 167.259 **Er** Erbium	69 168.934 **Tm** Thulium	70 173.045 **Yb** [12]	71 174.967 **Lu** Lutetium
**	89 (227) **Ac** Actinium	90 232.038 **Th** Thorium	91 231.036 **Pa** Protactinium	92 238.029 **U** Uranium	93 (237) **Np** Neptunium	94 (244) **Pu** Plutonium	95 (243) **Am** Americium	96 (247) **Cm** Curium	97 (247) **Bk** Berkelium	98 (251) **Cf** Californium	99 (252) **Es** Einsteinium	100 (257) **Fm** Fermium	101 (258) **Md** Mendelevium	102 (259) **No** Nobelium	103 (266) **Lr** Lawrencium

Standard atomic weights taken from the Commission on Isotopic Abundances and Atomic Weights (ciaaw.org/atomic-weights.htm). Adapted from Ivan Griffin's and Paul Danese's LaTeX Periodic Table. https://github.com/pdanese/periodic-table, 2017.

2.2.2 Oxides

Oxides have the advantage of high temperature and oxidation resistance, low toxicity and high abundance of the constituting elements. Due to their strong ionic character, they had long been overlooked as a thermoelectric material. A spike of interest some twenty years ago was fuelled by two important discoveries revealing large thermoelectric power along with low electrical resistivity in two oxide families.

The first of them are complex perovskites with a general formula $La_{1-x}Ca_xMnO_3$. They were studied mainly with respect to their ability to exhibit colossal magnetoresistance [103] which arises from competing metallic and antiferromagnetic insulating ground states. [108, 109]

The second family is the bronze-type Na_xCoO_2, $0.5 \leq x \leq 1$. In 1997, it was shown [104] that while the resistivity of Na_xCoO_2 is metallic, around 2×10^{-6} Ω.m, and at the same time, its Seebeck coefficient reaches unexpectedly large values around 100 $\mu V.K^{-1}$. Along with its low thermal conductivity, this leads to values of ZT reaching unity reported for single crystals. [105] A similar effect was soon observed in other oxides with a similar layered structure, namely $Ca_3Co_4O_9$ and $Bi_2Sr_2Co_2O_y$.

Other families, e.g. $SrTiO_3$ or ZnO, were also caught in the wake of this interest in thermoelectric properties. [106, 107] Web of Knowledge gives some 3700 hits for "thermoelectric oxides" since 1900, while 3300 of these date from the year 2000 onwards. Their research is both fundamental and applied. The former is to comprehend the connection between the electronic structure and the resulting thermoelectric potential. Specifically, the role of spin and orbital entropy in magnetic materials bordering between itinerant and localized electrical conductivity is of interest. Applied research deals with the optimization of the TE properties –let it be through (co-)doping, secondary phase inclusion, (nano)structuring or texturization–, manufacturing processes as well as the fabrication of actual TE modules. [110]

A lot of effort was put in trying to decrease the thermal conductivity, whose value is fairly large. This is caused by the relativity simple crystal structure and the strength of the chemical bond. This presents a major issue for the application of highly symmetric and oxide-based materials.

As Figure 2.8 illustrates, Na_xCoO_2 is made up of alternating Na and CoO_2 layers. The first layer is composed of randomly positioned Na^+ ions and serves to scatter phonons, lowering the thermal conductivity. The values of x generally fall between $0.5 - 0.9$. The second CdI_2-type layer serves for electron transport. This concept, dubbed nanoblock integration, where each of the two subsystems provides specific properties can be applied to other materials, e.g. $Ca_3Co_4O_9$ or $Bi_2Sr_2Co_2O_y$ (see Fig. 2.8). In the case of $Ca_3Co_4O_9$, the building blocks are the CoO_2 and a rocksalt-type Ca_2CoO_3 layer which are incommensurable along the b axis. Since the 3-4-9 composition is only approximate, this *misfit* cobaltate should be properly described as $(Ca_2CoO_3)_{0.62}(CoO_2)$. [105]

The layered cobaltates with decent thermoelectric performance are all p-type, as the n-type doping presumes injection of electrons into the CoO_2 layers which is electronically and chemically hardly achievable. Among the n-type oxides, the

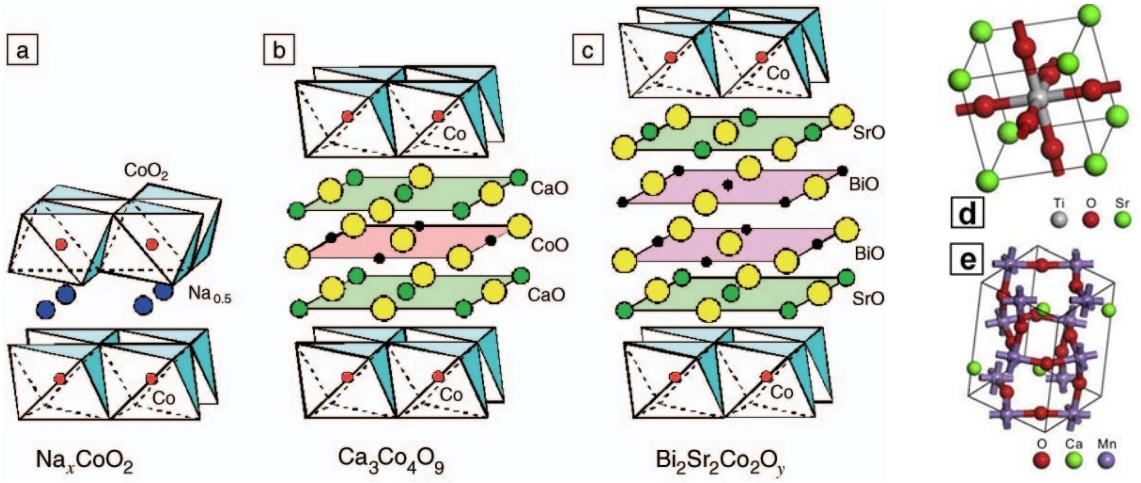

Figure 2.8: Schematic structure of a,b,c) CoO_2-based layered oxides, d) $SrTiO_3$, and e) $CaMnO_3$. *After [105, 106].*

current TE performance is much lower, however, with the most promising $CaMnO_3$ and $SrTiO_3$ giving $ZT \approx 0.3 - 0.4$. [106] $CaMnO_3$ crystallizes in the perovskite structure ABO_3 distorted from its ideal cubic symmetry (see Fig. 2.8). Its transport properties are influenced by substitutions and electron doping is achieved by replacing Ca^{2+} and Mn^{4+} by ions with higher valence, as well as through O^{2-} deficiency. Pure and lightly doped $CaMnO_3$ is antiferromagnetic with G-type ordering and Néel temperature around 125 K. [111]

2.2.3 Polymers

The use of polymer-based materials as thermoelectric components is a rather new concept in the thermoelectric field. [124–126] The advantages stem from the large abundance of base elements (C, H, O, ...) and inherently low thermal conductivity of these disordered systems. Other advantages include low toxicity, low weight or processability.

Polymers, thought of as plastics by many people, seem as unlikely candidates for a material which needs to have high electrical conductivity among other things. In 1977, it was shown [123] that polyacetylene exposed to iodine vapours augments its conductivity by several orders of magnitude. This discovery, which deserved a Nobel Prize in 2000, opened a new field of organic electronics. Further research showed that proper treatment can decrease the resistivity of polyacetylene below 10^{-6} $\Omega.\mathrm{cm}^{-1}$ [124] and that there are in fact many other conducting polymers. Figure 2.9 sketches the chemical structure of some conducting polymers considered for TE applications.

The backbone of conducting polymers is made up of sp^2 hybridized carbon atoms. Their three σ-bonds form the skeleton of the polymer, while the p_z orbitals form π-bonds between alternating pairs of atoms and create a conjugation path which allows electrons to exist in delocalized states over the chain. [126, 130] A polymer in this state will be insulating or semiconducting and to increase conduction and shift

Polymer	Structure	Polymer	Structure
Polyacetylene	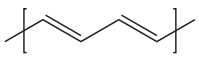	Polyaniline	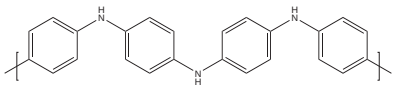
PEDOT (Poly(3,4-ethylene-dioxythiophene))	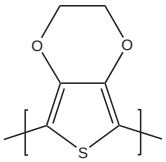	Polypyrrole	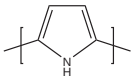
Polyalkyl thiophenes	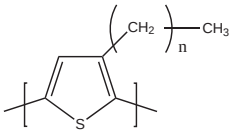	Poly(2-7carbazoles)	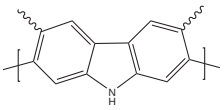

Figure 2.9: Schematic structure of some typical conductive polymers. *After [124].*

the system towards metallic state, it must be doped. This is commonly done by introducing an oxidising dopant (e.g. I_2, HCl, $FeCl_3$, $AgNO_3$, camphorsulfonic acid, PSS, tosylate) which intercalates in the structure and oxidises the polymer, creating a hole in its system of π-electrons which can then serve as a charge carrier. [126, 130] Such a polymer will be p-type which represents the majority of conducting polymers. Inducing n-type conductivity is analogous but unfortunately n-type polymers are typically unstable. [126] Electrical conductivity in conducting polymers can be often described by variable range hopping. [122]

Doped polyacetylene (PA) was the first truly conducting polymer but one of its main disadvantages is that it is unstable on air. There are various other conducting polymers, for example polyaniline (PANI), polypyrrole (PPy), polythiophene (PT) or poly(3,4-ethylenedioxythiophene) (PEDOT). They are researched for their applications in organic photovoltaics, organic LEDs (OLED), flexible electronics, transparent conducting layers and of course thermoelectrics. For a long time, their performance in the latter field was low, with $ZT = 0.001$ considered a good value. Things changed in 2011 when $ZT = 0.25$ was reported in PEDOT doped with tosylate (Tos). [134] This created a new impulse and a lot of interest in PEDOT, especially for doping with poly(styrenesulfonate) (PSS), and maximum reported ZT increased to 0.42 in PEDOT:PSS. [127, 131] The processes for improving the properties of PEDOT range from the optimization of doping and de-doping through mechanical treatment, such as straining, to fabricating composite materials based on PEDOT. [133] Among the latter are composites with another thermoelectric material, e.g. Bi_2Te_3 or $Ca_3Co_4O_9$, as well as carbon nanotubes or graphene which serve to improve electrical transport without affecting the thermal transport and Seebeck coefficient.

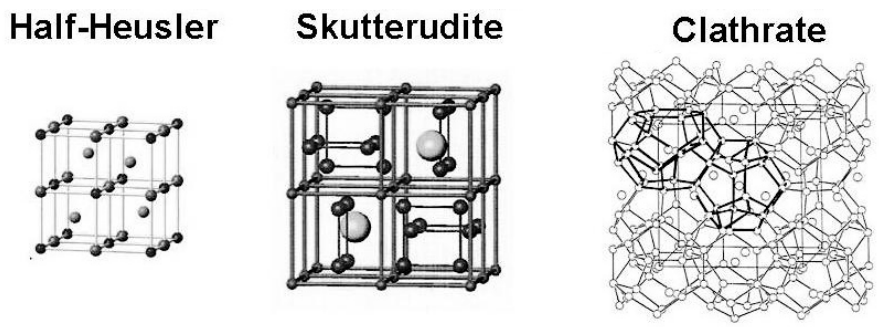

Figure 2.10: Half-Heusler, skutterudite and clathrate structures. *After [2].*

2.2.4 Other Families

Finally, we will present some other intensively studied and explored families of promising thermoelectric materials. Both Si and Ge have favourable electrical properties, however their thermal conductivity is very high, on the order of 100 $W.m^{-1}.K^{-1}$. When the two elements are alloyed, this value can drop below 10 $W.m^{-1}.K^{-1}$. For $Si_{0.7}Ge_{0.3}$, $ZT \approx 0.6$ has been achieved due to increased phonon-phonon and phonon-electron scattering. [8] The $\mathbf{Si_{1-x}Ge_x}$ alloys are a rare class of materials which can operate at temperatures as high as 1200 K. They belong among the classical thermoelectric materials discovered in the 1950's, along with materials based on $\mathbf{Bi_2Te_3}$ and **PbTe**. Even nowadays, the latter two still remain the most commonly used thermoelectrics, owing to their performance and technological maturity. Their top operating temperatures are around 350 K and 700 K, respectively.

Among the novel materials, we find the so-called **skutterudites**, mostly $CoSb_3$ and $FeSb_3$ based, whose structure is depicted in Fig. 2.10. They are based on the chemical formula MX_3, where M is a metal such as Co which forms a cubic lattice, and X represents a pnicogen atom (e.g. Sb, As, P) forming planar rings in the Co lattice voids. Not all voids are filled, however, and heavy atoms such as Yb can be placed inside them (the large spheres in 2.10). These loosely bound atoms will *rattle* at their positions with low frequency and high amplitude, impeding phonon transport and decreasing thermal conductivity. [2]

Clathrates share a similar idea with skutterudites on a slightly larger and more complex scale: a guest atom placed in a cage disrupts the phonon transport with its anharmonic behaviour (see Fig. 2.10). On a smaller scale, **half-Heusler** compounds are promising thermoelectrics. Standard Heusler alloys are characterized by three interpenetrating fcc lattices and an overall XY_2Z chemical formula, where X is a metal from the Ti or V groups, Y a metal from the Fe, Co, Ni groups and Z a p-block element such as Sb, Sn, Ga. [2] In a half-Heusler alloy the formula XYZ applies, suggesting voids in the structure. With three sublattices, each accepting a range of various elements, these materials allow a wide range of tuning various properties, be it electronic or phononic. Values of ZT close to unity have been obtained. [2]

Different materials have a different optimum temperature range for thermoelectric operation. Figure 2.11 shows the figure of merit ZT as a function of temperature

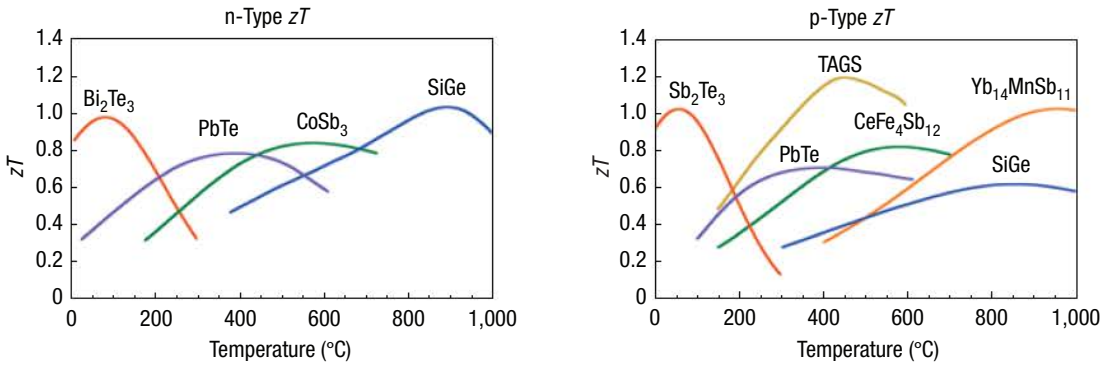

Figure 2.11: ZT of some of the common n-type and p-type thermoelectric materials as a function of temperature. *After [7].*

for some common n-type and p-type materials. By combining more of these materials in one module, we can fabricate a TE device which makes use of a larger range of temperatures, resulting in increased efficiency.

The list of materials we presented is far from exhaustive as many more families with various chemical compositions exist. To illustrate the broadness of the field, we provide some more in the form of a simple non-exhaustive list: magnesium silicides, higher manganese silicides, Zintl phases (e.g. $Yb_{14}MnSb_{11}$), Chevrel phases ($Me_xMo_6Se_8$ (Me=metal)), TAGS (Te-Ag-Ge-Sb alloys), SnTe, β-Zn_4Sb_3, $La_{3-x}Te_4$, colusites ($Cu_{26}V_2(Ge,Sn)_6S_{32}$), single element based thermoelectrics (Bi, Sb, Te, ...), and, as is in many fields, graphene.

Chapter 3

Experimental Methods

This chapter will provide an overview of the experimental methods used during the course of this thesis. The first part will describe how we obtained the actual samples which were measured – these were first fabricated by solid state synthesis or ball milling, followed by sintering into a form suitable for further characterization.

The second part will then deal with the actual measurements. We will describe the methods used for studying various sample properties, as well as the actual experimental setups along with experimental conditions. Ultimately, we studied the electrical and thermal properties both above and below room temperature. These were complemented by other measurements to study the structure, chemical composition or magnetic properties of the samples.

3.1 Synthesis and Sample Preparation

In the first part of this section, we will focus on the fabrication of the samples. We will describe the solid state synthesis which was used to prepare the large majority of the samples. There are three exceptions: natural tetrahedrites, for an obvious reason, natural–synthetic tetrahedrite mixtures, which were prepared by ball milling, and the polymer samples. The polymers were synthesized and supplied to us in the form of pellets or thin films by the team of Dr Jiří Pfleger and Dr Jaroslav Stejskal from The Institute of Macromolecular Chemistry of the Czech Academy of Sciences. The second part of this section will deal with sintering which was used to consolidate the samples to obtain bulk pieces suitable for measurements.

3.1.1 Solid State Synthesis

Conventional solid state synthesis was used to synthesize both tetrahedrite and oxide samples. This method consists of mixing stoichiometric amounts of initial elements, either as pure elements or their compounds, and subjecting the mixture to heat treatment to promote diffusion and reaction. Various other method of synthesis exist; these include hydrothermal or solvothermal synthesis, high energetic ball milling, sol–gel process, coprecipitation, etc.

Synthesis of all tetrahedrite samples was done in sealed evacuated quartz tubes at temperatures around 920 K. To fabricate the tubes, hollow quartz rods are used with an external diameter 18 mm and wall thickness generally 2 mm. These are cut in pieces 20 cm long and one end is closed using an oxygen/propane-butane torch to form a test tube. The same process is used to fabricate stoppers with an appropriate diameter. Tubes and stoppers are then cleaned in dilute HF acid, rinsed with water, cleaned in dilute HNO_3, rinsed with water and stored in ethanol for future use.

Prior to synthesis, each tube is thoroughly outgassed by pumping while heated to 900 °C for 2 or more hours. It is then moved to a glove box with Ar atmosphere and the desired elements are placed inside the tube in stoichiometric amount with the help of an analytical balance. For the purity, form and supplier of each element, refer to Table 3.1. The tube is then removed from the glove box and, with a stopper placed inside, quickly mounted to a vacuum system where it is pumped with a diffusion pump backed by a rotary vane pump. After one or two hours, when a pressure $p < 10^{-4}$ Pa is achieved, the tube is sealed with an oxygen/propane-butane torch. The material-containing portion is continuously cooled so it does not heat by more than a few tens of degrees above room temperature.

Table 3.1: List of elements used for sample synthesis.

element	purity	form	supplier
Ag	99.999+ %	powder	Strem Chemicals
Al	99.97 %	powder -325 mesh	Advanced Chemicals
As	99.999 %	powder	5N Plus
Ca	99.5 %	granules -16 mesh	Alfa Aesar
Co	99.998 %	powder -22 mesh	Alfa Aesar
Cu	99.99 %	powder <150 µm	ChemPur
Fe	99.9 %	powder -325 mesh	Cerac
Ge	99.999 %	powder -100 mesh	Alfa Aesar
In	99.999 %	shots 1-3 mm	ChemPur
Mg	99.99 %	powder	Neyco
Mn	99.95 %	powder	Neyco
Mo	99.999 %	powder -22 mesh	Alfa Aesar
Pb	99.999 %	granules	Strem Chemicals
S	99.999 %	pieces	Strem Chemicals
Sb	99.999 %	shots	5N Plus
Te	99.999 %	powder	5N Plus
TeI_4	99.9 %	powder	Strem Chemicals
Zn	99.9999 %	shots	Alfa Aesar

The sealed tube is placed vertically in a rocking furnace, heated to a desired temperature where it is kept for 12 hours and then slowly cooled down. Heating rate is kept low because of high vapour pressure of sulfur at elevated temperatures. For the same reason, the highest feasible temperature is 700 °C. Keeping this in mind, the top temperature is chosen so that as many elements as possible melt to

allow thorough mixing.

Synthetic tetrahedrite samples were prepared by mixing pure elements in a quartz tube under Ar atmosphere in a glove box. The tubes are then pumped, sealed and heated to 650 °C in a rocking furnace. Resulting ingots are ground, cold pressed to facilitate diffusion and once again sealed in evacuated quartz tubes. These are annealed at 450 °C for several days followed by quenching in water. A stainless steel Specac pellet press is used to cold press the powder, producing pellets with a 10 mm diameter and height around 1 cm. The force applied is 5 t which corresponds to isostatic pressure around 600 MPa.

In the case of oxide materials, oxides or carbonates of the desired elements (namely $CaCO_3$, $MnCO_3$, Yb_2O_3, WO_3, Er_2O_3) were mixed and homogenized in an agate mortar. The mixture was then repeatedly homogenized and calcinated in an inert crucible (e.g. Pt) at high temperatures under air atmosphere.

3.1.2 Ball Milling

Ball milling is an effective method for grinding and mixing powder materials. Figure 3.1 depicts the principle of a planetary ball mill. A grinding bowl containing grinding balls and the ground material rotates on a main disc with high speed. At the same time, the bowl rotates around its own axis but in the opposite sense. Due to the simultaneous action of the two centrifugal forces, the balls and material lift off the wall and strike the opposite wall with very high force producing the grinding action. This intense process can reduce the particle size well below 1 µm. Both the bowls and the balls are made of a hard and wear-resistant material such as ZrO_2, Al_2O_3, agate, Si_3N_4, steel or WC. Rotation speeds may exceed 1000 RPM.

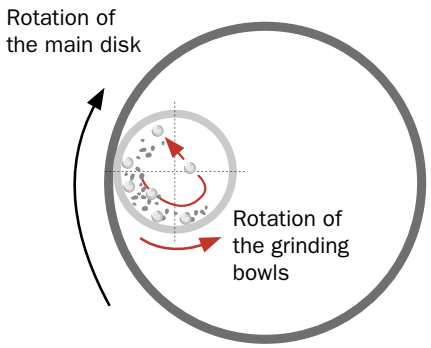

Figure 3.1: Principle of a planetary ball mill. *After [35].*

In this work, ball milling was used to mix synthetic $Cu_{12}Sb_4S_{13}$ with natural tetrahedrites. Pulverisette 7 premium or classic line made by Fritsch was used for this purpose. Grinding bowls made of ZrO_2 had 20 ml volume; the balls, 10 mm in diameter, were made of the same material. In all cases, the mass of the ground material was 3 g and six balls were placed in the bowl corresponding to a 6:1 ball-to-powder ratio. The powders were ground at 600 RPM for 90 min.

3.1.3 Sintering

After preparation or the synthesis process, samples are generally still not suitable for all measurements – following ball milling, they are in the form of a powder or, following annealing, in the form of porous, fragile and not necessarily homogeneous pellets. Pellets are ground in an agate mortar and suitable bulk samples are obtained by sintering the powder using the SPS method. The abbreviation stands for Spark Plasma Sintering which reflects the initial assumption about how the process worked. SPS is the prevailing way to call this method, so we will stick to that in this work. Sometimes other names are used which describe the method more accurately: Field Assisted Sintering Technology (FAST) or Pulsed Electric Current Sintering (PECS).

With SPS, the material to be sintered is placed inside a die with two pistons above and below. The die and pistons are commonly made of graphite but other materials such as SiC may be used. The sintering action is achieved by simultaneously applying pressure and heating the sample by passing current. If the sample is conductive enough, the current passes through, heating it via Joule heating. Nonconducting materials are heated by the heat resistively generated in the pistons and the die. SPS uses direct pulsed current with a period generally of the order of ms. Its magnitude reaches hundreds or even thousands of amperes; voltage is low, of the order of volts. Temperature is read with a thermocouple placed in a small hole in the side of the die close to where the sintered material is located. For temperatures above 700 °C, a pyrometer is used to monitor the temperature inside the hole. To prevent oxidation, sintering is performed in vacuum, either primary or secondary, or under controlled atmosphere, e.g. argon.

Initially, it was believed that sparks are generated between the grains of the sintered material, creating plasma and facilitating sintering. However, neither spark nor plasma has been observed. [34] As the exact mechanism of action is still a matter of controversy, we will not go into detail and limit ourselves to knowns facts, the most important one being that SPS is an established method capable of producing good results in a large number of cases. It allows good temperature control and rapid heating at rates reaching hundreds of $K.min^{-1}$, allowing the samples to be sintered within minutes. Besides saving time, short sintering times reduce grain growth, which is especially important for nanostructured materials.

In our experiments, we used the Dr Sinter 515S model manufactured by SPS Syntex. A high strength graphite die and pistons allowing pressures up to 80 MPa was used in all cases. Inner diameter of the die was 10.4 mm for all final samples; an 8.4 mm die was sometimes used for test runs to conserve material. Graphite sheet 0.2 mm thick was used to line the inside of the die and powder-facing sides of the pistons. After loading the powder, it is cold pressed with a hydraulic press at a pressure around 120 MPa before being placed in the sintering chamber. Minimum force 3.3 kN, corresponding to some 40 MPa, is applied and the chamber is pumped with a rotary vane pump until the pressure reaches some 7 Pa, at which point the sintering process is launched. Residual gas pressure may rise up to 40 Pa due to the chamber outgassing at higher temperatures but generally settles around 10 Pa after several minutes.

The sintering process starts by a one minute rise of the applied uniaxial pressure to the target value of 80 MPa which is maintained the whole time. The three-step temperature program is adopted from [12]. In the first step, the temperature is raised at 75 K.min^{-1} until it reaches 150 K below the target value. In the second step, the temperature rises to the target value at a slower rate, 37.5 K.min^{-1}. In the third step, the target temperature is maintained for 4 minutes. Then, both the electric current and pressure are switched off and the sample is left to cool to room temperature. Default target temperature is 723 K but for several samples this value had to be increased so the samples would be dense enough. For the natural samples, a different temperature program was used. First, a sample was heated at 100 K.min^{-1} to 20 K below the target value to avoid temperature overshoot, then to the target temperature in one minute. This temperature was held for approximately 90 s.

For every sintering run, a computer logs 7 process variables to a file for later analysis. These variables are sampled 10 times per second and include: die temperature, sintering voltage, sintering current, applied pressure, residual gas pressure, bottom ram position, and ram speed. Along with the temperature, the position of the ram, which is measured with a 0.01 mm resolution, is a very important quantity. As it is directly linked to the actual height of the sintered sample and therefore its density, it carries important information about the state of the process.

Figure 3.2 shows a typical course of sintering, in this case demonstrated with 1.54 g of $Cu_{10}Co_2Sb_2As_2S_{13}$ inside a 10.4 mm die. The figure shows several distinct phases of the sintering process:

1. Applied pressure is raised to the desired value 80 MPa, compressing the sample.
2. Temperature is raised, causing the sample to thermally expand.
3. At the 5:26 mark, the sample powder begins to sinter and therefore contract as its density rises.
4. Temperature ramp is lowered, the powder continues to sinter.
5. Target temperature is reached and held.
6. Sintering is finished as the sample reached maximum achievable density at the given temperature and pressure.
7. Pressure is released, causing the sample to expand, and current is switched off, allowing the sample to cool to room temperature.

SPS was used to sinter all tetrahedrite samples. In the case of oxides, SPS produced samples of inferior quality, which will be discussed later. The measurements presented in this thesis were therefore performed on samples synthesized and sintered by the CRISMAT laboratory in Caen, France. The samples were cold pressed and sintered at 1400 °C followed by slow cooling in order to avoid the formation of cracks when passing through the phase transition around 970 °C. Single-substituted oxides were uniaxially pressed into bar shaped samples; double-substituted oxides were isostatically pressed into pellets.

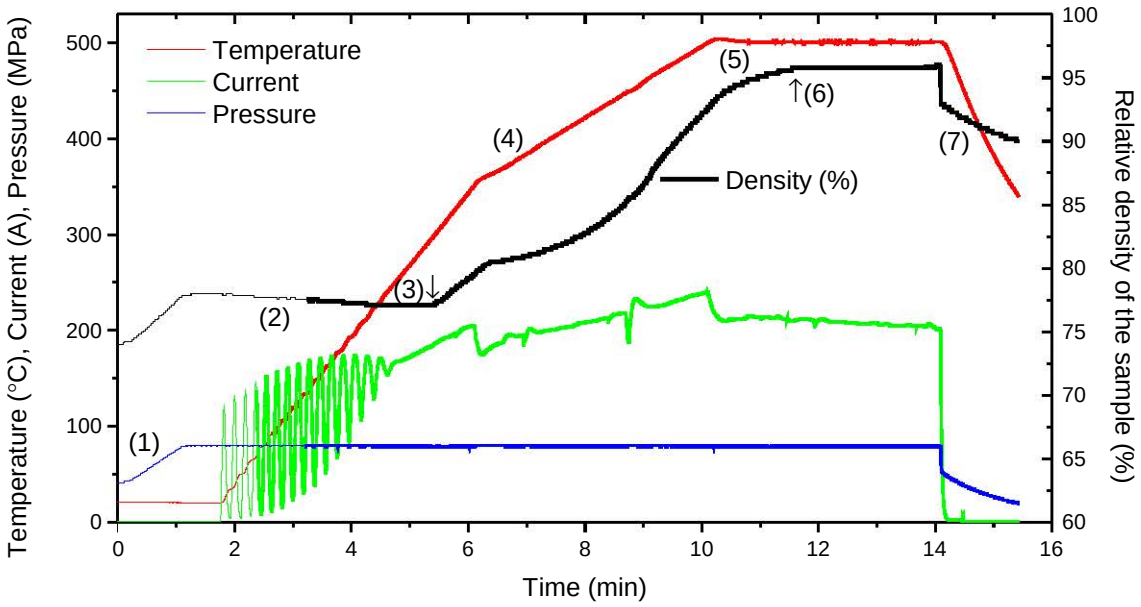

Figure 3.2: A typical course of sintering.

3.2 Characterization

The final goal is to measure thermoelectric properties of the samples, namely the electrical resistivity ρ, Seebeck coefficient S and total thermal conductivity κ. This is done both at low and high temperatures – down to ca 4 K and up to whatever temperature the material can withstand (ca 400 °C for tetrahedrites and 800 °C for oxides). Above room temperature, laser flash analysis (LFA) is used to determine the thermal diffusivity from which κ is calculated. The four probe method is used to measure ρ and S at all temperatures, either with a commercial or custom made apparatus. Below room temperature, the same method is used to determine all three parameters, again using a commercial or custom made set-up. Along the way, various supplementary techniques are also used to gather additional information about the samples and inspect their composition, structure and texture to make sure the obtained data are relevant. These methods include powder X-ray diffraction (XRD), scanning electron microscopy (SEM), electron probe microanalysis (EPMA) or heat capacity measurements.

The samples are generally obtained by sintering in the form of small round pellets, 10 mm in diameter and ca 4 mm in height. These are first polished to remove all carbon left on the surface from sintering. Then, a diamond wire saw is used to cut them up into smaller pieces geometrically suitable for further measurements, see Figure 3.3. First, a pellet is cut perpendicular to its axis to obtain a disc, roughly 1 mm in height, for laser flash analysis (left, green). The remaining pellet (right) is cut parallel to obtain two bar shaped samples for high and low temperature measurements. Leftover pieces are used for further analyses. All analyses are performed on pieces originating from a single pellet. Sample mass is determined with an analytical balance, the dimensions are measured multiple times with a digital calliper. Theor-

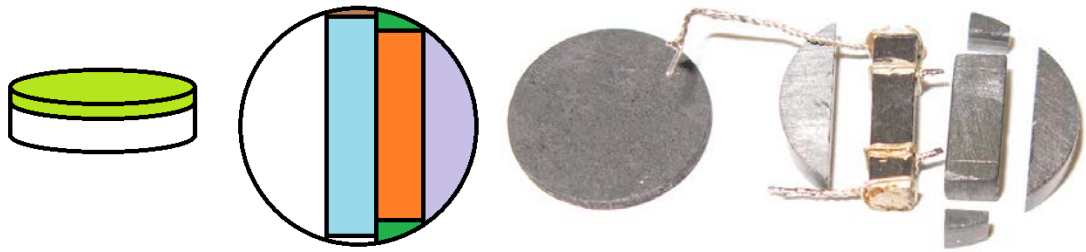

Figure 3.3: A pellet cut for various analyses, schematically and in a photo. Light green: LFA. Blue: low temperature transport, orange: high temperature electrical properties, dark green: XRD, purple: EPMA, brown: heat capacity.

etical density is calculated from molar mass, based on the chemical composition of the sample, and unit cell volume, based on XRD data.

3.2.1 Low Temperature Electrical and Thermal Properties

The measurements of the electrical resistivity ρ, both above and below room temperature, employ the four probe method. In the four probe setup, two of the probes are used to pass electric current through the sample. Another two probes are then used to measure the potential drop U on a section of the sample generated by the passing current I, as per Ohm's law: $R = U/I$. This allows us to measure solely the resistance of the actual sample regardless of contact quality (within reason). When using the two probe method, the measured resistance is the resistance of the sample plus the contacts plus the leads. Electrical resistivity, measured in Ω.m, is calculated using the sample dimensions:

$$\rho = R\frac{A}{l} = \frac{U}{I}\frac{A}{l}\,, \tag{3.1}$$

where A is the cross-sectional area of the sample and l is the distance between the voltage probes. The ratio l/A is referred to as the shape factor of the sample.

Measurement of the thermal conductivity is analogous. The analogue to Ohm's law is the Fourier's law for heat conduction, for the electric current (i.e. the flow of electric charge) we have the flow of heat, and for the electric potential drop we have the temperature drop:

$$\kappa = \frac{P}{\Delta T}\frac{l}{A}\,, \tag{3.2}$$

where P is the thermal power in W flowing through the sample and ΔT is the temperature drop. In reality, P is very difficult to accurately measure, unlike its electrical analogue I. It is usually determined from the power dissipated by a resistive heater but heat losses by radiation and by conduction through leads have to be accounted for. Radiation losses are extremely significant above room temperature and limit the temperature range in which the four probe method can be used for thermal measurements.

Measuring the Seebeck coefficient is fairly straightforward. It is defined as the ratio of a voltage drop induced by a small temperature drop on a material: $S =$

$-\Delta V/\Delta T$. And we can indeed measure it by directly measuring the voltage drop and the temperature drop and accounting for the Seebeck coefficient of the measurement leads themselves.

Two experimental setups were used in this thesis. One of them, a home made setup at the Institute of Physics, was used for most of the measurements. The other one is the Physical Property Measurement System (PPMS) commercial instrument by Quantum Design (QD) which was used by Prof Bertrand Lenoir to perform the measurements on natural tetrahedrites.

First, we will describe the home made instrument. The four contacts are made by wrapping four silver wires 0.2 mm thick around the bar-shaped sample and using silver paint to fill the gap between the sample and a wire. A thin layer of the paint is also applied to the two faces at the ends of the sample to ensure the equipotential planes are perpendicular to the sample. The paint is dried at around 200 °C by placing the sample on a hot-plate for some 10 minutes.

The sample is then affixed onto a sample holder, see Fig. 3.4. Its base is made of a copper plate onto which the sample is glued with the GE Varnish low temperature glue. A resistive heater in the form of an 8.2 kΩ SMD (surface-mount device) resistor is affixed on the top of the sample using the same glue and a small piece of a cigarette paper to electrically insulate the heater from the sample. The glue is dried at ca. 60 °C for tens of minutes. Four leads are soldered to the silver wires attached to the sample. Two type K thermocouples (chromel-alumel) with wires 0.1 mm thick serve both to measure the temperatures of the inner contacts as well as the voltage drop between them. Another type K thermocouple is soldered to the sample heater to better estimate radiation losses. A Lakeshore Cernox thin film thermometer is used to measure the temperature of the copper base which serves as the reference temperature for the thermocouples.

The sample holder is attached to the cooling head of a Sumitomo closed cycle helium refrigerator capable of cooling to 3 K. The sample holder is held in place by a screw and an Apiezon thermal grease ensures good thermal contact between the holder and the cooler. The measurement chamber contains two radiation shields and is pumped with a turbomolecular pump to ca. 10^{-3} Pa to prevent parasitic heat exchange through gas as well as gas adsorption on the sample.

The temperature of the system, referenced to a thermometer at the underside of the cooling head, is controlled by a Lakeshore 336 temperature controller. This controller is also used to read the temperature of the diode at the base of the sample holder. A Keithley 2401 current source is used to either supply DC current to the sample when measuring ρ or to feed the sample heater when measuring S and κ. The temperatures and voltages on the sample and on the sample thermometer are read with a Keithley 2001 multimeter equipped with a multiplexing card.

The whole measurement setup is controlled with a computer. The values of ρ, S and κ are measured at predefined temperature set points after temperature and voltage stability criteria have been met.

For the PPMS measurements, contacts were made by attaching thin, short and clean copper wires to the sample with conducting silver filled epoxy. A flattened end of the wire was attached to the top and bottom faces of the sample to serve as

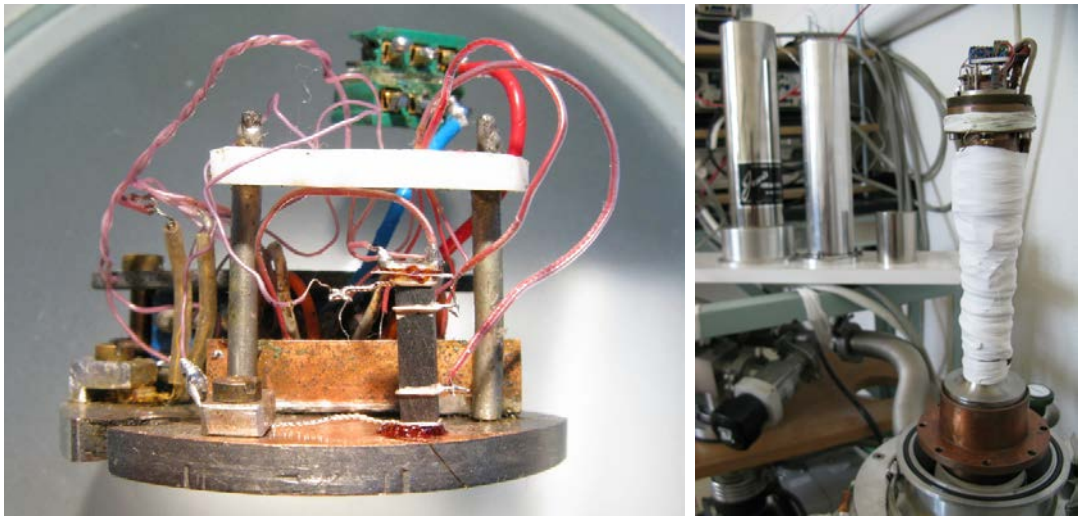

Figure 3.4: Low temperature experimental setup for measuring ρ, S and κ. The left photo shows the heatsink/sample holder with a mounted sample (grey bar). Note the heater on top as well as four silver contacts sticking to the sides with leads soldered on: thermocouples to the right and current leads to the left. The right photo shows the sample assembly mounted on a cold head of a He refrigerator which will be covered with radiation shields (in the background) and the whole sample chamber pumped with a turbomolecular pump (bottom left corner).

current contacts. In the case of potential contacts, two wires ran halfway around the sample.

PPMS is a sophisticated modular system. Its core is an inch-wide vacuum sample chamber in a liquid helium cryostat equipped with precision temperature control systems and a superconducting magnet coil. This allows the studied sample to be subjected to well-defined temperatures between 2 and 400 K and fields up to 7 or 14 T, depending on the model. There is a 12 pin connector at the bottom of the sample chamber which serves to electrically connect a sample holder with the outside world, e.g. with a current source or a voltmeter. Various experimental geometries can be envisaged for different sample holders which are nicknamed pucks by the manufacturer. To name a few, there are pucks for measuring electrical transport, heat capacity, thermal transport, etc.

The Thermal Transport Option (TTO) sample holder is used for simultaneous measurements of the electrical resistivity ρ (low frequency AC), Seebeck coefficient S and thermal conductivity κ. Its photo can be seen in Figure 3.5. The bottom electrode is clamped to the heat sink which also serves as the current electrode. To connect the other three electrodes, there are three *shoe* assemblies which are anchored to the electrodes with a tiny screw and are connected to the sample holder with long thin leads made of several individual wires. The wires are made of manganin with the exception of the copper-alloy wire carrying current to the sample which connects to the top electrode. Its shoe also contains a resistive heater which produces heat flow through the sample. The remaining two shoes are attached to the inner electrodes and are used to read their voltage and temperature. One

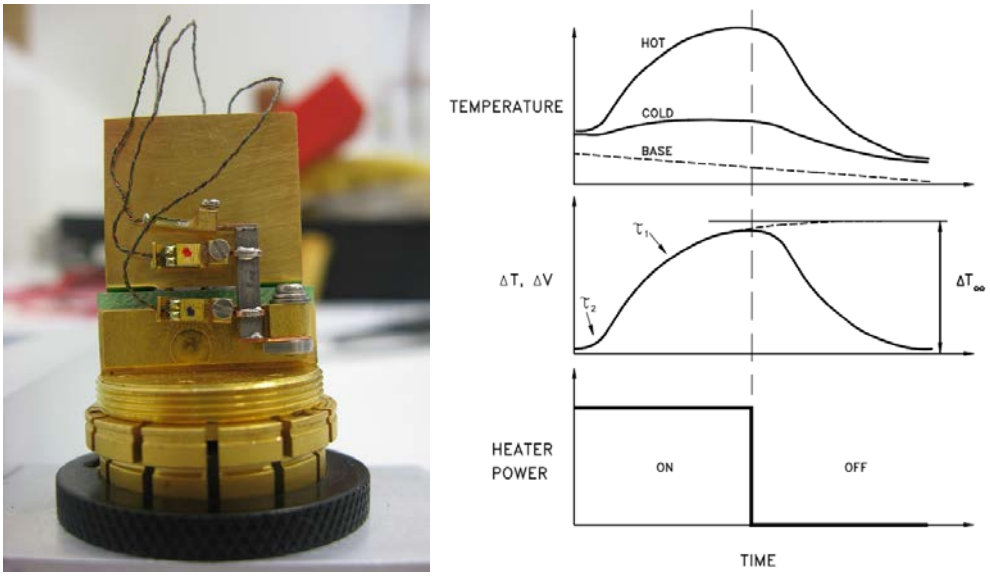

Figure 3.5: Left: A sample mounted on the sample holder for thermal and electrical transport measurements with PPMS. [36] Right: illustrative evolution of temperatures and voltage on the sample during measurement. Top panel: absolute temperatures of the inner hot and cold sample contacts. Middle panel: Corresponding voltage and temperature difference across the sample with an extrapolation to $t \to \infty$. [37]

wire soldered to the shoe is used for measuring the voltage and four wires are used to read the shoe thermometer which is electrically insulated from the shoe. The thermometer is a calibrated Cernox thin film whose resistance depends on temperature. There is one planar radiation shield which separates the sample from the lead connectors and another shield which covers the whole puck. [37]

The measurements with TTO can be performed either in a static or continuous mode. The intuitive static mode is the same as used with the home made instrument: the sample is cooled to a desired temperature and once the temperature is stabilised, a measurement is performed. In the continuous mode, the temperature of the whole system is slewed at a defined rate, which saves a big amount of time. Our measurements were performed in the continuous mode from 300 to 5 K with the slew rate around 0.35 K.min^{-1}.

Figure 3.5 right illustrates the evolution of thermal and voltage conditions during the measurement of one data point. The temperature of the base is linearly decreasing throughout the whole measurement. After the heater is turned on, a temperature gradient starts to establish across the sample, i.e. the temperature of the cold and hot electrode starts increasing. This projects into the temperature and voltage differentials which follow an exponential dependence, asymptotically tending to a certain value, with characteristic constants τ_i dependent on the thermal resistance of the sample and all thermal barriers as well as the heat capacity of the sample and the shoes. When the heater is turned off, the gradients decay exponentially. The measuring software uses a sophisticated algorithm, which also accounts for heat losses, to fit the temperature dependence of ΔT and ΔV. This model yields

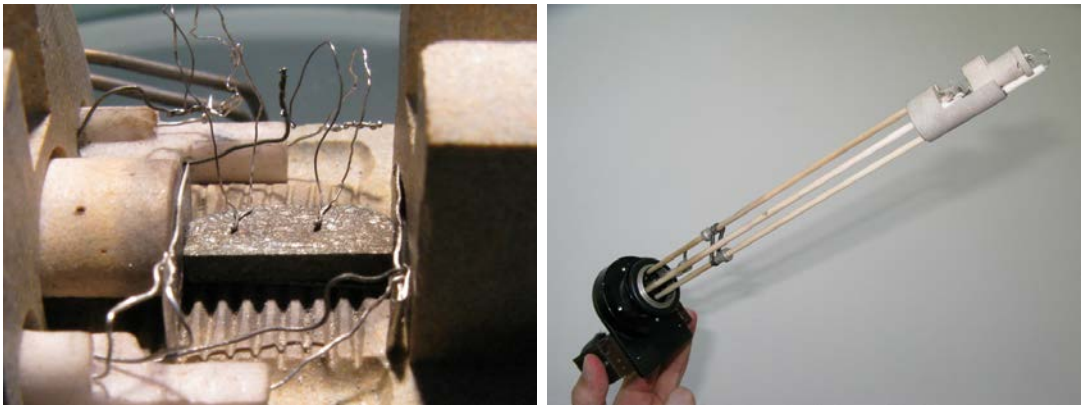

Figure 3.6: High temperature experimental setup for measuring ρ and S. The whole assembly is placed in a furnace.

the asymptotic values which are used to calculate S and κ. [37]

For samples comparable to ours, the manufacturer states the accuracy ±5 % for the Seebeck coefficient, ±0.2 % for electrical resistance, and ±5 % ±1 mW.K^{-1} for thermal conductance. When converting to resistivity and conductivity, we have to take into account the error in determining the sample dimensions which is several %. In the case of thermal conductivity, errors from radiation losses can become very significant when approaching room temperature. They can reach tens of % for samples with low thermal conductivity. Fortunately, the radiation-related errors cause a characteristic T^3 tail in $\kappa(T)$ which can be subtracted with further corrections. A comparison with the more reliable LFA method (see below) allows us to partially recover good values of κ.

3.2.2 High Temperature Electrical Properties

Electrical measurements above room temperature employ the same four probe geometry as below room temperature, the measurements of ρ and S are analogous. Due to very severe radiation losses, it is not possible to use this method to determine κ above 400 K. Two instruments were used for these measurements. One is a home made instrument at the Institute of Physics which was used for all samples besides tetrahedrites. The other one is the ZEM-3 commercial equipment manufactured by Ulvac-Riko which was used by Dr Christophe Candolfi to perform all measurements of tetrahedrites.

The sample assembly for the home made instrument is shown in Figure 3.6. The ceramic sample holder itself, shown on the left, is held by several ceramic capillaries which allow it to be suspended horizontally in a resistively heated furnace, taking care to position the sample in the centre of the furnace where the temperature distribution is the most homogeneous. The furnace can be heated to over 1000 K. On the other side of the capillaries is a fan-cooled connector which provides electrical connections to the sample as well as an inlet for inert gas.

The electrical leads running through the capillaries are made of thin platinum

wires chosen for of its oxidation resistance. Another set of leads is made of a Pt-Rh alloy which forms S-type thermocouples for measuring the temperature gradient across the sample. Four electrodes provide the contact with the sample. Each of the two current electrodes is made of thin platinum plates to which the Pt and Pt-Rh wires are clamped. The plates are pressed to the two opposite faces of the sample with a spring loaded capillary on one side and a resistive heater assembly on the other side. Two Pt/Pt-Rh thermocouples which rest atop the sample double as the voltage and temperature gradient probes. To provide firm contact to the sample, a thin mica sheet is placed across them and pressed down with a spring loaded arm.

The temperature of the furnace is controlled with a Eurotherm 3508 controller. The power to the sample heater is supplied by a custom made source. The current for sample resistivity measurements is provided by a custom made current source. An Agilent 34970A with a 34901A multiplexer card scan the voltage and temperatures on the sample.

The second instrumental setup for measuring ρ and S above room temperature is the ZEM-3 instrument made by Ulvac-Riko. The principle is again similar. An infrared gold image furnace serves as the sample chamber, the measurements are performed under helium atmosphere. The sample is pressed vertically between two blocs, one of which includes a heater. Thin graphite sheets are used for better mediation of current, heat and pressure from the blocks to the sample. Two thermocouples in capillaries are pressed to the side of the sample and their distance is measured with the help of an optical microscope. Again, they double as DC voltage probes for the determination of ρ, and temperature probes for the determination of S and ρ.

3.2.3 High Temperature Thermal Properties

We said earlier that the four probe method is not appropriate for determining thermal conductivity κ above room temperature because of severe losses through radiation. The radiation, however, is the cornerstone of another method: Laser Flash Analysis (LFA). This technique uses a short light pulse to heat one face of a thin sample. The heat diffuses through the sample and leads to a rise of temperature of the other face. This rise in temperature will manifest into increased radiation from this side, which is detected by a detector. The range of temperatures for which this technique is applicable is determined by the Stefan-Boltzmann law at the cold end of the range which lies between 100 and 150 K. The hot end of the range is limited mostly by the materials but can approach 2000 K.

As this is a dynamic method, we cannot directly measure the thermal conductivity κ of the sample but instead, we measure its thermal diffusivity α expressed in $\mathrm{m}^2.\mathrm{s}^{-1}$ (or in $\mathrm{mm}^2.\mathrm{s}^{-1}$ for more practical values). The two are linked together via the heat capacity of the sample:

$$\kappa = \alpha c_p D \,, \tag{3.3}$$

where c_p represents the specific heat capacity and D is the sample density.

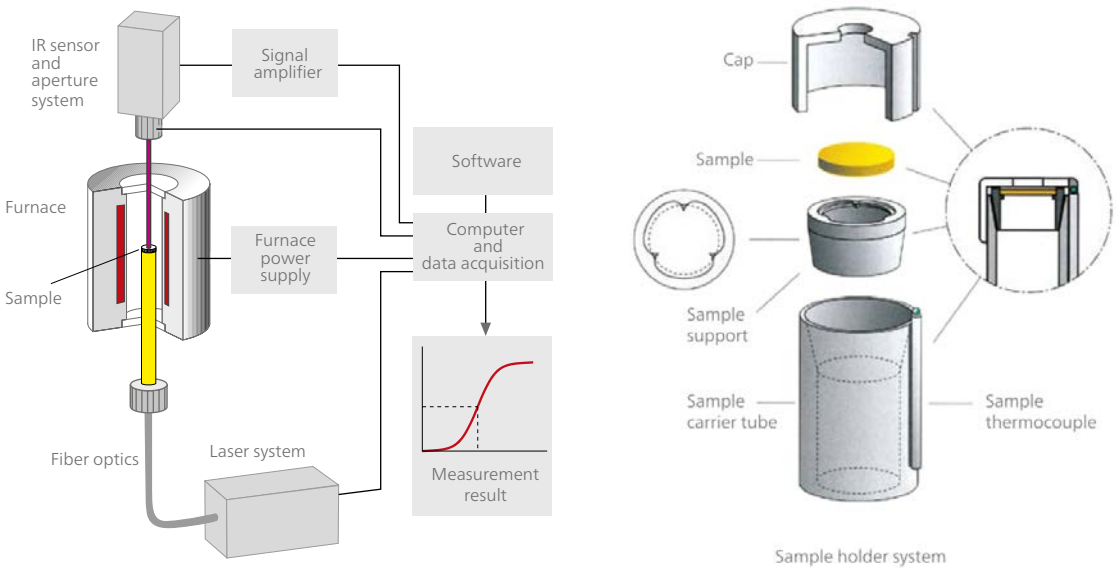

Figure 3.7: A schematic representation of the LFA instrument with a detailed view of the sample holder assembly. *After [39].*

Figure 3.7 schematically shows the workings of the Netzsch LFA-427 system which was used for all LFA measurements. The overall principle will be the same for other systems which may differ in the laser source, optics, sample holder etc. A near-infrared laser generates a short 0.3 ms impulse which is guided through an optical fibre into the furnace/sample chamber where it hits the sample. The chamber is continuously flushed with Ar at a 75 $cm^3.min^{-1}$ rate. The radiation originating from the other side of the sample passes through optical filters and is focused onto an InSb detector cooled by liquid nitrogen. The resulting voltage on the detector is amplified and acquired by a computer. The sample assembly is detailed in the right part of Figure 3.7. The laser pulse and argon flow come through an alumina tube with a thermocouple reading the temperature at the top. The sample rests on three small teeth of an Al_2O_3 sample holder which has the form of a centring cone which lays in the tube. This assembly is covered with a SiC cap.

The left part of Figure 3.7 also shows the shape of the registered signal which is a function of voltage over time. To obtain the value of thermal diffusivity a, the Parker model solves the heat equation in one dimension to get:

$$a = 0.1388 \frac{d^2}{t_{0.5}}, \tag{3.4}$$

where d is the thickness of the sample and $t_{0.5}$ is half the time it takes for the temperature of the hot side to rise to the final value. This adiabatic model is the simplest case and neglects, for example, heat losses. There are more sophisticated models, e.g. Cowan or Cape-Lehman, which take into account various losses of heat from both sides of the sample as well as lateral heat losses. [38] In reality, the value a is obtained by fitting the measured signal with a model. In most cases it is sufficient to use the Cowan model, which takes into account radiative and convective heat

losses from the surface into account, with an additional correction for the length of the heat pulse.

The sample has to be in the form of a flat disc or square with extra emphasis on the parallelity of the two faces. There are sample holders to accommodate samples between some 6 and 13 mm in width. The samples we measured were mostly round and 10 mm wide because of the SPS die used. Their thickness was between 0.5 and 1.3 mm but usually 1 mm. Each sample was carefully polished so that its thickness varied within ±0.02 mm but in most cases within ±0.01 mm. To assure well defined absorption of the laser pulse as well as emission from the opposite face, both faces of a sample were coated with a thin layer of graphite just prior to the measurement. This was done by very shortly spraying the face with graphite spray and blow-drying, followed by one more cycle of spraying and drying. The amount of graphite deposited on each side of a 10 mm wide pellet was around 0.25 mg which translates to roughly 3 µm, supposing 50 % porosity of the layer.

The measurements of diffusivity started at room temperature and generally continued in 50 K increments. At each temperature step, diffusivity was measured three times. The thermal conductivity of the samples was calculated from (3.3). The density was considered temperature independent and was calculated from the sample mass and dimensions which were measured with a digital calliper several times at several points. In the case of tetrahedrites, the heat capacity was estimated by the value given by the Dulong-Petit law; the molar mass was calculated from EPMA data for natural tetrahedrites and from the nominal composition for synthetic ones. The use of the Dulong-Petit value seems reasonable as the heat capacity of tetrahedrites does not change too much above 300 K. [12, 79] In the case of oxides, heat capacity was estimated from the literature and in the case of polymers, it was estimated from the measured data below room temperature, as will be discussed in the appropriate chapter. The electronic part κ_e of the thermal conductivity κ was calculated from (2.22). Unless otherwise stated, the value for free electrons was used. The diffusivity of six of the eight natural tetrahedrite samples was measured by Dr Jean-Baptiste Vaney.

Regarding the uncertainty of the thermoelectric measurements, we turn to the results of a complex study which involved several laboratories performing measurements of ρ, S, κ, and ZT on standardized skutterudite samples above room temperature. [43] We quote the main result: "The temperature-averaged (300–700 K) relative standard uncertainties at the confidence level of 68 % amount to 6 %, 8 %, 11 %, and 19 % for the Seebeck coefficient, electrical resistivity, thermal conductivity, and figure of merit ZT, respectively." The study also found that the determination of sample dimensions is a significant source of error and variation between laboratories. We argue that in our case, when one person with the same habits and patterns following the same procedures synthesised the samples, cut them to similar dimensions which were measured several times at several spots, which was followed by the same persons measuring the properties of the samples using the same instruments, then the samples can be compared to each other with reasonable accuracy even if their properties differ by less than the uncertainties given above.

3.2.4 X-ray Diffraction

X-ray diffraction (XRD) is a powerful experimental technique which is widely used to study crystal structure, microstructure, texture as well as to perform phase analysis. X-ray radiation with wavelength comparable to interatomic distances will be diffracted by regularly spaced atomic planes into specific directions. In the first approximation, this can be described by the famous Bragg equation:

$$n\lambda = 2d_{hkl} \sin\theta\,, \;\; n = 1, 2, 3, \ldots, \tag{3.5}$$

where λ is the wavelength of incident radiation, θ the angle between the radiation and the crystal surface, and d_{hkl} the interplane spacing.

With a more rigorous treatment, much more can be gained from XRD data by analysing the position, intensity, shape or width of the diffraction maxima. One example of such method is the Rietveld refinement for powder XRD. Here, a whole range of parameters is determined by fitting a simulated spectrum dependent on these parameter to the measured spectrum of intensity vs. θ. In powder diffraction, the sample is reduced to a fine powder of randomly oriented crystallites.

Our measurements were performed with a Bruker D8 Advance diffractometer in the θ-2θ Bragg-Brentano configuration. The radiation was Cu $K_{\alpha 1}$ ($\lambda = 1.54056$ Å) obtained with a germanium (111) monochromator. The samples were reduced to a fine powder and dispersed on a non-diffracting silicon sample holder with the help of two drops of cyclohexane. The sample holder rotated around its axis during spectrum acquisition. Phase analysis was performed with the help of the Diffrac.Eva software by Bruker working with the PDF-4 crystallographic database. The spectra of natural and successfully synthesised tetrahedrites were Rietveld-refined using the Fullprof software package.

3.2.5 Scanning Electron Microscopy

Another powerful and widely used experimental technique is Scanning Electron Microscopy (SEM). It uses a focused electron beam to scan (think old TV screens) across the surface of the sample located in a vacuum chamber. The beam interacts with the sample in a number of ways, producing various effects, e.g. back-scattering or diffraction of electrons, emission of secondary electrons, Auger electrons or characteristic X-rays or, for thin samples, the electrons can pass through the sample, as in a Transmission Electron Microscope (TEM). These effects can be used to study the sample morphology, crystal structure, texture, microstructure, local chemical composition etc.

Most of the SEM analyses presented in this thesis were performed using the Quanta 650 FEG instrument by FEI. The impeding electrons are scattered in the sample and their interaction with the sample is restricted to a relatively small volume with a typical shape resembling a pear. In the first several tens of nanometres, secondary electrons are produced. The SEM we used is equipped with an Everhart-Thornley detector (ETD) for their detection. Secondary electrons give information about the shape and morphology of the sample surface. Next, there are

back-scattered electrons (BSE) which originate from the first several hundreds of nanometres in the neck of the pear. The SEM is equipped with a back-scattered electron detector (BSED) for their detection. BSE can be understood as electrons which are elastically swung back by the positively charged nuclei. Heavier nuclei back-scatter more electrons than lighter ones, making areas of the sample with heavier atoms appear brighter on the obtained image. This allows qualitative chemical mapping of the sample. The last detector used for our purposes is a silicon drift detector by Bruker which detects the energy of characteristic X-rays generated in the whole pear-shaped volume of roughly $1\mu m^3$. These X-rays are produced by electrons from higher energy levels repopulating empty states which were left in lower energy shells by the beam knocking out electrons. This provides another probe into the chemical composition of the sample which goes by the name Energy Dispersive X-ray Spectroscopy (EDX or EDS). The EDX spectra are analysed with the Esprit 1.8 software by Bruker for qualitative analysis of the chemical composition of the samples (i.e. which elements are present), and also for semi-quantitative analysis (i.e. approximate concentrations of individual elements).

Bulk samples analysed with a SEM were polished using a sand paper with the grit size 2000 or 4000 and attached to an aluminium sample holder with double sided carbon tape. Samples which were in the form of a powder were first embedded in the Struers SpeciFix-20 cold mounting epoxy resin. This was done by first thoroughly dispersing the powder in a minute amount of the resin in a silicone mould so the powder could be kept close to the surface. More resin was then poured into the mould to obtain a larger specimen, and this process was done very carefully so the resin would not mix with the powder-resin mixture at the bottom. This specimen was then polished to uncover the powder. As the resin was electrically insulating, a thin layer of carbon was vacuum deposited to help remove the charge carried by the electron beam. SEM analyses of the powdered samples were performed by Dr Anne Dauscher. For secondary-electron imaging, the working voltage was generally 5 kV. For BSE imaging and EDX, the working distance was 11 mm and the working voltage 30 kV.

3.2.6 Electron Probe Microanalysis

In EDX, the X-ray detector is generally a solid state detector which detects the X-ray energies with a resolution around 100 eV. In Wavelength Dispersive X-ray Spectroscopy (WDX or WDS), the detection is done after the X-rays were first made to diffract on a crystal, decomposing the spectrum based on wavelength. This gives energy resolution better by an order of magnitude at the expense of longer count times. [40] To further improve the accuracy of chemical analysis, the concentration of an element in the sample is determined by comparing the intensity of its X-ray peak with the intensity of a peak from a standard of known composition. Such an analyser is often called the electron microprobe or the method the Electron Probe Microanalysis (EPMA).

To ensure accurate results, sample surface must be highly polished and parallel with the base. To achieve this, the samples were first embedded in a low melting

metal alloy composed of Bi (50 wt%), Sn (40 wt%) and Cd (10 wt%). This alloy has a melting point below 100 °C, is electrically conductive and fairly soft. The mount was placed in a Struers AccuStop sample holder which ensures very good parallelism of the two faces when polishing.

Increasingly fine sandpapers were used to polish the samples down to 4000 grit (ca. 5 µm particle size), spending several minutes at each step. Further polishing was performed with three Al_2O_3 suspensions of decreasing particle size, 0.5 µm being the last one. The polished surfaced was rinsed and inspected with an optical microscope between each step. A Struers OP-S colloidal silica suspension with 0.04 µm particle size was used for final polishing, followed by a thorough rinse in hot water and drying with a jet of warm air. To prevent the charging of nonconducting samples, their surface was coated with a thin layer of carbon deposited in vacuum.

Quantitative chemical analysis was performed with a Cameca SX 100 microprobe in collaboration with Dr Olivier Rouer at the Shared services centre for electronic microscopy and X-ray microanalysis at the Université de Lorraine. The standards used in the analyses are listed in Table 3.2 with their corresponding element. Several tens of points were analysed on each sample. After removing the outliers, the readings were averaged to give the final values. Results are normalized to 29 atoms per formula unit.

Table 3.2: Standards used for EPMA chemical analysis.

element	Cu	Ag	Zn	Fe	Hg	Co	Sb	As	S
standard	$CuFeS_2$	Ag	ZnS	FeS_2	HgS	Co	Sb_2S_3	GaAs	$CuFeS_2$

3.2.7 Magnetic Properties

Re-sintered samples of natural tetrahedrites were studied with respect to their magnetic properties. The measurements were performed with the MPMS-XL magnetometer manufactured by Quantum Design. Similarly to PPMS, this instrument consists of a liquid helium dewar container with a superconducting magnet and precise temperature control between 2 and 400 K. During a measurement, the sample moves through a system of superconducting detection coils which form a closed loop with a SQUID (Superconducting Quantum Interference Device). The magnetic moment of the sample induces proportional electric current in the loop. This very small change of electric current is detected by the SQUID, allowing us to determine the magnetic moment of the sample. [41]

Magnetic measurements were performed on D-shaped samples (see Fig. 3.3) weighing between 100 and 150 mg. Their magnetic moment M was measured with the temperature fixed at 300 K and varying the applied field H between 70 000 and −20 000 Oe, followed by measurements with the applied field fixed at 20 000 Oe and varying the temperature from 300 K to 2 K. During the field dependent measurements, the field was varied in steps ranging between 250 Oe at low fields and 10 000 Oe at high fields, and the superconducting magnet was in a persistent mode during each single measurement. During the temperature dependent measurements,

the temperature was swept at a rate of 0.5 K.min^{-1} between 2 K and 15 K and at 5 K.min^{-1} between 15 K and 300 K; measuring one data point took approximately 10 s.

3.2.8 Heat Capacity

Heat capacity C is the amount of heat it takes to increase the temperature of a substance by one degree. It is expressed in J.K^{-1} or, when related to the amount of the substance as the specific heat capacity, in J.mol^{-1}.K^{-1} or J.kg^{-1}.K^{-1}. Its value can be measured by various techniques and in solids, it is determined at constant pressure for practical reasons. Two common techniques are the relaxation method, which will be discussed later, and Differential Scanning Calorimetry (DSC). In DSC, the sample is placed in a crucible. This and another crucible with a reference material with known heat capacity are then placed on a platform in the measurement chamber. Both crucibles have individual heaters and thermometers. They are slowly heated in such a way that their temperatures are the same. The difference in heat flow required to fulfil this condition is used to calculate the heat capacity of the sample. A very similar method is the Differential Thermal Analysis (DTA) which uses constant heat flow to the two crucibles and their differing temperatures are used in the calculation.

The thermal relaxation method uses a defined heat pulse to the sample to slightly raise its temperature and the rate of change of temperature is used to determine the heat capacity. Heat capacity and therefore the relaxation times increase with temperature, which makes this method less suitable above room temperature. This method was used for heat capacity measurements within this thesis. The instrument used was once again the PPMS system by Quantum Design equipped with the Heat Capacity (HC) Option. The HC puck is a small calorimeter in which the sample rests on a 3×3 mm corundum platform suspended on eight thin wires, see Figure 3.8. The second purpose of these wires is to thermally anchor the samples and platform to the puck which serves as a heat sink. The thermal conductivity of the wires is calibrated to provide well defined heat flow between the platform and the sink. Other channels for heat flow are suppressed as much as possible – the puck is covered by a radiation shield to minimize radiation losses and the sample chamber is pumped with a turbomolecular pump to prevent heat loss through convection. The third purpose of the wires is to provide electrical contacts to the resistive heater and Lakeshore Cernox thermometer located on the underside of the platform.

The sample to be measured should be rather flat to reduce perpendicular heat flow and polished on the bottom side to enhance thermal contact with the platform. A small amount of grease is placed between the sample and the platform to provide good thermal coupling. When the heater is turned on, the temperature of the sample-grease-platform assembly starts rising. Normally, the evolution of temperature in time $T(t)$ can be described by a simple formula putting the heat flux absorbed by the assembly equal to the heater power minus conductive heat loss through the wires. The time constant of this system is directly related to its heat capacity. The heat capacity of the sample is obtained simply by subtracting the

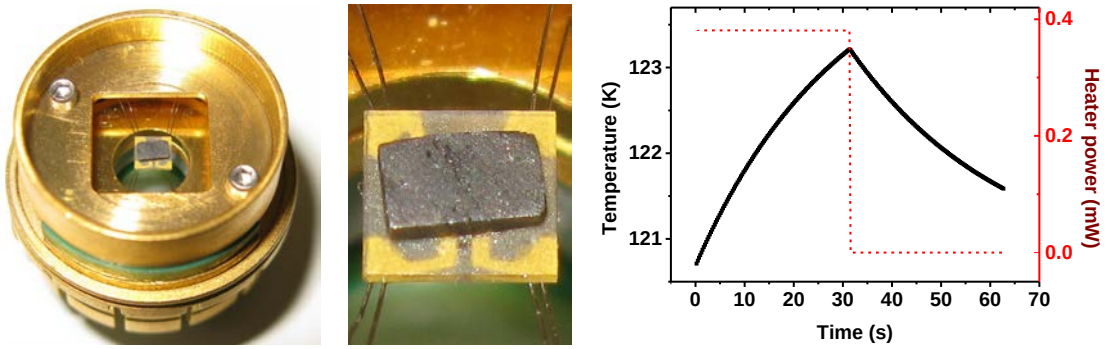

Figure 3.8: A sample mounted on a sample holder for heat capacity measurements with PPMS, a detail of the 3 × 3 mm sample platform and wires, and a typical temeperature vs. time trace. Heat capacity is calculated from the time constant which is determined by fitting the measured trace, both its heating and cooling section.

other contributions which were determined beforehand. When the thermal coupling between the sample and the platform is not good enough, the system will exhibit two time constants. If the coupling is not too bad, heat capacity can still be calculated using a more sophisticated model, named two-tau by the manufacturer. In both cases, the measured $T(t)$ trace is fitted with the model to obtain the heat capacity. [42]

In our measurements we used samples some 2 mm wide with a mass around 1 mg. They were coupled to the calorimeter platform with a small amount of Apiezon N grease. Determining this amount with analytical balance proved unsatisfactory. The contribution of the grease was therefore estimated by first measuring the heat capacity of the grease alone without the sample at 300 K. This value was used to calculate the contribution at other temperatures with the help of the specific heat of Apiezon measured previously between 2 and 300 K. The heat capacity of the sample was determined in 100 steps logarithmically spaced between 300 and 2 K. At each step, the system waited for the temperature to stabilise and then measured the heat capacity using a heat pulse which raised the temperature of the sample by 2 % of the absolute value.

3.2.9 Electronic Band Structure Calculations

Calculations of the electronic density of states (DOS) of the $Cu_{12}Sb_{4-x}As_xS_{13}$ series were performed by Prof. Janusz Tobola of the AGH University of Science and Technology in Krakow, Poland. The following description of the used technique and its settings was taken from [98]. The electronic densities of states (DOS) of $Cu_{12}Sb_{4-x}As_xS_{13}$ for $x = 0, 1, 2, 3$ and 4 were calculated using the Korringa-Kohn-Rostoker (KKR) method with the coherent potential approximation (CPA) that enables to treat explicitly the chemical disorder induced by As substitution on the Sb site. [99, 100] In these calculations, the local density approximation (LDA) parametrization of Perdew and Wang was employed for the exchange-correlation part. [101] The position of the Fermi level was determined accurately by the generalized Lloyd

formula. [102] For all compositions, the experimental lattice parameters and atomic coordinates determined from Rietveld refinements against the powder XRD data were used. For well-converged crystal potential and atomic charges (below 1 mRy and 10^{-3} e, respectively), the total-, site- and orbital-decomposed DOS were computed using a tetrahedron method for integration in the reciprocal k-space. [102] For $x = 0$ and 4, the complex energy dispersion curves were calculated in the first *bcc* Brillouin zone along high-symmetry directions. In the case of the two end-member compounds $Cu_{12}Sb_4S_{13}$ and $Cu_{12}As_4S_{13}$, their electronic structure was also calculated using the full-potential KKR method, which allows comparing with the KKR-CPA results obtained within the spherical crystal potential of the muffin-tin form.

Chapter 4

Results and Discussion

This chapter will present and discuss all the results obtained throughout the course of this thesis. It is divided into three parts, each belonging to one of the three material families studied: tetrahedrites, oxides and polymers. In the first and principal part, we study tetrahedrites in their natural and synthetic variants, as well as their mixtures. The second part deals with doped calcium manganese oxide and special emphasis is placed on their thermal conductivity. In the last part, we present data for three conducting polymers: PEDOT:PSS, PANI and PPy.

4.1 Tetrahedrites

The main focus of this thesis lies on the tetrahedrite family of materials, which are characterized by the general chemical composition $Cu_{10}Me_2Sb_4S_{13}$. Their investigation is divided into several sections. First, we characterize the thermoelecrical properties of natural tetrahedrites. Next, we mix natural tetrahedrites with synthetic $Cu_{12}Sb_4S_{13}$ using ball milling and study this process in detail, again interested in the resulting TE properties. The rest of the research is done on synthetic tetrahedrites. We study the effect of substitutions of arsenic for antimony on the properties of tetrahedrite with extra effort invested in understanding the thermal conductivity. Furthermore, we investigate various substitutions on the Cu site (e.g. Sn, Mg, Ca, Al, In, Ag).

4.1.1 Natural

Tetrahedrites have been known for decades and have been extensively studied from the geological, structural and chemical perspective, both in the natural and synthetic form. Up until 2012, their favourable thermoelectric properties went undiscovered and, as a consequence, there are virtually no data on electrical and thermal properties of natural tetrahedrites. We decided to fill this gap by performing a systematic study of these properties on 8 minerals.

We obtained several specimens from different parts of the world, for a list see Table 4.1. They were mostly bought from mineralogists at mineral fairs or online.

Table 4.1: Tetrahedrite minerals acquired for the study. Only the minerals in the first part of the table have been successfully characterized. Throughout this thesis, individual minerals are refered to by their *designation*.

designation	origin (country)	origin (location)	mass
France I	France	Isère	26 g
France II	France	Saint-Sylvestre mine, Vosges	13 g
Kazakhstan	Kazakhstan	Jezkazgan	3 g
Mexico	Mexico		24 g
Peru I	Peru		170 g
Peru II	Peru		31 g
Romania	Romania	Cavnic mine	6 g
Slovakia	Slovakia	Rudňany	8 g
	Bolivia	*Animas – Chocaya*	
	France	*Aveyron*	
	France	*Hérault*	
	Russia	*Dalnegorsk*	

Samples labelled Slovakia and France–Aveyron were donated by Prof Yves Moëlo from the Institut des Matériaux Jean Rouxel in Nantes, France. They came originally from Prof Michel Charlat from the Laboratoire de Minéralogie – Cristallographie of Université de Paris VI who used them in his studies of tetrahedrite chemistry and structure. Results concerning Slovakia and France-Aveyron can be found in [56, 57] under the references T7 and M5, respectively. The Mexico sample was donated by Prof Philippe Marion from the GeoRessources Laboratory. We are very grateful for all the contributions. Eight minerals, seen in Figure 4.1, were ground, sintered and characterized structurally, chemically, electrically, thermally and magnetically. All other samples were unsuitable for complete characterization.

Simple optical inspection of polished cross sections revealed that all minerals contained many cracks, both macroscopic and microscopic, see Figure 4.2. This fact, along with fluctuating chemical composition, prevented direct and relevant thermoelectric characterization, both due to the influence of interfaces and the fact that the minerals tended to crack and fall apart when heated. In the case of the Peru I specimen, we tried to cut a small bar shaped sample to measure the properties of the raw mineral. Only one bar out of three did not fall apart immediately but disintegrated into many pieces upon clamping between the electrodes of the ZEM-3 instrument and heating. The France I specimen was even more sensitive to heating and the heat from a table lamp while taking its photo caused several tiny chips to pop off the mineral.

It was therefore necessary to obtain samples in a more appropriate shape to measure the transport properties. We selected small pieces of the minerals and mechanically cleaned and sanded them to maximize the removal of surface layers or parasitic inclusions of foreign minerals (pyrite, chalcopyrite, quartz, ...) sometimes present. The products were then ground in an agate mortar into fine powders

Figure 4.1: Photos of the minerals. From top: France I & II, Kazakhstan & Mexico, Peru I & II, Romania & Slovakia.

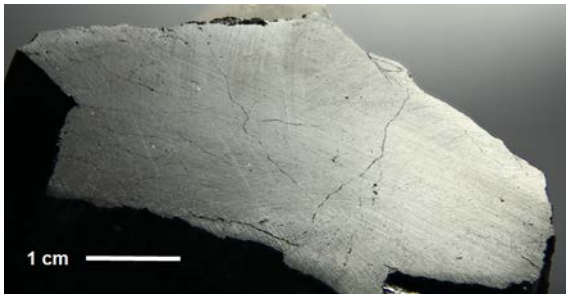

Figure 4.2: Cross section of the Peru I mineral showing numerous cracks.

to achieve mechanical and chemical homogenization and sintered by SPS. XRD patterns of all powders were acquired before and after sintering to rule out any decomposition or formation of other phases during the process.

Figure 4.3 shows several minerals which were discarded before further processing. This became obvious when the specimens were cut open. Generally, the minerals were discarded because separating pure tetrahedrite phase from the rest of the rock would be too difficult. In one case, XRD diffraction revealed that a mineral sold as tetrahedrite was in fact iron(II) sulfide.

For all sintered samples, we applied 80 MPa pressure, a heating rate of 100 K.min^{-1} and maintained the sintering temperature for roughly 90 s. This duration was enough for the samples to completely sinter, judged by the movement of the piston, and we did not want to keep it longer out of fear that the samples might decompose or be otherwise adversely affected by the elevated temperature. We began by sintering three samples (Mexico, Peru II, France II) at 723 K using the default temperature program described in subsection 3.1.3. However, the density of the sintered pellets reached only 82–85 % of the theoretical value.

To obtain denser samples we had to increase the sintering temperature as the sintering pressure was already at the maximum value for the SPS die. While 720 K is enough to produce dense pellets of synthetic $Cu_{12}Sb_4S_{13}$, temperatures 50—120 K higher were required to properly densify the natural minerals. At first, we performed differential thermal analysis (DTA) to try to determine the highest temperature each mineral can withstand. For the first two samples, Peru II and Mexico, we observed endothermic peaks with an onset around 830 K and 855 K, respectively. Indeed, sintering these two minerals at temperatures slightly below those determined by DTA yielded pellets with theoretical densities 94 % and 97 %, respectively. Further DTA experiments with two more minerals did not, on the other hand, reveal similar endothermic peaks. This could have been due to different behaviour of these samples as well as instrument malfunction. We therefore adopted a different approach.

In the end, the sintering temperature had to be optimized for each sample individually; this was done empirically by sintering each sample at different temperatures and monitoring the resulting density. In order to conserve material, these test runs were done with an 8 mm die and sintered pellets were ground and recycled for subsequent temperature steps. When the optimal temperature was found, freshly ground minerals with no thermal history were used to produce a final 10 mm pellet.

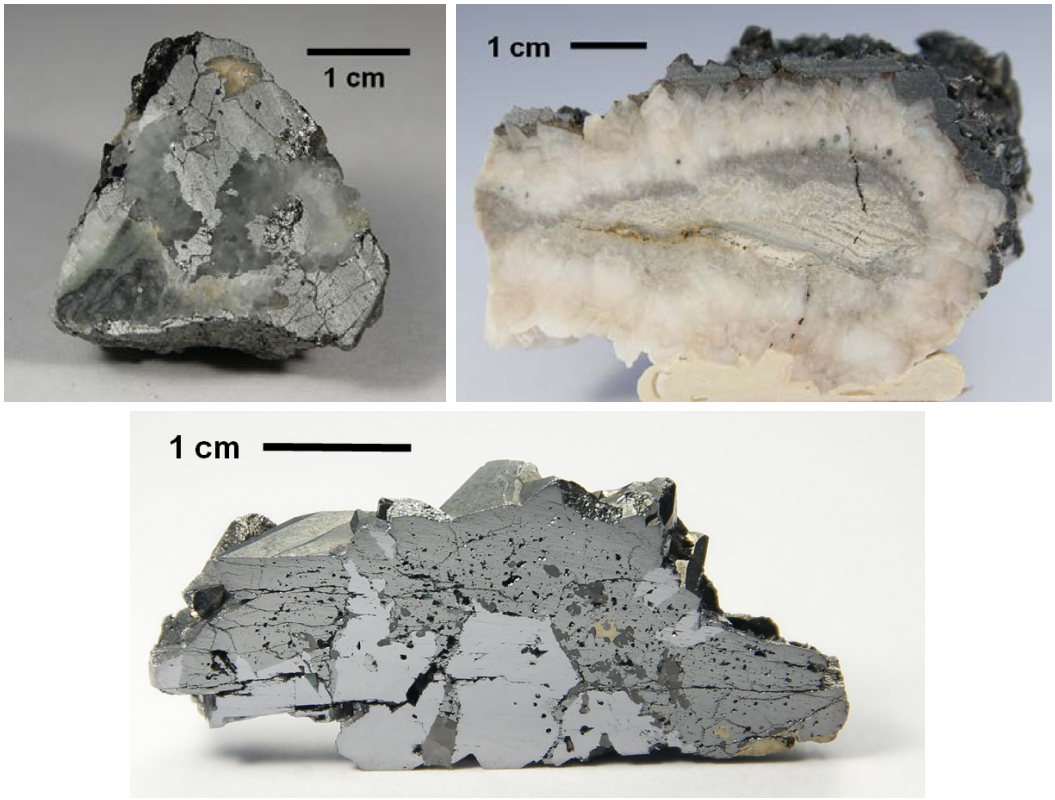

Figure 4.3: Minerals unsuitable for further characterization. From top: France (Aveyron & Hérault) Russia (Dalnegorsk).

Table 4.2: Properties of the samples sintered by SPS.

sample origin	sintering temp. (K)	relative density (%)	theoretical density ($g.cm^{-3}$)	cell parameter (Å)	molar mass ($g.mol^{-1}$)
France I	813	99	4.91	10.378(2)	1652
France II	823	94	4.89	10.360(9)	1638
Kazakhstan	823	96	4.62	10.220(8)	1484
Mexico	843	97	4.68	10.220(1)	1503
Peru I	793	94	4.71	10.288(1)	1543
Peru II	813	96	4.75	10.278(3)	1554
Romania	823	96	4.87	10.363(8)	1632
Slovakia	773	96	5.07	10.386(8)	1710

Table 4.2 lists the final densities of the samples used for measurements along with the optimum sintering temperatures.

Figure 4.4 shows the final XRD patterns of the sintered samples; all major peaks could be indexed to the tetrahedrite-tennantite phase with the exception of small impurities already present in the powder before for sintering. These include SiO_2 (quartz), FeS_2 (pyrite), $CuFeS_2$ (chalcopyrite) and ZnS (sphalerite). As these parasitic phases tend to grow on the surface of the minerals or the cracks extending into the minerals' interior (see Fig. 4.1), it is not possible to completely avoid their presence without the use of advanced techniques.

To rule out the possibility of decomposition and/or formation of secondary phases during sintering, the XRD patterns were compared with those collected before the sintering process. Compared with $Cu_{12}Sb_4S_{13}$, which decomposes above 750 K, [78] all the minerals studied show better thermal stability since they withstood the sintering temperatures 770–840 K without any observed degradation.

The samples were mirror-polished and EDX spectroscopy was used to identify all the elements present in the samples: these were Cu, Ag, Zn, Fe, Hg, Sb, As, and S representative of the tetrahedrite and tennantite minerals, as well as Si and O which form inclusions of both SiO_2 and pure Si. Electron Probe Microanalysis (EPMA) was then used to determine the chemical composition more precisely. The results, normalized to 29 atoms per formula unit, are summarized in Table 4.3.

Sample compositions agree well with what is expected for tetrahedrites and respect the following chemical formula: $Cu_{10}Me_2(Sb,As)_4S_{13}$, see [56, 59]. Tetrahedrite chemistry is known to be rather diverse, and we observe this attribute among our samples. The Sb:As ratio covers the whole possible range with France I being almost pure tetrahedrite (Sb end-member), Kazakhstan being almost pure tennantite (As end-member), and other minerals falling in between. Further variation is seen within the transition metals: Fe content ranges from ca. 0.1 atoms per formula unit (a.p.f.u.) for iron-poor minerals up to 0.7 a.p.f.u. for iron-rich minerals. The number of Fe atoms is complemented to 2 a.p.f.u. by Zn; in one case this role is assumed by Hg. The amount of Me metal atom is close to

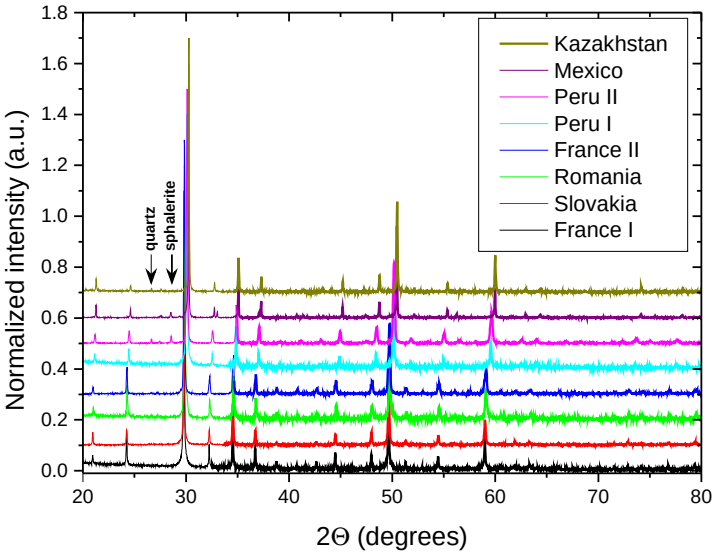

Figure 4.4: Powder XRD patterns of the studied minerals after sintering. All peaks could be indexed to the tetrahedrite-tennantite phase with the exception of small impurities (quartz, sphalerite, chalcopyrite, pyrite) which were already present in the powder before sintering.

Table 4.3: Chemical compositions of the studied minerals determined by EPMA.

	Atoms per formula unit ($Cu_{10}Me_2(Sb,As)_4S_{13}$)							
Sample origin	Cu	Ag	Zn	Fe	Hg	Sb	As	S
France I	10.21	0.02	1.15	0.71	0	3.82	0.02	13.06
France II	9.98	0.07	1.24	0.71	0	3.46	0.46	13.07
Kazakhstan	10.02	0.00	1.28	0.59	0	0.05	4.14	12.91
Mexico	9.93	0.01	1.56	0.37	0	0.46	3.66	12.97
Peru I	10.03	0.03	1.78	0.14	0	1.28	2.75	12.99
Peru II	10.03	0.04	1.82	0.11	0	1.45	2.59	12.92
Romania	10.07	0.06	1.82	0.11	0	3.13	0.86	12.94
Slovakia	10.29	0.01	0.27	0.68	0.85	2.56	1.33	13.01

2 a.p.f.u. for all the samples, suggesting rather full valence band and low electrical conductivity. Copper is substituted by a small amount of Ag, ranging between 0 and 0.1 a.p.f.u. As mentioned before, the Slovakian sample was studied some 40 years ago by Charlat et al. who determined its composition using EPMA to be $Cu_{10.19}Ag_{0.02}Zn_{0.22}Fe_{0.60}Hg_{0.97}Sb_{2.54}As_{1.36}S_{13.2}$. This agrees well with our results which gave $Cu_{10.29}Ag_{0.01}Zn_{0.27}Fe_{0.68}Hg_{0.85}Sb_{2.56}As_{1.33}S_{13.01}$. Especially the content of Sb and As is very similar in the two cases. Charlat reported slightly higher content of Hg at the expense of Zn and Fe. However, the sum Zn+Fe+Hg is strikingly similar: 1.79 a.p.f.u. measured by Charlat and 1.80 a.p.f.u. measured by us.

The cell parameters a of the samples listed in Table 4.2 are in good agreement with the general trends observed and studied e.g. in [57,59]. The Sb:As ratio has the main influence, with higher values leading to a larger unit cell. Additional increase in a can be seen for the Slovakian sample containing one Hg atom per formula unit. On the other hand, the widely varying Fe:Zn ratio is known to have negligible effect. [57, 59]

We probed the magnetic behaviour of six samples (Kazakhstan and Romania were not studied). First, we measured the field dependence of magnetization $M(H)$ of the samples at 300 K, then we measured the temperature dependence of magnetization $M(T)$ in 20 000 Oe down to 2 K.

Figure 4.5 shows the field-dependent magnetization at 300 K in the applied field H between −20 000 Oe and +70 000 Oe. The left part of the figure displays the measured magnetization shown per mole. Three distinct contributions superpose to give rise to the observed behaviour: 1) there is the weak omnipresent diamagnetism, 2) the positive slope of M reveals paramagnetism (PM), and 3) in four samples we also see the effect of ferromagnetism (FM). The first two contributions are characterized by a linear dependence of M(H), so it is easy to subtract this linear dependence to get a clear view of the FM contribution alone which is shown in the right part of the figure. Two features of ferromagnetism are evident: saturation and hysteresis (better seen in the inset).

Let us suppose that, for simplicity, this FM behaviour is caused by iron impurities located outside the tetrahedrite structure. If we take into account the saturation magnetization of metallic iron (221 emu.g^{-1} [44]), the saturation observed in our samples corresponds to the order of magnitude of 0.0001 atoms of ferromagnetic iron per tetrahedrite formula unit. More precise values are shown in Table 4.4. Since these values correlate well with the total amount of iron, and since the two iron-poor samples from Peru do not show the FM effect, we can rule out contamination and attribute the FM contribution to iron (or possibly iron oxide) impurities located outside the tetrahedrite phase.

Figure 4.6 shows the paramagnetic susceptibility $\chi = M/H$ of the samples measured in applied field of 20 000 Oe, corrected for the FM contribution. The measured data could be fitted with the Curie-Weiss law plus a temperature-independent diamagnetic term: $\chi = \chi_{dia} + C/(T - \Theta_C)$, where C is the Curie constant and Θ_C the Weiss constant. This paramagnetic response can be understood by supposing that the paramagnetic contribution originates mainly from the tetrahedrally coordinated Fe^{2+} ions in the tetrahedrite structure. [61, 62] In synthetic tetrahedrites containing

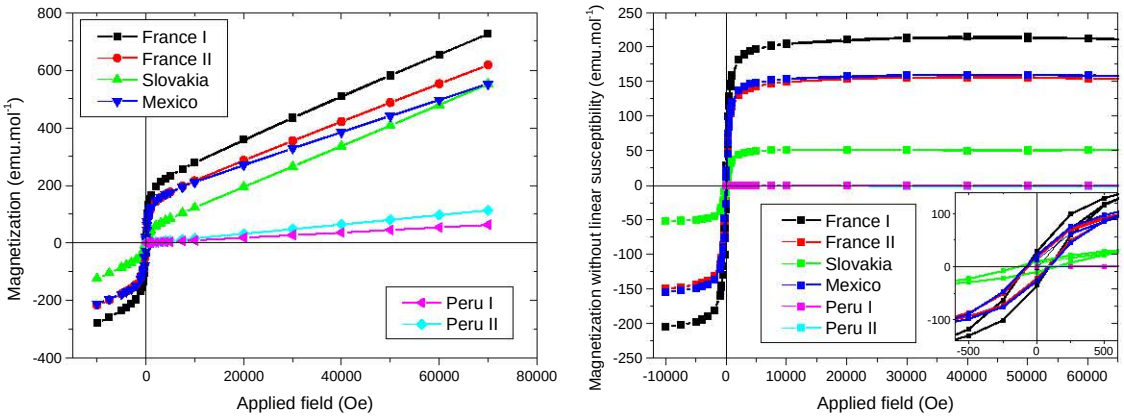

Figure 4.5: Magnetization curves $M(H)$ of natural tetrahedrites at 300 K. *Left: as measured. Right: extracted ferromagnetic contribution (inset shows a detail of the hysteresis loop).*

Table 4.4: Concentration of iron (in a.p.f.u.) in the natural samples determined by EPMA and from magnetic measurements. Ferromagnetic behaviour determined the concentration of iron in inclusions located outside the tetrahedrite structure. The M(T) dependence was fitted to obtain the concentration of paramagnetic Fe^{2+} ions along with the Weiss constant Θ_C.

Sample	EPMA	inclusions	paramagnetic fit	Θ_C (K)
France I	0.71	0.0006	0.82	-12
France II	0.71	0.0004	0.76	-12
Mexico	0.37	0.0004	0.62	-12
Peru I	0.14	0	0.14	-3
Peru II	0.11	0	0.21	-4
Slovakia	0.68	0.0001	0.76	-12

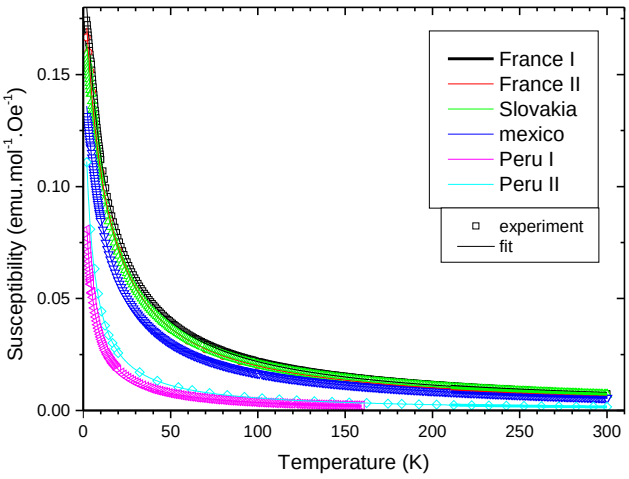

Figure 4.6: Temperature dependence of magnetic susceptibility of natural tetrahedrites measured in applied field of 20 000 Oe. *The ferromagnetic contribution has been subtracted from the data which are therefore showing only the diamagnetic and paramagnetic contribution.*

more than the natural amount of 10 Cu^{+} atoms per f.u., iron ions can compete with the extra copper ions formally in 2+ oxidation state to form Fe^{3+} species. All our samples, however, contain the standard number of ten Cu^{+} atoms, with the remaining two atoms on tetrahedral sites being a mixture of Fe, Zn or Hg. With the two latter being in the 2+ oxidation state, iron is also assumed to exist as Fe^{2+}, as predicted by Makovicky et al. [62]

Tetrahedrally coordinated Fe^{2+} ions are in the high spin d^6 configuration and have 4 unpaired electrons. With this in mind, we can extract the concentrations of the Fe^{2+} ions from the Curie constants. [16] The results are listed in Table 4.4 and correlate well with the concentrations determined by EPMA. The negative values of Θ_C point to antiferromagnetic interactions between iron atoms.

Figures 4.7, 4.8 and 4.9 show the measured temperature dependences of the four thermoelectric parameters, ρ, S, κ, and ZT, for all eight samples. The largest variation among the samples is seen in the case of electrical resistivity ρ which varies by one order of magnitude between the most and the least resistive samples. Electrical resistivity therefore has the largest impact on the figure of merit ZT. Based on the calculated band structure and chemical composition, we can expect the two metal ions to provide electrons to fill the holes in the valence band, rendering the samples semiconducting/insulating. This is indeed the case: all the samples display semiconducting behaviour with ρ decreasing fairly exponentially with increasing temperatures, a typical feature of lightly doped semiconductors.

This semiconducting behaviour is in contrast with the temperature variation of the Seebeck coefficient whose absolute values increase with increasing temperature for most samples, a feature seen in metals or highly-doped semiconductors. The

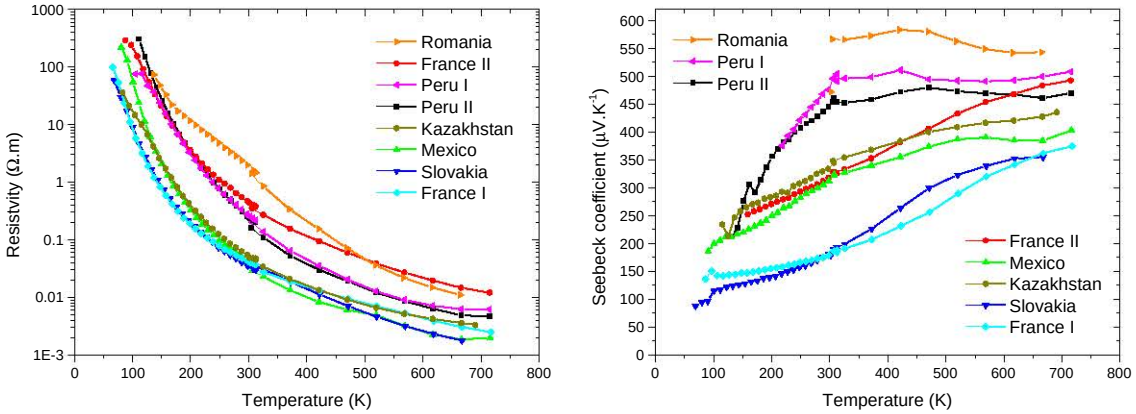

Figure 4.7: Temperature dependence of the electrical resistivity and Seebeck coefficient of natural tetrahedrites.

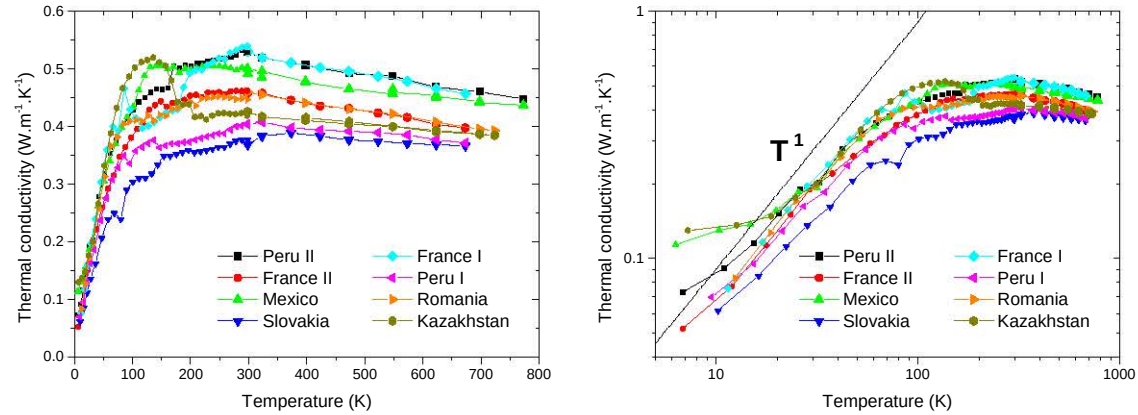

Figure 4.8: Temperature dependence of the thermal conductivity of natural tetrahedrites.

only samples with a fairly constant value of S above room temperature are Peru I, Peru II, and Romania, all of which contain significantly less iron than the other ones – 0.1 atoms per formula unit as opposed to 0.4–0.7. This difference in behaviour may be understood with the help of Figure 2.7 which shows calculated electronic density of states for $Cu_{11}Zn_1Sb_4S_{13}$ and $Cu_{11}Fe_1Sb_4S_{13}$. We see that Zn has no effect on the band structure near the Fermi level which is located near the top of the valence band (VB).[1] Iron, on the other hand, contributes additional impurity bands just above the VB. In this scenario, the iron-poor samples have a negligible impurity band and the Seebeck coefficient shows semiconducting behaviour. In iron-rich samples, this band is more pronounced and the steeper, metallic behaviour of $S(T)$ is caused by

[1]The effect of Hg ions is assumed to be analogous to that of Zn because of the similarity of their electron configurations.

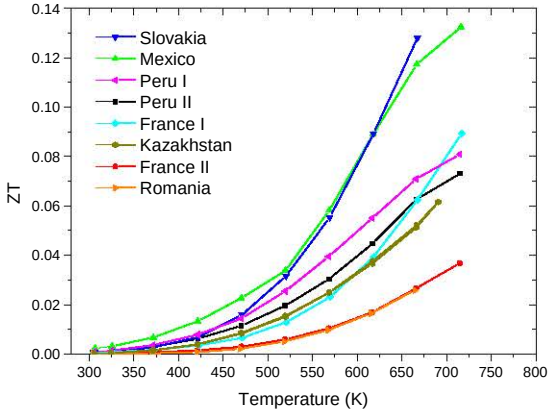

Figure 4.9: Temperature dependence of the figure of merit ZT of natural tetrahedrites.

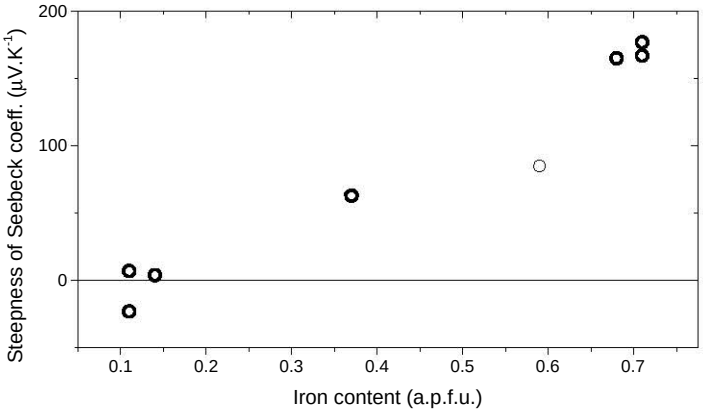

Figure 4.10: Steepness of the Seebeck coefficient as a function of Fe content. The steepness is calculated as the difference between the values of S at 673 and 300 K.

Fermi electrons populating the Fe impurity band.

Figure 4.10 presents a more quantitative approach to this assumption. It takes the steepness of S, calculated simply as the difference between its high- and room-temperature values, as the measure of metallicity. This is plotted as a function of Fe content which is responsible for the size of the impurity band. The three samples with a fairly constant value discussed above are located in the left part. We can clearly see that with increasing Fe content the steepness gradually increases as the samples become more metallic.

The magnitude of the electrical resistivity and its variation among the samples can be explained with the aid of Figure 2.6. $Cu_{12}Sb_4S_{13}$ is metallic, with the Fermi level below the edge of the valence band, whereas $Cu_{10}Zn_2Sb_4S_{13}$ is insulating because the additional electrons from Zn^{2+} atoms fill the holes in VB, pushing the Fermi level into the band gap. [69] If we assume that Hg^{2+} and Fe^{2+} atoms have

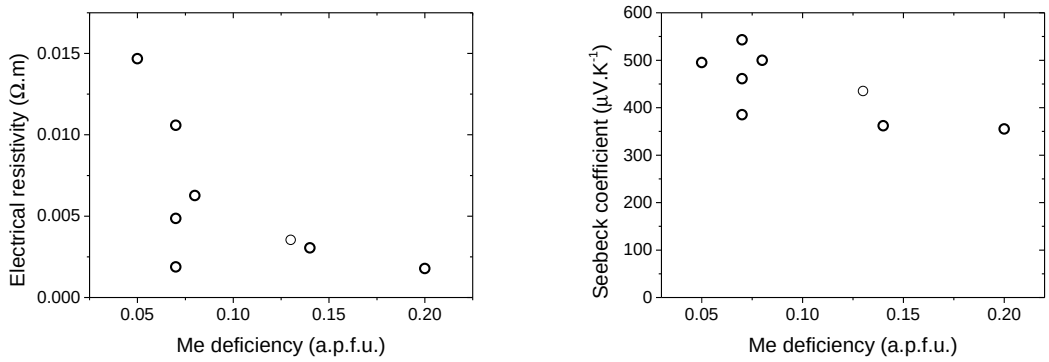

Figure 4.11: Electrical resistivity and Seebeck coefficient of natural tetrahedrites at 673 K as function of transition metal (Me) ion deficiency.

the same effect as Zn^{2+} (and neglect the effect of iron on the band structure), we can regard the Zn+Hg+Fe sum as a measure of filled holes. The lower the sum, the more holes will be available for charge transport. In other words, vacancies on the transition metal site will contribute to lower electrical resistivity. This can be seen in Figure 4.11 which shows ρ as a function of this deviation from full Me_2 stoichiometry. A similar trend is observed for S, where its value decreases as the system becomes more metallic with increasing hole concentration. In summary, the samples are not fully insulating because transition metal vacancies are responsible for their residual electrical conductivity.

Thermoelectric properties of mixtures of natural and synthetic tetrahedrites have been a subject of some studies. [13, 69, 70] Available data for pure natural minerals, however, remain scarce. For natural $Cu_{10.5}Fe_{1.5}As_{3.6}Sb_{0.4}S_{13}$, Lu et al. [69] reported values of ρ and S similar to those we measured for the Mexican sample. In the context of our data, their mineral therefore performs rather well. All attempts to improve TE properties of natural minerals by adding synthetic counterparts resulted in significantly higher ZT mainly because of the decrease of ρ by one or two orders of magnitude.

Tetrahedrites are known for their extremely low lattice thermal conductivity. [11, 69] This is valid for all our samples, which have thermal conductivity values above room temperature between 0.35 and 0.55 $W.m^{-1}.K^{-1}$. The electronic part of the thermal conductivity can be neglected because, according to the Wiedemann-Franz law, it represents less than ≈ 0.01 $W.m^{-1}.K^{-1}$ even for the most conducting sample. The apparent decrease of κ above room temperature is, to a certain part, caused by the fact that the Dulong-Petit law was used to estimate sample heat capacity. This tends to overestimate the real heat capacity in the lower part of the temperature range and in turn overestimate the thermal conductivity calculated from thermal diffusivity. The actual thermal conductivity should be flatter in the lower part of the measured range and approach the measured value in the upper part of the range. At low temperatures, the samples exhibit a T^1 dependence instead of following the standard T^3 law. This suggests that grain boundary scattering is not the dominant process here. In fact, with such a low lattice conductivity and

short mean free path, phonons get scattered multiple times on their journey from boundary to boundary.

We have not found any trends in κ which clearly depend on the chemical composition of the samples. We have especially focused on the antimony content because the atomic weight of Sb ($\approx$ 120 g.mol^{-1}) is much higher than that of other atoms contained in tetrahedrite ($\approx$ 30 g.mol^{-1} for S; $\approx$ 60 g.mol^{-1} for Cu, Zn, Fe; $\approx$ 75 g.mol^{-1} for As). This may possibly lower κ because of increased phonon scattering due to the mass difference. If the difference between Sb and other atoms played a role, we would see a decrease in Sb-rich samples. If the difference between Sb and As on the Sb site played a role, we would see a decrease in samples with Sb:As ratios close to 1. None of these cases was observed in the measured data. We can only remark that the sample containing heavy Hg ($\approx$ 200 g.mol^{-1}) has the lowest thermal conductivity.

The maximum ZT value we observed was 0.13 at $\approx$ 700 K for both the Slovakian and the Mexican sample. While this value is very low from the application point of view, we note it was obtained for samples without any important modification apart from simple grinding and re-sintering.

We characterized eight natural tetrahedrites from various places around the world. All the samples possessed very low thermal conductivity κ<0.5 W.m^{-1}.K^{-1} without a dielectric peak. At low temeperatures, κ followed the T^1 law, suggesting a different scatterring process than boundary scattering. The samples were not completely insulating but the resistivity was nevertheless high and varied by one order of magnitude between the least and the most resistive sample. This residual electrical conductivity is consistent with transition metal vacancies which supply carriers. Otherwise, we found no correlation between the thermoelectric properties and chemical composition (i.e. transition metal content, Sb-to-As ratio, etc.) On the other hand, all samples behaved as predicted by the theory and there were no surprises despite the varying composition, supporting the idea of the use of natural minerals in manufacturing TE devices. The best ZT was 0.13 at 720 K, a value spoilt mainly by the high electrical resistivity. Magnetic measurements below room temperature reflected the paramagnetism of Fe ions, as well as ferromagnetism of Fe outside the tetrahedrite structure.

4.1.2 Synthetic–natural Mixtures

In this section, we further investigate the idea presented in [13]. The authors demonstrated the fabrication of a tetrahedrite with optimal composition by mixing natural tetrahedrite mineral with synthetic $Cu_{12}Sb_4S_{13}$. The mixture was subjected to high energy ball milling and sintered. The resulting material was a perfect solid solution of the two ingredients and indeed showed favourable thermoelectric properties.

We performed several experiments mixing synthetic and natural tetrahedrite. The former, referred to as *synthetic* throughout this section, was $Cu_{12}Sb_4S_{13}$. The latter, referred to as *natural*, was the mineral designated Peru I in section 4.1.1 investigating natural tetrahedrites. Its chemical composition determined by EPMA

is $Cu_{10.03}Ag_{0.03}Zn_{1.78}Fe_{0.14}Sb_{1.28}As_{2.75}S_{12.99}$.

The first part of this section will deal with a 1:1 ratio mixture of the synthetic and natural compound. The mixture was ball milled for 90 minutes and throughout this process small amounts of powder were sampled at 10 minute intervals. These were then probed by XRD and SEM. The resulting powder was sintered and its TE properties measured. For comparison, another sample with a 1:1 ratio was prepared by simple grinding by hand in an agate mortar for some 15 minutes. This sample was also sintered, investigated by XRD and SEM and had its TE properties measured. For the second part, two more mixtures with 25:75 and 75:25 ratios were prepared and ball milled for 90 minutes. These were sintered and its thermoelectric properties are compared with the 50:50 mixture, as well as with pure synthetic and natural material.

4.1.2.1 1:1 Ratio

Figure 4.12 shows an XRD pattern of the 50:50 mixture prior to ball milling, along with patterns of its two constituent phases. Evidently, the pattern of the mixture is an average of the two. Because there is a small difference between the cell parameters of the two phases (a_{synt}=10.320, a_{nat}=10.288), the diffraction pattern of one phase is slightly shifted with respect to the other one. This results in an apparent split of the tetrahedrite diffraction peaks and allows us to distinguish each of the two phases in a diffraction pattern of the mixture (see inset of Fig. 4.12). There is a small amount of Cu_3SbS_4 present in the synthetic phase, as evidenced by its main diffraction peak at 28.7 °.

The mixture was then high energy ball-milled for 90 minutes. To monitor its evolution throughout the process, a very small amount of powder was taken after every 10 minutes of milling. Two additional samplings were performed in the beginning – after 2 and 5 minutes. This allows us to see the evolution of XRD patterns which are shown in Figure 4.13.

As the milling progresses, the diffraction peaks significantly broaden, which can be attributed to the reduction of the crystallite size well into the sub-micrometre range. This goes hand in hand with reduced peak intensity; it should be noted that the peak intensity also depends on the amount of diffracting material which somehow varied among the samples. By looking at 11 patterns, the decreasing trend is clearly seen though.

At first, it may seem as if the "left" peaks corresponding to the synthetic phase disappear and only single peaks remain. Careful inspection reveals that the angular position of the "right" peaks remains unchanged the whole time. Similarly, there is no observed shift of the left peaks within the first 30 minutes when they can still be told apart by eye. We therefore argue that the intensity of the left peaks, associated with the synthetic phase, simply decays faster than that of the right peaks, associated with the natural phase. After a certain time, the broad, latter peaks obscure the former ones. The faster decay can be explained by the fact that the synthetic phase is softer than the natural one, which leads to faster reduction of particle size during milling. A study on mechanical properties of tetrahedrite

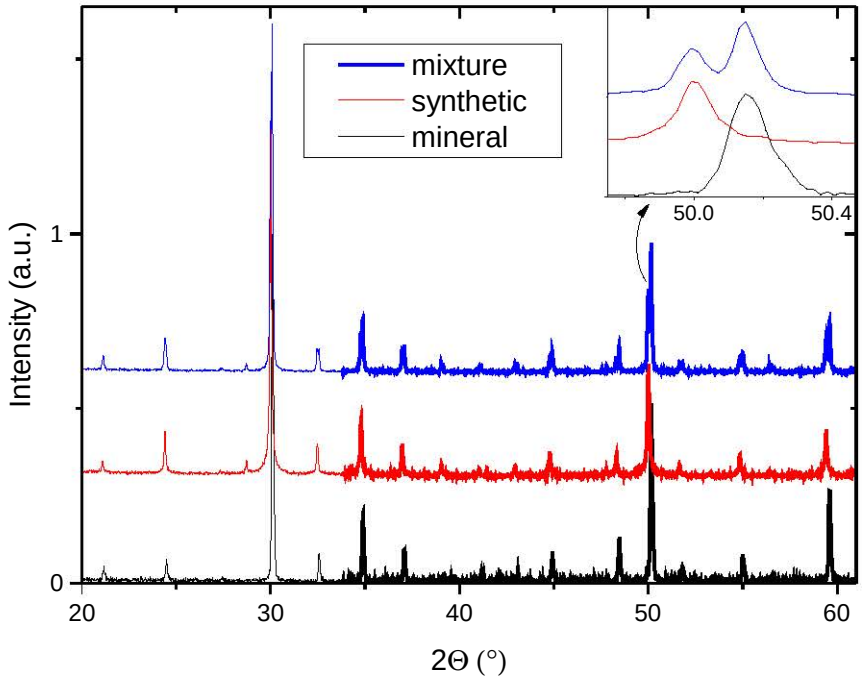

Figure 4.12: Initial powder XRD patterns of samples from the ball-milling experiment with 50:50 synthetic to natural tetrahedrite mixture.

[74] found synthetic $Cu_{12}Sb_4S_{13}$ to be softer than a natural tetrahedrite with a composition very similar to ours. Specifically, the Young's modulus, shear modulus and hardness of the synthetic variant were measured to be over 40 % lower that those of the natural variant.

The cell parameter of tetrahedrite is rather sensitive to chemical composition. The fact that the angular position of the diffraction maxima remains unchanged signifies that the two-phase composition of the sample is maintained throughout the milling process and no reaction between the two phases takes place. Furthermore, no formation of secondary phases could be detected.

Next, we investigated the evolution of the mixture by scanning electron microscopy. Powders after 0, 10, 20, 30, 60 and 90 minutes of ball milling were prepared for the analysis by dispersing a small amount of powder (on the order of milligrams) in an epoxy-based mounting resin. The results of chemical analyses are shown in Figures 4.14 and 4.15. The first set of images consists of back-scattered electron images. The second set maps the distribution of antimony by EDX. The images within each set are to scale and the two sets show the same 60×40 µm areas of the samples milled for 0, 10, 20, 30, and 60 minutes.

Back-scattered electron imaging, see Figure 4.14, distinguishes between different phases based on the atomic weight. Antimony is much heavier than other elements present in the samples and therefore has the largest influence. The heavier synthetic

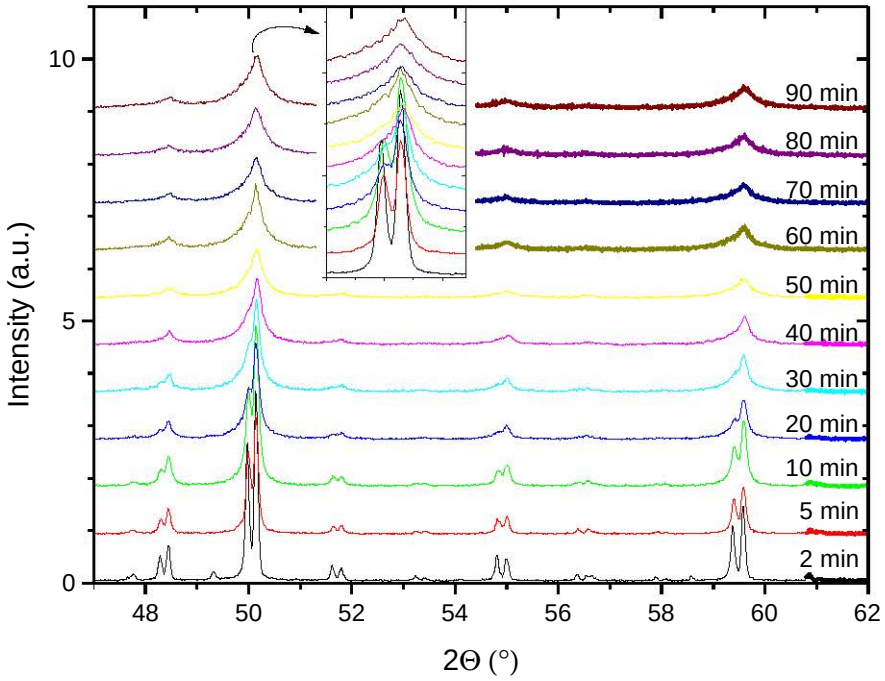

Figure 4.13: Evolution of XRD patterns during ball milling of a 50:50 mixture of synthetic and natural tetrahedrite.

phase, containing 4 atoms of Sb per formula unit, back scatters more electrons and shows up brighter in the images. The lighter natural phase, containing 1.3 a.p.f.u., back scatters less and shows up darker. The images clearly confirm the decrease of particle size of both phases, from the order of 10 µm at the beginning to the order of 1 µm after 30 min of milling. After 60 minutes, the two phases cannot be distinguished any more, presumably because the size of their particles is below the resolution of the BSE imaging method which is on the order of hundreds of nm for our material. [40] Another reason could be the chemical merging of the two phases into one but this seems very improbable because of the XRD results discussed earlier.

Figure 4.15 once again shows and confirms the reduction of particle size. The resolution of this method is slightly worse than in the case of BSE imaging. The pear shaped region below the surface from which the characteristic X-rays are produced has a volume roughly 1 μm^3. When the size of the particles of the two phases is much smaller than this volume, many particles are effectively averaged to produce a homogeneous image.

An important feature seen in Figure 4.14 (until the 30 minute mark when the two phases are still distinguishable), we see only two distinct shades of grey. This further supports the fact that despite the high energy present in the milling process, the two phases do not chemically interact and the two-phase composition is maintained at

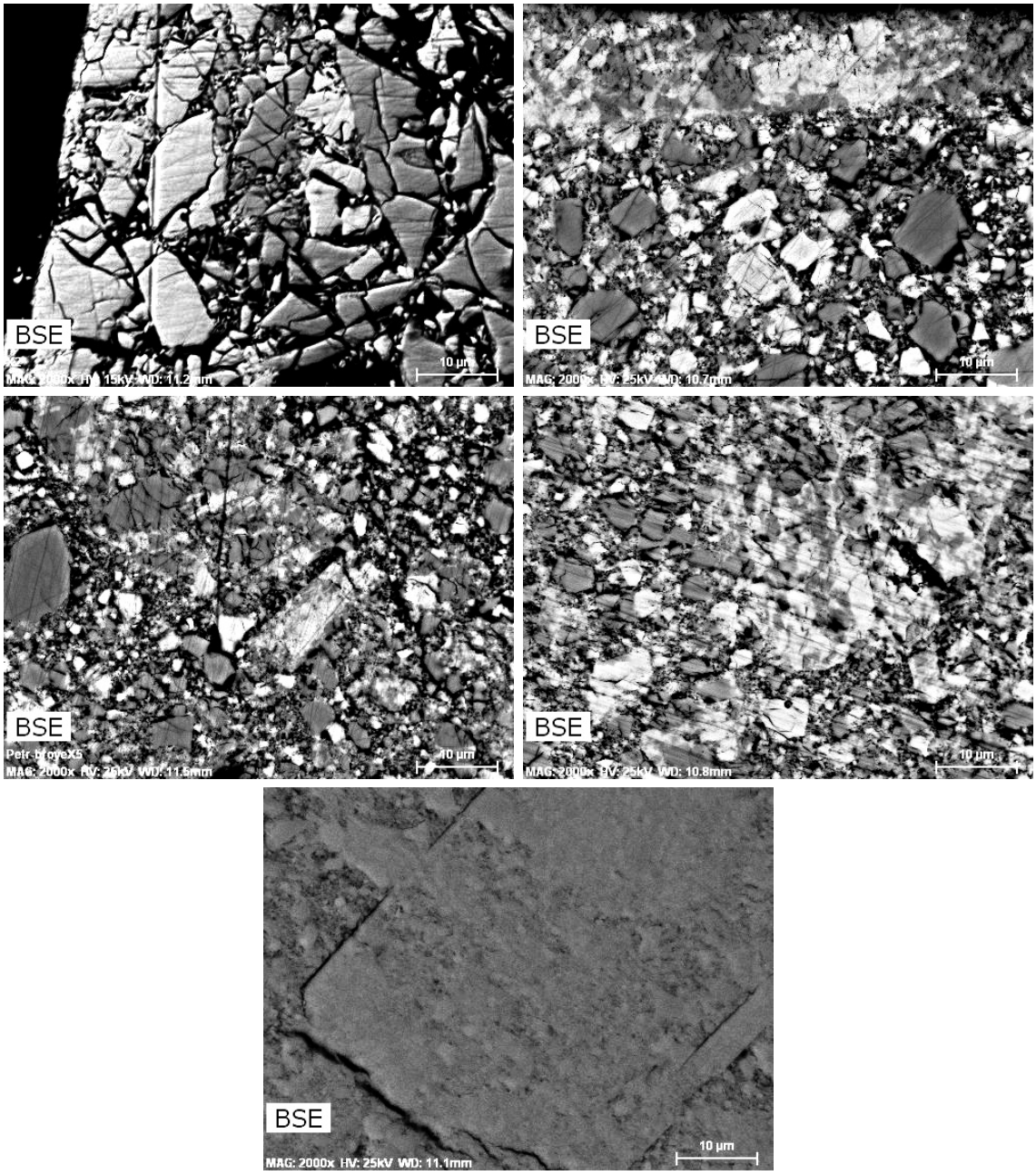

Figure 4.14: Back-scattered electron images of a synthetic–natural tetrahedrite mixture after 0, 10, 20, 30, and 60 minutes of ball milling. The images are to scale; their width is 60 µm. Darker colour indicates the natural phase, lighter colour indicates the synthetic phase.

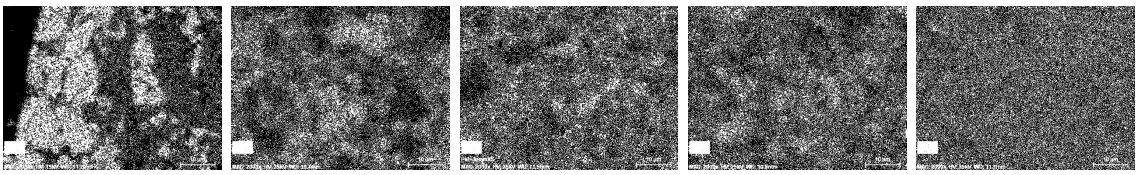

Figure 4.15: Distribution of antimony in a synthetic–natural tetrahedrite mixture throughout ball milling, as determined by EDX spectroscopy. The images are to scale, their width is 60 µm and they show the same area as those in Fig. 4.14.

least for the first 30 minutes. An effect of the high energy is demonstrated in Figure 4.16 left, which details a larger piece of a material apparently composed of much smaller particles of the two phases. The two clearly distinct phases are seamlessly welded together on a single particle.

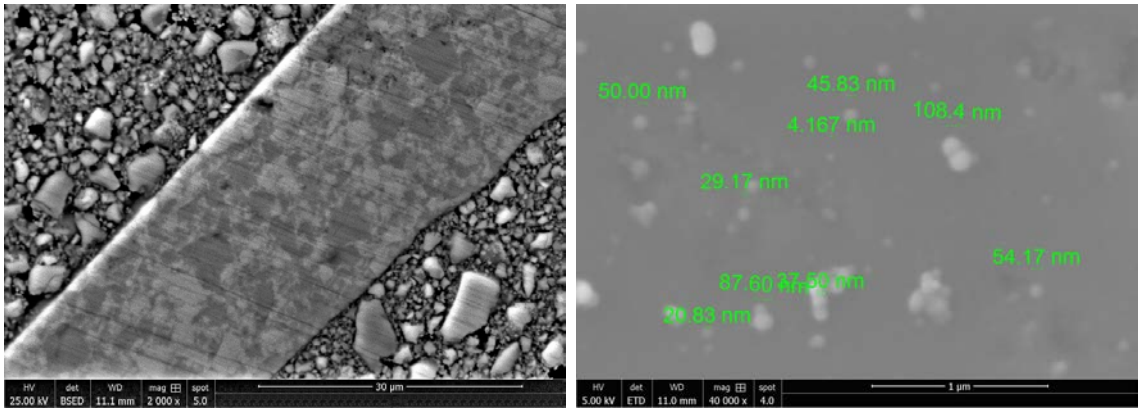

Figure 4.16: SEM images of ball milled synthetic–natural tetrahedrite mixtures. Left is a back-scattered electron image of a sample ball milled for 30 min. It details a larger piece apparently composed of much smaller particles of the two phases welded together. Right is a secondary electron image of a sample after 90 min of ball milling which gives an idea about the size of the particles.

Figure 4.16 right shows the sample after 90 minutes of milling. The powder was dispersed in a larger amount of mounting resin that in the case of other powders. This secondary electron image gives an idea about the size of the particles – on the order of tens of nanometres. This size is well bellow the spatial resolution of BSE imaging and EDX.

Figure 4.17 compares the XRD pattern of the final sample ball milled for 90 minutes with its initial state before ball milling, and the two constituent phases. Previously discussed peak widening due to reduced crystallite size is apparent. A small peak at 28.7 °, just left of the main peak, indicates that a small amount of Cu_3SbS_4 was present in the synthetic phase and therefore in the mixture. This phase apparently persisted during ball milling. No other phases were formed.

The powder after 90 minutes of milling was sintered by SPS. Figure 4.18 plots the evolution of relative sample density during sintering as a function of temperature. For comparison, the figure shows data for the 50:50 ball milled sample along with the 50:50 hand ground sample, and the 25:75 and 75:25 ball milled samples. The sintering programme was identical for all samples. The first thing to note is the lower initial density of the ball milled samples. A straightforward explanation is that the much lower particle size of the milled samples leads to increased total surface area, which impedes their packing.

Another thing to note is that the ball milled samples sinter at much lower temperatures than the hand ground material, whose density vs. temperature curve is fairly representative of all other non-milled tetrahedrites encountered throughout this thesis. The milled samples start sintering as soon the heating is started and

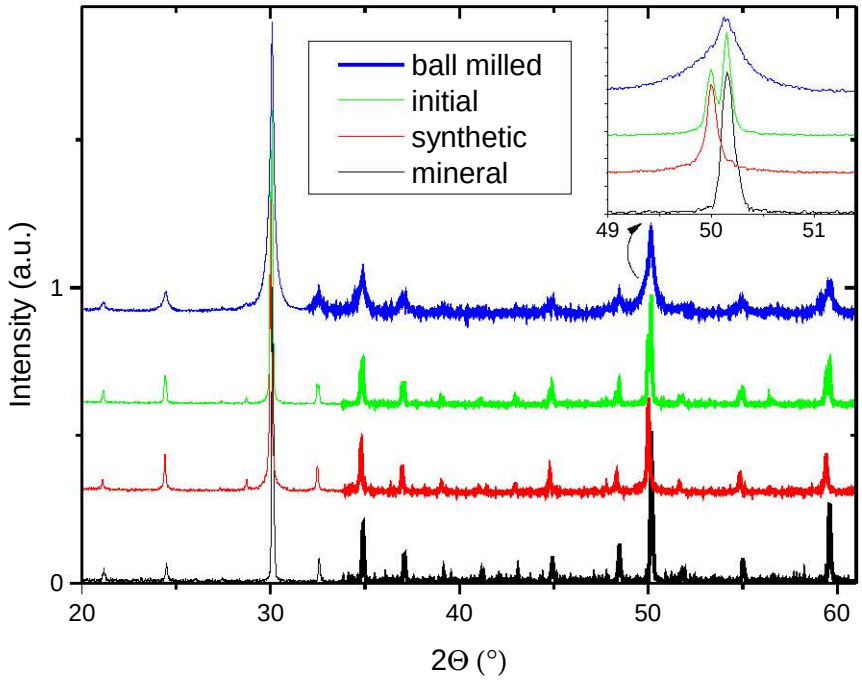

Figure 4.17: Powder XRD pattern of a 50:50 synthetic to natural tetrahedrite mixture ball milled for 90 min, along with initial XRD patterns for comparison.

rapidly reach 95 % relative density around 300–350 °C after which they slowly reach virtually full density. Once again, this marked difference between standard and milled samples is probably due to the largely increased surface of the nano-scaled samples.

Figure 4.19 shows the XRD pattern of the 50:50 ball milled sample after sintering. Patterns before sintering and before milling are shown for comparison. In the inset, we can clearly see a single diffraction peak where two peaks were initially present. This implies that a perfect solid solution of the two phases has formed. The new peak is exactly between the two initial ones, meaning that the new cell parameter is an average of the initial two. Sintering caused significant grain growth, as evidenced by the narrow peaks when compared to the ball milled powder. A small amount of a Cu_3SbS_4 phase was present in the initial powder and persisted throughout milling but was absorbed during sintering. The XRD spectrum of the hand ground sample (see Fig. 4.20) was completely unaffected by sintering.

Scanning electron microscopy on sintered samples showed the ball milled sample to be chemically homogeneous down to sub-micrometre level, i.e. to the spatial resolution limit. The hand ground sample preserved its two-phase composition, see Fig. 4.20 which shows a back-scattered electron image clearly showing the two phases. A closer look reveals that the sample is composed of darker islands of the natural phase in a rather homogeneous lighter matrix of the synthetic phase.

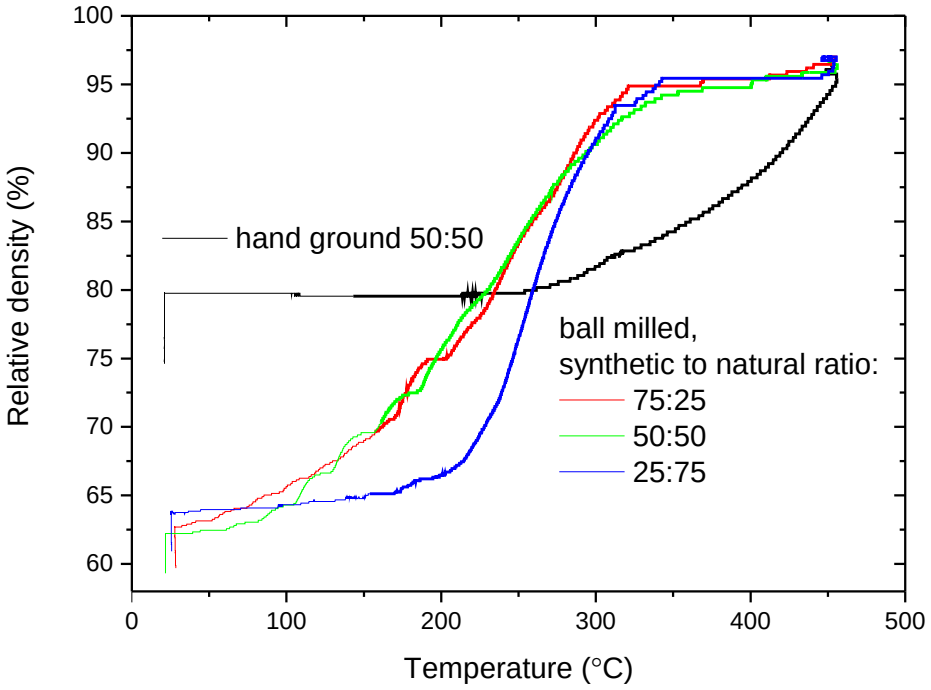

Figure 4.18: Evolution of relative sample density as a function of temperature during sintering of synthetic–natural mixtures.

The synthetic $Cu_{12}Sb_4S_{13}$ phase is softer [74] and less thermally stable [78] than the natural phase and therefore acted as a sort of a buffer, absorbing pressure and reshaping during sintering. This is in contrast with the harder natural phase which, at least in the case of its larger particles, retained its form.

Let us now have a look at the thermoelectric properties of the ball milled mixture. Figure 4.21 shows the temperature dependence of its electrical resistivity and Seebeck coefficient; the hand ground and pure synthetic samples are shown for comparison. The measurements were performed only in the 300–570 K range because of concerns about thermal stability (this will be further explained when discussing LFA measurements). The resistivity of the ball milled sample is constant in the measured temperature range, around 2.7×10^{-5} Ω.m. This value is about 2.5× higher than in pristine $Cu_{12}Sb_4S_{13}$. This increase can be easily explained by the Zn and Fe atoms filling the holes in the valence band, which goes hand in hand with an increase of S from 80 to 105 $\mu V.K^{-1}$. The absolute values of ρ and S are comparable to those observed for other $Cu_{11}Me_1Sb_4S_{13}$ substitutions. This further confirms the formation of a solid solution between the two constituent phases.

The hand ground sample, on the other hand, shows a different behaviour. Despite being prepared from identical starting materials as the ball milled sample, its

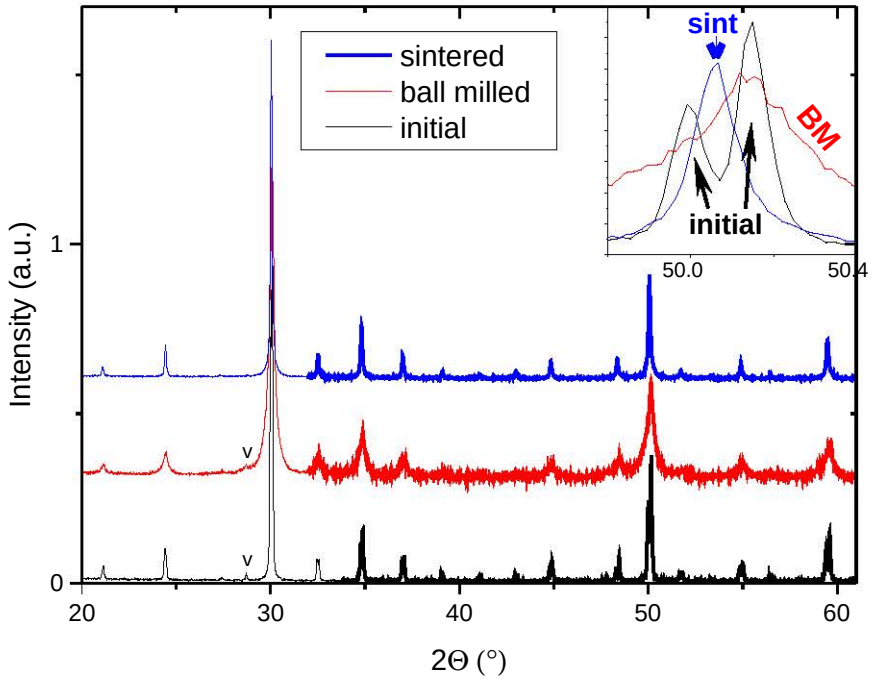

Figure 4.19: A comparison of powder XRD patterns of the initial, ball milled, and sintered mixture of synthetic and natural tetrahedrites. A small amount of a Cu_3SbS_4 phase is marked by ^{v}.

resistivity is higher by a factor of ≈2.3 and shows a semiconducting temperature dependence. The hand ground sample is essentially a composite material. Because of this, the transport mechanism is fundamentally different between the two samples. The composite nature can be nicely viewed from the back scattered electron image in Figure 4.20: it consists of semiconducting ($\rho \approx 10^{-2} - 10^{-1}$ Ω.m) islands embedded in a conducting ($\rho \approx 10^{-5}$ Ω) matrix. Interestingly, the Seebeck coefficient is the same for both samples.

Figure 4.22 shows the thermal conductivity of the samples as well as the factor ZT. The lattice contribution to the thermal conductivity above room temperature is around 0.4 $W.m^{-1}.K^{-1}$ in tetrahedrites – this is nicely represented by the natural sample whose electronic contribution to total κ is negligible. The drop in κ between the synthetic and the ball milled sample can be easily explained with the Wiedemann-Franz law linking the decrease of the electronic part to the 2.5× drop of ρ discussed above. The hand ground sample shows even lower values of κ. This could be expected, given its lower ρ, but we cannot apply the Wiedemann-Franz law in this case. This is because of the composite nature of the sample which is composed of two distinct phases – synthetic one with low ρ and high κ_e and natural one with high ρ and negligible κ_e.

The ball milled sample deformed during the LFA measurement – the originally

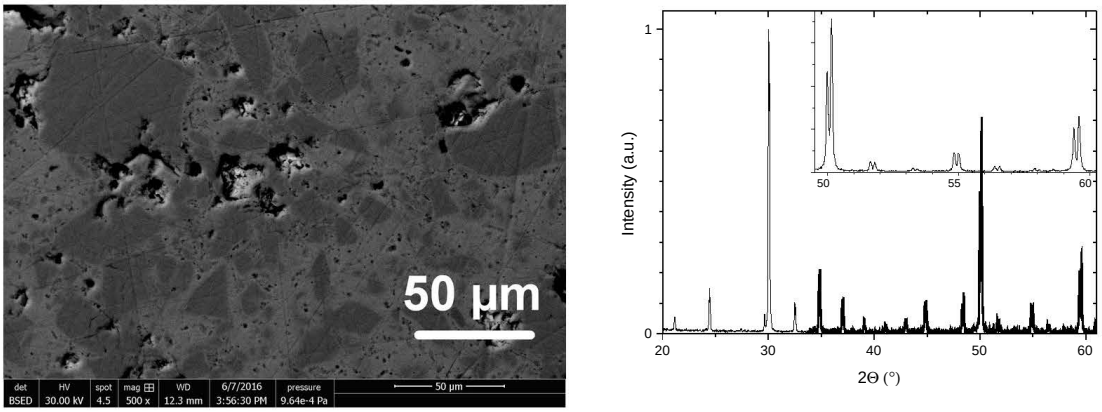

Figure 4.20: Back-scattered electron image and powder XRD pattern of a hand-ground synthetic–natural tetrahedrite mixture after sintering. Darker colour indicates the natural phase, lighter colour indicates the synthetic phase.

disc shaped sample bulged, having a contact lens shape when the LFA instrument was opened after the experiment had finished. This event occurred somewhere around 650 K, judging from the markedly decreased values of κ measured from this point onwards. These values cannot be considered relevant and have therefore been excluded from the graph as the shape of the sample differed from the correct geometry required for LFA measurements. Because of concerns about thermal stability, ρ and S were subsequently measured only up to 570 K. We were not able to replicate the deformation when heating the samples in a furnace. The reason for the deformation is not known. Possibly, the formation of a solid solution from the two phases did not have enough time to completely finish during the several minutes of sintering. Or, even if this process was completed, residual stresses may still have been present. The link to the solid solution formation is supported by the following facts: an anomalous increase of ρ and S around 650 K is seen in another ball milled sample (25:75 synthetic:natural ratio, see Fig. 4.25), and no anomaly was observed in the hand ground sample in which the phase composition is not influenced upon heating or sintering.

How does all that translate into the factor ZT when compared with the synthetic $Cu_{12}Sb_4S_{13}$? For the ball milled sample, the combination of increased S, decreased ρ and consequently decreased κ led to an increase of ZT around 17 % in the whole measured temperature range 300–573 K. In the hand ground sample, high resistivity led to an overall decrease of ZT. This decrease is best described in absolute terms as a drop by about 0.1 in the measured temperature range; in relative terms, this corresponds to a drop between 50 % around room temperature and 20 % at 550 K. All in all using identical starting ingredients, the two methods gave rise to two different materials with ball milling producing a superior sample with respect to thermoelectric properties. The crucial advantage is the ability to reduce the particle size enough to allow mixing of the two constituent phases on the atomic level. The resulting single homogeneous solid solution was thermoelectrically superior to

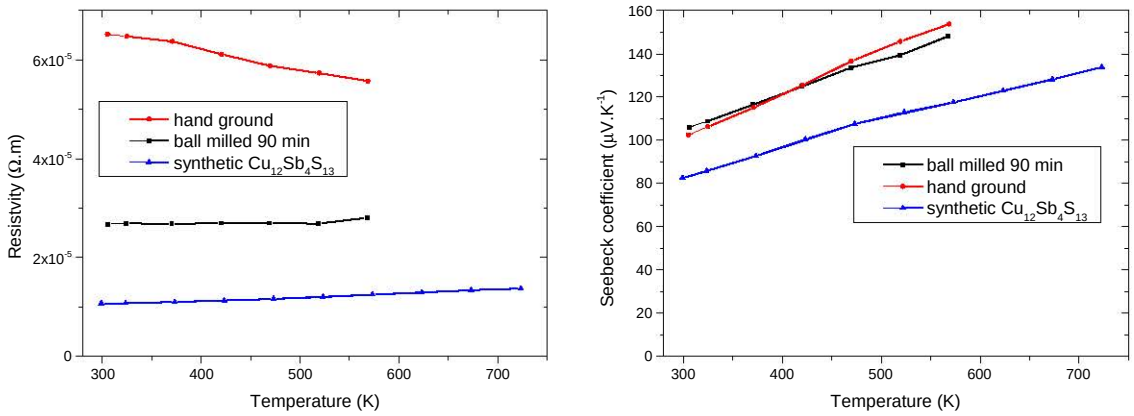

Figure 4.21: Temperature dependence of the electrical resistivity and Seebeck coefficient of a 50:50 mixture of synthetic and natural tetrahedrites prepared by ball milling and by hand-grinding.

a composite sample made up of two distinct phases.

Let us now compare our data with other published results. To the best of our knowledge, there are only two articles reporting on synthetic–natural tetrahedrite mixtures, both by Lu and Morelli. In the first article [13], the authors prepared two series of samples by ball milling two natural tetrahedrites with synthetic $Cu_{12}Sb_4S_{13}$ in 1:3, 1:1 and 3:1 ratios. According to XRD and EDX analyses, their hot pressed samples were single phase solid solutions. The chemical composition of their natural phases was determined by EDX to be $Cu_{10.5}Fe_{1.5}As_{3.6}Sb_{0.4}S_{13}$ and $Cu_{9.7}Zn_{1.9}Fe_{0.4}As_4S_{13}$. In our case, the composition of the natural phase was determined by WDX to be $Cu_{10.0}Ag_{0.03}Zn_{1.8}Fe_{0.1}Sb_{1.3}As_{2.7}S_{13}$. In a subsequent article [70], the same authors ball milled the latter mineral from the first article directly with elemental Cu, Sb and S in a 12:4:13 molar ratio. Thermoelectrically best performing samples from this study were prepared from 1:1 mineral:elements ratio after 3 and 6 hours of milling. Their values of ρ, S, κ and ZT are very similar to the 1:1 mineral:$Cu_{12}Sb_4S_{13}$ sample from the first article, and the samples also formed dense single phase homogeneous solid solutions.

Figure 4.23 compares ρ, S, κ and ZT of our ball milled sample with the 1:1 samples of Lu and Morelli. The electronic properties are determined largely by iron concentration. One zinc atom can only supply one electron as Zn^{2+} to fill the valence band holes in tetrahedrites. Iron, on the other hand, can exist both as Fe^{2+} and Fe^{3+}, supplying one or two electrons, respectively, as needed. Mixing a filled natural tetrahedrite with $Cu_{12}Sb_4S_{13}$, containing 2 holes per formula unit, creates an electron deficient system. As there are most often close to 2 a.p.f.u. of Zn and Fe in natural tetrahedrites, the ability to fill the holes is determined by the amount of iron available to give the extra electron. This effect, already described in [13], is in agreement with the ρ and S curves in Figure 4.23: Lu's iron-rich sample is the most resistive with the highest S, while our sample, very poor in iron, shows the

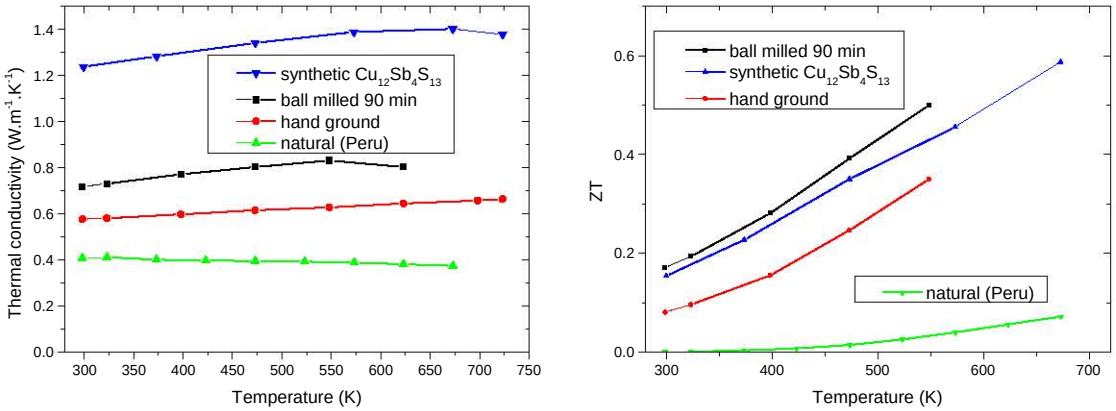

Figure 4.22: Temperature dependence of the thermal conductivity and ZT of a 50:50 mixture of synthetic and natural tetrahedrites prepared by ball milling and by hand-grinding.

lowest values of ρ and S.

When looking at the temperature dependence of thermal conductivity, we see that our sample shows much higher values of κ than Lu's samples. Qualitatively, this seems correct because of its lower resistivity. Quantitatively, however, the difference should be much smaller. To put an upper limit on the electronic part of κ, we can calculate it with the Wiedemann-Franz law using Lorenz number L for free electrons. This gives us values between 0.25 and 0.5 $\mathrm{W.m^{-1}.K^{-1}}$ at 300 K and 600 K, respectively. In reality, L in degenerate semiconductors is lower than for free electrons, so κ_e should be even lower. Still, the calculated lattice thermal conductivity of our sample at lower temperatures is higher than the total κ reported by Lu. The discrepancy is also illustrated by data for our natural sample, which should represent pure lattice contribution. We note that this was the second least thermally conducting of the eight natural samples we measured (see Fig. 4.8).

What could be the reasons for the inconsistency described above? Not porosity as both our and Lu's samples were around 98 % dense. Nanostructuring is unlikely to play a role as Lu reported the grain size of his samples in the range of hundreds of nm, but the phonon mean free path in tetrahedrite is on the order of interatomic distances. Furthermore, his samples were hot pressed for 30 min, as opposed to our sintering time of just 4 min (the temperature was the same). If anything, our samples should be more structured and less thermally conductive. In reality though, we saw that even 4 minutes were enough for the atoms to diffuse and form one homogeneous phase, so we may argue that all potentially significant nanostructuring in Lu's samples was eliminated during sintering.

We can compare our sample with another of Lu's samples with similar TE properties. In fact, his sample prepared from 3 parts synthetic tetrahedrite and 1 part natural with lower iron content shows very similar values of ρ and S, so we can expect an equivalent value of κ_e (see Fig. 3, open triangles, in [13]). However,

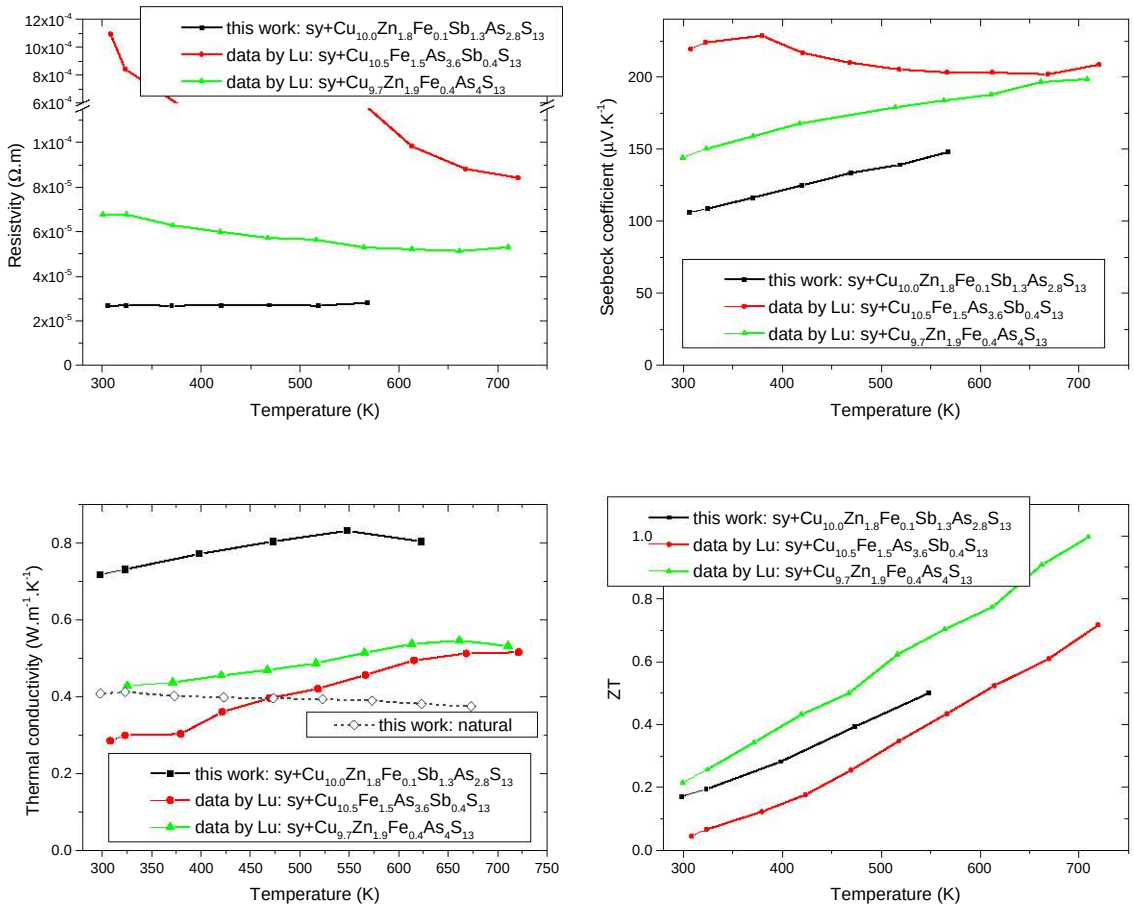

Figure 4.23: Comparison of thermoelectric properties of ball milled 50:50 synthetic:natural tetrahedrite mixtures from this work and from the work of Lu and Morelli [13].

this sample has a thermal conductivity between 0.52 and 0.65 $\mathrm{W.m^{-1}.K^{-1}}$ at 300 K and 600 K, respectively, which is much lower than $0.7-0.8$ $\mathrm{W.m^{-1}.K^{-1}}$ seen in our sample. It is highly improbable that this difference is caused by lower lattice thermal conductivity of Lu's sample. This is because our natural sample was already the second least thermally conducting among the 8 we measured and that the difference between the least and the most conducting was $0.1-0.15$ $\mathrm{W.m^{-1}.K^{-1}}$ (see Fig. 4.8). We can also compare our and Lu's $Cu_{12}Sb_4S_{13}$ samples but we have to keep in mind that, prior to sintering, he ball milled it while we hand ground it. Both samples have very similar values of ρ and S. As for κ, our sample shows values around 1.3 $\mathrm{W.m^{-1}.K^{-1}}$, Lu's values are actually $0-0.1$ $\mathrm{W.m^{-1}.K^{-1}}$ higher. This is in contrast with the lower values seen in mixed samples. Whatever the reason for that inconsistency is, it only applies to doped tetrahedrites or to samples with very low thermal conductivity.

The most probable explanation seems to be an experimental error. In both cases, thermal conductivity κ was obtained as a product of thermal diffusivity α,

density D, and heat capacity c_p. Unfortunately, Lu did not provide the individual factors, so we cannot compare them with our measurements. In both cases, α was determined by LFA manufactured by Netzsch (LFA-427 and LFA-457 models), so there should not be a significant error in measuring this quantity. As for D, our measurements are very consistent with negligible porosity observed with a SEM and theoretical density which can be measured accurately enough by XRD. We can assume that Lu performed the same check. The last factor is c_p. Lu measured this quantity using differential scanning calorimetry (DSC), while we estimated it using the Dulong-Petit law. In principle, when the strenuous DSC measurement is performed correctly, it should give more accurate values. Our estimate tends to overestimate the real value which approaches the Dulong-Petit value from below with increasing temperature. At the same time, this overestimation is slightly reduced as the Dulong-Petit law gives us c_v which is always lower than c_p obtained by experiment. Based on available heat capacity data for tetrahedrites [12, 79], the overall difference should be below 10 %. Quantitatively, the difference between our and Lu's data is rather surprising; more measurements of c_p above room temperature should be performed to clarify this issue.

The factor ZT of our sample lies between the values measured by Lu for his samples [13]. A direct comparison is somehow tricky given the inconsistency in measured thermal conductivity discussed above. If it really stems from experimental error, we may argue that our sample should have values of ZT comparable to that of Lu's better performing sample.

4.1.2.2 Different Ratios

For the second part of the synthetic–natural section, we prepared two more mixtures, one with a 25:75 ratio and the other with a 75:25 ratio. Both were ball milled for 90 minutes so they are comparable to the ball milled sample from the first part. No hand ground samples were prepared from the mixtures this time. However, data for samples made solely of either the synthetic or natural phase (i.e. 100:0 and 0:100 ratios, respectively) will be shown for comparison, and these were hand ground.

Figure 4.24 shows powder XRD patterns of the synthetic–natural mixtures mixed in the three different ratios. No secondary phases were formed during ball milling. There is just a small peak at 28.7 °, just left of the main peak, indicating the small amount of Cu_3SbS_4 which was already present in the synthetic phase before milling. Regarding the two-phase composition, we may make the same conclusion as for the 50:50 sample. As a reminder: Figure 4.13 showed that the diffraction peaks of the two constituent phases decreased in intensity and broadened during milling, indicating decreased particle size, but their position remained constant, suggesting they did not interact and still co-exist. The intensity of the left peaks, belonging to the synthetic phase, decreased more, presumably because the synthetic phase is softer than the natural phase and its particles were milled to a smaller size. Consequently, the left peaks are obscured by the larger right peaks. Looking at Figure 4.24, we see that the peaks belonging to the 25:75 sample are at the same

angular positions as those of the 50:50 sample. This suggests that, just as in the case of the 50:50 sample, the two constituent phases persisted throughout ball milling. This is probably also true for the 75:25 sample even though its peaks are slightly left shifted because of a bigger weight of the synthetic phase spectrum.

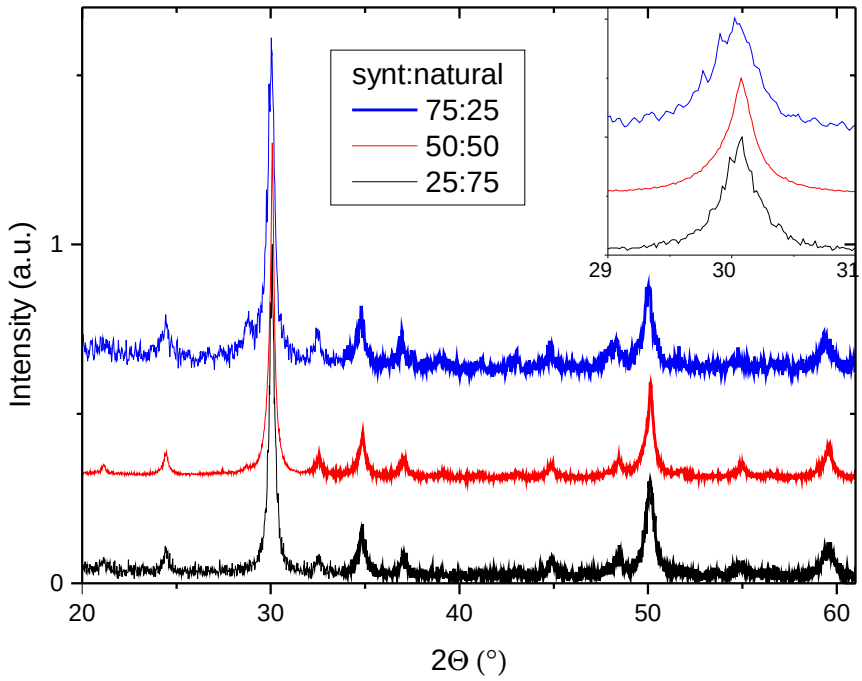

Figure 4.24: Powder XRD patterns of different ratios of synthetic–natural tetrahedrite mixtures after 90 min of ball milling.

Figures 4.25–4.27 show the temperature dependence of ρ, S, κ and ZT of the milled samples. Data for hand ground 100:0 and 0:100 samples are also shown for comparison. As expected, reduced carrier concentration leads to an increase of ρ and S and a decrease of κ with increasing content of the natural mineral. The 25:75 sample shows hysteresis – both ρ and S are higher on the cooling run. The value of ρ increases by some 30 %. The 75:25 sample also shows hysteresis, although smaller, its resistivity increases by some 10 % on the cooling run. In both cases, the increase starts around 600–650 K which is similar to the temperature where the 50:50 sample bulged during the LFA measurement, as was discussed previously. This suggests that the formation of a solid solution between the two phases was not entirely finished during sintering. The decrease of thermal conductivity, see Figure 4.26, nicely reflects the increase of resistivity with increasing content of the natural component.

Interestingly, the hysteresis exhibited by the 25:75 sample has virtually no effect on ZT – the increase of ρ is cancelled out by the increase of S and decrease of κ. Overall, ZT of this sample at room temperature is slightly lower than that of the

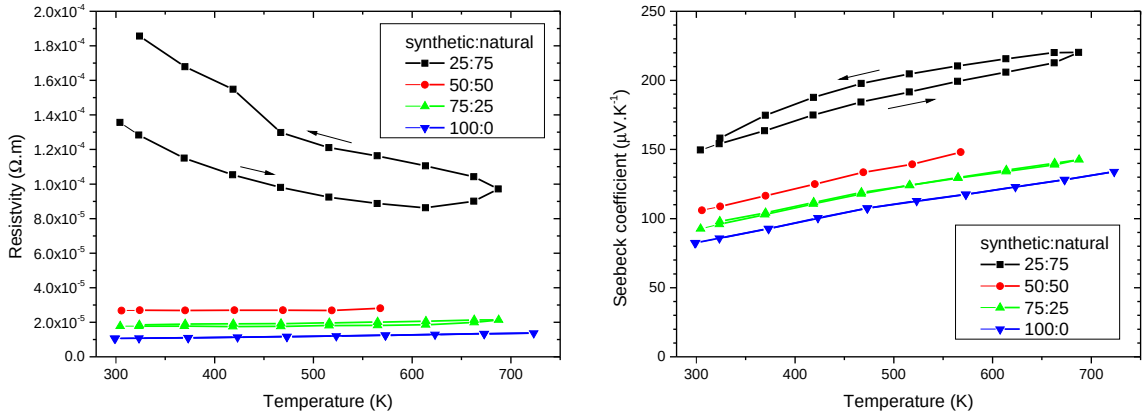

Figure 4.25: Temperature dependence of the electrical resistivity and Seebeck coefficient of ball milled mixtures of synthetic and natural tetrahedrites with different ratios of the two components. The synthetic (100:0) sample was not prepared by ball milling.

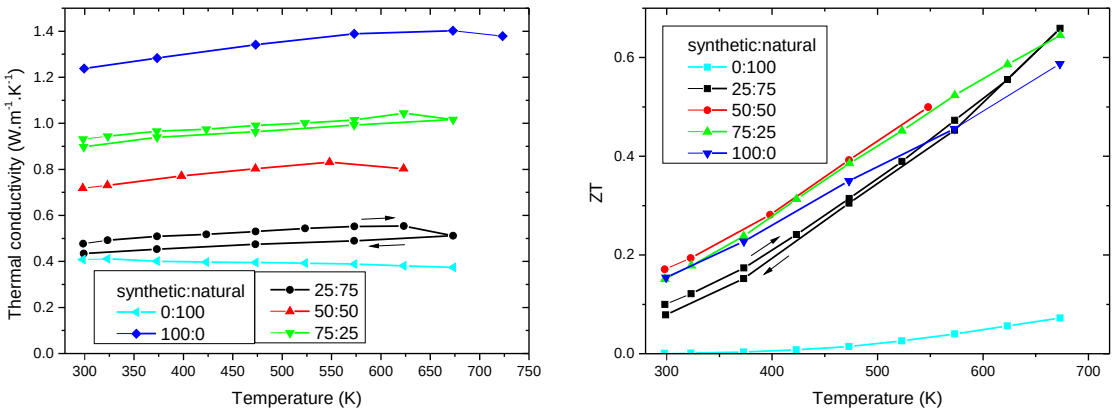

Figure 4.26: Temperature dependence of the thermal conductivity and ZT of ball milled mixtures of synthetic and natural tetrahedrites with different ratios of the two components. The synthetic (100:0) and natural (0:100) samples were not prepared by ball milling.

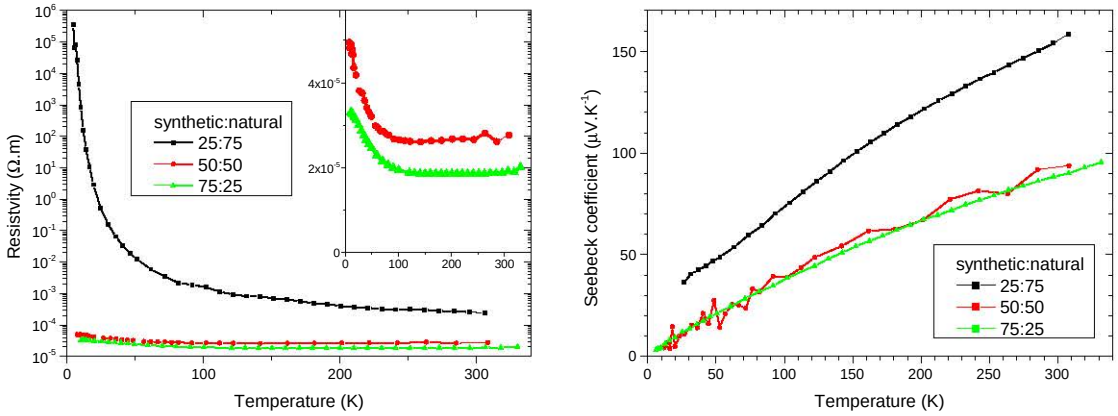

Figure 4.27: Temperature dependence of low temperature electrical resistivity and Seebeck coefficient of ball milled mixtures of synthetic and natural tetrahedrites with different ratios of the two components.

synthetic sample but increases faster with temperature, becoming slightly higher above 550 K. The factor ZT of the 50:50 sample is almost identical to that of the 75:25 sample, both being slightly higher than for the synthetic sample. The 25:75 and 75:25 samples posses the same value of ZT around 0.65 at 673 K, which represents a modest increase around 10 % when compared to pristine $Cu_{12}Sb_4S_{13}$.

The TE performance of the natural-rich samples of Lu and Morelli [13] was worse than that of other samples with different ratios. This was explained by the presence of Fe in the minerals which could fill more holes by being in the 3+ oxidation state. In the case of the natural-rich samples, this resulted in too low a carrier concentration. Their two minerals contained 1.5 and 0.4 atoms of iron per formula unit and this projected into the TE performance of the natural-rich samples: in the case of the Fe-rich sample, the performance was seriously degraded, and in the case of the other sample, it was partially degraded. Our mineral contained only 0.1 atoms of Fe per f.u. which resulted in the natural-rich sample possessing similar TE properties as the other samples despite the relatively high mineral content. Furthermore, this sample has very low thermal conductivity which probably results in us underestimating its value and consequently the ZT, as was discussed previously. It is probable that the ZT of this sample is the same as that of the other samples in the whole temperature range. Nevertheless, our results complement those of Lu and Morelli, confirming the decisive role of Fe content. We also showed that a mineral with Fe content low enough can constitute up to 75 % of the total volume of a decently performing TE material.

Low temperature electrical data are shown in Figure 4.27. The sample containing 75 % of the natural component is clearly semiconducting as evidenced by the rapid increase of ρ at lower temperatures. Resistivity of the 50:50 and 75:25 samples, on the other hand, is rather metallic and shows little dependence on temperature down to around 100 K where it starts to rise as both samples go through a metal-

to-semiconductor transition (MST). The transition, however, is largely suppressed by both the presence of As and reduced carrier concentration. This results in ρ increasing by a factor of 2 between the transition temperature and the lowest temperatures. The transition is not evident in the Seebeck coefficient which decreases smoothly.

To summarize this section dedicated to natural–synthetic mixtures: we mixed a natural tetrahedrite (Peru I) with synthetic $Cu_{12}Sb_4S_{13}$ using ball milling. First, we thoroughly tracked the milling process of a 50:50 mixture, then we analysed structural, electrical and thermal properties of samples sintered from 25:75, 50:50, and 75:25 mixtures.

By sampling the powder several times throughout milling, we observed a gradual decrease of particle size below 100 nm using XRD and SEM. We determined that the two phases coexist the whole time and only form a solid solution during the course of sintering. The sintering time of 4 minutes seems slightly insufficient for a complete formation of a perfect solid solution. The factor ZT was some 15 % higher than for the pure synthetic material. A mortar-ground control sample showed particle size $\approx 10^1$ µm and maintained its two-phase composition throughout sintering. The resistivity of this composite system was double that of the solid solution, and ZT was inferior to both the ball milled and pure synthetic sample. When confronted with published results [13], our measured data are comparable, however we may be overestimating the thermal conductivity of tetrahedrites with the lowest values of κ, possibly due to the overestimation of heat capacity. Electrical and thermal properties of mixtures with different natural to synthetic ratios followed the varying carrier concentration. From the thermoelectric point of view, the 50:50 and synthetic-rich samples behaved the best, both exhibiting ZT some 10 % higher than the pure synthetic sample, although the natural-rich sample also catches up at higher temperatures.

4.1.3 Influence of As Substitution for Sb

Any number of Sb atoms in tetrahedrite may be substituted by As, the two end-members form a perfect solid solution. In natural tetrahedrites, As is almost always present, as reported e.g. in [56, 59] as well as in this thesis. Our research on natural minerals did not bring conclusive results about the influence of As on TE properties. For this reason, we synthesized and studied several tetrahedite-tennantite series, namely $Cu_{12}Sb_{4-x}As_xS_{13}$, $Cu_{10}Co_2Sb_{4-x}As_xS_{13}$, and $Cu_{10}Zn_2Sb_{4-x}As_xS_{13}$, where $x = 0, 1, 2, 3, 4$.

4.1.3.1 $\mathbf{Cu_{12}Sb_{4-x}As_xS_{13}}$

The first series to synthesize was pure-copper $Cu_{12}Sb_{4-x}As_xS_{13}$, $x = 0, 1, 2, 3, 4$. The synthesis was successful, as can be seen in Figure 4.28 which shows powder XRD patterns of the final sintered samples. There was no change in the patterns during sintering. A small amount of secondary phases is present: in Sb-rich samples ($x = 0, 1, 2$) a solid solution between famatinite and luzonite (tetragonal $Cu_3(Sb,As)S_4$)

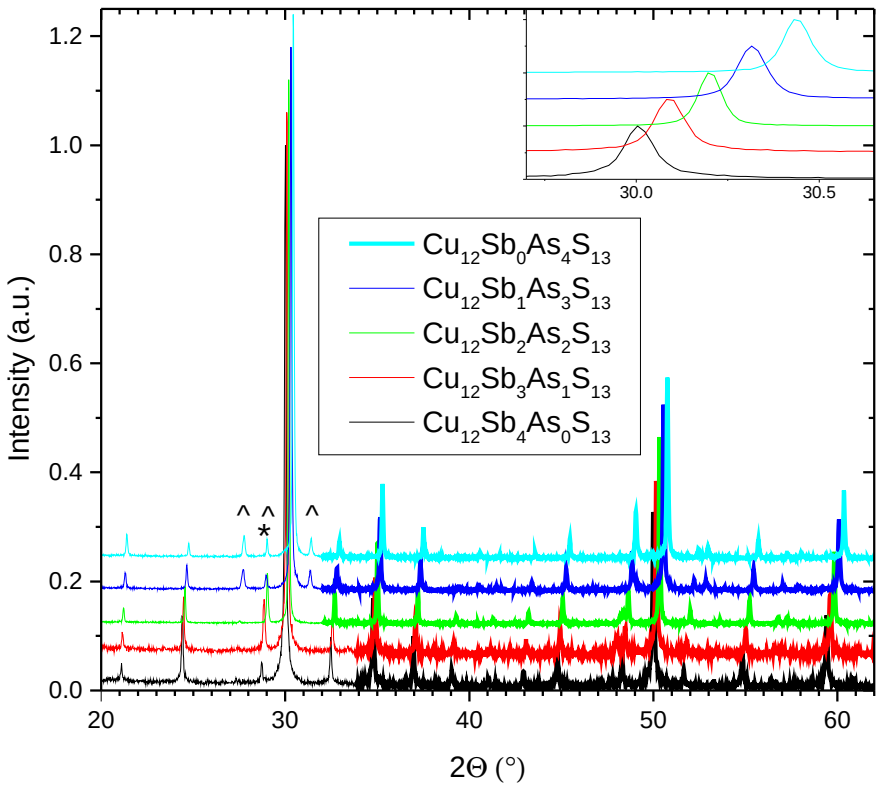

Figure 4.28: Powder XRD patterns of sintered samples from the $Cu_{12}Sb_{4-x}As_xS_{13}$ series. All main peaks could be indexed to the tetrahedrite-tennantite phase. A small amount of secondary phases is present: famatinite-luzonite solid solution (tetragonal $Cu_3(Sb,As)S_4$) in $x = 0, 1, 2$ marked by $*$, and enargite (orthorhombic Cu_3AsS_4) in $x = 3, 4$ marked by $\hat{}$.

appears. In As-rich samples ($x = 3, 4$) we can see enargite (orthorhombic Cu_3AsS_4 which does not have an Sb analogue). The cell parameter a decreases by 0.039 Å with each additional As atom, see Figure 4.29. This can be well explained by the smaller size of the arsenic atom. The value is in good agreement with 0.039 Å reported in [57] and 0.037 Å in [59], as well as with the values of a reported in [52].

At first, all the samples in the series were sintered at 723 K. This temperature was not high enough to produce dense samples in all cases. With increasing As content, the relative density decreased in the following manner: $D_{Sb\to As} = 98, 98, 97, 95, 92$ %. This trend was also seen during the course of sintering: with increasing As content, the samples started to sinter at increasingly higher temperatures. The shift of the sintering onset was approximately 25 K per each additional As atom.

The Seebeck coefficient remains largely unaffected by porosity. Porosity, however, has an effect on the resistance, both electrical and thermal, of a sample, increasing the perceived values which then differ from the values intrinsic to the material. The substitution of As for Sb in tetrahedrite has a relatively small effect on the transport properties; having samples of similarly low porosity was therefore especially important in order to obtain relevant values. We sintered the porous samples again

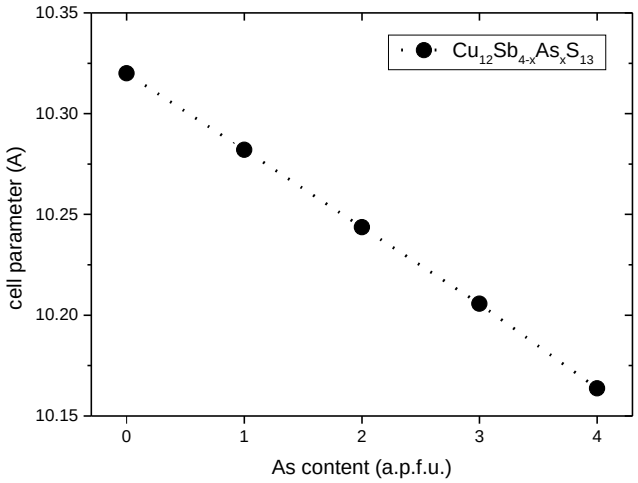

Figure 4.29: Dependence of the cell parameter on As content in $Cu_{12}Sb_{4-x}As_xS_{13}$.

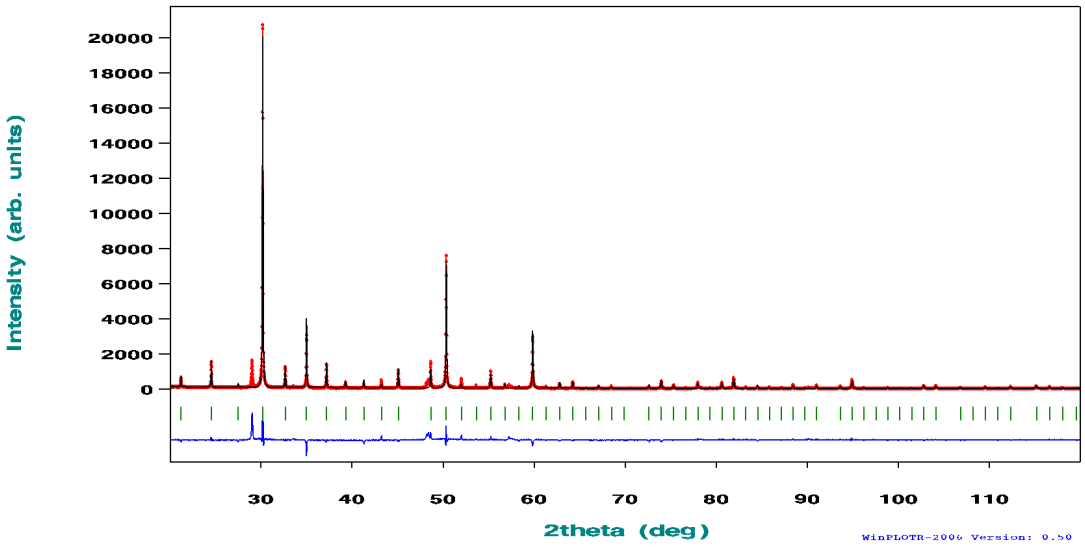

Figure 4.30: Rietveld refinement graph for $Cu_{12}Sb_2As_2S_{13}$. $\chi^2 = 6.84$. Additional reflections come from a small amount of a famatinite-luzonite solid solution (tetragonal $Cu_3(Sb,As)S_4$).

at higher temperatures: 475, 500, and 525 K for $x = 2, 3, 4$, respectively. Fresh powder was used, pellets from the first sintering were not recycled. In this manner, the relative density of all five sintered samples was over 98 %.

Figure 4.31 shows back-scattered electron images of the sintered samples. As already shown with XRD, the samples are mostly composed of the desired tetrahedrite-tennantite phase. There is some presence of secondary phases in the form of isolated inclusions, mainly $Cu_3(Sb,As)S_4$ with grain size in the order of 10 µm. A minute amount of $CuSbS_2$ is also present. The images confirm very low porosity of the samples. Results of quantitative chemical analysis are shown in Table 4.5. The actual chemical composition is in very good agreement with the desired stoichiometry.

Table 4.5: Chemical compositions of the samples from the $Cu_{12}Sb_{4-x}As_xS_{13}$ series determined by EPMA.

Desired	Atoms per formula unit			
As content	Cu	Sb	As	S
$x = 1$	12.10	3.03	0.98	12.89
$x = 2$	11.95	2.01	2.05	12.99
$x = 3$	11.94	0.98	3.12	12.97
$x = 4$	11.94	0.00	4.24	12.81

High temperature thermoelectric properties of the $Cu_{12}Sb_{4-x}As_xS_{13}$ series can be seen in Figures 4.32–4.34. Isovalent substitution of As for Sb was not expected to have a substantial effect on the transport properties because the electronic density of states at the top of the valence band, where the Fermi level is located, is composed mainly of Cu and S orbitals. Orbitals of Sb, and presumably As, form the conduction band which has little influence on electrical transport in tetrahedrites. The figures indeed show that the differences between the samples are small. Caution has to be taken when interpreting the data because of measurement uncertainty.

The Seebeck coefficient shows metallic behaviour for all the samples and rises linearly with increasing temperature. With each additional As atom, S drops by some 3 %, deteriorating the TE properties. Resistivity shows metallic behaviour as well but the absolute values are too close to confidently tell a trend, around 10^{-5} Ω.m at 300 K. We can tentatively say that ρ seems to drop between $x = 0$ and $x = 1$ samples and then slowly rise with increasing As content before reaching a similar value for $x = 4$ as for $x = 0$. A similar trend can be seen in the data reported in [52]. The absolute values of room-temperature ρ reported therein are some 20 % higher, which can be explained by lower density of the samples which was around 80 %.

Total thermal conductivity is around 1.3 $W.m^{-1}.K^{-1}$ for all the samples in the whole temperature range. The electronic part κ_{el} is dominant, especially at high temperatures. In fact, if we tried to calculate κ_{el} from ρ using the Lorenz number for free electrons, we would obtain a value larger than the total κ measured. A modified value (2.23) has to be used. In Figure 4.33, we see that κ_{lat} as well as κ seem to reach slightly lower values for $x = 1$ and $x = 2$. While it is tempting to explain this observation by increased phonon scattering due to mass fluctuation on the Sb/As site, this may not be true for two reasons: 1) this drop in κ_{lat} was not observed

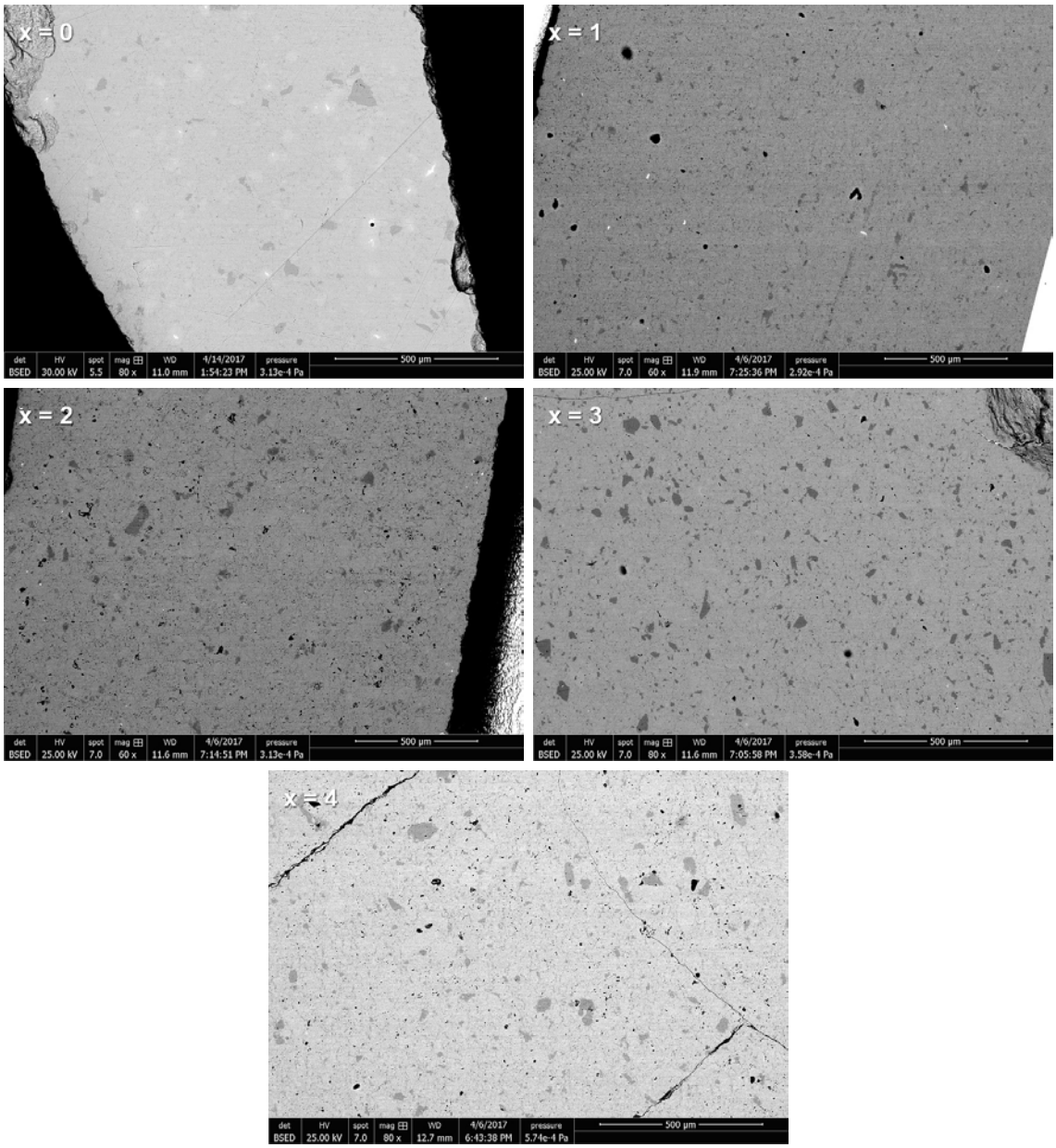

Figure 4.31: Back-scattered electron images of polished surfaces of the sintered samples from the $Cu_{12}Sb_{4-x}As_xS_{13}$ series. The samples are mostly composed of the desired tetrahedrite-tennantite phase. Darker spots indicate $Cu_3(Sb,As)S_4$, white spots indicate $CuSbS_2$, black spots are voids.

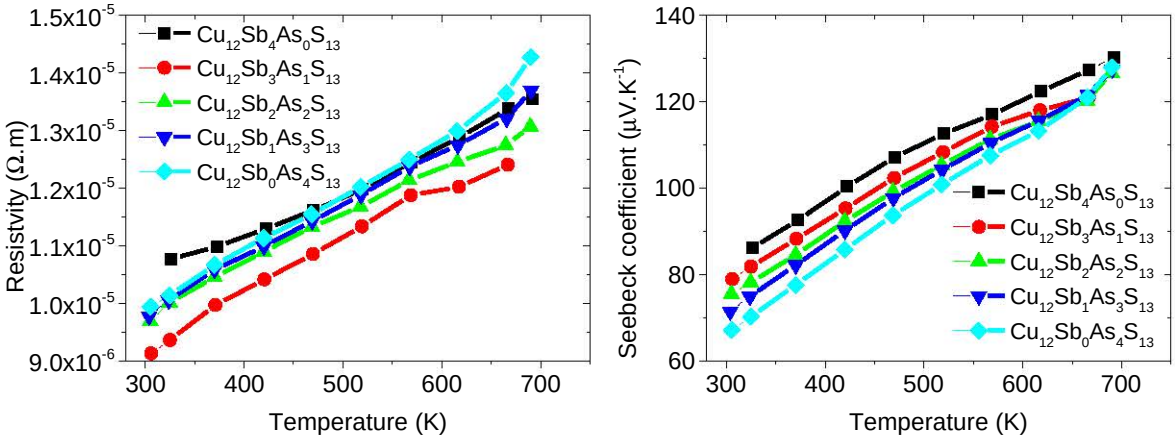

Figure 4.32: High temperature dependence of the electrical resistivity and Seebeck coefficient of $Cu_{12}Sb_{4-x}As_xS_{13}$.

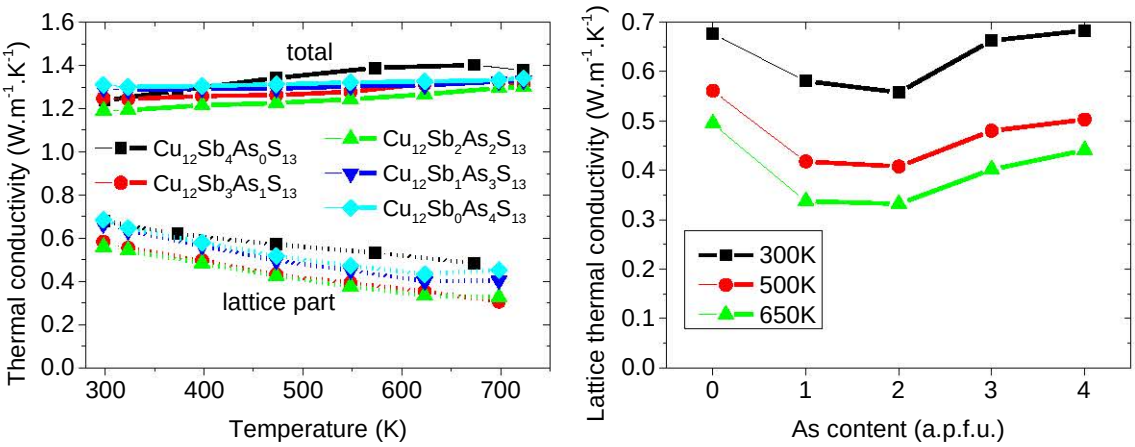

Figure 4.33: Temperature dependence of the thermal conductivity of $Cu_{12}Sb_{4-x}As_xS_{13}$.

in the $Cu_{10}Co_2Sb_{4-x}As_xS_{13}$ series discussed later on, and 2) κ_{lat} was obtained by subtracting a very large value of κ_{el} which is calculated based on a theoretical model. All the inaccuracies of the model will easily propagate into calculated κ_{lat}. What we can say with relative certainty is that As substitution has a small effect on lattice thermal conductivity of tetrahedrite and a search for more specific trends remains inconclusive.

The values of ZT are again very similar, reaching a peak value around 0.7 at 720 K for all samples. A slight drop of ZT with increasing As content is caused mainly by the decreasing Seebeck coefficient: for the pure As sample the peak value is 10 % lower than for the pure Sb one. Samples with $x = 0$–2 perform the best because of the slightly lower values of ρ and κ for $x = 1, 2$. Once again, we urge caution because of the large measurement inaccuracy when determining ZT.

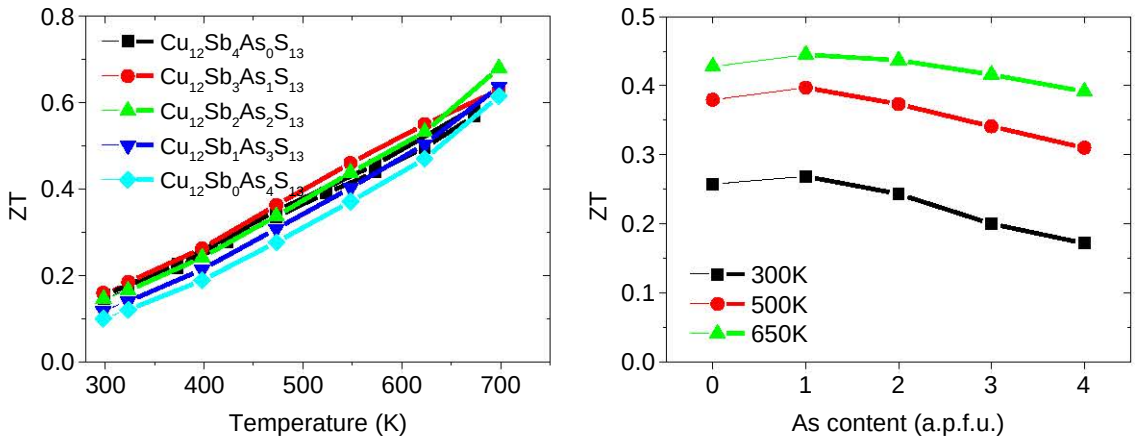

Figure 4.34: Evolution of ZT with temperature and As content in $Cu_{12}Sb_{4-x}As_xS_{13}$.

As discussed earlier, As-rich samples had to be sintered at higher temperatures (800 K for $x = 4$ as opposed to 720 K for $x = 0$) and withstood the higher temperatures without any observed degradation, suggesting better temperature stability than $Cu_{12}Sb_4S_{13}$. We have not done any proper temperature stability tests on our samples but it is possible that while the value of ZT is lower in As-rich samples at lower temperatures, it would reach similar values to Sb-rich samples at temperatures too high for those to withstand.

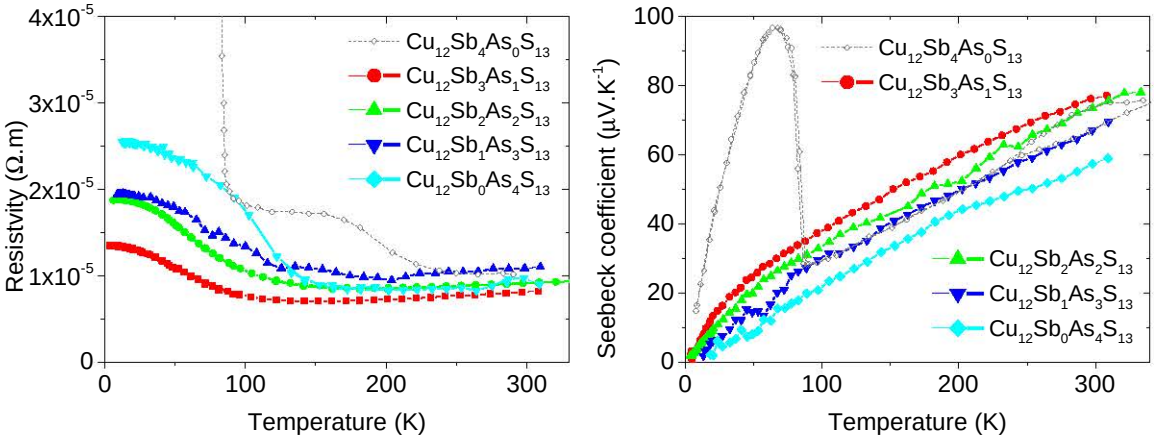

Figure 4.35: Low temperature dependence of the electrical resistivity and Seebeck coefficient of $Cu_{12}Sb_{4-x}As_xS_{13}$. Data for ρ and S of $Cu_{12}Sb_4S_{13}$ are taken from [52] and [11], respectively.

$Cu_{12}Sb_4S_{13}$ undergoes a metal-to-semiconductor transition at 85 K which manifests itself with an increase of ρ by an order of magnitude and an increase of S by a factor of three. [11] It has been shown that even slight substitution of As greatly suppresses this transition but a small increase in ρ remains throughout the whole Sb-As substitution range. [52] The transition temperature moves to higher values

with increasing As content. Our data for ρ, shown in Figure 4.35, corroborate those reported in [52]. Surprisingly enough, the marked anomaly in S for $Cu_{12}Sb_4S_{13}$ completely disappeared for the $x = 1 - 4$ samples.

Figure 4.36 shows calculated electronic density of states (DOS) for the members of the $Cu_{12}Sb_{4-x}As_xS_{13}$ series. The first pair of images highlights calculations for the two end members $x = 0$ and $x = 4$, respectively, in a wider range of energies. The results for $Cu_{12}Sb_4S_{13}$ agree well with those already published in the literature. [50,69] This system is a semiconductor with a band gap around 1.4 eV. The valence band is composed mainly of the d-states of Cu and p-states of S. The conduction band is composed mainly of the p-states of Sb. Two states are unoccupied, placing the Fermi level some 0.1 eV below the top of the valence band and resulting in metallic-like behaviour.

The calculations for the arsenic end-member $Cu_{12}As_4S_{13}$ show that the main influence of As is on the conduction band. The density of states due to As is much larger than in the case of Sb and these states are located at a lower energy. This results in the reduction of the band gap size to ca. 0.9 eV. We also see that the whole valence broadens and the s-states of S, located around $E_F - 6$ eV, also shift to lower energy, separating from the valence band. These properties should not, however, have any important influence on the transport properties. The Fermi level is still located around 0.1 eV from a band edge, so it will only be the electrons and therefore the DOS around this energy which determine the transport properties. The density of states is very similar for both end-members, suggesting that the isoelectronic As substitution will have only a little effect on electronic transport properties. The graphs for $x = 0, 1, 2, 4$ in Figure 4.36 show that the same is valid for all the members in the series. This agrees well with our experimental data which showed only a weak link between As substitution and ρ or S. Let us note that the situation is different in the case of isoelectronic substitution for S which contributes to DOS around the Fermi level. When Se substitutes for S, band convergence causes the resistivity to decrease without affecting the Seebeck coefficient, resulting in improved TE performance. [86,87]

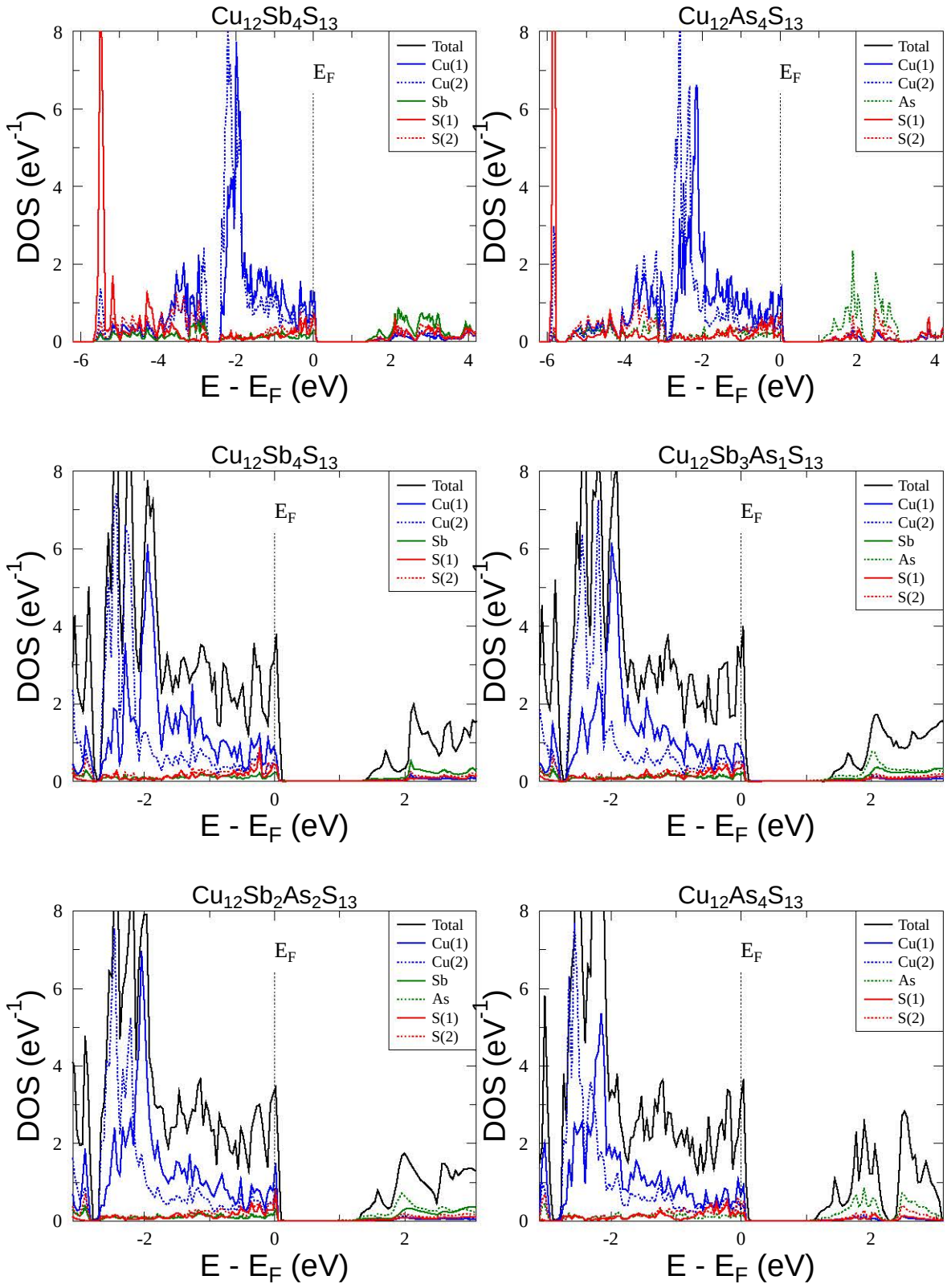

Figure 4.36: Calculated partial electronic density of states for $Cu_{12}Sb_{4-x}As_xS_{13}$.

4.1.3.2 $Cu_{10}Me_2Sb_{4-x}As_xS_{13}$

The electronic thermal conductivity constitutes a large part of the total value of κ, eclipsing the lattice part. We decided to synthesize samples with reduced carrier concentration to get a clearer view of κ_{lat}. This would be done by preparing a $Cu_{10}Me_2Sb_{4-x}As_xS_{13}$, $x = 0 - 4$, series where the two Me atoms provide extra electrons to fill the holes responsible for conduction in $Cu_{12}Sb_{4-x}As_xS_{13}$. Zinc was a natural first choice of Me atoms as it frequently occurs in natural tetrahedrites and does not change the band structure in or around the band gap.

The preparation of $Cu_{10}Zn_2Sb_{4-x}As_xS_{13}$ was, however, only partially successful. There was substantial outgassing of sulfur during annealing in the $Cu_{10}Zn_2As_4S_{13}$ sample. This was apparent from a yellow layer on the inside of the quartz tube, see Fig. 4.38. This series was nevertheless characterized and the results will be presented later on.

To obtain more relevant data, we looked for more suitable Me atoms. As it was the arsenic-rich sample which posed problems, a $Cu_{10}Me_2As_4S_{13}$ series was synthesized to find the best element. Fe, Co and Mn were tested. Figure 4.37 shows XRD patterns of ground ingots after synthesis, i.e. before annealing, for Fe, Co, and Mn along with Zn. Already after this first step, we saw a substantial difference in phase purity between the Zn sample and the other ones. The Co sample was composed almost entirely of the desired phase with a small amount of a pyrite analogue CoS_2. The Fe sample was also largely single phased with a small amount of luzonite (tetragonal Cu_3AsS_4). The majority of the Mn sample was made up of the desired phase but there was a significant amount of $Cu_4As_2S_5$ and smaller amounts of enargite (orthorhombic Cu_3AsS_4) and MnS. Besides the desired phase, the Zn sample contains a significant amount of $Cu_4As_2S_5$ as well as enargite, ZnS and a copper-zinc alloy. This is, however, not a problem in this phase of the process as annealing can drastically improve the phase composition.

The standard annealing temperature 723 K is based on the phase diagram and experience with $Cu_{12}Sb_4S_{13}$. It is not necessarily the best temperature for tetrahedrites with a different chemical composition. In fact, we saw that As substitution necessitates increased sintering temperatures and such samples are stable up to higher temperatures. The same can be said when a Me is substituting for the two Cu atoms. A tennantite phase diagram for the Cu-Me-As-S system, which would help us in adjusting the temperature, is not known. For each of the three samples we therefore annealed one pellet at 723 K and another one at 823 K.

Figure 4.38 shows a photo of the 2×3 tubes after annealing at 723 K and 823 K (450 °C and 550 °C) along with the tube with the Zn sample annealed at 723 K for comparison. We see that only the $Cu_{10}Co_2As_4S_{13}$ sample passed the annealing process without any visible outgassing of sulfur. The Mn samples show some level of outgassing, Zn and Fe samples show thicker deposits. Higher temperature led to stronger outgassing which was very significant for $Cu_{10}Fe_2As_4S_{13}$ annealed at 823 K. The amount of sulfur lost was estimated to be 0.1–0.4 atoms per formula unit. This was done by weighing the tube before and after carefully heating it with a flame to evaporate the visible yellow deposits.

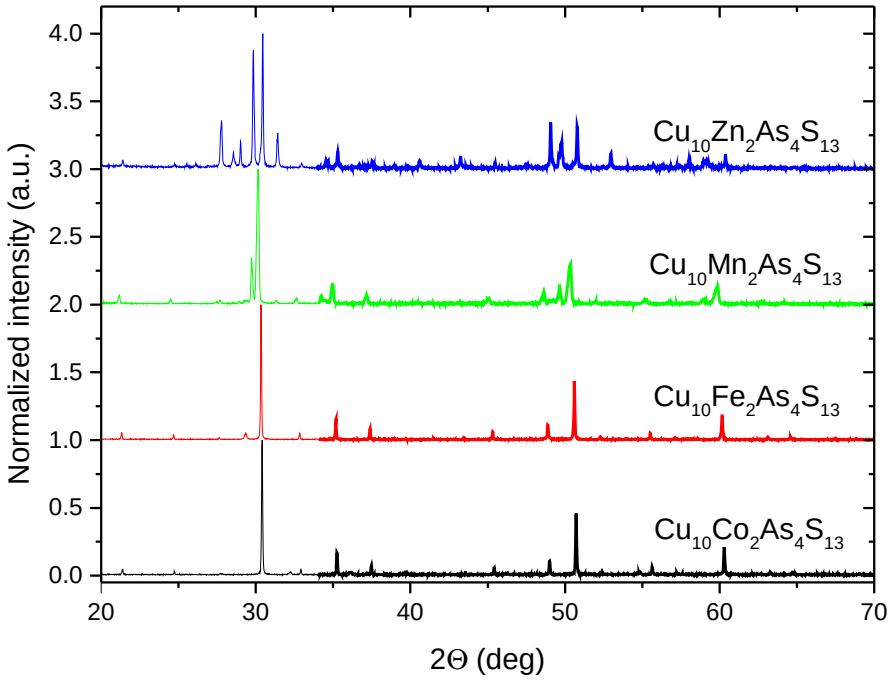

Figure 4.37: Powder XRD patterns of $Cu_{10}Me_2As_4S_{13}$, Me = Fe, Co, Ni, Zn, after synthesis.

Figure 4.39 shows XRD patterns of the samples annealed at both temperatures along with the patterns after synthesis for comparison. In all cases, annealing improved the phase composition of the samples. The Fe-containing sample was the only one in which a new phase was formed: a minute amount of pyrite (FeS_2) appeared for both annealing temperatures. On the other hand, the luzonite phase completely disappeared. In the Zn-containing sample, the amount of $Cu_4As_2S_5$ and ZnS decreased. The enargite and copper-zinc alloy phases completely disappeared. In the Mn-containing sample, the amount of the main secondary phase, $Cu_4As_2S_5$, was significantly reduced at 723 K and disappeared at 823 K. Similarly, the amount of MnS significantly reduced at 723 K and even more at 823 K. The enargite phase disappeared completely. In the Co-containing sample, the amount of CoS_2 decreased at 723 K and even more at 823 K.

Figure 4.40 compares the cell parameters of the four samples after each of the three steps along with pure Cu sample for comparison. The trend generally follows the decreasing atomic radii of the elements along the period: ${}_{25}Mn > {}_{26}Fe > {}_{27}Co > {}_{29}Cu > {}_{30}Zn$. After annealing, we can see an obvious increase despite the observed sulfur outgassing. This would suggest that the loss of sulfur does not create vacancies in the structure, $Cu_{10}Me_2As_4S_{13-x}$, or at least does not have a significant effect on the unit cell size. Instead, we may suspect better incorporation of Me atoms in the structure: $Cu_{12-x}Me_xAs_4S_{13}$, where x is getting closer to 2 with prolonged time and

Figure 4.38: $Cu_{10}Me_2As_4S_{13}$ pellets after annealing showing substantial sulfur outgassing. Left: Me = Zn annealed at 723 K. Right: 3 pairs of tubes for Me = Fe, Co and Mn marked with the annealing temperature in °C.

higher temperature during annealing. Indeed, actual x in our samples is lower than the ideal value $x = 2$ (see Table 4.6 and discussion below). Another explanation may be enriched content of copper and arsenic, $Cu_{10+x}Me_2As_{4+y}S_{13}$, inflating the unit cell.

The zinc sample shows a questionably large increase of the cell parameter during annealing; the value after synthesis, 10.161 Å, is very close to the value for the pure copper sample $Cu_{12}As_4S_{13}$: 10.164 Å. It is therefore possible that this pure copper phase was in fact the main tetrahedrite phase present after synthesis, and zinc was incorporated in the structure during annealing, which is responsible for the seeming increase of the cell parameter.

The Mn, Fe and Co samples annealed at 823 K were sintered at this temperature. Only the Co one was dense enough, its density was measured to be 98 % of the theoretical value. The Mn and Fe samples did not sinter very well, both were around 90 % dense. Based on the obtained results, cobalt was chosen as the most suitable element. The reasons were the attainable phase purity, neglibile sulfur outgassing during annealing and sinterability.

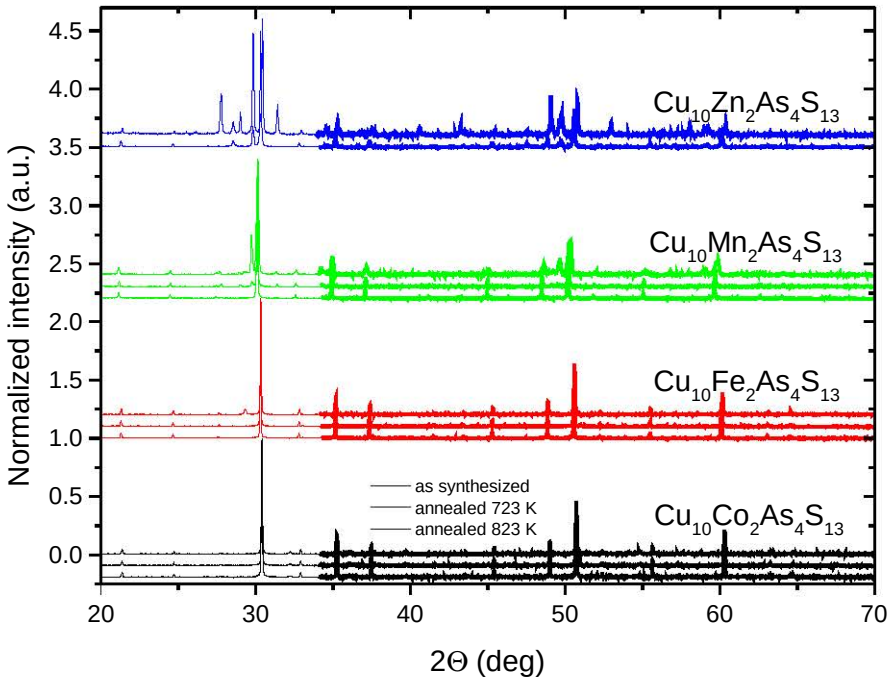

Figure 4.39: Powder XRD patterns of $Cu_{10}Me_2As_4S_{13}$, Me = Fe, Co, Ni, Zn, after synthesis and annealing.

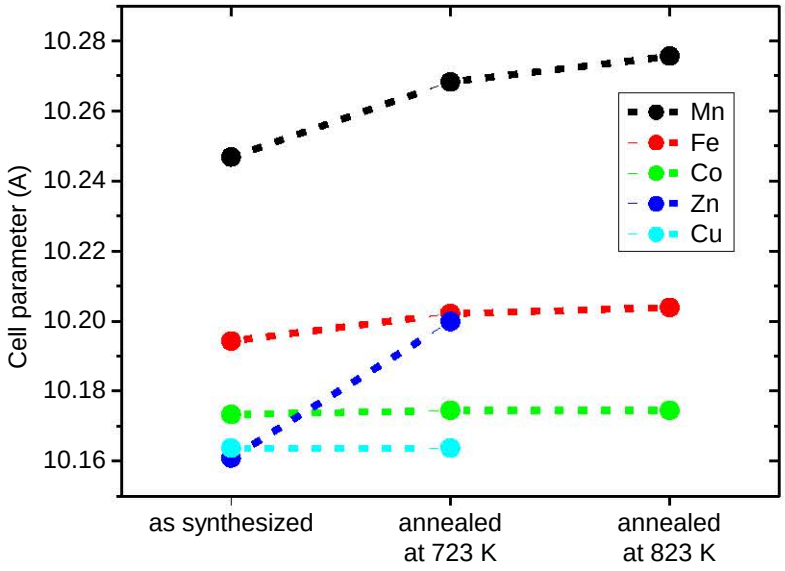

Figure 4.40: Cell parameters for $Cu_{10}Me_2As_4S_{13}$, Me = Fe, Co, Ni, Zn, after synthesis and annealing at 723 K and 823 K.

4.1.3.3 $Cu_{10}Co_2Sb_{4-x}As_xS_{13}$

A $Cu_{10}Co_2Sb_{4-x}As_xS_{13}$, $x = 0, 1, 2, 3, 4$ series was synthesized. The samples were annealed at 773 K. Sintering at 773 K was successfull, all the samples were over 98 % dense. XRD patterns of the sintered samples can be seen in Figure 4.41. All the samples are composed mainly of the desired tetrahedrite phase. According to the XRD measurements, a small amount of a pyrite analogue CoS_2 is present in the As-rich samples, along with Cu_2S_3 in Sb-rich samples.

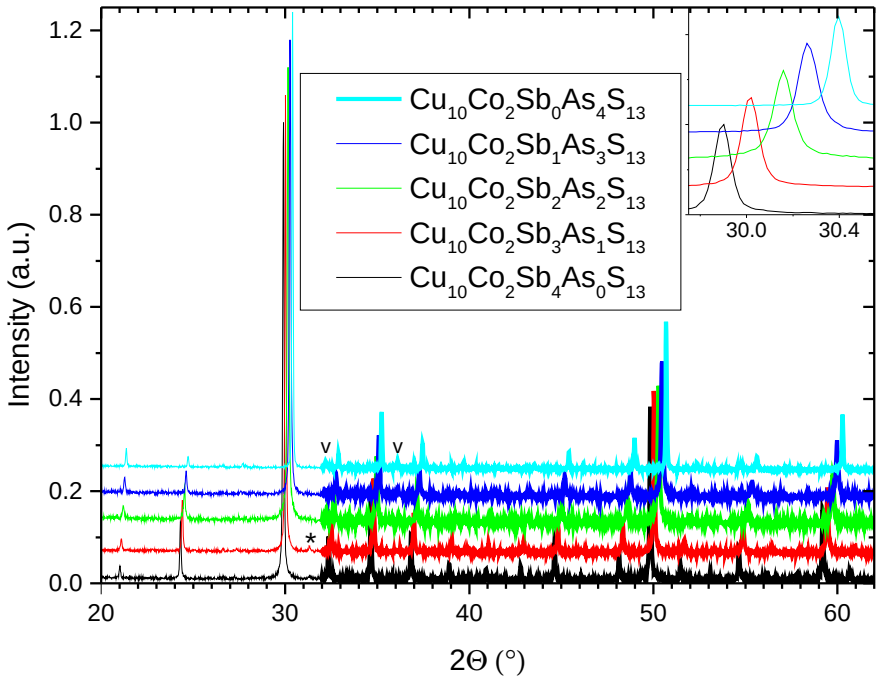

Figure 4.41: Powder XRD patterns of sintered samples from the $Cu_{10}Co_2Sb_{4-x}As_xS_{13}$ series. All main peaks could be indexed to the tetrahedrite-tennantite phase. A small amount of a pyrite analogue CoS_2, marked by ^{v}, and Co_2S_3, marked by *, is present.

Back-scattered electron images are shown in Figure 4.42. They confirm that the samples are composed mainly of the desired tetrahedrite-tennantite phase with some secondary phases present, such as CoS_2 or $CuSbS_2$. The $x = 3$ sample contains domains of As-rich and Sb-rich tetrahedrite.

Table 4.6 shows the chemical composition of the majority phase of the samples. Good agreement with the general formula $(Cu,Co)_{12}(Sb,As)_4S_{13}$ confirms successful synthesis of a tetrahedrite-tennantite solid solution. The most important finding is the deviation of the actual Co content from the desired one. With increasing As content, the amount of Co found in the tetrahedrite structure decreases. This points to lower willingness of tennantite to accept cobalt.

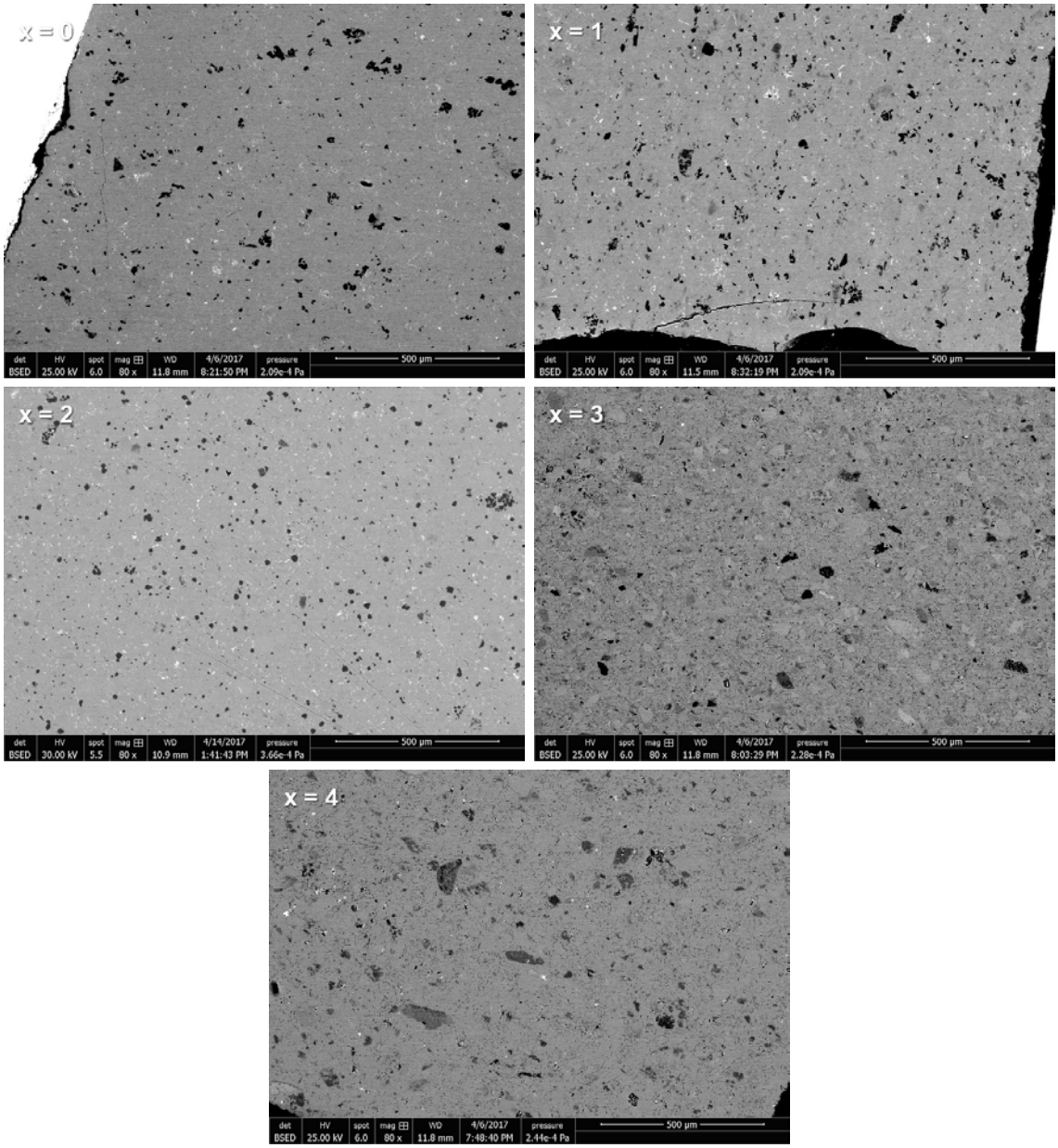

Figure 4.42: Back-scattered electron images of polished surfaces of the sintered samples from the $Cu_{10}Co_2Sb_{4-x}As_xS_{13}$ series. The samples are mostly composed of the desired tetrahedrite-tennantite phase. Some secondary phases are present, such as CoS_2 (black) or $CuSbS_2$ ($x = 0, 1$, white), the $x = 3$ sample contains domains of As-rich and Sb-rich tetrahedrite (different shades).

Table 4.6: Chemical compositions of the samples from the $Cu_{10}Co_2Sb_{4-x}As_xS_{13}$ series. Data for $x = 0, 1, 3, 4$ were determined by EPMA, data for $x = 2$ were determined by EDX.

Desired As content	Atoms per formula unit				
	Cu	Co	Sb	As	S
$x = 0$	10.22	1.80	4.06	0	12.91
$x = 1$	10.48	1.64	3.11	0.91	12.86
$x = 2$	10.02	1.66	2.22	1.97	13.12
$x = 3$	10.24	1.72	1.07	3.08	12.90
$x = 4$	10.60	1.36	0	4.22	12.82

Figure 4.43 shows the electrical resistivity and Seebeck coefficient of the samples. In contrast to metallic $Cu_{12}\ldots$, resistivity shows semiconducting temperature dependence and largely increased values for all the samples, which is expected as a result of Co^{2+} filling the holes in the valence band and therefore reducing carrier concentration. The actual content of cobalt in the tetrahedrite dictates the absolute values which are, above room temperature, $\rho_0 \approx 30 \cdot 10^{-5}$ Ω.m for the antimony end-member with 1.8 Co atoms per f.u., $\rho_{1-3} \approx 10 \cdot 10^{-5}$ Ω.m for samples containing both Sb and As with some 1.65 cobalt atoms per f.u., and $\rho_4 \approx 5 \cdot 10^{-5}$ Ω.m for the arsenic end-member containing 1.36 cobalt atoms per f.u. For comparison: the value for $Cu_{12}\ldots$ samples is around $\rho_{Cu12\ldots} \approx 1 \cdot 10^{-5}$ Ω.m. The Seebeck coefficient reflects the decreased carrier concentration and its magnitude increases just as the resistivity increases with increased Co content in Sb-rich samples.

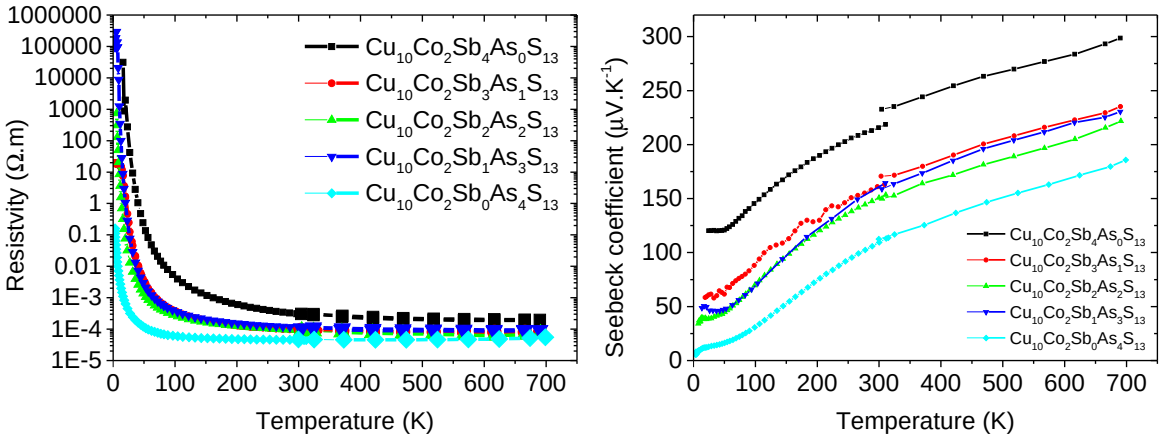

Figure 4.43: Temperature dependence of the electrical resistivity and Seebeck coefficient of $Cu_{10}Co_2Sb_{4-x}As_xS_{13}$.

Measuring the Hall coefficient in tetrahedrites has proven to be tricky. Three groups have attempted, but did not succeed: [82] in Zn-Fe co-doped compounds, [81] for Mn doping, and [12] in Te-based compounds. The only successful report is [51] for Ni doping which gives negative values of the hall coefficient R_H – a disagree-

ment with the positive Seebeck coefficient and the picture painted by electronic structure calculations. Using a simplistic conversion $R_H = -1/(ne)$ supposing only negative carriers, the measured value corresponds to their concentration on the order of 10^{22} cm^{-3}. We tried to measure the Hall coefficient of $Cu_{10}Co_2Sb_4S_{13}$ and $Cu_{10}Co_2Sb_3As_1S_{13}$. The results were not very clear, so we will not go into too much detail, but they were clear enough to qualitatively support the surprising conclusion from [51], i.e. that the sign of the Hall coefficient is negative, which suggests the existence of light electrons which also take part in conduction. Our order-of-magnitude value for concentration was 10^{21} cm^{-3}. Furthermore, our measurements at higher temperatures showed that the sign switched to positive around 400 K. This was not a confident result but it certainly suggests that there may be interesting effects to observe when measuring the Hall coefficient in tetrahedrites.

Thermal conductivity κ of the samples, shown in Figure 4.44, decreased by almost one half when compared to the Cu_{12}... series. The electronic part κ_{el} is rather low, as desired. Its values are lower than 0.15 W.m^{-1}.K^{-1} at room temperature and lower than 0.25 W.m^{-1}.K^{-1} at 700 K. Varying κ_{el} among the samples is responsible for the differences in the total κ, and is directly related to electrical resistivity which was discussed in the previous paragraph. After subtracting κ_{el}, we see that the lattice part does not change with As content, see Figure 4.44. Markedly low values were measured for the $x = 3$ sample. This does not seem to be caused by the presence of As atoms in the crystal lattice but instead by the microstructure of the sample which differs from that of the other samples. Figure 4.42 shows it to be less homogeneous, with domains of As-rich and Sb-rich tetrahedrite.

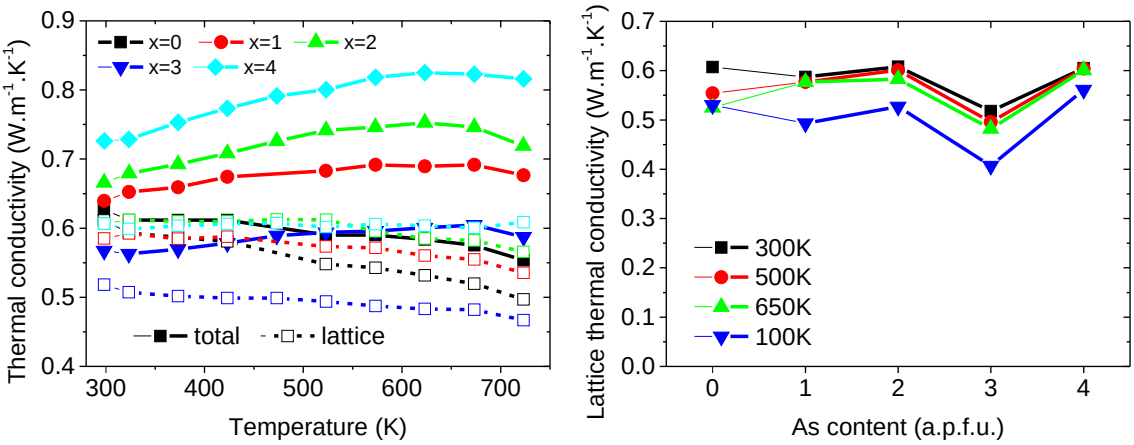

Figure 4.44: Evolution of the thermal conductivity with temperature and As content in $Cu_{10}Co_2Sb_{4-x}As_xS_{13}$.

While thermoelectric performance was not an important matter in this series of Co-substituted samples, it is still worth mentioning. The maximum values of ZT are around 0.7 at 720 K for the $x = 1, 2, 3$ samples and 0.6 for the $x = 0, 4$ ones, see Figure 4.45. Low variation of ZT with respect to a wide range of substitutions confirms the robustness of the tetrahedrite system for thermoelectric applications.

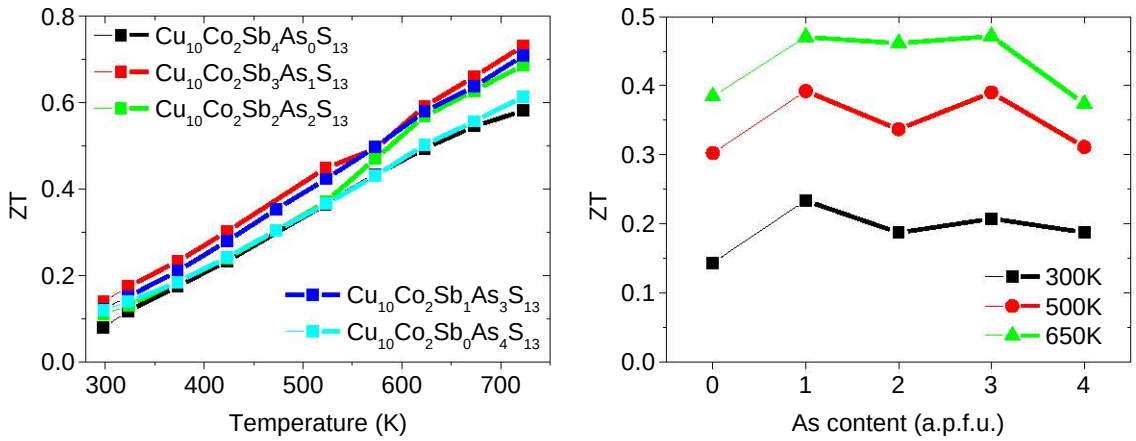

Figure 4.45: Evolution of ZT with temperature and As content in $Cu_{10}Co_2Sb_{4-x}As_xS_{13}$.

To conclude this part: a $Cu_{10}Co_2Sb_{4-x}As_xS_{13}$, $x = 0, 1, 2, 3, 4$ series was rather successfully synthesized. The goal was to get a clearer look at the lattice part of the thermal conductivity by reducing the electronic part through the filling of the large number of holes. As it turned out, the solubility of Co in tetrahedrite decreases with increasing As content. For this reason, the reduction of κ_{el} in As-rich samples was less effective than expected but still enough to achieve the initial goal. No correlation between κ_{lat} and As content was observed. The Hall coefficient is of opposite sign than S, a feature worth further investigation.

4.1.3.4 $Cu_{10}Zn_2Sb_{4-x}As_xS_{13}$

We previously mentioned that the preparation of a Zn-substituted tetrahedrite-tennantite series was only partially successful. There was visible outgassing of sulfur during annealing in the $Cu_{10}Zn_2As_4S_{13}$ sample and, to a lesser extent, in the $Cu_{10}Zn_2Sb_1As_3S_{13}$ sample. The whole series was prepared all at once, so when the degassing issue was discovered, all the samples already existed. We therefore decided to sinter and characterize them anyway.

Figure 4.46 shows XRD patterns of the samples after synthesis. The samples contain various different phases, namely one or more tetrahedrite phases, ZnS and various copper antimony/arsenic sulfides. Most of these phases were reduced or eliminated in favour of the desired tetrahedrite-tennantite phase during annealing, see Figure 4.47 which shows XRD patterns of annealed samples before sintering. The spectra are much cleaner and all main peaks could be indexed to the tetrahedrite-tennantite phase. A small amount of another tetrahedrite phase with a larger cell parameter (10.37 Å) is present in the $x = 2 - 4$ samples; its presence in the $x = 0, 1$ samples cannot be determined because of overlapping peaks. The ZnS phase is still present but in smaller quantities than right after synthesis. This suggests that during the synthesis step, Zn primarily reacts with sulfur to form zinc sulfide causing the initial tetrahedrite-tennantite phase to be Zn-poor or even Zn-free. During

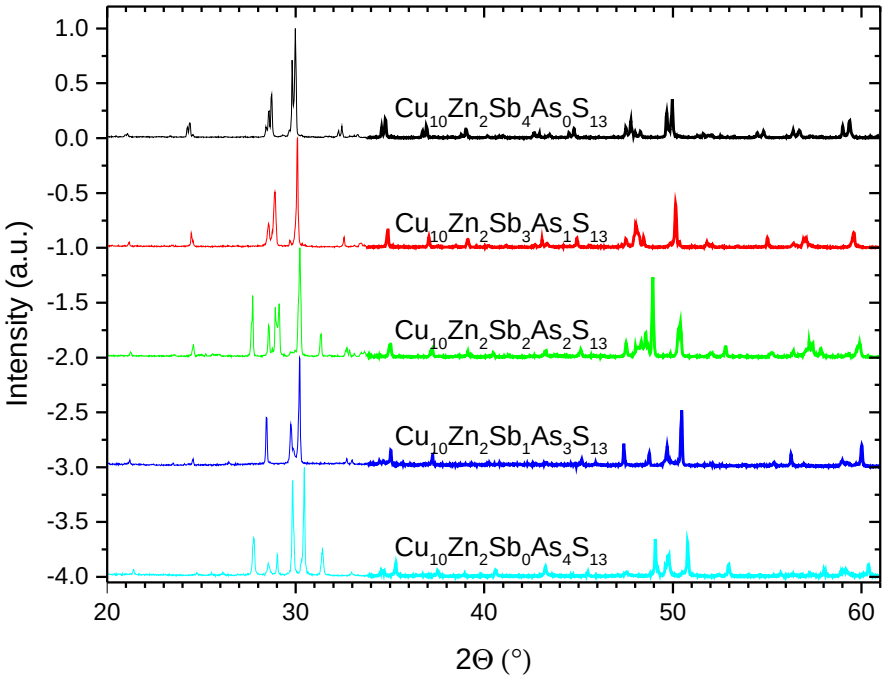

Figure 4.46: Powder XRD patterns of the samples from the $Cu_{10}Zn_2Sb_{4-x}As_xS_{13}$ series after synthesis. The samples contain various different phases; most of them are reduced or eliminated in favour of the desired tetrahedrite-tennantite phase during annealing.

annealing, zinc gets incorporated in the tetrahedrite structure. Indeed, the main phase cell parameters in all five samples after synthesis are very close to the values for corresponding pure copper phases ($Cu_{12}Sb_{4-x}As_xS_{13}$). After annealing, all the peaks of the main phase shift towards larger unit cell size reflecting the incorporation of zinc.

Figure 4.48 compares the dependence of the cell parameter on As content in tetrahedrite-tennantite solid solutions for the case of cobalt, zinc and copper substitutions. With each additional As atom, the cell parameter decreases by 0.039 Å for the case of copper, 0.042 Å for the case of cobalt, and 0.043 Å for the case of zinc substitution. This can be well explained by the smaller size of the arsenic atom. This effect is complemented by lower concentrations of slightly larger Co and Zn atoms in As-rich samples, which is responsible for further decrease of the cell parameter. These values are in good agreement with 0.039 Å reported in [57] and 0.037 Å in [59].

The $Cu_{10}Zn_2Sb_{4-x}As_xS_{13}$ samples were sintered at 773 K and all of them reached over 96 % of their theoretical density. Polished samples were then examined by scanning electron microscopy. They are mostly composed of the desired tetrahedrite-tennantite phase; the chemical compositions of this phase determined by EDX are

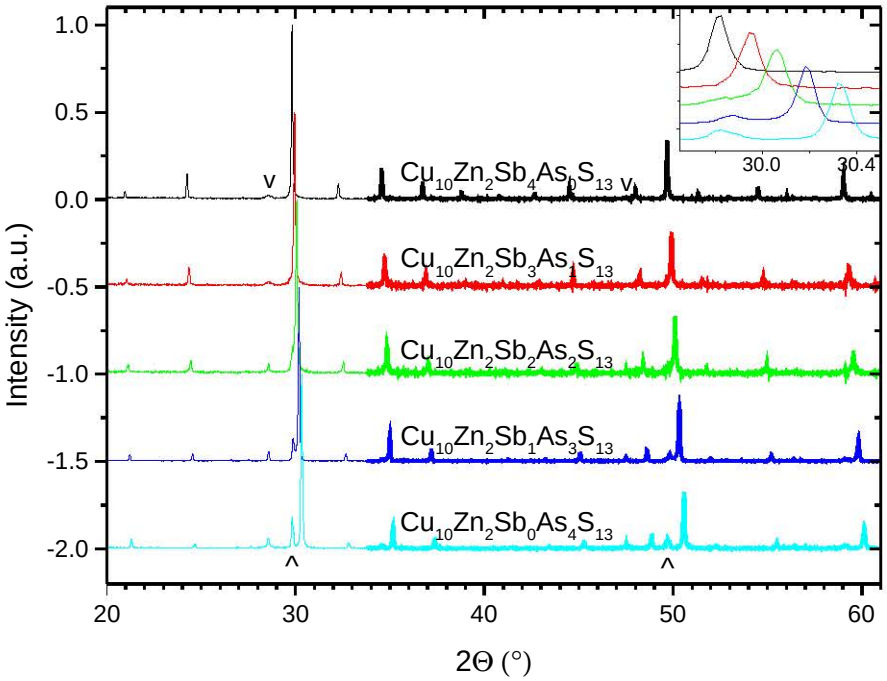

Figure 4.47: Powder XRD patterns of annealed samples from the $Cu_{10}Zn_2Sb_{4-x}As_xS_{13}$ series before sintering. All main peaks could be indexed to the tetrahedrite-tennantite phase. A small amount of another tetrahedrite phase, marked by ^, is present along with ZnS, marked by v.

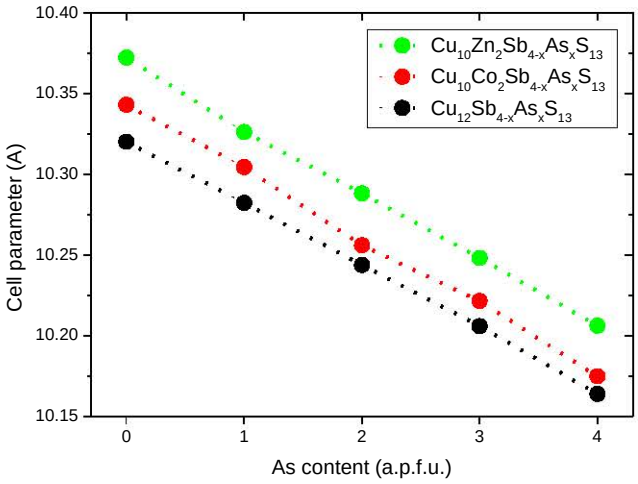

Figure 4.48: Dependence of the cell parameter on As content in copper, cobalt and zinc substituted tetrahedrite-tennantine solid solutions.

Table 4.7: Chemical compositions of the samples from the $Cu_{10}Zn_2Sb_{4-x}As_xS_{13}$ series determined by EDX.

Desired As content	Atoms per formula unit				
	Cu	Zn	Sb	As	S
$x = 0$	9.49	1.76	4.60	0	13.15
$x = 1$	10.01	1.64	3.43	0.98	12.93
$x = 2$	10.16	1.50	2.23	2.02	13.09
$x = 3$	10.39	1.60	1.16	2.93	12.92
$x = 4$	10.97	1.34	0	3.77	12.91

shown in Table 4.7. We can see a trend analogous to the cobalt samples: increasing As content causes less Zn to be incorporated in the tetrahedrite phase at the expense of Cu. Both zinc and cobalt are therefore found to be less soluble in As-bearing tetrahedrites. Surprisingly enough, all the samples contain around 13 atoms of sulfur per tetrahedrite f.u. despite the observed outgassing. This points to the fact that the sulfur was not lost from the tetrahedrite phase but originated from the secondary phases. These are discussed in the next paragraph and, indeed, do not contain sulfur in the case of the $x = 4$ sample. EDX analyses averaged over a 2×1 mm^2 area of the samples gave the following concentrations of sulfur per 29 atoms, sorted by increasing As content: 13.14, 13.20, 13.10, 12.79, 12.61. This is in line with the observed outgassing of sulfur in As-rich samples.

Figure 4.49 shows back-scattered electron images of the samples. Some minority phases are present. These were identified by EDX to be ZnS (dark areas) in all the samples, and various other phases (brighter areas), mostly sulfides, which differ among the samples. In the case of the $x = 0, 1$ samples, $CuSbS_2$ was identified. In the case of the $x = 2$ sample, this is an Sb-rich phase containing around 0.5 atoms of As per formula unit. The Zn content of this phase is higher than that of the majority phase, around 1.8 vs. 1.5, and is similar in composition to the $x = 0$ sample. This is in line with lower solubility of Zn in As-bearing tetrahedrites, as previously discussed. In the case of the $x = 3$ sample, there is an Sb-rich phase containing around 2.5 atoms of As per f.u. Lastly, in the case of the $x = 4$ sample, Zn_3As_2 was identified.

Figure 4.50 shows the electrical resistivity and Seebeck coefficient of the samples. In contrast to metallic Cu_{12}... and analogously to $Cu_{10}Co_2$..., resistivity shows semiconducting temperature dependence and increased values for all the samples, which is expected as a result of Zn^{2+} filling the holes in the valence band and therefore reducing the carrier concentration. The actual content of substituting Zn atoms is lower than desired with increasing As content, just as in the case of the Co-substituted samples. This is responsible for the differences in resistivity and Seebeck coefficient among the samples. The room-temperature values are $\rho_0 \approx 30 \cdot 10^{-4}$ Ω.m for the antimony end-member with 1.8 Zn atoms per f.u., $\rho_{1-3} \approx 5 \cdot 10^{-4}$ Ω.m for the samples containing both Sb and As with some 1.6 zinc atoms per f.u., and $\rho_4 \approx 1 \cdot 10^{-4}$ Ω.m for the arsenic end-member containing 1.34 zinc atoms per f.u. For comparison: the value for Cu_{12}... samples is around $\rho_{Cu12...} \approx 1 \cdot 10^{-5}$ Ω.m.

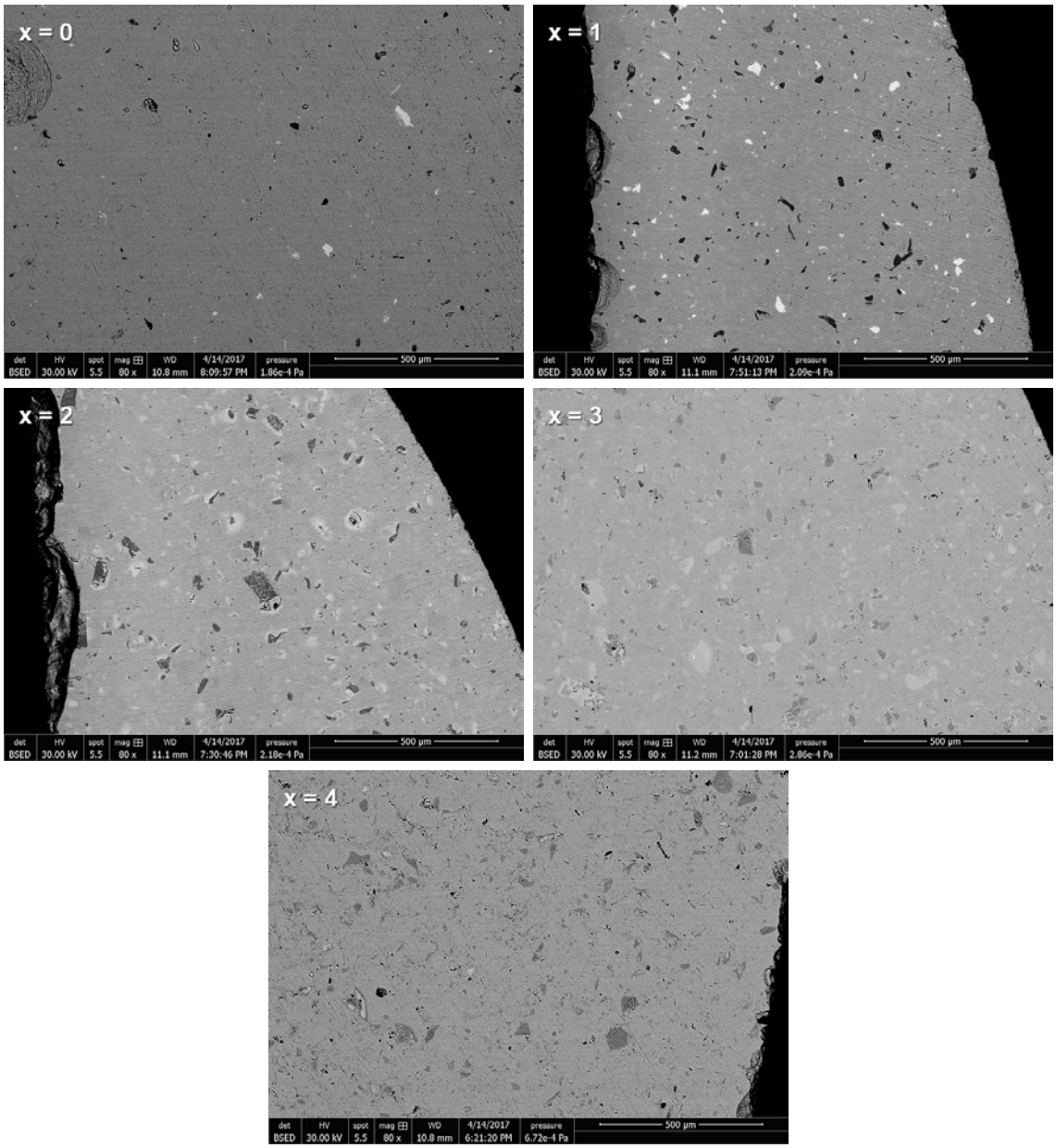

Figure 4.49: Back-scattered electron images of polished surfaces of the sintered samples from the $Cu_{10}Zn_2Sb_{4-x}As_xS_{13}$ series. The samples are mostly composed of the desired tetrahedrite-tennantite phase. Some ZnS is present (dark areas), along with various sulfides (brighter areas).

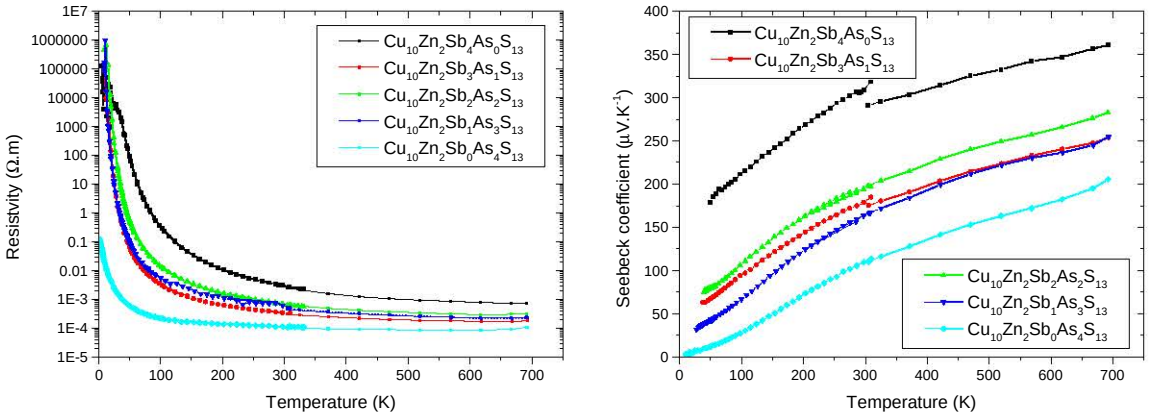

Figure 4.50: Temperature dependence of the electrical resistivity and Seebeck coefficient of $Cu_{10}Zn_2Sb_{4-x}As_xS_{13}$.

Even though the actual Zn and Co atomic contents are very similar in samples with corresponding As content, the electrical resistivity is systematically higher in the zinc samples. At room temperature, it differs by a factor of 2, 5 or 10 for the pure-As, mixed and pure-Sb samples, respectively. A possible explanation may come from the fact that the electronic band structure around the Fermi level is not changed by zinc substitution (see Fig. 2.7), while cobalt introduces some additional states leading to lower electrical resistivity for the same concentration of substituting atoms.

Thermal conductivity κ of the samples, shown in Figure 4.51, is slightly lower than in the cobalt samples because of the lower contribution of the electronic part. The values of κ_{el} are below 0.1 $W.m^{-1}.K^{-1}$ for all the samples in the whole measured temperature range. Figure 4.51 right shows the dependence of lattice thermal conductivity on As content. The values above room temperature were obtained by subtracting κ_{el} from LFA-derived values of κ. The values below room temperature are taken simply as equal to κ measured by the four-point method. This is justified because at the temperature displayed in the graph, 50 K, κ_{el} is virtually zero because of very high electrical resistivity. Similarly, we can safely assume very low radiation losses which can otherwise introduce large experimental error at higher temperatures, especially when measuring such low values of thermal conductivity.

No obvious dependence of κ on arsenic content can be deduced from the data. The seemingly lower value for the $x = 0$ sample may be just an artefact related to a specific sample and not intrinsic to the material – similarly to the anomalously low value measured for the $x = 3$ sample from the Co series (see Fig. 4.44). Despite measuring higher values of κ_{lat} for the $x = 4$ sample, both above and below room temperature, we cannot confidently attribute them to the influence of arsenic – we do not consider these data entirely relevant because of the loss of sulfur during annealing.

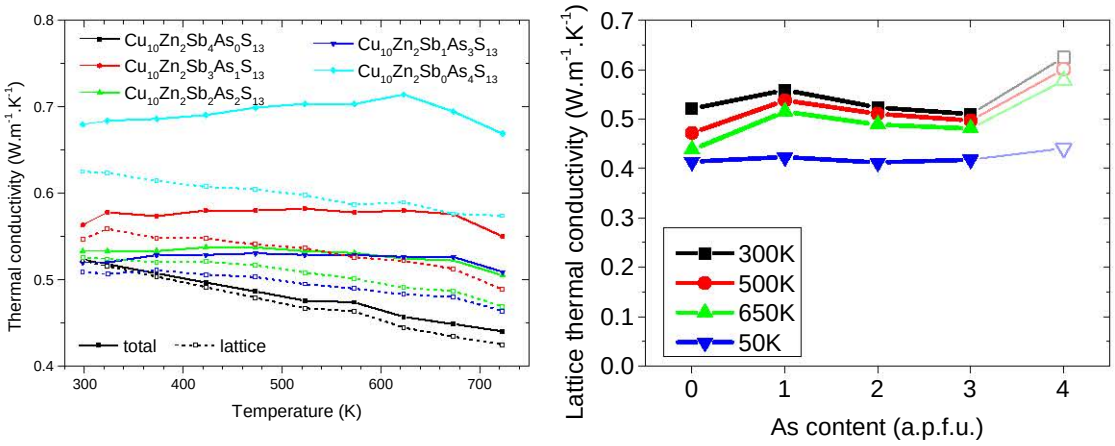

Figure 4.51: Evolution of the thermal conductivity with temperature and As content in $Cu_{10}Zn_2Sb_{4-x}As_xS_{13}$. The data for $x = 4$ cannot be treated as entirely reliable due to sulfur degassing from the sample during annealing.

4.1.3.5 $Cu_{10}Me_2As_4S_{13}$

To top the study on As substitution off, we present the data for ρ, S and κ of the arsenic end-member tennantite, $Cu_{10}Me_2As_4S_{13}$ where Me = Mn, Fe, Co, Zn, Cu. We already presented the data for the last three samples in the appropriate sections. Only the data for the first two samples are new. These samples are by-products of the search for a suitable substituting element but since they were already synthesized and annealed, we measured their properties and present the results in graphs comparing the tennantites, see Figures 4.52 and 4.53.

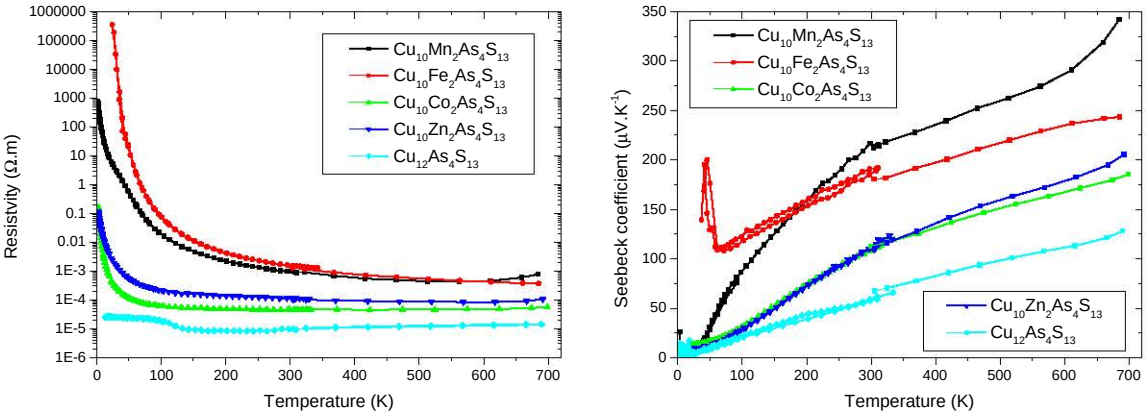

Figure 4.52: Temperature dependence of the electrical resistivity and Seebeck coefficient of $Cu_{10}Me_2As_4S_{13}$, Me = Mn, Fe, Co, Zn, Cu.

We urge caution when interpreting the results for several reasons. First, we saw that the doping level varies from sample to sample because of different willingness

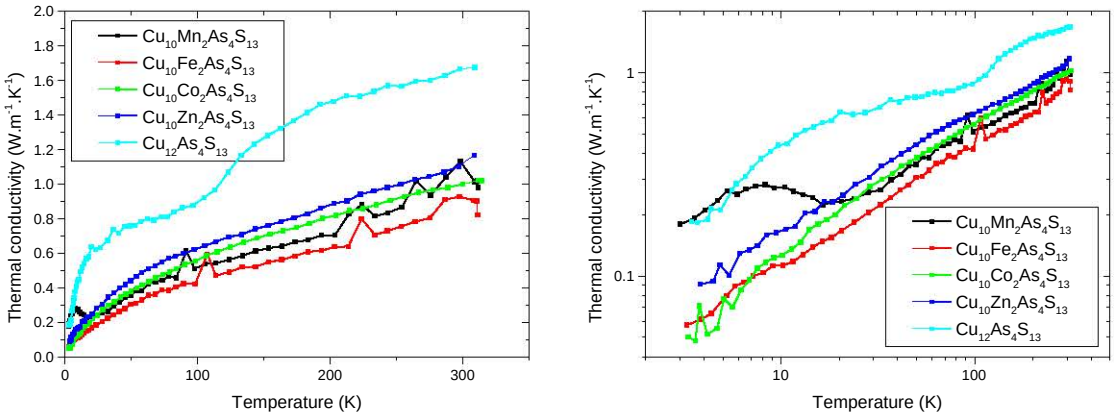

Figure 4.53: Temperature dependence of the thermal conductivity of $Cu_{10}Me_2As_4S_{13}$, Me = Mn, Fe, Co, Zn, Cu.

of different atoms to enter As-rich samples. Second, some samples suffered sulfur loss during annealing, further influencing the actual composition. Third, we did not perform chemical analyses of the Mn and Fe samples (the XRD data, see Fig. 4.39, however, appeared surprisingly clean). All the samples except the Cu_{12} one display semiconducting temperature dependence. The ones containing Mn and Fe are the most resistive. In the case of the manganese sample, this suggests higher willingness of Mn to enter tennantite, resulting in a larger number of filled VB holes. In the case of Fe, we cannot make any conclusions about its actual concentration because iron in tetrahedrite can exist both in the 2+ and 3+ oxidation states and is therefore capable of effectively filling the VB holes even at lower concentrations. Unlike for other samples, the Seebeck coefficient of the Fe sample does not tend to zero with decreasing temperature. Similar behaviour is seen in Fe-substituted tetrahedrite $Cu_{10}Fe_2Sb_4S_{13}$. [11] Additionally, when temperature drops below 60 K, the Fe tennantite exhibits a sudden increase of S just before it becomes unmeasurable due to excessive resistance.

Thermal conductivity of the Cu_{12} sample shows a marked drop around 120 K (better seen in the linear plot) which is attributed to a decrease of the electronic part due to the sudden increase of resistivity. With decreasing temperature, thermal conductivity of this sample somewhat recovers (better seen in the logarithmic plot) and attains values higher than the other samples. One exception is the Mn sample which exhibits a small peak around 10 K. Its κ is comparable to the Cu_{12} sample at the lowest temperatures, while being comparable to the other substituted samples above 25 K.

To conclude this section: three series of tetrahedrite-tennantite solutions were synthesized and characterized, one with only Cu atoms on the Cu site, the other two with Co and Zn substitutions. The first two were synthesized successfully, while the Zn series suffered from sulfur degassing during annealing of As-rich samples. It was confirmed that the isovalent substitution of As has only a small effect on the

thermoelectric properties. In the pure-Cu samples, ρ varies within a few percent among the samples, S drops by 3 % with each As atom, peak ZT of the As end-member is 10 % lower than that of the Sb end-member. While S increases sharply with the metal-to-semiconductor transition in $Cu_{12}Sb_4S_{13}$, the $S(T)$ dependence of all the samples containing As is completely smooth.

Electrical properties of the Co and Zn series were determined by the concentration of the Co and Zn atoms which got successfully incorporated in the tetrahedrite-tennantite structure. With increasing As concentration, the concentration of Co and Zn decreased, leading to increased carrier concentration and higher position of the Fermi level. The dependence of lattice thermal conductivity on As content gave somehow different results for each of the three series: the pure Cu series showed a drop for samples containing both Sb and As, indicating alloying effect (see Fig. 4.33); the Co series showed rather constant values, indicating no effect (see Fig. 4.44); the Zn series did not reveal any obvious dependence, again pointing towards no effect of As (see Fig. 4.51). Combining these results, we can tentatively say that As does not seem to significantly influence the lattice thermal conductivity of tetrahedrite, with the exception of a mild alloying effect.

4.1.4 Substitutions on the Cu Site

A wide variety of atoms can substitute into tetrahedrite, as can be seen from the table on page 25. The range of Cu-site substitutions is particularly diverse. Several of these, namely the 3d elements Mn, Fe, Co, Ni, and Zn, have already been thoroughly studied for their thermoelectric and other properties. In this section, we investigate the properties of synthetic tetrahedrites with lesser-known substitutions on the Cu site. One way to approach this issue is to consult the literature for substitutions which are known to exist, synthesize the samples and measure those properties which have not yet been measured. A second way is trying to discover substitutions which are not yet known.

For the former approach, the works of Makovicky, Karup-Møller et al. are particularly useful. They synthesised hundreds of samples to determine which elements substitute to what extent on which sites. [63–68] In 2003, the authors showed that the metalloids Sn and Ge, not found in natural specimens, in fact enter tetrahedrite when prepared synthetically. [66] Thermoelectric properties of these compounds were reported in 2017. [53] Indium, also not found in natural specimens, can substitute on the Cu site, as demonstrated in [88]. This study reported solely the $Cu_{11}In_1Sb_4S_{13}$ composition whose optical properties were studied in detail, the electrical resistivity and Seebeck coefficient being only given for room temperature. We will study the In substitution in more detail.

In an attempt to find other elements which can substitute on the Cu site, we turn to Shannon's database of ionic radii [45]. We take the cations and narrow their list down. The substitutions take place on the Cu(1) crystallographic site which is tetrahedrally coordinated. We therefore limit ourselves to ions with 4-fold standard coordination, disregarding e.g. square coordination. We only consider ions of reasonable size, eliminating those smaller than 0.3 Å. We also discard elements

known to substitute on the Sb and S sites. This leaves us with the following list, ordered by increasing ionic radius: Mn^{5+}, Cr^{5+}, V^{5+}, Ru^{8+}, Re^{7+}, Ru^{7+}, Al^{3+}, $\underline{\mathbf{Ge}^{4+}}$, Mn^{4+}, Os^{8+}, Cr^{4+}, Mo^{6+}, I^{7+}, Ti^{4+}, W^{6+}, Ga^{3+}, Nb^{5+}, $\underline{\mathbf{Fe}^{3+}}$, U^{6+}, $\underline{\mathbf{Ni}^{2+}}$, Rh^{5+}, $\underline{\mathbf{Sn}^{4+}}$, $\underline{\mathbf{Cu}^{2+}}$, Mg^{2+}, $\underline{\mathbf{Co}^{2+}}$, Hf^{4+}, Li^{1+}, Zr^{4+}, $\underline{\mathbf{Cu}^{1+}}$, $\underline{\mathbf{Zn}^{2+}}$, $\underline{\mathbf{In}^{3+}}$, $\underline{\mathbf{Fe}^{2+}}$, Mo^{5+}, $\underline{\mathbf{Pb}^{4+}}$, $\underline{\mathbf{Mn}^{2+}}$, Tl^{3+}, $\underline{\mathbf{Cd}^{2+}}$, $\underline{\mathbf{Hg}^{2+}}$, Na^{1+}, $\underline{\mathbf{Ag}^{1+}}$, K^{1+}.

The elements known to enter tetrahedrite are set in bold and underlined. We see that all the elements currently known to substitute for Cu are in this list and that their ionic radius lies between 0.49 Å for Fe^{3+} and 1.02 Å for Ag^{1+}. Inversely, most of the ions in this range are known to substitute in tetrahedrite. A single exception is germanium with the radius 0.39. Three elements are currently known not to enter tetrahedrite: Cr [63], V [63] and Yb [12]. Ytterbium is not in this list because Shannon's database only lists it with coordination numbers 6 and higher. Chromium and vanadium are at the beginning of our list, suggesting than in the 4-fold coordination they are too small to be a part of stable tetrahedrite structure. We also note that manganese enters tetrahedrite in the 2+ oxidation state, while its 4+ ions seems to be too small (0.39 Å) to exist in the higher oxidation state.

Based on this phenomenological approach, we can predict more elements to enter tetrahedrite. One of them is Mg in the 2+ oxidation state with the radius 0.57 Å. We will test this hypothesis experimentally. Another element which might enter tetrahedrite is Zr in the 4+ oxidation state. The same is valid for Hf which is chemically very similar. We may also expect Tl^{3+} which is in a favourable part of the list and three of its neighbouring elements in the periodic table (Hg, In, Pb) have been reported in tetrahedrite. In the case of Ga, its smaller radius (0.47 Å) may pose a problem but its substitution into tetrahedrite might as well be possible – neighbouring In, albeit larger (0.62 Å), willingly enters tetrahedrite, Zn is a prototypical substituent, and Ge is known to substitute for Cu tetrahedrite despite its small ionic radius.

4.1.4.1 Tin, Germanium

It has been shown [66] that Sn and Ge can partially substitute into tetrahedrite, a situation not observed in nature. They willingly substitute on the Cu site, although it is possible for them to enter the Sb site as well. We decided to study the effect of Sn and Ge substitutions on the thermoelectric properties. To do that, we synthesized 5 samples from the $Cu_{12-x}Sn_xSb_4S_{13}$ series with $x = 0.25$, 0.5, 0.75, 1.0, and 1.5, as well as 3 samples from the $Cu_{12-x}Ge_xSb_4S_{13}$ series with $x = 0.25$, 0.5, and 1.0. Unbeknownst to us, a different team of authors was working on this issue at the same time. Their results were published [53] around the time we were measuring the TE properties of the first three samples. On that account, we did not carry on with the experiments. We will now present the partial results we obtained, mostly to confirm the published data and to complement them slightly. For proper information about the influence of the Sn and Ge substitutions, we vividly recommend the publication [53] which treats the issue in a thorough and clear manner.

Figure 4.54 shows powder XRD patterns of the samples from the $Cu_{12-x}Sn_xSb_4S_{13}$ series after synthesis. All the samples are composed mostly of the tetrahedrite phase.

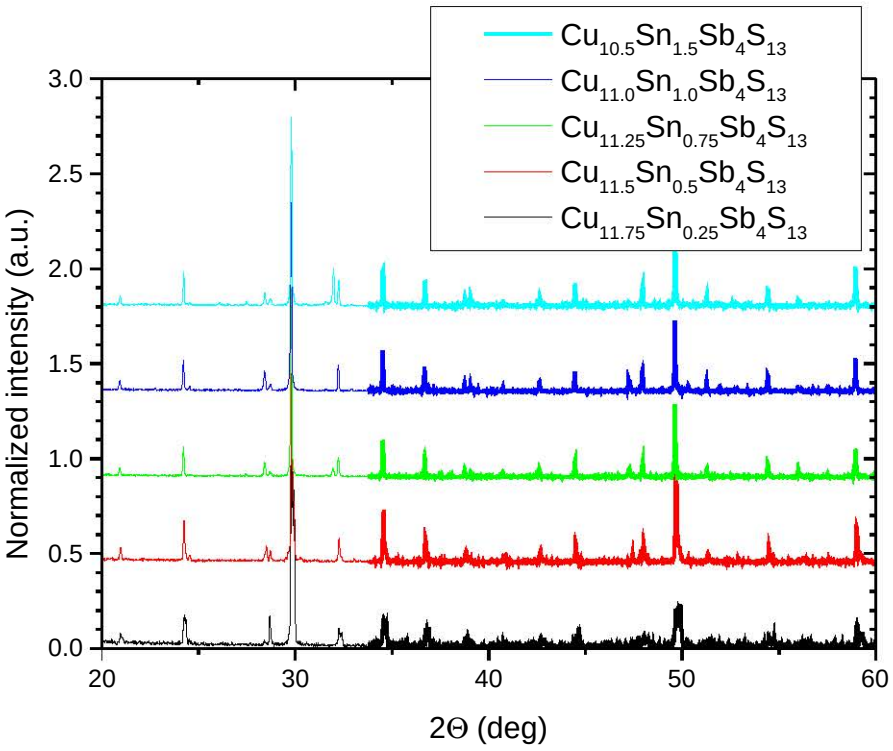

Figure 4.54: Powder XRD patterns of the samples from the $Cu_{12-x}Sn_xSb_4S_{13}$ series after synthesis.

The $x = 0.25$ sample actually contains two tetrahedrite phases, as evidenced by the split peaks. Only three of the samples, namely $x = 0.25$, 0.5 and 0.75, were investigated further. They were annealed and Figure 4.55 shows their XRD patterns after this step. The samples are composed mostly of the tetrahedrite phase with some minor amounts of Cu_3SbS_4. Annealing caused the two tetrahedrite phases seen previously in the $x = 0.25$ sample to merge. The peaks gradually shift, implying linear increase of the cell parameter with x, see Figure 4.56. The results are consistent with [53]. The authors also report on the actual chemical composition of the samples which was in fair agreement with the nominal composition. The Sn atoms occupied solely the Cu sites, not the Sb sites.

Our samples sintered well, their density was over 98 % of the theoretical value. Figure 4.57 shows the temperature dependence of their electrical resistivity and Seebeck coefficient. The results show a slight mismatch between S measured by the low- and high-temperature instrument, the origin of this mismatch is not known. Otherwise, the results agree well with those in [53] and are consistent with the Sn atoms being in the 4+ oxidation state, supplying 3 electrons per atom, and not influencing the band structure around the Fermi level. They have an effect analogous to three times the amount of Zn^{2+} atoms. Low temperature data show that the metal-to-semiconductor transition at 85 K is greatly suppressed in the $x = 0.25$ sample.

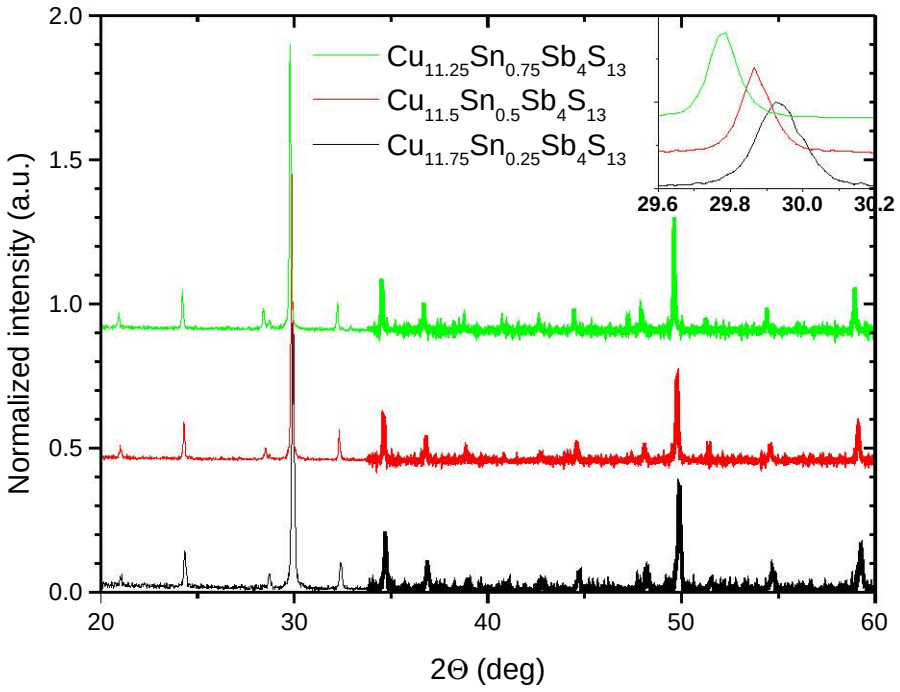

Figure 4.55: Powder XRD patterns of the samples from the $Cu_{12-x}Sn_xSb_4S_{13}$ series before sintering. All main peaks could be indexed to the tetrahedrite-tennantite phase.

The high values of electrical resistivity and Seebeck coefficient of the $x = 0.75$ sample, $\rho = 10^{-1}$ Ω.m^{-1} and $S = 500$ µV.K^{-1} at room temperature, are comparable with the values obtained for natural tetrahedrites. Such high values suggest that the Sn^{4+} atoms provided enough electrons to fill almost all holes in the valence band. The actual concentration of Sn has to be close to the 0.67 a.p.f.u. limit. Exceeding this limit with the nominal composition did not lead to n-type conductivity by doping the excess electrons into the conduction band.

Figure 4.58 shows the effect of Sn doping on the thermal conductivity and ZT. The reduction of the total thermal conductivity can be attributed mainly to the reduction of the electronic part. The overall effect on ZT is positive, the $x = 0.25$ and 0.5 samples exhibit almost identical values which are some 20 % higher than in pristine $Cu_{12}Sb_4S_{13}$. The peak ZT we obtained was 0.7 at 673 K. The results are consistent with [53]. The $x = 0.75$ sample is too resistive, causing its ZT to drop one order of magnitude below that of the other samples.

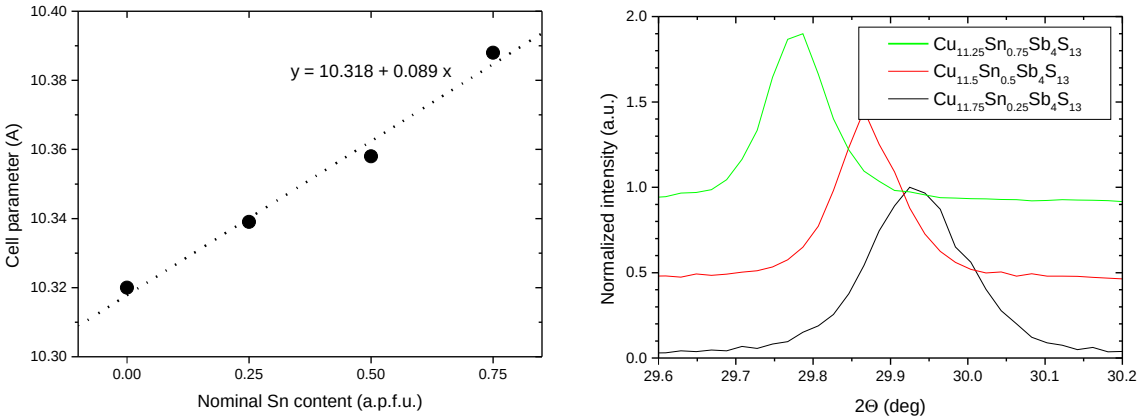

Figure 4.56: Dependence of the cell parameter on Sn content in $Cu_{12-x}Sn_xSb_4S_{13}$. Right part details the shift of the main diffraction peak.

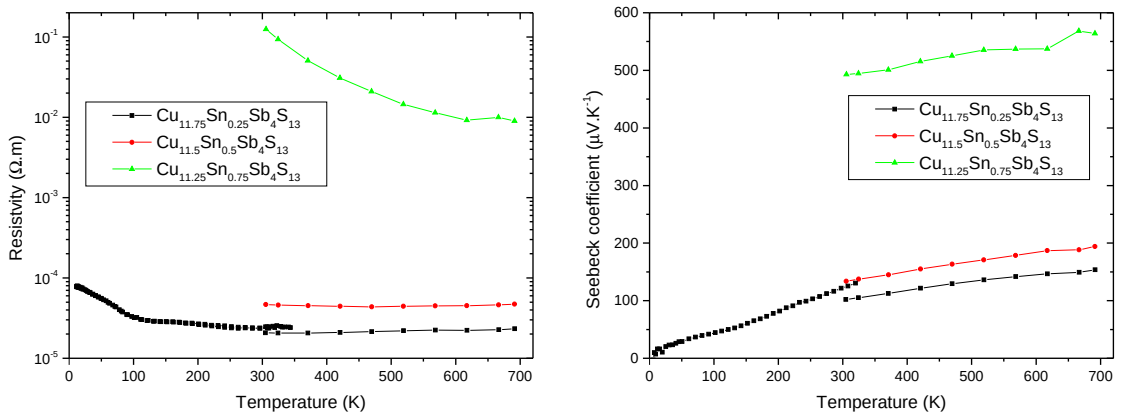

Figure 4.57: Temperature dependence of the electrical resistivity and Seebeck coefficient of $Cu_{12-x}Sn_xSb_4S_{13}$.

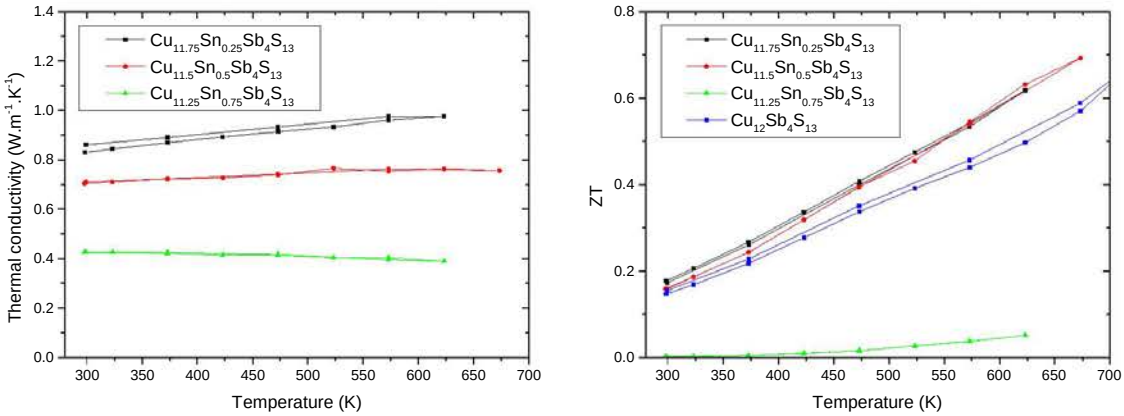

Figure 4.58: Temperature dependence of the thermal conductivity and ZT of $Cu_{12-x}Sn_xSb_4S_{13}$.

4.1.4.2 Magnesium, Calcium, Aluminium

In this section, we will investigate the substitution of Mg, Ca and Al for Cu in tetrahedrite, focusing mainly on Mg. Based on our previous discussion, we expect Mg to enter tetrahedrite, Ca not, and Al maybe. First, we attempted to synthesize the three following samples: $Cu_{11.5}Mg_{0.5}Sb_4S_{13}$, $Cu_{11.5}Ca_{0.5}Sb_4S_{13}$ and $Cu_{11.75}Al_{0.25}Sb_4S_{13}$.

In the case of the Mg sample, the synthesis process was uneventful. In the case of the Al and Ca samples, however, the material got stuck to the quartz tubes. This can be seen in Figure 4.59. Evidently, some kind of reaction occurred between the material and the tube. While fused silica is generally very resistant, it can be attacked, especially at high temperatures. Molten aluminium penetrates into quartz and reacts to form silicon and alumina. [47] At the temperature we used to synthesize our materials, the penetration rate is around 5 µm per hour.

Figure 4.59: Photos showing material stuck to the reaction tubes after an attempted synthesis of $Cu_{11.75}Al_{0.25}Sb_4S_{13}$ (left) and $Cu_{11.5}Ca_{0.5}Sb_4S_{13}$ (right). The shards are 2 mm thick.

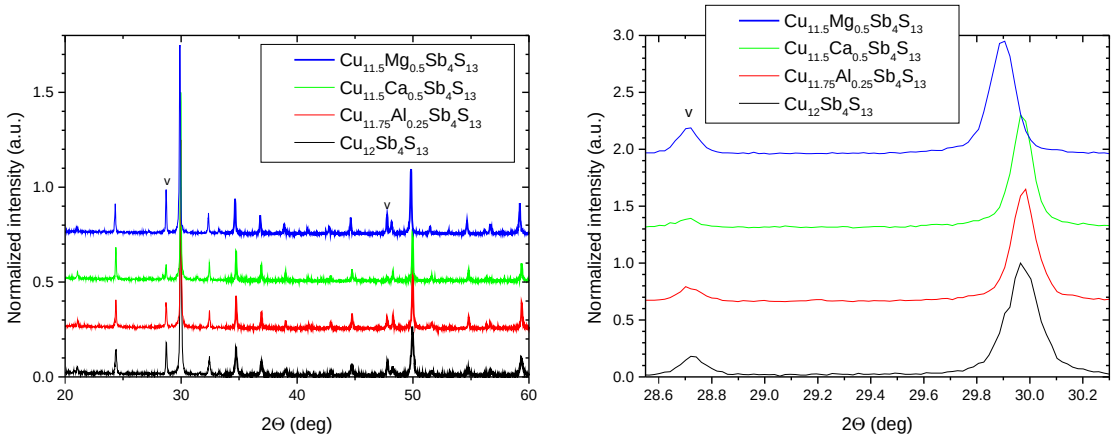

Figure 4.60: Powder XRD patterns of annealed samples with Al, Ca, and Mg substitutions on the Cu site of $Cu_{12}Sb_4S_{13}$. An unsubstituted sample is also shown for comparison. All main peaks could be indexed to tetrahedrite; Cu_3SbS_4 is marked by ^{v}.

Despite the encountered reaction, we proceeded with cold pressing and annealing the three samples. We have to keep in mind though, that the stoichiometry of the annealed pellets probably differs from the initial one. Figure 4.60 shows powder XRD patterns of the three samples after annealing, along with pristine $Cu_{12}Sb_4S_{13}$ for comparison. All the samples are composed mostly of the tetrahedrite phase and, as usual, there is some Cu_3SbS_4 present. Minor amounts of CaS and $CuAlS_2$ were also detected. The presence of MgS could not be detected by XRD because the main diffraction peaks of MgS and tetrahedrite overlap. It was however confirmed by EDX as well as by the characteristic smell of H_2S which developed when MgS in the sample reacted with moisture. A close-up view in the right part of the figure shows apparent peak shift in the Mg sample, suggesting that the substitution was successful, enlarging the unit cell size. There is no shift seen for the Ca and Al samples. We therefore decided to focus only on Mg substitutions, which will be discussed later. We did not perform further experiments regarding Ca and Al substitution and we will only finish the discussion about these two samples.

The lack of peak shift means that in our case, the substitution of calcium into tetrahedrite did not occur because the influence of the large Ca atom on the unit cell size should be clearly evident from the XRD data. We have to be careful when linking this observation to the general conclusion that Ca does not enter tetrahedrite. As mentioned above, we lost some material between the synthesis and annealing steps and we do not know how much calcium got lost. In an extreme case, all the calcium would be stuck to the tube and the annealed compound would be pristine tetrahedrite with no peak shift, regardless of the ability of Ca to substitute in tetrahedrite. We know that this is not the case because CaS was detected with XRD. We will see later that in the case of Mg substitution, most of the magnesium forms a sulfide during the synthesis step and approximately one half of magnesium then migrates into tetrahedrite during annealing. We may argue that if calcium was able

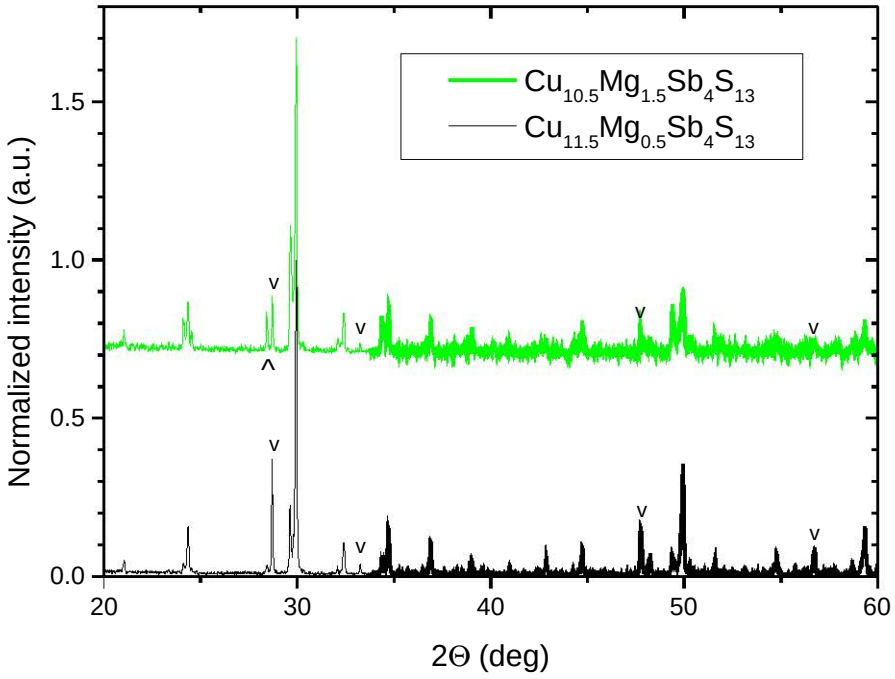

Figure 4.61: Powder XRD patterns of annealed samples from the $Cu_{12-x}Mg_xSb_4S_{13}$ series after synthesis. Both samples are composed mostly of a mixture of two tetrahedrite phases with slightly different cell parameters, resulting in split peaks. Peaks from secondary phases are present, these are marked by ^{v} for Cu_3SbS_4 and by $^{\wedge}$ for $CuSbS_2$.

to substitute into tetrahedrite, an analogous process would happen and the presence of CaS in the material should result in incorporation of Ca into tetrahedrite during annealing. As we detected CaS but no peak shift, we may suppose that Ca does not indeed enter tetrahedrite. Based on the previous discussion about Shannon's database of ionic radii, this is an expected result because the lowest coordination number listed therein for Ca is 6. Regarding Al, the discussion is more difficult. Aluminium ions are small and it is possible that a substitution of Cu by Al would not change the cell parameter. Our data about Al entering tetrahedrite therefore remain inconclusive.

Following the success with magnesium, we synthesized two more sample to obtain a $Cu_{12-x}Mg_xSb_4S_{13}$ series with $x = 0.5$, 1, 1.5. Figure 4.61 shows powder XRD patterns of two samples from this series after synthesis. Both samples are composed mostly of a mixture of two tetrahedrite phases with slightly different cell parameters which results in split peaks. There are secondary phases present, namely Cu_3SbS_4 and $CuSbS_2$. Annealing improves phase purity of the sample, as can be seen in Figure 4.62: the annealed samples are composed of a single tetrahedrite phase and the amount of Cu_3SbS_4 of $CuSbS_2$ decreased.

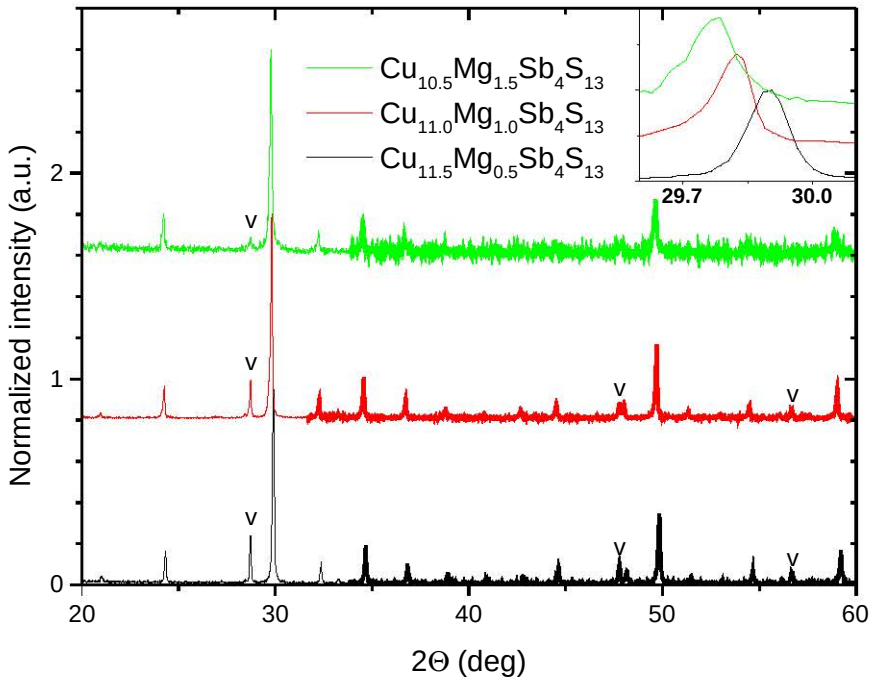

Figure 4.62: Powder XRD patterns of annealed samples from the $Cu_{12-x}Mg_xSb_4S_{13}$ series before sintering. All main peaks could be indexed to the tetrahedrite phase. A certain amount of a Cu_3SbS_4 phase, marked by ^{v}, is present.

Figure 4.63 shows a detailed comparison of the as-synthesized and annealed samples along with pristine $Cu_{12}Sb_4S_{13}$. We can see that the cell parameter of the main tetrahedrite phase is almost the same as that of pristine phase. The minor phase can be classified as the copper-rich tetrahedrite $Cu_{13.8}Sb_4S_{13}$ with the cell parameter 10.44 Å which is sometimes seen in synthetic tetrahedrites. [89] It is a mystery why the samples containing relatively less copper form a copper-rich tetrahedrite phase. After annealing, only one tetrahedrite phase is present and its cell parameter closely follows the increasing Mg content, as evidenced by the gradually shifting peaks. This suggests that MgS is not in the tetrahedrite structure right after the synthesis but enters inside during annealing.

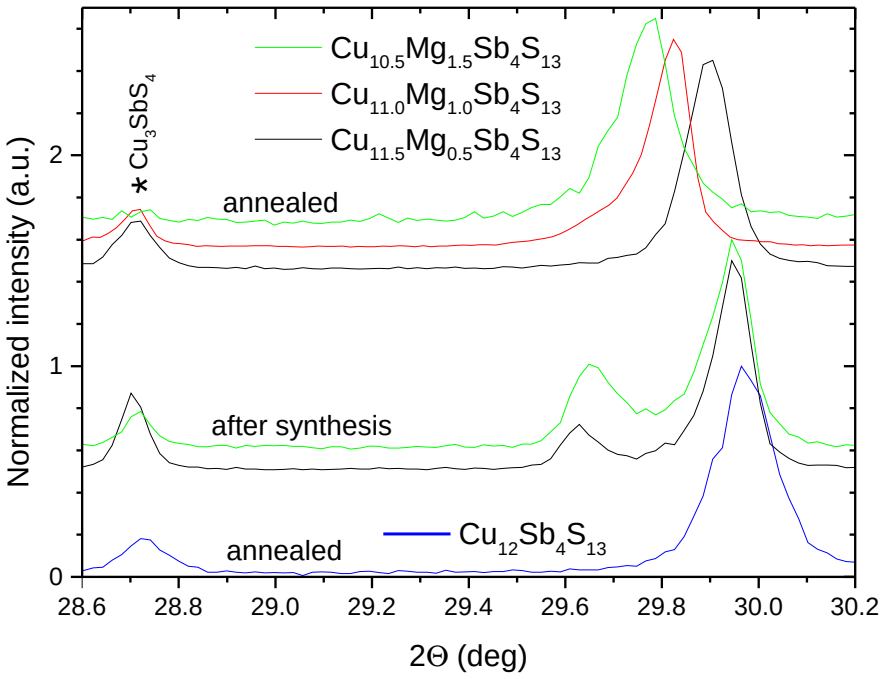

Figure 4.63: A detail of powder XRD patterns of the samples from the $Cu_{12-x}Mg_xSb_4S_{13}$ series showing the main diffraction peak (222) of tetrahedrite, as well as the main peak (112) of Cu_3SbS_4 marked by *. $Cu_{12}Sb_4S_{13}$ is shown for comparison. After synthesis, the Mg-substituted samples are composed of two tetrahedrite phases, as evidenced by peak splitting; annealing promotes the formation of a single phase with the cell parameter following magnesium content.

Figure 4.64 shows the evolution of the cell parameter a in $Cu_{12-x}Mg_xSb_4S_{13}$ as a function of the *nominal* content x of magnesium. We stress the nominal content because semi-quantitative EDX analysis showed that approximately only one half of the total magnesium is contained in the main tetrahedrite phase. The other half is present in MgS impurities. The cell parameter nicely follows the line $a = 10.320+0.044x$ Å, so the actual increase of the cell parameter is close to 0.09 Å

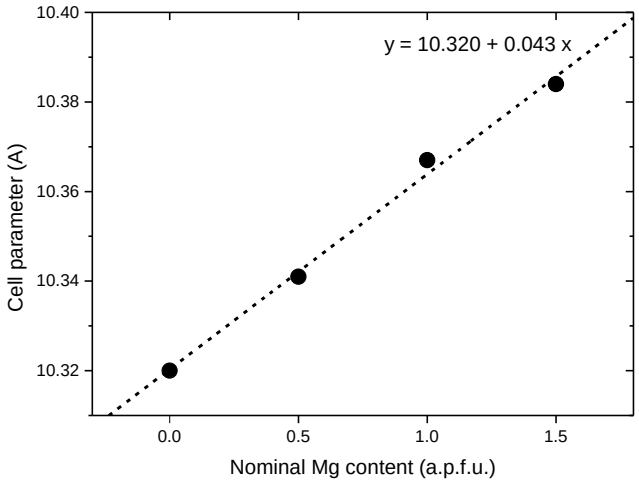

Figure 4.64: Dependence of the cell parameter on Mg content in $Cu_{12-x}Mg_xSb_4S_{13}$.

per one Mg atom. This value is greater than what we could expect based on Shannon's ionic radius which is comparable to other d-block elements. The value we estimated for Mg is closer to 0.1 Å which was measured for substitutions by large atoms such as Hg [67] and Cd [84].

The samples were sintered successfully, their relative density was between 95 % and 98 %, the sample with the least Mg being the densest. Back-scattered electron images of the sintered samples can be seen in Figure 4.65. They are mostly composed of the desired tetrahedrite phase containing, according to EDX, half of the total Mg atoms. The other half is contained in MgS inclusions also visible in the BSE image. We can also see some Cu_3SbS_4 phase along with a small amount of $CuSbS_2$; according to EDX, neither of these two phases contains any magnesium.

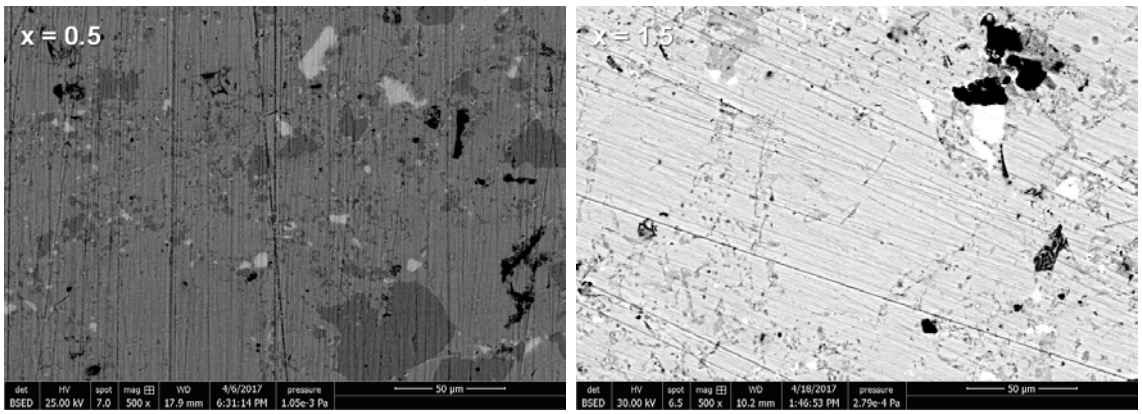

Figure 4.65: Back-scattered electron images of polished surfaces of the sintered samples from the $Cu_{12-x}Mg_xSb_4S_{13}$ series. The samples are mostly composed of the desired tetrahedrite phase. Darker areas indicate Cu_3SbS_4, white spots indicate $CuSbS_2$, and black spots indicate MgS.

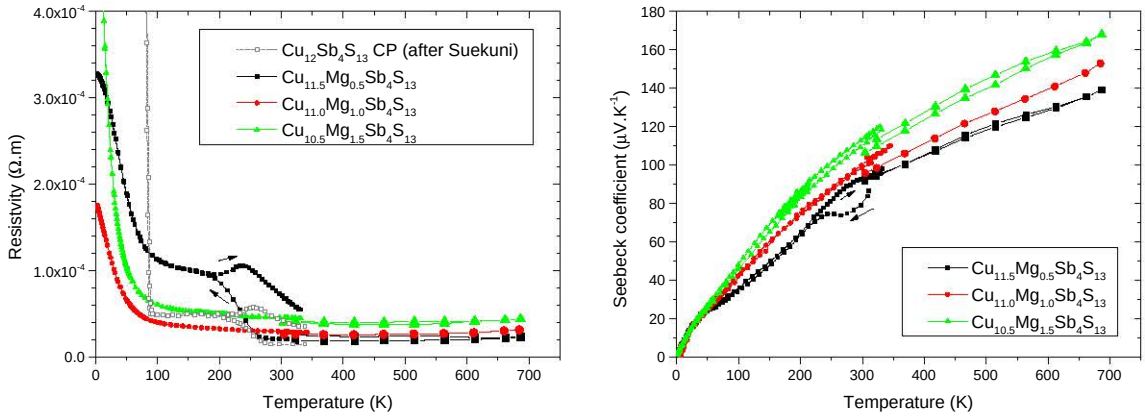

Figure 4.66: Temperature dependence of the electrical resistivity and Seebeck coefficient of $Cu_{12-x}Mg_xSb_4S_{13}$. Low temperature data for the pristine compound were taken from [11].

The thermoelectric properties are shown in Figure 4.66 (ρ and S) and Figure 4.67 (κ and ZT). Looking at data at and above room temperature, we see behaviour consistent with other substitutions on the Cu site: Mg^{2+} fills the valence band holes, increasing the electrical resistivity and Seebeck coefficient and decreasing the thermal conductivity mainly by reducing its electronic part. The magnitude of this effect is comparable with other substituents [53, 81] and supports the fact that only a part of the Mg atoms are inside tetrahedrite. Magnesium substitution leads to slight deterioration of ZT when compared to unsubstituted tetrahedrite although at higher temperatures, the difference is within experimental error. Peak value 0.55 at 673 K was obtained for the $x = 0.5$ and $x = 1$ samples.

Low temperature data show an interesting anomaly in the electrical resistivity and, to a lesser extent, in the Seebeck coefficient. Both parameters show hysteresis and increase upon cooling from room temperature to some 200 K. This closely resembles the hysteresis observed by Suekuni et al. [11] in cold pressed $Cu_{12}Sb_4S_{13}$ with rather low density around 80 %. Otherwise, the samples behave rather normally. Their resistivity shows semiconducting temperature dependence, the metal-to-semiconductor transition (MST) is strongly reduced, S goes monotonically to 0. Below 40 K, the Seebeck coefficients of the $x = 0.5$ and $x = 1$ samples converge to that of the $x = 1.5$ sample. The gentle hump exhibited by S below 100 K is probably a remnant of the MST.

In summation, we attempted to synthesize samples with Mg, Ca and Al substitutions on the Cu site. Calcium does not seem to enter tetrahedrite, data about aluminium were inconclusive and magnesium was shown to enter into tetrahedrite. The effect of Mg is similar to that of other polyvalent substituents, its influence on ZT is minimal. To our best knowledge, this is the first report of an s-block element in tetrahedrite.

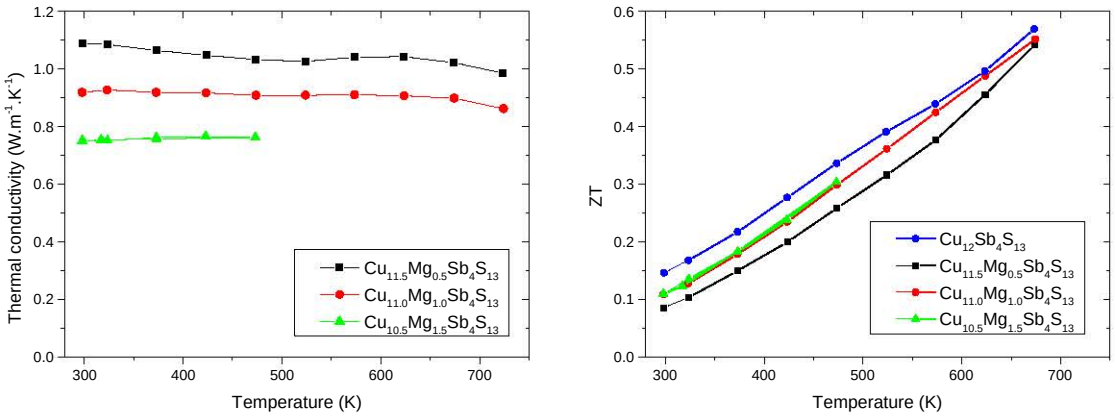

Figure 4.67: Temperature dependence of the thermal conductivity and ZT of $Cu_{12-x}Mg_xSb_4S_{13}$.

4.1.4.3 Other Atoms (In, Ag)

We will study the influence of In substitution for Cu. We synthesized two samples: $Cu_{12-x}In_xSb_4S_{13}$ with $x = 0.5$, 1. Figure 4.68 shows powder XRD patterns of the samples after synthesis. The $x = 0.5$ sample is composed mainly of the tetrahedrite phase as well as some other phases, such as $CuSbS_2$, $CuInS_2$ and $CuIn_5S_8$. The phase purity of the $x = 1$ sample is much worse. The tetrahedrite phase is also present but the sample contains large amounts of Cu_3SbS_3 and there are other phases present, such as $CuSbS_2$ and $CuIn_5S_8$.

Annealing improved the phase composition, as can be seen from Figure 4.69. The improvement is especially significant in the case of the $x = 1$ sample. Both samples are composed mainly of the desired tetrahedrite phase and there is some famatinite Cu_3SbS_4 and $CuInS_2$. The shift of the diffraction peaks suggests incorporation of In in the tetrahedrite structure. An EDX analysis supported this fact and also confirmed the presence of the $CuInS_2$ phase. The increase of the unit cell size with In content can be seen in Figure 4.70. Its magnitude, 0.048 Å per a.p.f.u., is very similar to that seen for manganese substitutions [81].

Sintering the powders yielded pellets 99 % and 93 % dense, the In-rich sample being less dense. Figures 4.71 and 4.72 show the temperature dependence of the thermoelectric properties of the samples. Indium substitution has an analogous effect to that of other standard polyvalent substituents, i.e. filling the valence band holes. The $x = 1$ sample was rendered semiconducting by the substitution. In the $x = 0.5$ sample, the substitution increased ρ by a factor of 2.5 when compared to pristine tetrahedrite and greatly suppressed the metal-to-semiconductor transition below at 85 K. A remnant of the MST is seen as a very gentle hump of the Seebeck coefficient.

Comparing the absolute values of ρ and S to those obtained for Zn^{2+} and Sn^{4+} [52] gives us an approximate concentration of holes around 0.8 and 1.7 per formula unit for the $x = 0.5$ and $x = 1$ samples, respectively. This confirms the 3+ oxidation

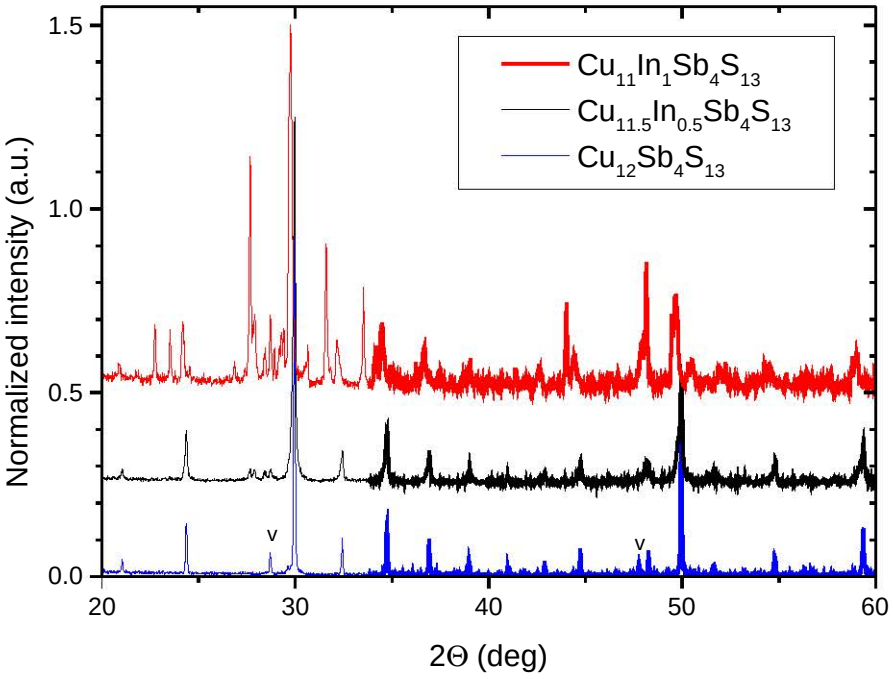

Figure 4.68: Powder XRD patterns of the samples from the $Cu_{12-x}In_xSb_4S_{13}$ series after synthesis. A pattern for $Cu_{12}Sb_4S_{13}$ is given for comparison; a Cu_3SbS_4 impurity is marked by ^{v}. The samples, especially the In-rich one, contain various different phases; these are largely reduced or eliminated in favour of the desired tetrahedrite phase during annealing.

state of In and suggests that the real x is somewhere around 0.4 and 0.8. Two samples of $Cu_{11}In_1Sb_4S_{13}$ investigated in [88] were prepared by hot pressing a powder obtained via the solid state route, and by electron beam deposition and annealing of thin films with the thickness of the order of 100 nm. The bulk sample apparently had more atoms incorporated into the tetrahedrite structure than our $x = 1$ sample, resulting in lower carrier concentration. This is evidenced by the fairly high room temperature values of S over 300 $\mu V.K^{-1}$ and ρ two orders of magnitude higher than for our sample. This proximity to the nominal composition may be stem from the longer annealing time which was 3 weeks; we annealed for one week. While 5 days can be largely enough for many samples, it is possible that this is not the case in $Cu_{11}In_1Sb_4S_{13}$ which contained a large amount of secondary phases after synthesis and may need longer time for their elimination. The combined effect of filling the valence band holes on ρ, S and κ resulted in the ZT of the $x = 0.5$ sample being almost identical to that of pristine tetrahedrite, and only slightly lower for the $x = 1$ sample despite its resistivity being one order of magnitude higher. The peak value we obtained was $ZT = 0.6$ at 673 K.

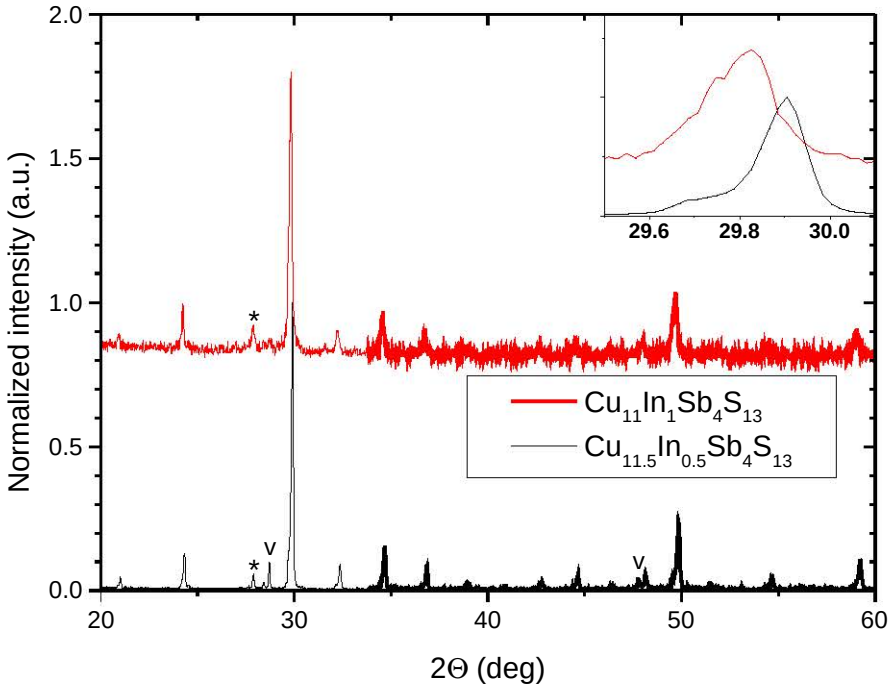

Figure 4.69: Powder XRD patterns of annealed samples from the $Cu_{12-x}In_xSb_4S_{13}$ series before sintering. All main peaks could be indexed to the tetrahedrite phase. A small amount of a Cu_3SbS_4 phase, marked by ^{v}, is present along with $CuInS_2$, marked by *.

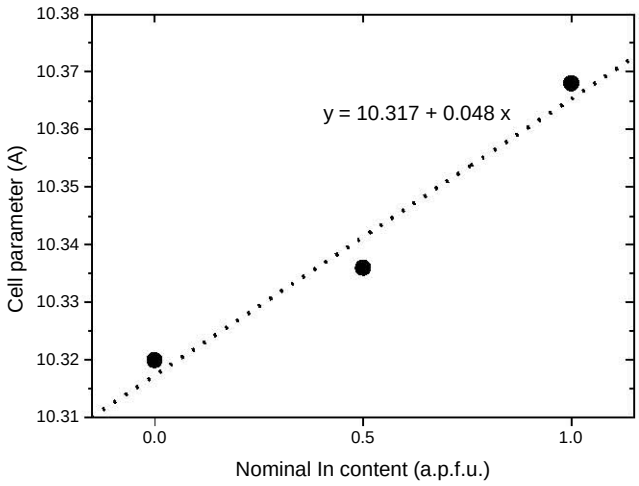

Figure 4.70: Dependence of the cell parameter on In content in $Cu_{12-x}In_xSb_4S_{13}$.

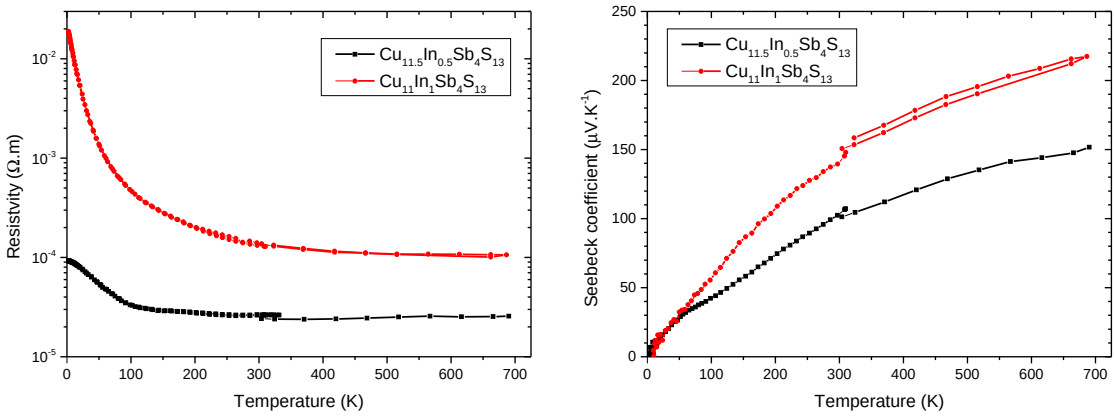

Figure 4.71: Temperature dependence of the electrical resistivity and Seebeck coefficient of $Cu_{12-x}In_xSb_4S_{13}$.

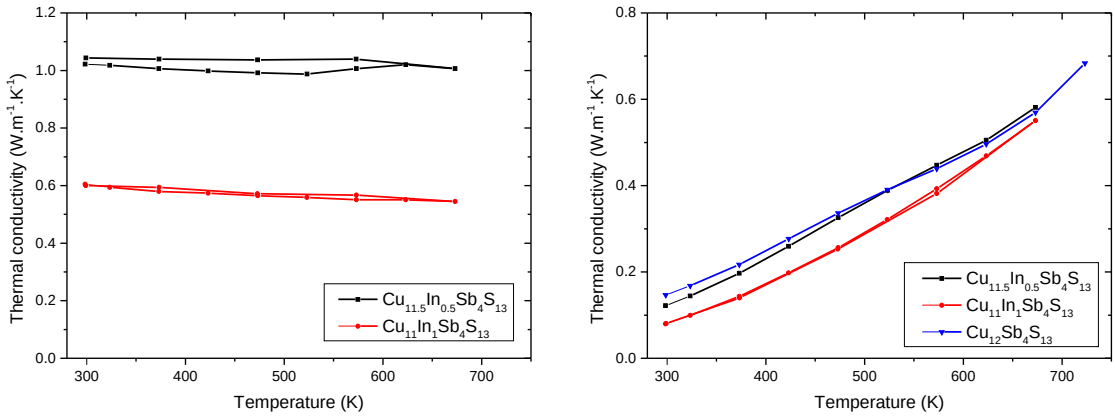

Figure 4.72: Temperature dependence of the thermal conductivity and ZT of $Cu_{12-x}In_xSb_4S_{13}$.

Silver is a standard substituent in natural tetrahedrites. On one hand, it is usually present only in small amounts. On the other hand, it may substitute for a large number of Cu atoms. Nevertheless, we have not found any report about its influence on the thermoelectric properties. It would be interesting to see the effect of such a substitution by a similar atom on the electrical properties as well as on the metal-to-semiconductor transition. We tried to synthesize a $Cu_{11}Ag_1Sb_4S_{13}$ sample without too much success. Figure 4.73 shows the XRD patterns of the sample after various types of heat treatment. We see that the as-synthesized sample was actually the best one, it was composed mainly of the tetrahedrite phase along with some Cu_3SbS_4. Annealing at 450 °C seriously degraded the sample, shifting its composition towards the Cu_3SbS_4 phase and forming an additional Cu_3SbS_3 phase. Homogenizing, cold pressing and annealing the sample again at 500 °C reduced the amount of secondary phases present but their amount was still fairly high. At this point, we stopped experimenting with $Cu_{11}Ag_1Sb_4S_{13}$.

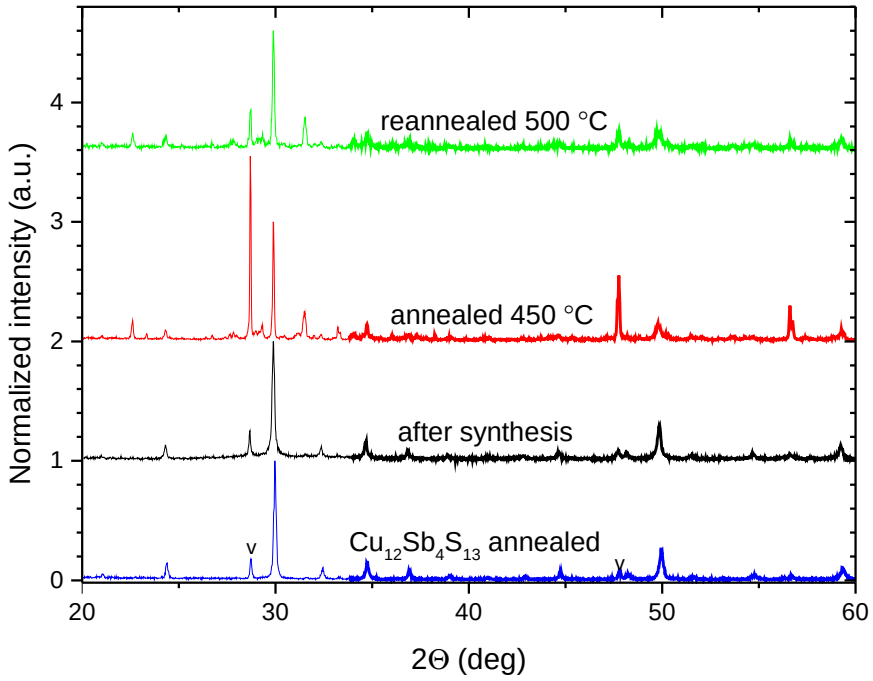

Figure 4.73: Powder XRD patterns of the $Cu_{11}Ag_1Sb_4S_{13}$ sample after synthesis, annealing at 450 °C, and re-annealing at 500 °C. Unsubstituted tetrahedrite is also shown for comparison, Cu_3SbS_4 is marked by ^{v}.

4.2 Oxides

This section of the thesis is devoted to $CaMnO_3$ doped with Yb and co-doped with Yb and W. Emphasis is put on thermal conductivity, which is analysed in more detail. Lastly, we shortly discuss the problem of contacts.

In this work, we did not try to optimize the electronic properties through doping, as this was already performed by many research groups. Rather we focused on the thermal conductivity and its analysis in the hope of understanding the potential for its further reduction. For this goal, single- and double-substituted calcium manganites were synthesized. Their composition was chosen to lie in the range of optimal TE performance according to published data.

4.2.1 Yb and Yb-W Doping

Here we present the data for single- and double-substituted n-type manganites, namely $Ca_{1-x}Yb_xMnO_3$ ($x = 0.015$, 0.03, 0.06, 0.09, 0.12) and $Ca_{1-x}Yb_xMn_{1-x}W_xO_3$ ($x = 0.01$, 0.02, 0.03, 0.04). For all the samples, their electrical resistivity and Seebeck coefficient is measured in the 4–1000 K temperature range, while the thermal conductivity is measured below room temperature. Thermal conductivity above room temperature is measured only for three selected samples and the data are presented in the next section.

The first batch of synthesized samples was sintered by SPS. Unfortunately, this sintering method turned out to be completely unsuitable. First of all, the samples were of poor mechanical quality. Their density was low and they contained numerous cracks and faults, to the point that it was not uncommon for them to fall apart. This obviously had an influence on the electrical and thermal properties. For example, when $Ca_{0.9}Yb_{0.1}MnO_3$ was sintered by SPS, it showed semiconducting resistivity with $\rho = 29000$ mΩ.cm, $S = -260$ µV.K^{-1} and $\kappa = 1.6$ W.m.K^{-1} at 300 K. When it was cold pressed and annealed, the resistivity was metallic with $\rho = 5$ mΩ.cm, $S = -95$ µV.K^{-1} and $\kappa = 1.8$ W.m.K^{-1} at 300 K.

Another example demonstrating how unsuitable SPS is can be seen in Figure 4.74 which shows ρ and S data for two pieces of undoped $CaMnO_3$ sintered by SPS. Reducing conditions of vacuum and a graphite die during sintering likely caused high oxygen off-stoichiometry of the sample. The deficiency of O^{2-} ions brought additional electrons into the system, causing the absolute value of S being fairly low due to the high carrier concentration. During the high temperature measurements, oxygen from air reentered the sample, bringing the stoichiometry closer to the three atoms per formula unit. Each added oxygen atom removed two free electrons from the system and this decrease of charge carrier concentration lead to increased value of $|S|$ upon cooling. The described effect cannot be seen in ρ which is greatly increased by the low quality of the sample, obscuring the effect of changes in charge carrier concentration. Data for a good quality $Ca_{0.97}Yb_{0.03}MnO_3$ sample sintered classically are also shown in the graphs for comparison. Its Seebeck coefficient is comparable to the formally undoped sample on the cooling run, which suggests the same carrier concentration. Quantitatively speaking, Yb^{3+} substituting for Ca^{2+}

supplies one electron, while the removal of one O^{2-} ion supplies two electrons. The substitution of $Yb_{0.03}$ therefore has an analogous effect as a deficit of $O_{0.015}$.

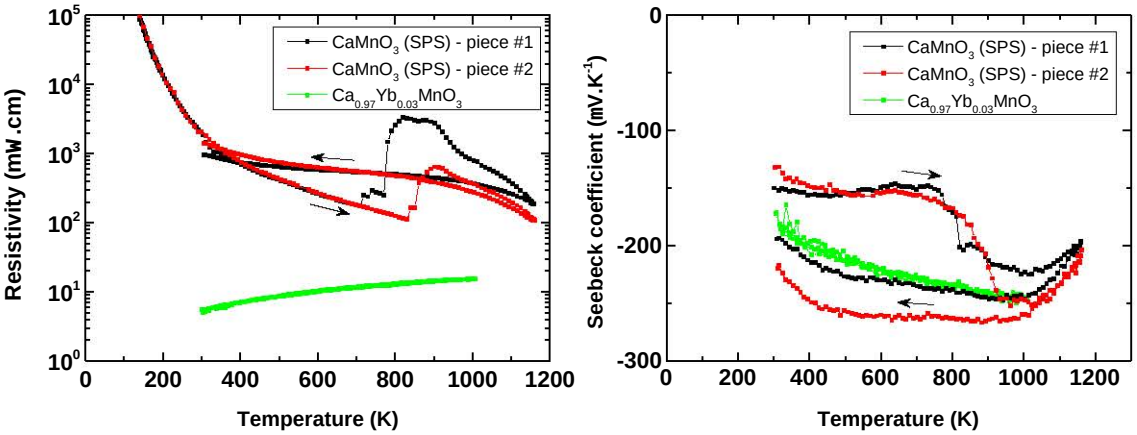

Figure 4.74: Temperature dependence of the electrical resistivity and Seebeck coefficient of a low quality $CaMnO_3$ sample sintered by SPS compared to a good quality $Ca_{0.97}Yb_{0.03}MnO_3$ sintered classically.

Because of these problems, we obtained samples prepared by classical sintering from the CRISMAT laboratory in Caen, France. These samples were single-phased and over 98 % dense but unfortunately contained numerous cracks, see Figure 4.75. As other attempts to produce samples of better quality were not successful, we decided to proceed anyway and with the help of an optical microscope selected the best parts for thermoelectric characterization, keeping in mind the reduced relevance of measured data. Mechanical properties therefore remain a problem which will need to be overcome in the future. One way to achieve this may be to intentionally introduce porosity into the sample. A similar approach is an introduction of secondary phases, either nanoscopic or not, for example precipitates of the chemically and thermally very stable marokite ($CaMn_2O_4$). [110]

The measured data are presented in Figures 4.78 and 4.79. For clarity, we will first discuss the electrical resistivity, Seebeck coefficient and thermal conductivity with the help of Figures 4.76 and 4.77 which contain only data for the most doped, least doped and undoped sample for comparison.

Electronic transport in $Ca^{2+}_{1-x}RE^{3+}_{x}MnO_3$ is close to adiabatic hopping – i.e. phonon assisted "jumps" of carriers. The concentration of electrons participating in conduction is tightly linked to the concentration of Mn^{3+}. Due to a strong Jahn-Teller effect of the Mn^{3+} particles, the decreased degeneracy of e_g orbital leads to a strong local distortion of the Mn^{3+} octahedron, which is coupled to the e_g electron, and leads to the formation of a so-called Jahn-Teller polaron. Polaronic activation energy is on the order of tens of meV. [110, 113, 114, 118]

A simple equation describing this behaviour is [113]

$$\rho = ATe^{E_A/(k_BT)}\,, \tag{4.1}$$

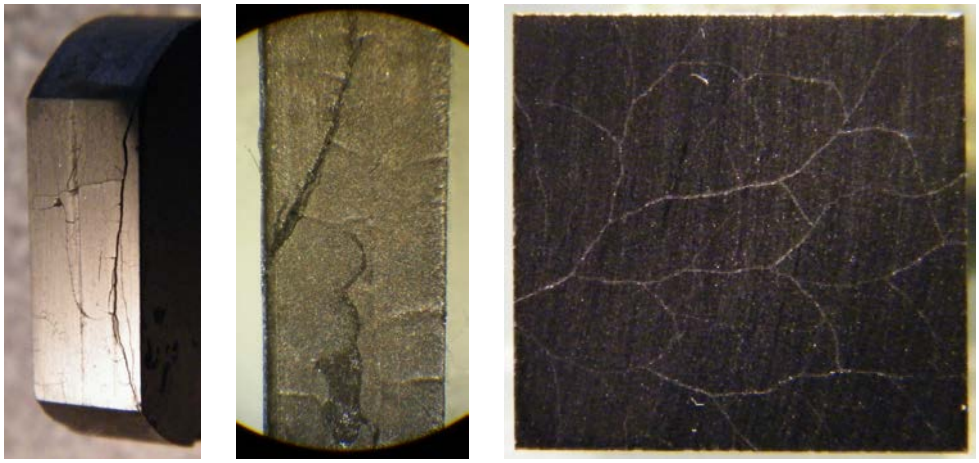

Figure 4.75: Photos showing the defects in sintered samples of doped $CaMnO_3$.

where A is constant and E_A is the activation energy of electrical conductivity which includes both the hopping energy and the energy of carrier excitation over the gap. For low concentrations of carriers, as is the case for our materials, A is inversely proportional to their concentration. [113] In the case of undoped $CaMnO_3$, ρ evolves smoothly around $T_N \approx 123$ K, see Fig. 4.76 left. For higher levels of doping ($x > 0.05$), a clear anomaly at T_N is seen and the system retains low values of resistivity down to the lowest temperatures.

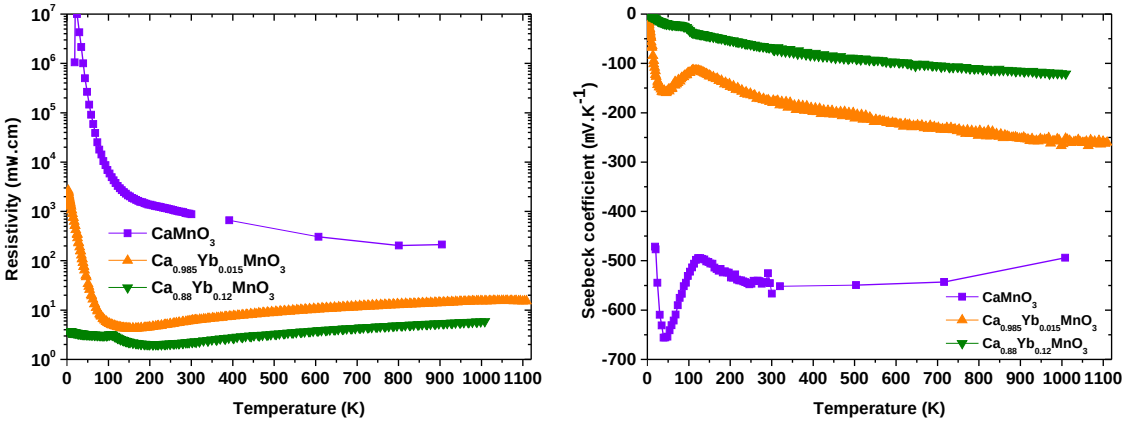

Figure 4.76: A comparison of the temperature dependence of the electrical resistivity and Seebeck coefficient of pure and Yb-doped $CaMnO_3$. Data for the undoped material were taken from [112].

This anomaly associated with magnetic transition is even more pronounced in the temperature dependence of the Seebeck coefficient, shown in Figure 4.76 right. In pure $CaMnO_{3-\delta}$, where the carriers are associated with oxygen substoichiometry δ, the rather temperature independent Seebeck coefficient at high temperatures can be explained with the high temperature limit of polaronic conduction by the generalized

Heikes fomula [25]:

$$S = -\frac{k_B}{e} \ln\left(\beta \frac{1-c}{c}\right), \tag{4.2}$$

where $c = n/N$ is the ratio of the number of carriers to the number of available sites, and β is an additional term reflecting a part of configurational entropy. For a system with a mixed valent cation $M^{n+}/M^{(n+1)+}$ where the spin values of M are S_n and S_{n+1}, respectively, we have

$$\beta = \frac{2S_{M^{n+}} + 1}{2S_{M^{(n+1)+}} + 1}. \tag{4.3}$$

Taking the absolute value of $S \approx -550$ μV.K^{-1} and $\beta = 5/4$, we can calculate the concentration of electrons as $n \approx 3.2 \times 10^{19}$ cm^{-3}, supposing $N \approx 1.8 \times 10^{22}$ cm^{-3}. The increase of $|S|$ at T_N indicates a decrease of charge carrier concentration associated with the G-type AFM order. Upon doping with Yb and W, the transport character changes towards metallic and the Heikes approximation for S is replaced by the well known Mott formula (2.12). The absolute value and temperature dependence of S are then determined by the energy dependence of the density of states at E_F and carrier mobility.

For samples where semiconducting-like low temperature resistivity dominates, the magnetic transition at T_N is accompanied by an increase of $|S|$ which is, as for the pure $CaMnO_3$, explained by the decrease of carrier concentration. In contrast to that, samples with $x > 0.08$, which exhibit low-temperature resistivity with activation energy $\ll k_B T$, complement their metallic-like electrical transport by a decrease of $|S|$ at the magnetic ordering temperature. For a typical sample $Ca_{0.88}Yb_{0.12}MnO_3$ (Fig. 4.76), this decrease amounts to ≈ 20 μV.K^{-1} in the $T_N \pm 15$ K temperature window. Interestingly enough, this value corresponds surprisingly well to the theoretically predicted magnetic entropy associated with electron like carriers in Mn^{4+} background

$$S_{mag} = -\frac{k_B}{e} \ln \frac{2S_{M^{n+}} + 1}{2S_{M^{(n+1)+}} + 1} = \frac{k_B}{e} \ln \frac{5}{4} = -19 \text{ μV.K}^{-1}. \tag{4.4}$$

Apart from the electric transport, doping also has a profound effect on the thermal transport, see Figure 4.77 for the thermal conductivity. In pure $CaMnO_3$, a combined effect of magnetic fluctuations above T_N and a strong deformation of the local environment of Mn^{3+} species is responsible for relatively low and temperature independent thermal conductivity above T_N. [115] The substantial increase of κ below T_N is explained by significantly decreased magnetic fluctuations as long range magnetic order is stabilised.

The impact of increased doping on the thermal conductivity is illustrated with the $x = 0.015$ and $x = 0.12$ samples. First, there is the standard decrease of the absolute value which is directly associated with enhanced scattering of phonons by Mn^{3+} polaronic species. Two more phenomena can be seen: (1) despite the significant doping level of 12 % of Yb replacing Ca, the absolute values of κ at 300 K does not drop dramatically below 3 W.m^{-1}.K^{-1}, and (2) in the case of the $x =$

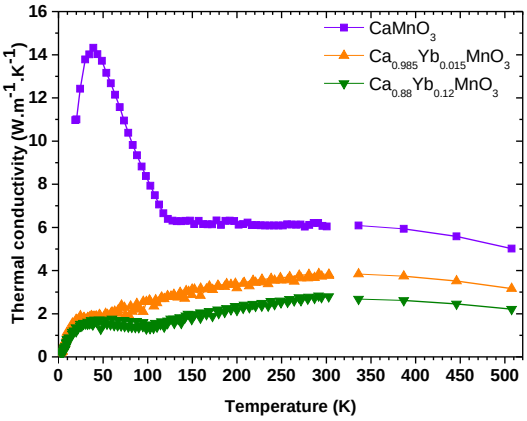

Figure 4.77: A comparison of the temperature dependence of thermal conductivity of pure and Yb-doped $CaMnO_3$. Data for the undoped material and κ above room temperature were taken from [112].

0.12 sample, the thermal conductivity recovers below T_N despite a huge distortion associated with the substitution. The thermal conductivity will be the subject of a more detailed individual analysis.

The complex measurements of the thermoelectric properties of Yb-doped and Yb-W co-doped n-type manganites are presented in Figures 4.78 and 4.79, respectively. For all levels of doping, even the lowest one, the samples exhibit metallic electrical resistivity between ca. 200 K and 1000 K. The maximum power factor PF was measured for the lowest doped samples despite the fact that their resistivity is among the highest. Their concentration of carriers is around $n \approx 5\times10^{20}$ cm^{-3}. This concentration, influenced by Ca and Mn substitution as well as oxygen substoichiometry, corresponds to the formal valency $Mn^{3+}/Mn^{4+} \approx 0.03$. This value is lower than $Mn^{3+}/Mn^{4+} \approx 0.1$ which is generally accepted to be the best with respect to the optimization of thermoelectric properties.

The power factor decreases with increased doping. Furthermore, in the best performing samples it also decreases with temperature. Quantitatively, it ranges between 500 µW.m^{-1}.K^{-2} ($Ca_{0.985}Yb_{0.015}MnO_{3-\delta}$ around room temperature) and 250 µW.m^{-1}.K^{-2} (highly doped and co-doped samples at 1000 K). The latter value seems to be a robust and composition weakly dependent property which can therefore be taken as a technological limit for eventual applications. An important finding is that the impact of alloying (W and Yb substitution), which is a routine technique used to decrease the thermal conductivity, seems to be less efficient. This is likely a result of an additional effective and robust acoustic phonon scattering mechanism or due to a significant role of optical phonon contribution as discussed in next section.

Last but not least, we note that despite the observed fluctuations of the chemical composition on microscopic scale (EPMA analysis reported in [112], reproduced in Fig. 4.80) these fluctuations have no detectable impact on the thermoelectric properties. The oxygen deficiency likely has a negligible impact for $Mn^{3+}/Mn^{4+} >$

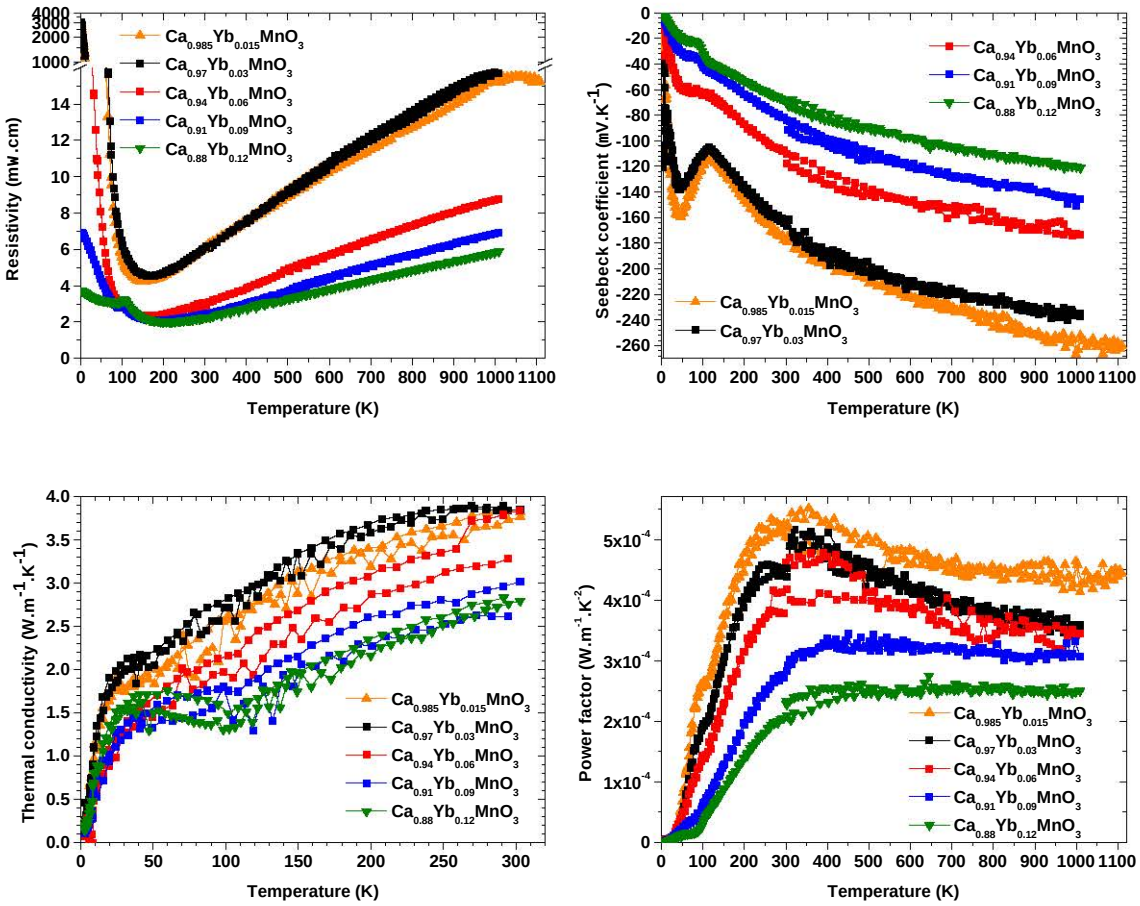

Figure 4.78: Temperature dependence of the electrical resistivity, Seebeck coefficient, thermal conductivity and power factor of $Ca_{1-x}Yb_xMnO_3$.

0.03 as in this case the thermoelectric properties are defined by cationic composition. The issue is non-trivial for $Mn^{3+}/Mn^{4+} < 0.03$, i.e. close to pure $CaMnO_{3-\delta}$. In this case it is very difficult to accurately control the oxygen stoichiometry and, as a consequence, the carrier concentration is a function of both the cationic composition and oxygen stoichiometry.

An interesting property of $CaMnO_3$-based thermoelectrics is that both the power factor and thermoelectric compatibility factor are rather robust with respect to doping. The thermoelectric compatibility factor $CF = (\sqrt{1-ZT}-1)/(ST)$ [46] varies only by some 25 % between the low doped ($S_{1000K} = -260$ µV.K^{-1}) and high doped ($S_{1000K} = -115$ µV.K^{-1}) manganites. This provides a nice opportunity to tune the thermoelectric properties without a significant impact on its compatibility with a suitable thermoelectric material in the colder part of a segmented TE leg.

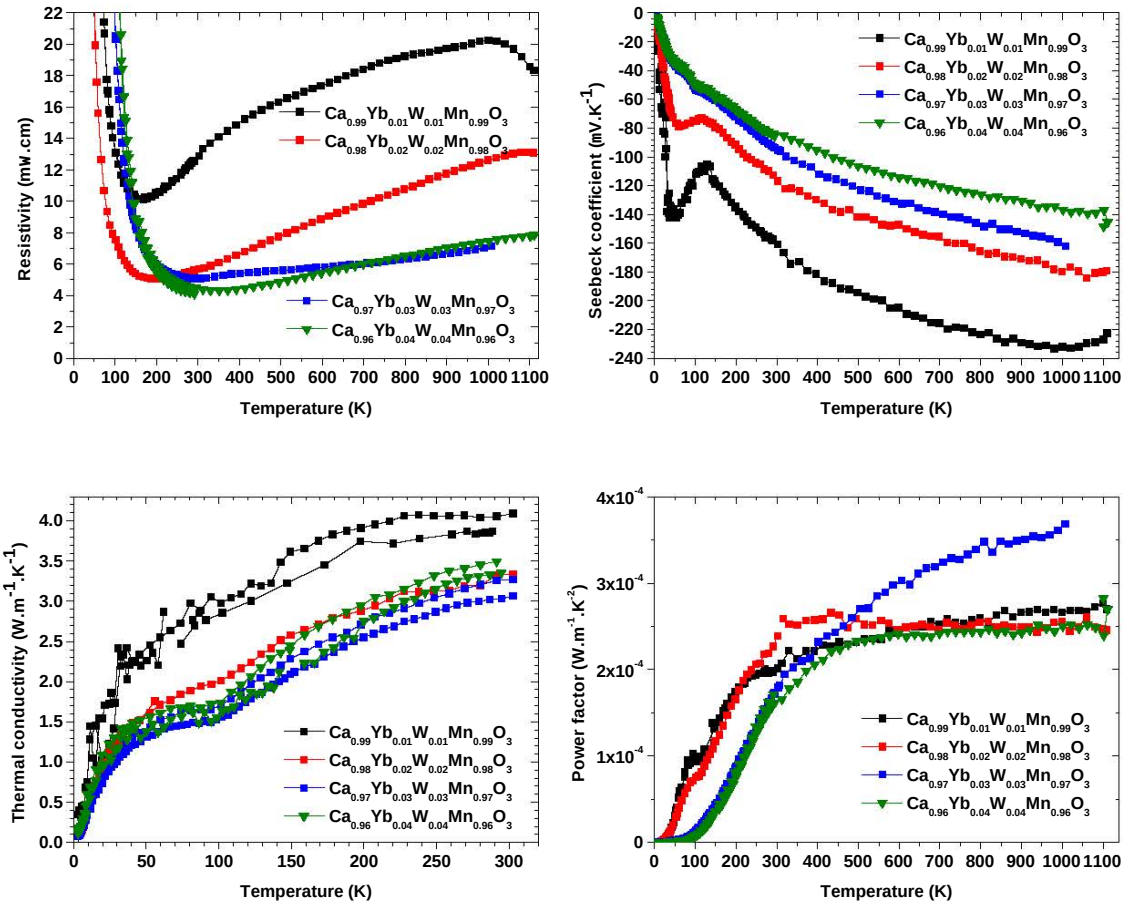

Figure 4.79: Temperature dependence of the electrical resistivity, Seebeck coefficient, thermal conductivity and power factor of $Ca_{1-x}Yb_xMn_{1-x}W_xO_3$.

4.2.2 Thermal Conductivity Analysis

Manganites have been studied for a long time, however, data about their thermal conductivity are not plentiful. This includes both analyses of low temperature thermal conductivity as well as experimental data ranging from cryogenic temperatures to 1000 K. In this section, we therefore analyse the thermal conductivity of

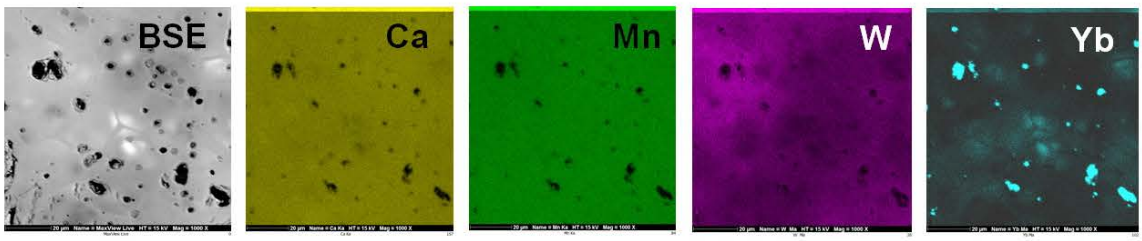

Figure 4.80: Map of a chemical composition of a 100 × 100 µm area of $Ca_{0.96}Yb_{0.04}Mn_{0.96}W_{0.04}O_3$. *After [112].*

calcium manganites in more detail. First, we measured κ between 4 and 1000 K for three lightly doped samples and used the Callaway model to fit the data in order to gain better understanding of the scattering processes. Then, we calculated the theoretical minimum thermal conductivity of $CaMnO_3$ using the Cahill model.

We picked three samples of $CaMnO_3$ with different levels of electron doping to study their thermal conductivity in more detail. The selected samples were $Ca_{0.99}Yb_{0.01}Mn_{0.99}W_{0.01}O_3$, $Ca_{0.925}Er_{0.075}MnO_3$ and $Ca_{0.96}Yb_{0.04}Mn_{0.96}W_{0.04}O_3$, containing 0.03, 0.075 and 0.12 Mn^{3+} ions per formula unit, respectively. In addition to the standard thermoelectric measurements below room temperature and electric measurements above room temperature, we measured their thermal conductivity between 300 and 1000 K using LFA. Heat capacity was estimated from literature [116–118].

Figure 4.81 presents the measured data for total κ as well as curves for the lattice part κ_l only. The electronic part κ_e is quite low, less than 0.3 $W.m^{-1}.K^{-1}$ at the highest temperatures. We see that κ decreases with increased doping which is caused by more frequent scattering on Mn^{3+} ions acting as point impurity scatterers and will be discussed later. A marked notch in κ is evident at the Néel temperature around 120 K. At higher temperatures, we observe the Umklapp process, most apparent for the most conducting sample.

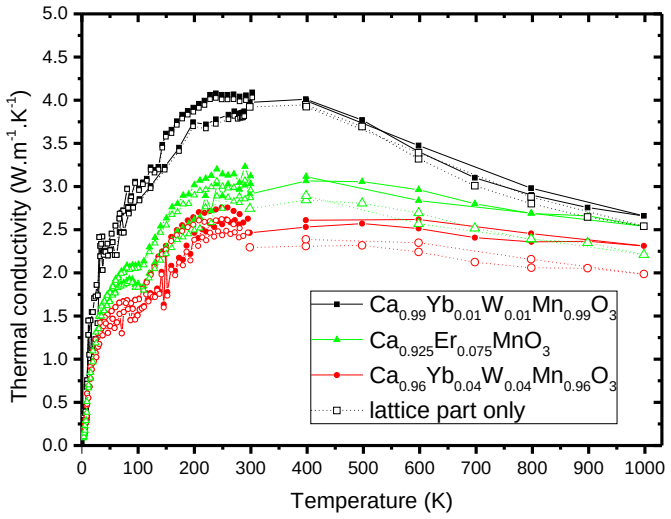

Figure 4.81: Temperature dependence of the thermal conductivity of doped $CaMnO_3$.

Next, we tried to fit the measured data with a theoretical model. We used the Callaway model for thermal conductivity [31]; a similar approach was taken e.g. in [32, 33, 119]. The lattice part of thermal conductivity (obtained simply by subtracting the electronic part calculated with the Wiedemann-Franz law from the measured values of total κ) served as the experimental data points. The fitted curves were a sum the acoustic and optical phonon contributions.

The acoustic phonon contribution was modelled with Equation (2.17). Apart from the physical constants and free parameters, there are two more inputs into the equation: the Debye temperature Θ_D and the speed of sound v. We took both values from [115] where the authors estimated $\Theta_D = 650$ K and $v = 4800$ m.s^{-1} for $Ca_{0.9}RE_{0.1}MnO_3$ (RE=rare earth).

The parameter τ encompasses the scattering processes which all decrease the thermal conductivity. We took its form from (2.18) and employed the grain boundary, point impurity, and Umklapp processes. Quantitatively, they are represented by the free parameters L, A and B, respectively.

For simplicity, we did not consider the contributions of individual optical phonons but used (2.19) to account for all the optical modes together. Experimental data for optical phonons are generally difficult to come by. We could not find any data for v_{opt}. The dispersion of optical phonons is much flatter than that of acoustic phonons, which results in a much lower group velocity. Keeping this fact in mind, we drew inspiration from [119] where the authors took v_{opt} approximately an order of magnitude lower than v_{ac} which they obtained from published data. In our calculations we took $v_{opt} = 0.1 v_{ac}$. This may be considered an oversimplification, however, (2.19) depends on v_{opt} in a rather straightforward way and variations of v_{opt} mostly affect only scaling, not the shape of the calculated curve. As for Θ_E, we could not find any data either, so we treated it as a free parameter. Scattering rate τ had the same form as for the acoustic phonons; grain size L was considered identical to that for the acoustic contribution, while the other two parameters, A_{opt} and B_{opt} were considered specific to the optical contribution.

Figure 4.82 plots the final fits for the three samples along with the measured data points and Figure 4.83 details one of the samples with its acoustic and optical contributions to $\kappa_l(T)$. The calculated parameters for acoustic phonons are shown in Table 4.8. Parameters for optical phonons were $A_{opt} = 6.3 \times 10^{-47}$ s^3, $B_{opt} = 10^{-26}$ s.K^{-1} and $\Theta_E = 300$ K.

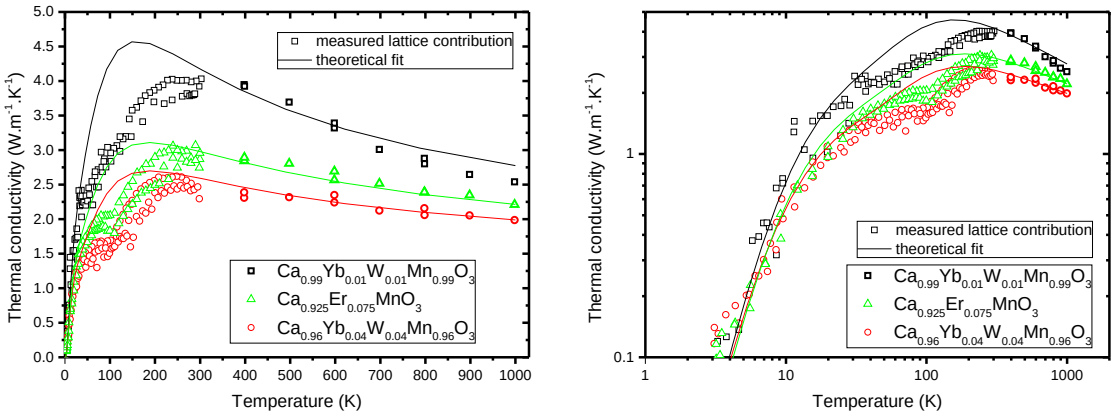

Figure 4.82: Theoretical fits on measured temperature dependence of the thermal conductivity of doped $CaMnO_3$.

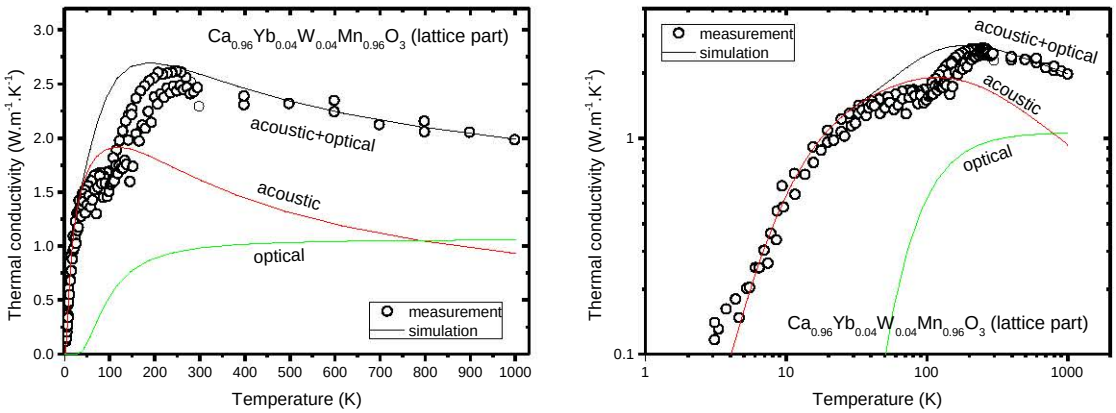

Figure 4.83: Detailed theoretical fit of measured thermal conductivity of $Ca_{0.96}Yb_{0.04}Mn_{0.96}W_{0.04}O_3$.

Table 4.8: Acoustic mode fitting parameters for grain size L, point defect scattering A and Umklapp scattering B for three doped manganites.

sample composition	Mn^{3+}/Mn (%)	L (µm)	A (10^{-42} s^3)	B (10^{-18} $s.K^{-1}$)
$Ca_{0.99}Yb_{0.01}Mn_{0.99}W_{0.01}O_3$	3	1.1	3.2	3.2
$Ca_{0.925}Er_{0.075}MnO_3$	7.5	1.1	7.9	2.5
$Ca_{0.96}Yb_{0.04}Mn_{0.96}W_{0.04}O_3$	12	1.1	13	3.2

The fitted curves agree fairly well with the measured data. The only significant difference is around the Néel temperature around 120 K. We unsuccessfully tried to model the increase at T_N as an onset of optical phonons, an approach taken in [119] for $YMnO_3$ with $T_N = 75$ K. Low values of Θ_E can produce a rise of κ which is similarly abrupt as the one observed in our measured data. However, in this case it occurs at a temperature too low to be consistent with the measured data. While increasing Θ_E shifts the onset to higher temperatures, it also causes it to occur more gradually over a wider range of temperatures. With values of Θ_E high enough to match the temperature of optical phonon onset with T_N, it is already too gradual to account for the increase seen in the measured data. The sudden rise of κ observed in our samples therefore cannot be explained by optical phonon onset. We tentatively consider it to be an anomaly caused by spin ordering around the temperature of phase transition.

The parameter A, linked with point defect scattering, can be further analysed. [32] When the concentration of the scatterers is low enough, as it is in our case, A is proportional to this concentration. Table 4.8 shows a strong correlation between A and the concentration of Mn^{3+} ions. We note that the very similar numerical values are only a nice coincidence. The total concentration of the doping atoms (i.e. Yb, Er, W), on the other hand, shows poor correlation with A, providing an argument against relevant impact of alloying on κ reduction. We conclude that the decrease of

thermal conductivity is caused by the increased concentration of Mn^{3+} ions which serve as point defect scatterers.

For the best thermoelectric performance, thermal conductivity has to be as low as possible. It is therefore convenient to estimate the minimum thermal conductivity attainable for a given material to assess how big a potential there is in reducing it. For this purpose we will use (2.20) which is a result of the Cahill model. To evaluate it, we require three material parameters. The first is the number density of atoms n which can be easily obtained from the molar mass and density, taken as 4.57 g.cm^{-3}, giving $n = 9.62 \times 10^{22}$ cm^{-3}. The second and third parameters are v_t, the transversal speed of sound, and v_l, the longitudinal speed of sound.

For the longitudinal speed of sound v_l we found published data for $CaMnO_3$ [120] and $CaMn_{0.96}Mo_{0.04}O_3$ [121] between approximately 60 and 400 K. The first publication gives a value around 6800 m.s^{-1}, the second around 6000 m.s^{-1}. We could not find any data for the transversal speed of sound v_t. We estimated v_t as $0.55v_l$ which results in the average of v_t, v_t and v_l (counting v_t twice to account for two transversal modes) being around 4800 m.s^{-1} – that is the same as the mean velocity of phonons given in [115] and used above in the Callaway model.

Figure 4.84 shows the calculated minimum thermal conductivity κ_{min} as a function of temperature. To account for the uncertainty of actual v_l, we show κ_{min} for both values given above. We see that above some 500 K, as the Debye temperature is approached, the curves flatten and stay at an almost constant value around 1.5 W.m^{-1}.K^{-1}. Thermal conductivity of the $Ca_{0.96}Yb_{0.04}Mn_{0.96}W_{0.04}O_3$ sample, measured to be between 2.0 and 2.5 W.m^{-1}.K^{-1} above room temperature (see Fig. 4.81), is therefore very close to this calculated minimum value. Even the other samples come close in the high temperature region, which is where ZT attains values meaningful for electricity generation. This implies that there is not much potential in increasing ZT through lowering of the thermal conductivity, for example by nanostructuring. It should be noted that the approximations we made for v_t and v_l are not significant enough to change our conclusion.

To summarize the thermal conductivity analysis: we measured experimental data for three samples and performed their analysis with the help of the Callaway model to show that Mn^{3+} ions serve as point defects which scatter acoustic phonons, reducing κ. Furthermore, a certain part of the thermal conductivity at high temperatures is associated with optical phonons. Then we calculated the minimum thermal conductivity κ_{min} according to Cahill [30] to be around 1.5 W.m^{-1}.K^{-1}. Given the fact that we measured $\kappa \approx$ 2.5 W.m^{-1}.K^{-1} at high temperatures, only a very modest improvement of TE properties is achievable by further manipulating thermal conductivity. The ZT of our best samples was 0.16 at 1000 K, we may not expect values significantly larger in nanostructured samples (considering that at the same time the charge carrier transport remains unaffected).

4.2.3 Electrical Contacts

Finally, we shortly address the question of electrical contacts on manganites, a typical application issue. We studied the contact resistance between different

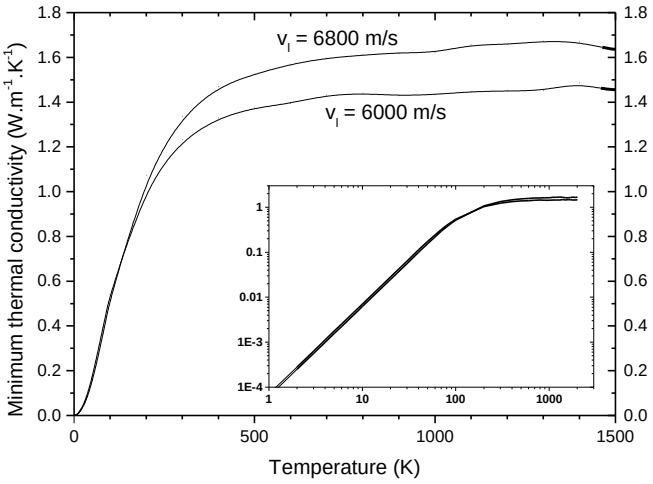

Figure 4.84: Calculated minimum thermal conductivity of $CaMnO_3$ for two values of longitudinal sound velocity v_l.

silver based pastes and manganite ceramics. The experiments were performed with ca 5 mm cubes cut from a $Ca_{0.98}Yb_{0.02}Mn_{0.98}W_{0.02}O_3$ pellet.

Sandwiches made of a manganite cube between two Al_2O_3 plates, mimicking a TE module, were prepared. This was done using screen printing by the Elceram company based in Hradec Králové, Czech Republic. Figure 4.85 shows photos of one of the legs from different angles. The following pastes were used to create the electrical contact and bind the manganite to the alumina substrates:

- Ag paste filled with fibre glass to improve adhesion: 9912-A by Electro Science Laboratories, Inc.
- Ag/Pt paste: C 1076 SD by Heraeus
- Ag/Pd paste: C 20340 by Heraeus

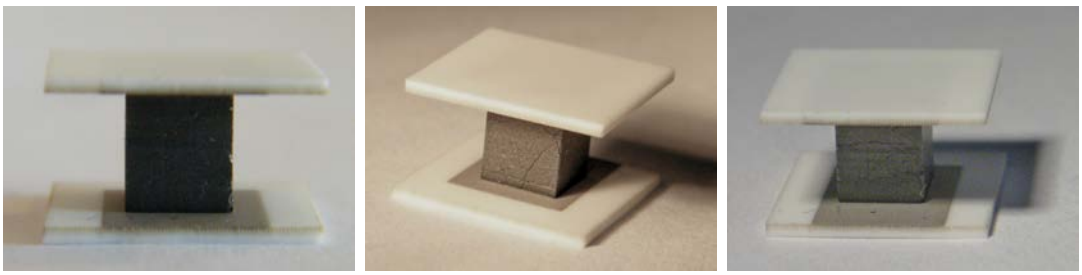

Figure 4.85: Photos of a manganite unicouple with Ag/Pd contacts fabricated by screen printing.

The best results were obtained using the Ag paste. The contact resistance was measured to be around 0.27 $m\Omega.cm^2$. For the Ag/Pt paste the value was approximately one order of magnitude higher. For the Ag/Pd paste, it surpassed the resistance of the sample itself by several orders of magnitude, rendering it unusable.

Unfortunately, the Ag paste, unlike the others, also showed poor mechanical resistance. This obviously presents an important technological issue, so the paste cannot serve as an interfacing material as-is but we can state that the good electrical properties make the Ag-only composition a good starting point for further development.

We can estimate the share of the contact resistance on the total resistance of the module assembly. For that we consider the average resistivity of the manganites studied to be around 3 mΩ.cm at room temperature and 10 mΩ.cm at 1000 K. The length of the thermoelectric leg is assumed as 5 mm. While this is more than what is considered standard for modules, it seems a reasonable assumption because of the large thermal gradient due the high temperature of the hot side. For the Ag paste these assumptions put the contact resistance at some 20 % of the leg resistance at room temperature or 5 % at 1000 K. In any case, the high temperature value is more important; for low temperatures the ZT factor of oxide thermoelectrics is too low for any reasonable generation of electricity. They are therefore expected to operate mainly at high temperatures, for example, as a hot part of a cascaded module.

4.3 Polymers

Based on the collaboration with Dr Jiří Pfleger and Dr Jaroslav Stejskal from the Institute of Macromolecular Chemistry, who synthesized and supplied all polymer samples, we characterized three types of conducting polymers: PEDOT:PSS, PANI and PPy. The first polymer was in the form of thin layers on a substrate. PANI and PPy were in the form of thin cold pressed pellets, some 13 mm wide and roughly 1 mm thick. The focus was not put on the improvement of thermoelectric properties but rather on gaining experience with this specific family of materials.

4.3.1 PEDOT:PSS

Among the polymers considered for thermoelectric applications, poly(3,4-ethylenedioxythiophene) doped with polystyrene sulfonate (PEDOT:PSS) has attracted the most attention. It therefore seems appropriate to start the measurements with this polymer. The studied samples were in the form of thin films. They were made by depositing a PEDOT:PSS solution on a substrates with the approximate dimensions 15×12×0.5 mm and drying at room temperature, 50 °C or 70 °C. Four gold electrodes were sputtered onto the substrates before film deposition. The thickness of the films was estimated using a micrometer at 20 µm for the sample dried at room temperature and 10 µm for the samples dried at elevated temperature. Photographs of the samples are shown in Figure 4.86. We note the different sample thickness, especially in the case of the sample dried at room temperature. Unfortunately, this sample also exhibited several tears.

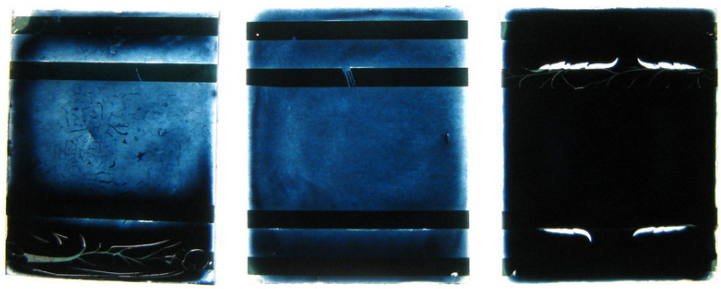

Figure 4.86: A photo of the PEDOT:PSS films on substrate (12 × 15 mm). From left to right: dried at 70 °C, 50 °C, room temperature.

Figure 4.87 shows a photo of the sample holder modified for measuring thin films. Unlike in the standard arrangement, the sample is clamped to a heat sink, represented by a small metal holder anchored to the copper base, with a screw. The resistive heater is glued to the top of the sample from the side. The main electrical contact with the film is achieved through the gold electrodes along its whole width. The silver wires are attached to the sample with silver paint only at the sides, where the gold is exposed, and at the back side of the substrate for better mechanical adhesion and heat redistribution. The substrate has low thermal conductivity, around 2 $W.m^{-1}.K^{-1}$ at room temperature, with temperature dependence typical

for amorphous solids.

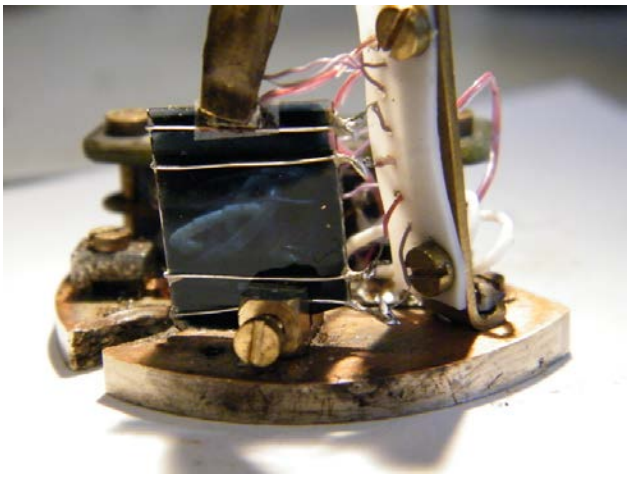

Figure 4.87: Photo of a sample holder modified for measuring thin films on a substrate. Here, a PEDOT:PSS sample is mounted. The heater at the top of the sample is temporarily being held in place by a peg, while the glue attaching the heater is drying.

Figure 4.88 shows the resistivity as a function of temperature for the three PEDOT:PSS films dried at different temperatures. At room temperature, the resistivity is around 10^3 mΩ.cm^{-1}, a value which is rather high but standard for as-prepared PEDOT:PSS without further treatment to increase conductivity. [127] The temperature dependence of ρ is the same for all samples, differing only in scaling. This suggests that the films have essentially the same properties and only differ in thickness which was not determined precisely. Some step jumps are seen on the curves, especially the room temperature one, which are probably caused by tearing of the samples with the changing temperature.

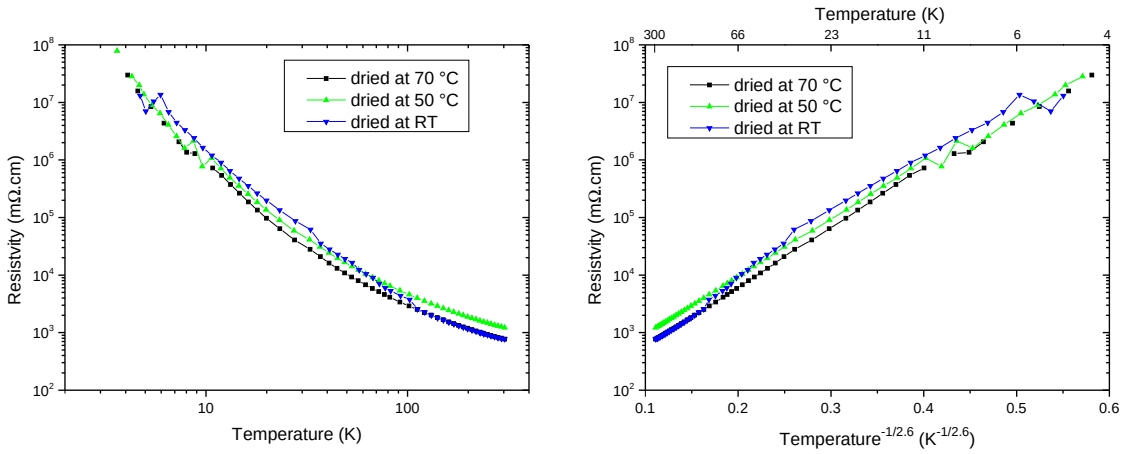

Figure 4.88: Temperature dependence of the electrical resistivity of thin PEDOT:PSS films dried at different temperatures. The right graph accentuates the $T^{-1/2.6}$ dependence characteristic of variable range hopping.

The evolution of ρ points towards the variable range hopping mechanism of conduction as the curves can be described rather well with the $\ln \rho \sim (T_0/T)^{-1/(1+1.6)}$ dependence, see (2.11) and Fig. 4.88 right. This quasi-2D VRH was observed in [132] for a pristine PEDOT:PSS sample with similar resistivity and was attributed to hopping between localised states on quasi-2D sheets. The Seebeck coefficient, see Figure 4.89, is positive with the room temperature value around 12 $\mu V.K^{-1}$, showing good agreement with published literature [127] for untreated PEDOT:PSS. Its temperature dependence resembles the $\sqrt{T}$ law expected for VRH. Room temperature ZT of these samples was of the order of 10^{-5}.

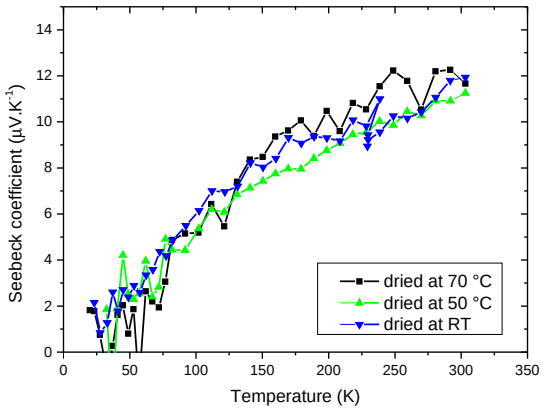

Figure 4.89: Temperature dependence of the Seebeck coefficient of thin PEDOT:PSS films dried at different temperatures.

4.3.2 Polypyrrole (PPy)

Next, we investigated three samples of polypyrrole (PPy) with different morphology and levels of doping. One of them was globular polypyrrole, the other two nanotubular polypyrroles. $FeCl_3$ was used as the oxidizing agent. The group from the Institute of Macromolecular Chemistry supplied samples very similar to those whose synthesis and properties they described in [135–137]. The samples were in the form of cold pressed pellets, see a photo in Figure 4.91.

The electrical resistivity of the samples is shown in Figure 4.90. The most conducting sample, one of the nanotubular ones, exhibits a fairly low value below 10 $m\Omega.cm^{-1}$ at room temperature. The other nanotubular sample is one order of magnitude more resistive and the resistivity of the globular sample is yet another order of magnitude higher. These differences are discussed in [135, 136]. Resistivity increases upon cooling for all three samples. The right graph in Figure 4.90 shows the logarithm of resistivity as a function of $T^{-1/4}$ to accentuate the characteristic dependence of variable range hopping (2.11). The data points of the most resistive sample lie on a straight line, pointing towards the VRH mechanism of conduction. The same is true for the sample with intermediate resistivity. The least resistive

sample departs from this behaviour. Hopping conduction is commonly seen is PPy. [139, 141, 149]

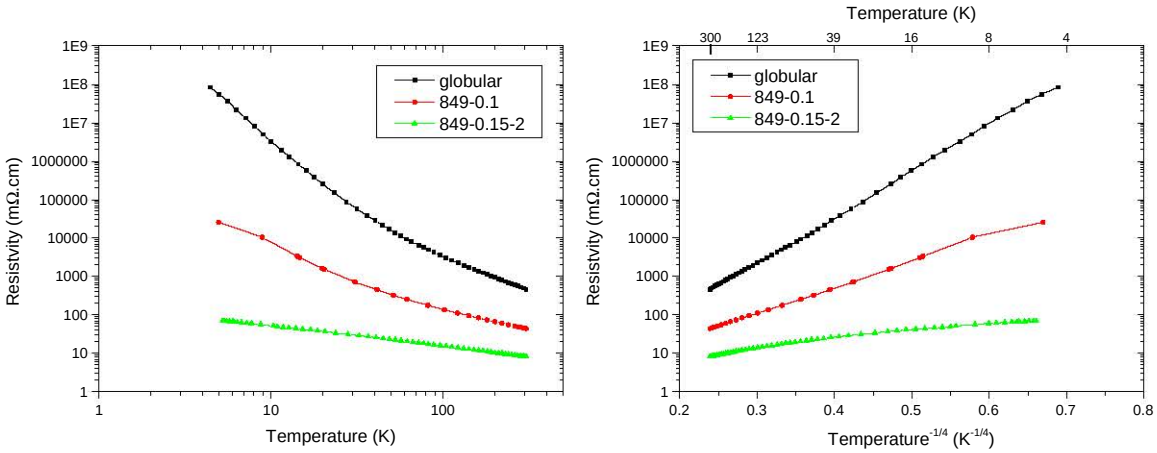

Figure 4.90: Temperature dependence of the electrical resistivity of PPy. The right graph accentuates the $T^{-1/4}$ dependence characteristic of variable range hopping.

The semiconducting temperature dependence of resistivity contrasts with that of the Seebeck coefficient which is typically metallic, see Figure 4.91, i.e. linearly decreasing with temperature and exhibiting low values. At room temperature, we measured positive values between 5 and 7 μV.K^{-1}, the less resistive samples possessing the lower values. The linear decrease does not actually tend to zero at 0 K but to slightly negative values. The $T = 0$ intercept is between -0.4 and 1 μV.K^{-1}. Negative intercept has been observed in PPy [140, 141] and the overall metallic temperature dependence is a known and common feature of doped polypyrrole [130, 139–141]. While not fully clarified, it is believed that heterogeneity is responsible for the observed behaviour. In this picture, the material is composed of small metallic islands separated by nonmetallic barriers. The islands are responsible for the metal-like Seebeck coefficient, while the barriers greatly enhance resistivity and give it the semiconducting temperature dependence. [141]

We picked one sample, the one with intermediate ρ, and determined its thermal conductivity from an LFA measurement between room temperature and 373 K. Unlike for tetrahedrites, the temperature dependence of polymer heat capacity does not allow us to simply use the Dulong-Petit approximation to calculate the heat capacity. We measured the heat capacity of the sample between 2 and 300 K using the relaxation method and the PPMS instrument. The data are shown in Figure 4.92.

Our value 1.2 J.g^{-1}.K^{-1} at 300 K is somewhat higher than 0.8 J.g^{-1}.K^{-1} and 1.0–1.1 J.g^{-1}.K^{-1} reported in [137] and [138], respectively. The temperature dependence is typical for polymers, i.e. a Debye contribution from skeletal vibrations is responsible for the initial rise at low temperatures. This contribution eventually saturates but a myriad of optical modes from group vibrations then take on and, as they are progressively excited with increasing temperature, cause the heat capa-

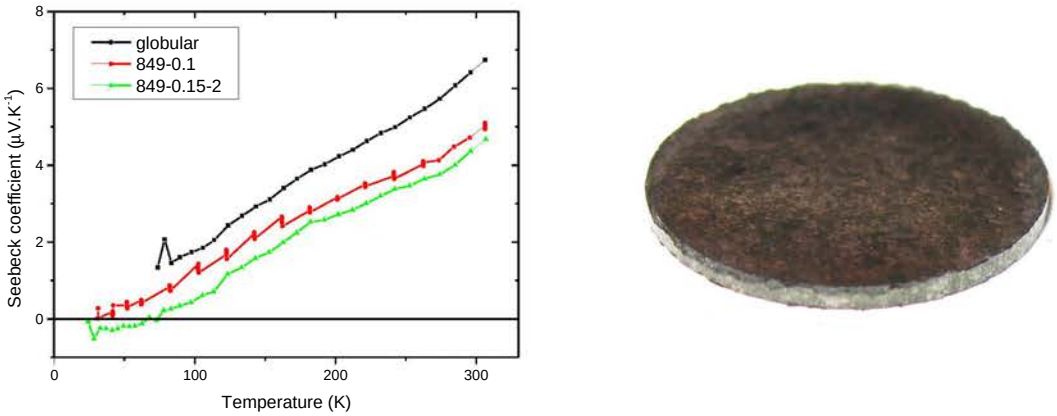

Figure 4.91: Temperature dependence of the Seebeck coefficient of PPy and a photo of a PPy pellet. The pellet is 13 mm wide and around 0.6 mm thick.

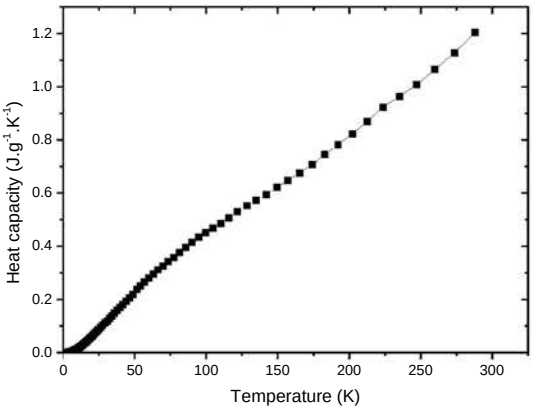

Figure 4.92: Temperature dependence of the heat capacity of PPy.

city to grow almost linearly with T. [128] No phase transitions are evident in the measured data.

To calculate κ from the measured thermal diffusivity, we took a linear extrapolation of $C_p(T)$. Published data [137, 138] for different polypyrroles show that the heat capacity indeed increases linearly and smoothly between 280 and 340 K. Furthermore, the values of diffusivity that we measured were virtually constant for all temperatures, further suggesting that there were no phase transitions or other effects which would cause the heat capacity to depart from the assumed shape. The density of the sample was 1.01 g.cm^{-3}.

Figure 4.93 left shows that the two nanotubular samples, only differing in the doping level, exhibit the same values of κ. The globular sample, on the other hand, is roughly only half as thermally conductive. The electronic part of κ is negligible for all the samples. Even more interesting is the discrepancy between the low and

high temperature data. The high temperature measurement gave a value around 0.3 W.m^{-1}.K^{-1} at 300 K, while the low temperature measurement yielded almost 1 W.m^{-1}.K^{-1} for the same sample at this temperature.

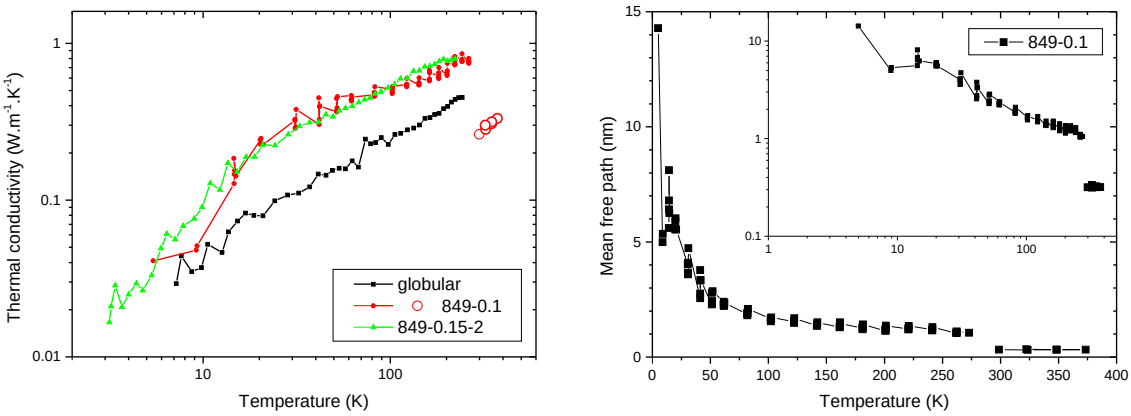

Figure 4.93: Temperature dependence of the thermal conductivity and phonon mean free path of PPy.

A probable explanation is that cold pressing the sample into a disc gave rise to preferential orientation of the polymer tubules and the polymer chains were ordered rather perpendicular to the direction of pressure. In the case of low temperature measurements, heat is run along a long piece cut from the disc. The heat therefore propagates along the chains more easily and the measurement yields higher values of κ. In the case of high temperature measurements, a heat pulse is sent across the disc and the more difficult interchain transport results in lower values of thermal conductivity.

We can also view the thermal transport data in terms of the phonon mean free path l (we are taking some liberty in using the term *phonon* since the notion of collective excitations is in this case somewhat questionable; the term *thermal excitations* is probably more appropriate). We can estimate l from Equation (2.16): $\kappa = \frac{1}{3} C_v v l$. For $\kappa(T)$, we use the measured values. For $C_v(T)$, we neglect the difference $C_p - C_v$ and use the measured data for $C_p(T)$. We can take v as temperature independent [129] and a reasonable estimate of its value is 2000 m.s^{-1}, which is roughly valid for a broad range of polymers. [130]

Figure 4.93 right shows the mean free path as a function of temperature. The value above room temperature stays virtually constant at 0.3 nm, comparable to the interatomic spacing which is a minimum reasonable value. The increase of thermal conductivity with temperature is purely due to the increase of the heat capacity. At low temperatures, decreased scattering allows the mean free path to reach higher values, about 10 nm at 10 K. Increasing temperature causes l to decrease although above 100 K it seems to saturate around 1 nm.

Our measured values of κ agree with those reported in the literature. One group measured κ of a cold pressed pellet in the perpendicular direction using LFA and

obtained a value similar to ours: 0.20 $W.m^{-1}.K^{-1}$ at 300 K. [137] Different authors measured κ along thin (100 µm) films using a.c. calorimetry and obtained 0.8–1.2 $W.m^{-1}.K^{-1}$. [138] Apparently, PPy fibres have a tendency to orient along the long dimension of the sample.

It is obvious that the thermoelectric performance of our samples is insignificant, mainly because of the very low S. In the best cases, the values of ZT were of the order of 10^{-5}–10^{-4}.

4.3.3 Polyaniline (PANI)

The last polymer we investigated was polyaniline (PANI) treated with HCl, again supplied by the Institute of Macromolecular Chemistry in the form of two cold pressed pellets. One pellet was used for thermal diffusivity measurements using LFA, the other was cut up to measure its electrical and thermal properties as well as heat capacity. A photo of a part of the PANI pellet is shown in Figure 4.95.

Resistivity data for two measurements below and above room temperature performed on two pieces cut from one pellet are shown in Figure 4.94. The measurement above room temperature shows a marked hysteresis, the values increasing anomalously upon heating and showing a threefold increase upon cooling back to 300 K when compared to the initial value. This is probably caused by a variation of water content or possibly the dopant content in the sample. Let us first recap the conditions which the sample encounters during the measurements. In the case of measurements below room temperature, the sample chamber is continuously pumped with a turbomolecular pump to pressures around 10^{-3} Pa. In the case of measurements above room temperature, the sample is subjected to a flow of argon and gradual heating throughout the experiment. In the former case, vacuum can quickly remove the water from the sample, while in the latter case, the presence of atmospheric pressure does not allow an immediate loss of water which is instead lost over time as the sample is heated. On the cooling run, the sample yields different values of $\rho(T)$ corresponding to its water depleted form.

Numerous studies investigated the influence of water on the resistivity of PANI and found it to decrease with water content. [142–146] This is in line with our data. Furthermore, resistivity can be also increased by evaporative loss of the doping agent. [142, 143] In both cases, the Seebeck coefficient should be influenced as well, which indeed happened and can be seen in Figure 4.95. Interestingly enough, the room temperature value obtained by the low temperature instrument matches that obtained by the high temperature instrument at the beginning of the experiment and not after recooling as was the case with the resistivity. The reason for this remains unknown, possibly it is caused by a combination of both water and dopant loss. In any way, it is not possible to judge without at least a repeated measurement after re-humidifying the sample.

The values of ρ are fairly high, of the order of thousands of mΩ.cm at and above room temperature and rising to 10^5 mΩ.cm at 150 K below which temperature it could not be measured. The right graph shows the logarithm of resistivity as a function of $T^{-1/2}$ to accentuate the temperature dependence characteristic of variable

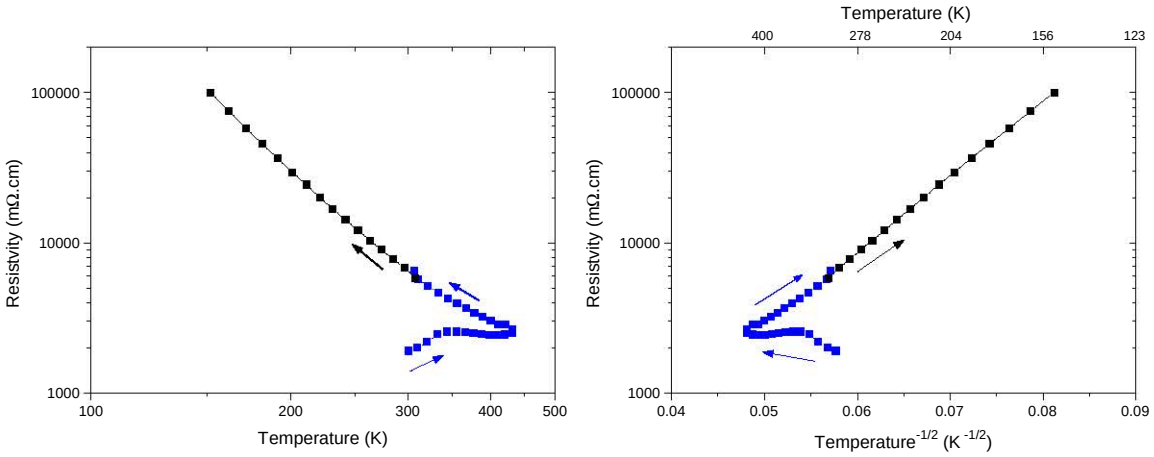

Figure 4.94: Temperature dependence of the electrical resistivity of PANI. Black and blue colour is used to differentiate between separate measurements below and above room temperature on two pieces cut from one pellet. The right graph accentuates the $T^{-1/2}$ dependence characteristic of variable range hopping.

range hopping, see (2.11). Below room temperature, the data points in this graph fall rather well on a straight line pointing to the hopping mechanism of conduction which commonly seen in PANI [130, 147–149]. More specifically, fitting the data yielded $\ln(\rho) \sim (T_0/T)^{1/(1+1.6)}$.

Above 300 K, the behaviour departs from this dependence which may as well be caused by the mechanisms responsible for the hysteresis. Water and dopant evaporation takes time and it may be hours before equilibrium is reached. [143] This is a long time compared to our measurement which takes the sample to 430 K in some 5 hours and back to 300 K in another 5 hours.

The Seebeck coefficient (Fig. 4.95) is of a negative value which is unusual for polymers, which are p-type in the large majority of cases. PANI is known to exhibit n-type conductivity for certain dopants and their concentration. [142, 147, 148]

We measured and analysed the thermal conductivity of PANI similarly to PPy in the previous section. Above room temperature, we used LFA to measure the diffusivity of a pellet 1.2 mm thick. Heat capacity was measured using PPMS in the 2–300 K range, the data are shown in Figure 4.96.

Reported values of C_p at room temperature vary and our value $C_p \approx 1.5$ J.g^{-1}.K^{-1} is on the higher side. The reported values range from 1.6 J.g^{-1}.K^{-1} [154], through 1.1 J.g^{-1}.K^{-1} [153], to 0.5–1.2 J.g^{-1}.K^{-1} [150] and 0.13–0.92 J.g^{-1}.K^{-1} [151] for various dopants.

No phase transitions or anomalies were evident in the measured diffusivity data nor in $C_p(T)$ in the measured temperature range reported in the literature [150]. We therefore estimated the $C_p(T)$ of our sample above 300 K by linearly extrapolating the data below this temperature. The density of the sample was 1.37 g.cm^{-3}, indicating rather low porosity.

Figure 4.97 left shows the thermal conductivity of the sample. The electronic

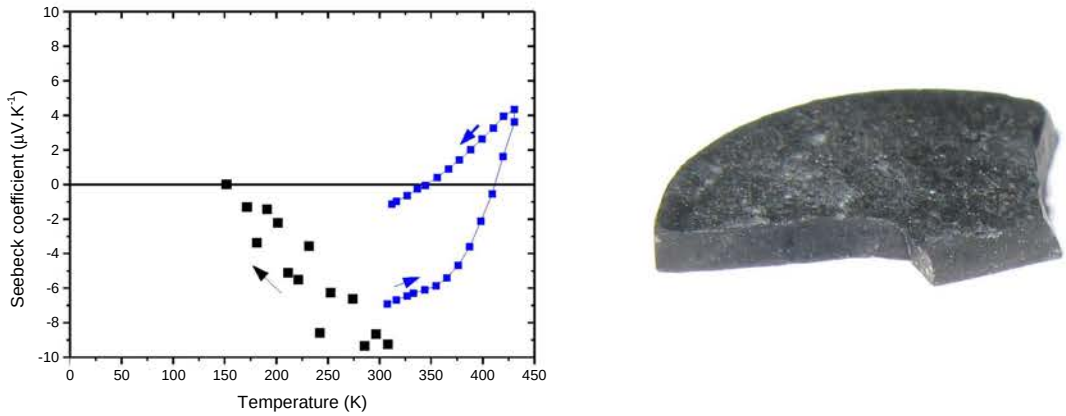

Figure 4.95: Temperature dependence of the Seebeck coefficient of PANI and a photo of a part of a PANI pellet. The diameter of the pellet is 13 mm and the thickness is around 1.2 mm.

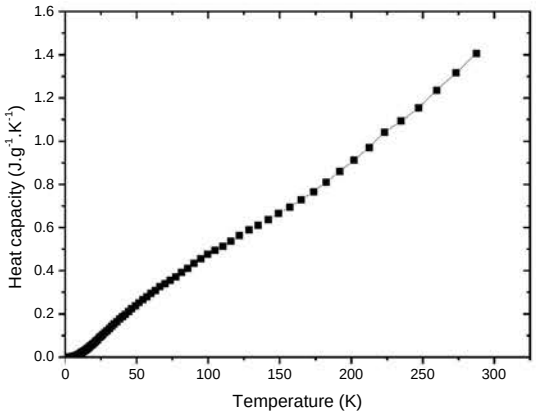

Figure 4.96: Temperature dependence of the heat capacity of PANI.

part is negligible. There is no phonon peak present and the values are very low, as is typical for polymers. We obtained 0.4 $\mathrm{W.m^{-1}.K^{-1}}$ at 300 K and 0.55 $\mathrm{W.m^{-1}.K^{-1}}$ at 450 K. Contrary to the results obtained for PPY, the PANI pellet exhibits a good match between the low and high temperature data, which reflect κ along and across the pellet, respectively. This isotropy of κ suggests low preferential orientation of the polymer chains.

Figure 4.97 right shows the thermal transport data in terms of the phonon mean free path l estimated from (2.16). For $\kappa(T)$, we used the measured values. For $C_v(T)$, we neglected the difference $C_p - C_v$ and used the measured data for $C_p(T)$. We can take v as temperature independent [129] and, similarly to PPy, we used 2000 $\mathrm{m.s^{-1}}$ as a reasonable estimate of its value, which is roughly valid for a broad range of polymers [130].

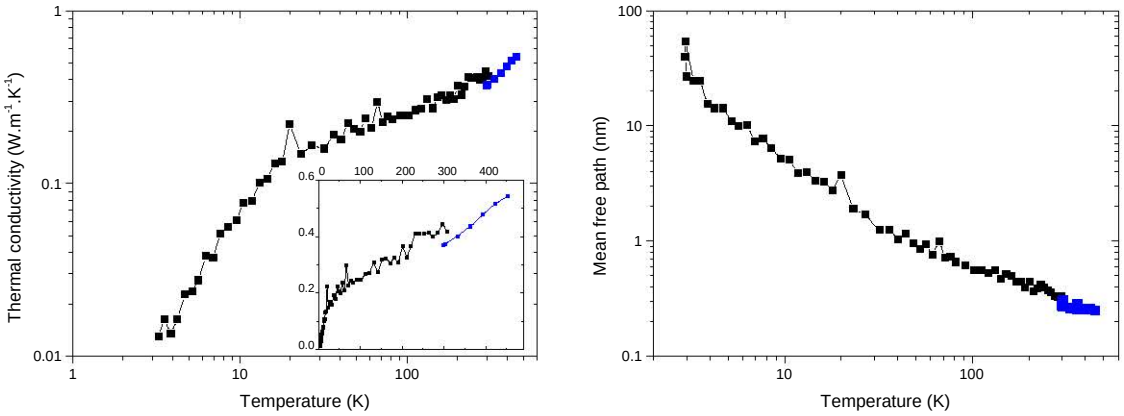

Figure 4.97: Temperature dependence of the thermal conductivity and phonon mean free path of PANI. Black and blue colour is used to differentiate between measurements below and above room temperature.

The value of l above room temperature seems to saturate between 0.2 and 0.3 nm which is comparable to the interatomic spacing, a minimum reasonable value. The increase of thermal conductivity with temperature above 300 K is mainly due to the increase of the heat capacity. The phonon mean free path increases with decreasing temperature due to decreased scattering, reaches some 6 nm at 10 K which is comparable to PPy, and increases to tens of nm upon further cooling.

A majority of the measurements of thermal conductivity reported in literature was performed on thin films ranging from 100 nm to over 100 µm. One study [153] measured in-plane κ of PANI nanofibres formed into pellets and these samples exhibited a phonon peak around 27 K which was attributed to sample crystallinity. Our data do not show any such feature. Their κ at 300 K was 0.5–0.6 W.m^{-1}.K^{-1} which is slightly higher than our value and may be also caused by the higher crystallinity of their samples. Otherwise, the steady increase of κ between 100 K and 400 K is consistent with this as well with other studies [150, 152, 153].

Regarding the absolute values, the other studies dealt with PANI films. For a film $\approx$ 0.4 mm thick, Famengo et al. [154] reported 0.39 W.m^{-1}.K^{-1} for in-plane and 0.47 W.m^{-1}.K^{-1} for cross-plane thermal conductivity, albeit with the uncertainties being 18 % and 10 %, respectively. This agrees well with our data, although it is questionable to which degree their measured anisotropy points to actual anisotropy within the sample which was formed without pressure by drying a polymer paste spread on a substrate. A different study reported the room temperature value 0.6 W.m^{-1}.K^{-1} for a film 5 µm thick. [152] The peculiarity of thin films and synthesis of organics is demonstrated by the fact that the same study also reported κ = 0.1 W.m^{-1}.K^{-1} for a film 100 nm thick and another study reported values ranging from 0.02 to 0.24 W.m^{-1}.K^{-1} for twelve films $\approx$ 40 µm thick with various dopants and their concentrations. [150]

The following paragraphs summarize the results obtained for the three polymers,

PEDOT:PSS films and PPy and PANI pellets. Overall, we gained experience with polymers and showed that we are able to successfully measure the thermoelectric properties even in the case of this specific family of materials. The sensitivity to humidity is a tricky factor which has to be taken into account in the case of further studies.

The PEDOT:PSS samples demanded a modification of the sample holder to be able to accommodate thin samples. The measured electrical resistivity and Seebeck coefficient of the samples corresponded to variable range hopping and is in agreement with the literature.

Polypyrrole (PPy) is an interesting polymer with a typically metallic Seebeck coefficient but semiconducting resistivity. Our data correspond to the literature which suggests heterogeneity of the polymer to explain this behaviour, with metallic islands responsible for S which are separated by non-metallic barriers responsible for ρ. Cold pressing created significant anisotropy in the thermal conductivity of the nanotubular sample. The cross-plane values were around 0.3 $\mathrm{W.m^{-1}.K^{-1}}$ around room temperature while the in-plane values were higher by a factor of three. Above room temperature, the phonon mean free path stays constant and its value is comparable to the interatomic spacing, i.e. the lowest reasonable value. Below room temperature it grows to some 10 nm at 10 K.

Polyaniline (PANI) showed semiconducting temperature dependence which corresponded to variable range hopping below room temperature. There was a mismatch between the low and high temperature measurements which showed hysteresis. This was attributed to changes in sample humidity and possibly dopant evaporation, effects known to strongly influence the electrical properties of PANI as well as of other polymers. Unlike for PPy, the thermal conductivity of the pellet was isotropic with the value 0.4 $\mathrm{W.m^{-1}.K^{-1}}$ at room temperature. At low temperatures, the phonon mean free path was above 10 nm, as for PPy, and decreased with increasing temperature, converging to an order-of-magnitude value of interatomic spacing above room temperature.

Chapter 5

Conclusions

This thesis experimentally studied thermoelectric materials which allow direct conversion between heat and electricity, either for electricity generation or for cooling. The efficiency of the conversion is rather low, which has restricted the use of thermoelectric materials to niche applications. Following the discovery of new materials and concepts, along with the society's focus on more environmental technologies, the field is currently quite an active one. We studied three distinct families of materials: tetrahedrites, which represent the bulk of this thesis, calcium manganese oxides and polymers.

Tetrahedrites

The tetrahedrite family of materials was the main focus of this thesis. First, eight natural ores from various locations were characterized electrically and thermally. Their fairly uniform and predictable behaviour supports their partial use in manufacturing thermoelectric devices. This idea was further developed in a study of mixtures of natural and synthetic tetrahedrite. Furthermore, the influence of As, which in natural tetrahedrites usually partially substitutes for Sb, was studied in detail in synthetic samples. Data revealed its mildly negative influence on TE properties. Other synthetic samples were studied as well, for example with substitutions of Sn, Mg, Ag or In on the Cu site.

First, we characterized eight natural tetrahedrites from various places around the world. The samples possessed very low thermal conductivity κ<0.5 W.m^{-1}.K^{-1} without a dielectric peak. At low temperatures, κ followed the T^1 law, suggesting a different scattering process than boundary scattering. The samples were not completely insulating but the resistivity was nevertheless high and varied by one order of magnitude between the least and the most resistive sample. This residual electrical conductivity is consistent with transition metal vacancies which supply carriers. Otherwise, we found no correlation between the thermoelectric properties and chemical composition (i.e. the transition metal content, Sb-to-As ratio, etc.) On the other hand, all samples behaved as predicted by the theory and there were no surprises despite the varying composition, supporting the idea of using these natural minerals in manufacturing TE devices. The best ZT was 0.13 at 720 K, a value

spoilt mainly by the high electrical resistivity. Magnetic measurements below room temperature reflected the paramagnetism of Fe ions, as well as ferromagnetism of Fe impurities located outside the tetrahedrite structure.

Next, we studied mixtures of natural and synthetic tetrahedrite in detail. We mixed a natural tetrahedrite with synthetic $Cu_{12}Sb_4S_{13}$ using ball milling. First, we thoroughly tracked the milling process of a 50:50 mixture, then we analysed structural, electrical and thermal properties of samples sintered from 25:75, 50:50, and 75:25 mixtures. By sampling the 50:50 powder several times throughout milling, we observed a gradual decrease of particle size below 100 nm using XRD and SEM. We determined that the two phases coexist the whole time and only form a solid solution during the course of sintering. The sintering time of 4 minutes seems slightly insufficient for a complete formation of a perfect solid solution. The factor ZT was some 15 % higher than for the pure synthetic material.

A mortar-ground control sample exhibited particle size $\approx 10^1$ µm and maintained its two-phase composition throughout sintering. The resistivity of this composite system was double that of the solid solution, and ZT was inferior to both the ball milled and pure synthetic sample. When confronted with published results [13], our measured data are comparable, however we may be overestimating the thermal conductivity of tetrahedrites with the lowest values of κ, possibly due to the overestimation of heat capacity. Electrical and thermal properties of mixtures with different natural to synthetic ratios followed the varying carrier concentration. From the thermoelectric point of view, the 50:50 and synthetic-rich samples behaved the best, both exhibiting ZT some 10 % higher than the pure synthetic sample.

Any number of Sb atoms in tetrahedrite may be substituted by As, the two end-members form a perfect solid solution. In natural tetrahedrites, As is almost always present. [56, 59] Our research on natural minerals did not bring conclusive results about the influence of As on TE properties. For this reason, we synthesized and studied three tetrahedite-tennantite series, namely $Cu_{10}Me_2Sb_{4-x}As_xS_{13}$, $x = 0, 1, 2, 3, 4$, Me = Cu, Co, Zn.

The Cu and Co series were synthesized successfully, while the Zn series suffered from sulfur degassing during annealing of As-rich samples. It was confirmed that the isovalent substitution of As has only a small effect on the thermoelectric properties, a result supported by electronic band structure calculations. In the pure-Cu samples, ρ varies within a few percent among the samples, S drops by 3 % with each As atom, peak ZT of the As end-member is 10 % lower than that of the Sb end-member. While S increases sharply with the metal-to-semiconductor transition in $Cu_{12}Sb_4S_{13}$, the $S(T)$ dependence of all the samples containing As is completely smooth.

The electrical properties of the Co and Zn series were determined by the concentration of Co and Zn atoms which got successfully incorporated in the tetrahedrite-tennantite structure. With increasing As concentration, the concentration of Co and Zn decreased, leading to increased carrier concentration and higher position of the Fermi level. The dependence of lattice thermal conductivity on As content gave somehow different results for each of the three series: the pure Cu series showed a drop for samples containing both Sb and As, indicating alloying effect; the Co series showed rather constant values, indicating no effect; the Zn series did not reveal any

obvious dependence, again pointing towards no effect of As. By combining these results, we can tentatively say that As does not seem to significantly influence the lattice thermal conductivity of tetrahedrite, with the exception of a mild alloying effect.

We investigated various substitutions on the Cu-site. First, we predicted some new elements which may enter tetrahedrite: Mg, Zr, Hf, Ga. Then we attempted to synthesize samples with In, Mg, Ca and Al substitutions on the Cu site. Indium is known to enter tetrahedrite and the ZT we measured for a substitution of 0.5 a.p.f.u. was identical to that of an unsubstituted tetrahedrite. Calcium does not seem to enter tetrahedrite, data about aluminium were inconclusive, magnesium was shown to enter into tetrahedrite, confirming our hypothesis. The effect of Mg is similar to that of other polyvalent substituents and its influence on ZT is minimal. To our best knowledge, this is the first report of an s-block element in tetrahedrite.

Oxides

Two series of doped thermoelectric manganites with the following general formula $Ca_{1-x}Yb_xMn_{1-y}W_yO_3$ were studied. The maximum power factor at 1000 K was $PF \approx 400$ µW.m^{-1}.K^{-2} obtained for ($x = 0.02$, $y = 0$), i.e. for $Mn^{3+}/Mn^{4+} \approx 0.02$. Upon doping to $Mn^{3+}/Mn^{4+} \approx 0.12$ the value moderately decreased to approximately 260 µW.m^{-1}.K^{-2}.

An analysis of the thermal conductivity was based on experimental data measured in a large temperature range between 4 and 1000 K. Electron doping forms polaronic-like quasiparticles which are characterized by locally distorted MnO_6 octahedra due to the Jahn-Teller effect. Because of strong electron-phonon coupling these quasiparticles dramatically depress the thermal conductivity which attains glass-like behaviour below room temperature. According to our analysis, a certain part of the thermal conductivity at high temperatures is associated with optical phonons. The thermal conductivity measured at high temperatures is close to the theoretical minimum value calculated with the Cahill model. Only a very modest improvement of TE properties is therefore achievable by further manipulating thermal conductivity, e.g. by nanostructuring. The ZT of our best samples was 0.16 at 1000 K, we may not expect values much larger for nanostructured samples.

An interesting advantage of $CaMnO_3$-based thermoelectrics is that both the power factor and thermoelectric compatibility factor are rather robust with respect to doping. The latter varies only by some 25 % between the low doped and high doped manganites. This provides a nice opportunity to tune the thermoelectric properties without a significant impact on its compatibility with a suitable thermoelectric material in the colder part of a segmented TE leg. Silver paste was determined to be suitable for electrical contacts although its poor mechanical adherence to an alumina substrate needs to be improved.

Polymers

We studied electrical and thermal properties of three polymers, PEDOT:PSS films and PPy and PANI pellets. Overall, we gained experience with polymers and showed that we are able to successfully measure the thermoelectric properties even in the case of this specific family of materials, opening a way for possible future collaboration. The sensitivity to humidity is a tricky factor which has to be taken into account in the case of further studies.

The PEDOT:PSS samples demanded a modification of the sample holder to be able to accommodate thin samples. The measured electrical resistivity and Seebeck coefficient of the samples corresponded to variable range hopping and is in agreement with the literature. Polypyrrole (PPy) is an interesting polymer with a typically metallic Seebeck coefficient but semiconducting resistivity. Our data correspond to the literature which suggests heterogeneity of the polymer to explain this behaviour, with metallic islands responsible for S which are separated by non-metallic barriers responsible for ρ. Cold pressing created significant anisotropy in the thermal conductivity of a nanotubular sample. The cross-plane values were around 0.3 $\mathrm{W.m^{-1}.K^{-1}}$ around room temperature while the in-plane values were higher by a factor of three.

Polyaniline (PANI) showed semiconducting temperature dependence which corresponded to variable range hopping below room temperature. Above room temperature, the sample proved to be tricky because of its sensitivity to humidity. Unlike for PPy, its thermal conductivity was isotropic with the value 0.4 $\mathrm{W.m^{-1}.K^{-1}}$ at room temperature. For both PPy and PANI, the phonon mean free path above room temperature showed little variation with temperature and was on the order of magnitude of interatomic spacing, i.e. the lowest reasonable value. It increased with decreasing temperature, reaching values above 10 nm below 10 K.

Future Outlooks

There is still a lot to do and discover among the materials studied as well as thermoelectrics in general. Tetrahedrites, being the newest and the most studied family in this thesis, leave various open questions. One of them is their Hall response. Measuring it was often unsuccessful but those few who succeeded report on a negative Hall coefficient, which contrasts with the Seebeck measurements and DFT simulations. Further attempts with less doped and thin (or even thin-film) samples should be attempted to shed light on this issue. The metal-to-semiconductor transition in pristine Cu tetrahedrite, which was not discussed in detail in this thesis, was investigated in several studies but is still awaiting its elucidation. Studying Ag-substituted tetrahedrites might give us some clue. From a more technological point of view, studying the influence of different parameters of ball milling of natural–synthetic tetrahedrite mixtures would deserve attention, and an attempt to upscale the process should also be done. Another very important technological issue is the stability of tetrahedrites over long time scales when subjected to the demanding operating conditions, i.e. high temperatures and current densities. The latter should be investigated in particular, as copper ions are known to be tricky when it comes

to electromigration.

Last but not least, new discoveries are highly encouraged, let it be in an attempt to improve properties, or simply for pure scientific curiosity. This can be done on different levels: the first level being new substitutions in tetrahedrites which have quite a rich chemistry and there is a decent chance that another element currently unknown to enter tetrahedrite can be discovered (e.g Zr, Ga or Au). One level up are other minerals which already exist, are known or even studied by geologists, but their promising thermoelectric properties still go undiscovered, just as was the case of tetrahedrites for decades until 2012. At the third level, we may consider other materials in general, either those yet unknown, or materials known in one field which could secretly possess good thermoelectric properties. We can tentatively suggest topological insulators, among which we find Bi_2Te_3, a prototypical thermoelectric, some of the Half-Heusler alloys, a vividly investigated thermoelectric family, or lillianites, compounds with a modulated structure which have recently been investigated with respect to their thermoelectric properties.

Bibliography

[1] H. J. Goldsmid: *Introduction to Thermoelectricity*. Berlin: Springer, 2010. 242 p. ISBN: 978-3-642-00715-6.

[2] E. Maciá: *Thermoelectric Materials: Advances and Applications*. Boca Raton, FL: CRC Press, 2015. 364 p. ISBN: 978-9-814-46352-2.

[3] D. M. Rowe: *Thermoelectrics Handbook: Macro to Nano*. Boca Raton, FL: CRC Press, 2005. 1014 p. ISBN: 978-0-849-32264-8.

[4] D. M. Rowe: *CRC Handbook of Thermoelectrics*. Boca Raton, FL: CRC Press, 1995. 701 p. ISBN: 0-8493-0146-7.

[5] G. S. Nolas, J. Sharp, H. J. Goldsmid: *Thermoelectrics: Basic Principles and New Materials Developments*. Springer, 2001. 293 p. ISBN: 978-354041245-8.

[6] C. Uher: *Materials Aspect of Thermoelectricity*. CRC Press, 2016. 624 p. ISBN: 978-149875490-3.

[7] G. J. Snyder, E. S. Toberer: *Complex thermoelectric materials*. Nature Materials **7**, 105-114 (2008). doi:10.1038/nmat2090

[8] T. M. Tritt: *Thermoelectric Phenomena, Materials, and Applications*. Annu. Rev. Mater. Res. **41**, 433–448 (2011). doi:10.1146/annurev-matsci-062910-100453

[9] B. Lenoir, J.-P. Michenaud, A. Dauscher: *Thermoélectricité : des principes aux applications*. Editions T.I. article K 730 (2010).

[10] X. Zhang, L.-D. Zhao: *Thermoelectric materials: Energy conversion between heat and electricity*. Journal of Materiomics **1**, 92-105 (2015). doi:10.1016/j.jmat.2015.01.001

[11] K. Suekuni, K. Tsuruta, T. Ariga, M. Koyano: *Thermoelectric Properties of Mineral Tetrahedrites $Cu_{10}Tr_2Sb_4S_{13}$ with Low Thermal Conductivity*. Applied Physics Express **5** 051201 (2012). doi:10.1143/APEX.5.051201

[12] Y. Bouyrie: *Identification, synthèse et caractérisation de phases tétraédrites pour la conversion d'énergie par effets thermoélectriques*. PhD thesis. Université de Lorraine, Nancy, France (2015).

[13] X. Lu, D. T. Morelli: *Natural mineral tetrahedrite as a direct source of thermoelectric materials*. Phys. Chem. Chem. Phys. **15** (2013). doi:10.1039/C3CP50920F

[14] N. W. Ashcroft, N. D. Mermin: *Solid State Physics*. Boston, MA: Cengage Learning, 1976. 848 p. ISBN: 978-0-03083993-1.

[15] J. R. Hook, H. E. Hall: *Solid State Physics*. 2nd ed. Chichester, Englang: John Wiley & Sons, 2010. 496 p. ISBN: 978-0471-92805-8.

[16] C. Kittel: *Introduction to Solid State Physics*. 8th ed. Wiley, 2004. 704 p. ISBN: 978-0471-41526-8.

[17] A. Anselm: *Introduction to Semiconductor Theory*. Prentice Hall, 1982. 645 p. ISBN: 978-013496034-0.

[18] R. Vracar: *Développement de matériaux $Mg_2Si_{1-x}Sn_x$ de type n et p pour applications thermoélectriques dans la gamme de température 300–600 ˚C*. PhD thesis. University of Grenoble, Grenoble, France (2006).

[19] K. Favier: *Etude de matériaux composites à base de nanosiliciures de métaux de transition pour la thermoélectricité*. PhD thesis. Montpellier 2 University, Montpellier, France (2006).

[20] P. Tomeš: *Thermoelectric properties of oxide/oxynitride materials and thermoelectric oxide modules (TOMs) for high-temperature solar applications*. PhD thesis. University of Bern, Bern, Switzerland (2010).

[21] O. Bubnova: *Thermoelectric properties of conducting polymers*. PhD thesis. Linköping University, Linköping, Sweden (2013).

[22] X. Lu: *Thermoelectric Properties of Natural Mineral Based Tetrahedrite Compounds*. PhD thesis. Michigan State University, East Lansing, MI, USA (2014).

[23] N. F. Mott, E. A. Davis: *Electronic Processes in Non-Crystalline Materials*. 2nd ed. Oxford University Press, 2012. 608 p. ISBN 978-0-1996-4533-6.

[24] P. M. Chaikin: *An Introduction to Thermopower for Those Who Might Want to Use It to Study Organic Conductors and Superconductors*. In: Organic Superconductivity. Boston, MA: Springer, 1990, pp. 101-115. ISBN: 978-1-4899-2605-0. doi:10.1007/978-1-4899-2605-0_11

[25] J.-P. Doumerc: *Thermoelectric Power for Carriers in Localized States: A Generalization of Heikes and Chaikin-Beni Formulae*. Journal of Solid State Chemistry **109**, 2 (1994). doi:10.1006/jssc.1994.1124

[26] J. Hejtmánek: *Thermal and Electrical Properties of Oxides*. [PPT file] (2011).

[27] M. Cassart: *Transport Properties of High-T_C Superconductors*. PhD thesis. Université Catholique de Louvain, Louvain-la-Neuve, Belgium (1994).

[28] H.-S. Kim, Z. M. Gibbs, Y. Tang, H. Wang, G. J. Snyder: *Characterization of Lorenz number with Seebeck coefficient measurement.* APL Mater. **3**, 041506 (2015). doi:10.1063/1.4908244

[29] P. G. Klemens: *Thermal Conductivity and Lattice Vibrational Modes.* Solid State Physics **7**, 1-98 (1958). doi:10.1016/S0081-1947(08)60551-2

[30] D. G. Cahill, S. K. Watson, R. O. Pohl: *Lower limit to the thermal conductivity of disordered crystals.* Phys. Rev. B **46**, 6131 (1992). doi:10.1103/PhysRevB.46.6131

[31] J. Callaway: *Model for Lattice Thermal Conductivity at Low Temperatures.* Phys. Rev. B **113**, 1046 (1959). doi:10.1103/PhysRev.113.1046

[32] M. Puyet et al.: *Low-temperature thermal properties of n-type partially filled calcium skutterudites.* Journal of Physics: Condensed Matter **18**, 49 (2006). doi:10.1088/0953-8984/18/49/021

[33] B. Ramachandran, K. K. Wu, Y. K. Kuo, M. S. R. Rao: *Phonon thermal transport and phonon-magnon coupling in polycrystalline $BiFeO_3$ systems.* Journal of Physics D: Applied Physics **48**, 11 (2015). doi:10.1088/0022-3727/48/11/115301

[34] D. M. Hulbert et al.: *The absence of plasma in "spark plasma sintering".* J. Appl. Phys. **104**, 033305 (2008). doi:10.1063/1.2963701

[35] Fritsch: *Product leaflet Planetary mills Premium line.* (2016)

[36] B. Lenoir: *Introduction au PPMS et à ses options.* Laboratory seminar [PPT file] (2015).

[37] Quantum Design: *Thermal Transport Option User's Manual.* [PDF file] (2002).

[38] Netzsch: *Proteus Help LFA-Analysis.* [Software help files] version 5.2.0 (2010).

[39] Netzsch: *Laser Flash Apparatus LFA 427.* [PDF file].

[40] C. B. Boothroyd: *Microanalysis in the electron microscope.* [PDF file] Technical University of Denmark (2010).

[41] M. McElfresh: *Fundamentals of Magnetism and Magnetic Measurements.* [PDF file] Quantum Design (1994).

[42] Quantum Design: *Heat Capacity Option User's Manual.* [PDF file] (2015).

[43] E. Alleno et al.: *Invited Article: A round robin test of the uncertainty on the measurement of the thermoelectric dimensionless figure of merit of $Co_{0.97}Ni_{0.03}Sb_3$.* Review of Scientific Instruments **86**, 011301 (2015). doi:10.1063/1.4905250

[44] D.R. Lide: *CRC Handbook of Chemistry and Physics 2007-2008*. 88th edn. Boca Raton, FL: CRC Press, 2008. ISBN: 978-084930488-0.

[45] R. D. Shannon: *Revised effective ionic radii and systematic studies of interatomic distances in halides and chalcogenides*. Acta Crystallographica A **32**, 751–767 (1976). doi:10.1107/S0567739476001551

[46] G. J. Snyder, T. S. Ursell: *Thermoelectric Efficiency and Compatibility*. Phys. Rev. Lett. **91**, 148301 (2003). doi:10.1103/PhysRevLett.91.148301

[47] A. E. Standage, M. S. Gani: *Reaction Between Vitreous Silica and Molten Aluminum*. Journal of the American Ceramic Society **50** 2, (1967). doi:10.1111/j.1151-2916.1967.tb15049.x

[48] K. Suekuni, T. Takabatake: *Research Update: Cu–S based synthetic minerals as efficient thermoelectric materials at medium temperatures*. APL Mater. **4**, 104503 (2016). doi:10.1063/1.4955398

[49] R. Chetty, A. Bali, R. C. Mallik: *Tetrahedrites as thermoelectric materials: an overview*. J. Mater. Chem. C **3**, pp. 12364-12378 (2015). doi:10.1039/c5tc02537k

[50] K. Suekuni, Y. Tomizawa, T. Ozaki, M. Koyano: *Systematic study of electronic and magnetic properties for* $Cu_{12-x}TM_xSb_4S_{13}$ *(TM=Mn, Fe, Co, Ni, and Zn) tetrahedrite*. Journal of Applied Physics **115**, 143702 (2014). doi:10.1063/1.4871265

[51] K. Suekuni et al.: *High-performance thermoelectric mineral* $Cu_{12-x}Ni_xSb_4S_{13}$ *tetrahedrite*. J. Appl. Phys. **113**, 043712 (2013). doi:10.1063/1.4789389

[52] H. I. Tanaka et al.: *Metal–Semiconductor Transition Concomitant with a Structural Transformation in Tetrahedrite* $Cu_{12}Sb_4S_{13}$. J. Phys. Soc. Jpn. **85**, 014703 (2016). doi:10.7566/JPSJ.85.014703

[53] Y. Kosaka et al.: *Effects of Ge and Sn substitution on the metal–semiconductor transition and thermoelectric properties of* $Cu_{12}Sb_4S_{13}$ *tetrahedrite*. Phys. Chem. Chem. Phys. **13** (2017). doi:10.1039/c7cp00351j

[54] L. Pauling, E. W. Neumann: *The crystal structure of binnite* $(Cu,Fe)_{12}As_4S_{13}$*, and the chemical composition and structure of minerals of the tetrahedrite group*. Z. Kristallogr. **88**, 54 (1934).

[55] B. J. Wuensch: *The crystal structure of tetrahedrite,* $Cu_{12}Sb_4S_{13}$. Z. Kristallogr. **119**, 437 (1964). doi:10.1524/zkri.1964.119.5-6.437

[56] M. Charlat, C. Lévy: *Substitutions multiples dans la série tennantite-tétraédrite* [Multiple substitutions in the tennantite-tetrahedrite series]. Bull. Soc. Fr. Minéral. Cristallogr. **97**, pp. 241-250 (1974).

[57] M. Charlat, C. Lévy: *Influence des principales substitutions sur le paramètre cristallin dans la série tennantite-tétraédrite* [Influence of main substitutions on the lattice constant in the tennantite-tetrahedrite series]. Bull. Soc. Fr. Minéral. Cristallogr. **98**, pp. 152-158 (1975).

[58] M. L. Johnson, R. Jeanloz: *A Brillouin-zone model for compositional variation in tetrahedrite*. American Mineralogist **68**, pp. 220-226 (1983).

[59] N. E. Johnson, J. R. Craig, J. D. Rimstidt: *Compositional trends in tetrahedrite*. Can. Mineral. **24**, pp. 385-397 (1986).

[60] M. J. O'Leary, R. O. Sack: *Fe-Zn exchange reaction between tetrahedrite and sphalerite in natural environments*. Contributions to Mineralogy and Petrology **96** 4, pp. 415-425 (1987). doi:10.1007/BF01166687

[61] J. M. Charnock, C. D. Garner, R. A. D. Pattrick, D. J. Vaughan: *EXAFS and Mössbauer spectroscopic study of Fe-bearing tetrahedrites*. Mineral. Mag. **53**, 193 (1989). doi:10.1180/minmag.1989.053.370.06

[62] E. Makovicky, K. Forcher, W. Lottermoser, G. Amthauer: *The role of Fe^{2+} and Fe^{3+} in synthetic Fe-substituted tetrahedrite*. Miner. Petrol. **43**, 1 (1990). doi:10.1007/BF01164223

[63] E. Makovicky, S. Karup-Møller: *Exploratory studies on substitution of minor elements in synthetic tetrahedrite .1. Substitution by Fe, Zn, Co, Ni, Mn, Cr, V and Pb - unit-cell parameter changes on substitution and the structural role of Cu^{2+}*. Neues Jahrbuch fur Mineralogie. Abhandlungen **167**, 1, pp. 89–123 (1994).

[64] S. Karup-Møller, E. Makovicky: *Exploratory studies of element substitutions in synthetic tetrahedrite. Part II. Selenium and tellurium as anions in Zn-Fe tetrahedrites*. Neues Jahrbuch für Mineralogie - Monatshefte **1999**, 9, pp. 385–399 (1999).

[65] M. H. Klünder, S. Karup-Møller, E. Makovicky: *Exploratory studies on substitutions in the tetrahedrite-tennantite solid solution series Part III. The solubility of bismuth in tetrahedrite-tennantite containing iron and zinc*. Neues Jahrbuch für Mineralogie - Monatshefte **2003**, 4, pp. 153–175 (2003). doi:10.1127/0028-3649/2003/2003-0153

[66] M. K. Hansen, E. Makovicky, S. Karup-Møller: *Exploratory studies on substitutions in tetrahedrite–tennantite solid solution. Part IV. Substitution of germanium and tin*. Neues Jahrbuch für Mineralogie - Abhandlungen **179**, 1 (2003). doi:10.1127/0077-7757/2003/0179-0043

[67] E. Makovicky, S. Karup-Møller: *Exploratory studies of element substitutions in synthetic tetrahedrite. Part V. Mercurian tetrahedrite*. Neues Jahrbuch fur Mineralogie. Abhandlungen **179**, 1, pp. 73–83 (2003). doi:10.1127/0077-7757/2003/0179-0073

[68] S. Karup-Møller, E. Makovicky: *Exploratory studies of the solubility of minor elements in tetrahedrite. VI. Zinc and the combined zinc-mercury and iron-mercury substitutions*. Neues Jahrbuch für Mineralogie - Monatshefte **2004**, 11, pp. 508–524 (2004). doi:10.1127/0028-3649/2004/2004-0508

[69] X. Lu, D. T. Morelli et al.: *High Performance Thermoelectricity in Earth-Abundant Compounds Based on Natural Mineral Tetrahedrites*. Adv. Energy Mater. **3** (2013). doi:10.1002/aenm.201200650

[70] X. Lu, D. T. Morelli: *Rapid synthesis of high-performance thermoelectric materials directly from natural mineral tetrahedrite*. MRS Commun. **3**, 3 (2013). doi:10.1557/mrc.2013.26

[71] X. Lu, D. T. Morelli, Y. Xia, V. Ozolins: *Increasing the Thermoelectric Figure of Merit of Tetrahedrites by Co-Doping with Nickel and Zinc*. Chem. Mater. **27**, 2 (2015). doi:10.1021/cm502570b

[72] X. Lu, D. T. Morelli: *The Effect of Te Substitution for Sb on Thermoelectric Properties of Tetrahedrite*. J. Electron. Mater. **43**, 6 (2014). doi:10.1007/s11664-013-2931-2

[73] Y. Bouyrie et al.: *Crystal structure, electronic band structure and high-temperature thermoelectric properties of Te-substituted tetrahedrites* $Cu_{12}Sb_{4-x}Te_xS_{13}$ *(*$0.5 \leq x \leq 2.0$*)*. Journal of Materials Chemistry C **40** (2015). doi:10.1039/c5tc01636c

[74] X. Fan, E. D. Case, X. Lu, D. T. Morelli: *Room temperature mechanical properties of natural-mineral-based thermoelectrics*. J. Mater. Sci. **48**, 21 (2013). doi:10.1007/s10853-013-7569-1

[75] X. Lu et al.: *Band structure engineering in highly degenerate tetrahedrites through isovalent doping*. Journal of Materials Chemistry A **43** (2016). doi:10.1039/c6ta07015a

[76] W. Lai, Y. Wang, D. T. Morelli, X. Lu: *From Bonding Asymmetry to Anharmonic Rattling in* $Cu_{12}Sb_4S_{13}$ *Tetrahedrites: When Lone-Pair Electrons Are Not So Lonely*. Advanced Functional Materials **25**, 24 (2015). doi:10.1002/adfm.201500766

[77] S. Kitagawa et al.: *Suppression of Nonmagnetic Insulating State by Application of Pressure in Mineral Tetrahedrite* $Cu_{12}Sb_4S_{13}$. J. Phys. Soc. Jpn. **84**, 093701 (2015). doi:10.7566/JPSJ.84.093701

[78] T. Barbier et al.: *Structural stability of the synthetic thermoelectric ternary and nickel-substituted tetrahedrite phases*. J. Alloys Compd. **634** (2015). doi:10.1016/j.jallcom.2015.02.045

[79] E. Lara-Curzio et al.: *Low-temperature heat capacity and localized vibrational modes in natural and synthetic tetrahedrites*. J. Appl. Phys. **115** (2014). doi:10.1063/1.4878676

[80] J. Y. Wang, X. Y. Li, Y. F. Bao: *Thermoelectric Properties of Mn Doped $Cu_{12-x}Mn_xSb_4S_{13}$ Tetrahedrites*. Materials Science Forum **847**, pp. 161–165 (2016). doi:10.4028/www.scientific.net/MSF.847.161

[81] R. Chetty et al.: *Thermoelectric properties of a Mn substituted synthetic tetrahedrite*. Physical Chemistry Chemical Physics **17** (2014). doi:10.1039/C4CP04039B

[82] X. Lu et al.: *High Performance Thermoelectricity in Earth-Abundant Compounds Based on Natural Mineral Tetrahedrites*. Advanced Energy Materials **3**, 3 (2013). doi:10.1002/aenm.201200650

[83] R. Chetty et al.: *Thermoelectric properties of Co substituted synthetic tetrahedrite*. Acta Materialia **100** (2015). doi:10.1016/j.actamat.2015.08.040

[84] D. S. P. Kumar et al.: *Thermoelectric properties of Cd doped tetrahedrite: $Cu_{12-x}Cd_xSb_4S_{13}$*. Intermetallics **78** (2016). doi:10.1016/j.intermet.2016.08.003

[85] D. S. P. Kumar et al.: *Thermoelectric Properties of Bi Doped Tetrahedrite*. Journal of Electronic Materials **46**, 5 (2017). doi:10.1007/s11664-016-4826-5

[86] X. Lu et al.: *Phase Stability, Crystal Structure, and Thermoelectric Properties of $Cu_{12}Sb_4S_{13-x}Se_x$ Solid Solutions*. Chemistry of Materials **28**, 6 (2016). doi:10.1021/acs.chemmater.5b04796

[87] X. Lu et al.: *Band structure engineering in highly degenerate tetrahedrites through isovalent doping*. Journal of Materials Chemistry A **4**, 17096-17103 (2016). doi:10.1039/c6ta07015a

[88] J. Heo et al.: *Design Meets Nature: Tetrahedrite Solar Absorbers*. Advanced Energy Materials **5**, 7 (2015). doi:10.1002/aenm.201401506

[89] P. Vaqueiro et al.: *The Influence of Mobile Copper Ions on the Glass-Like Thermal Conductivity of Copper-Rich Tetrahedrites*. Chemistry of Materials **29**, 9 (2017). doi:10.1021/acs.chemmater.7b00891

[90] Y. Bouyrie et al.: *From crystal to glass-like thermal conductivity in crystalline minerals*. Physical Chemistry Chemical Physics **30** (2015). doi:10.1039/c5cp02900g

[91] D. J. James, X. Lu, D. T. Morelli, S. L. Brock: *Solvothermal Synthesis of Tetrahedrite: Speeding Up the Process of Thermoelectric Material Generation*. ACS Applied Materials & Interfaces **7**, 42 (2015). doi:10.1021/acsami.5b07141

[92] L. Wang et al.: *Synthesis and characterization of hydrazine solution processed $Cu_{12}Sb_4S_{13}$ film*. Solar Energy Materials and Solar Cells **144** (2016). doi:10.1016/j.solmat.2015.08.016

[93] D. P. Weller et al.: *Thermoelectric Performance of Tetrahedrite Synthesized by a Modified Polyol Process*. Chemistry of Materials **29**, 4 (2017). doi:10.1021/acs.chemmater.6b04950

[94] J. van Embden, K. Latham, N. W. Duffy, Y. Tachibana: *Near-Infrared Absorbing $Cu_{12}Sb_4S_{13}$ and Cu_3SbS_4 Nanocrystals: Synthesis, Characterization, and Photoelectrochemistry*. J. Am. Chem. Soc. **135**, 31 (2013). doi:10.1021/ja402702x

[95] A. P. Gonçalves et al.: *Fast and scalable preparation of tetrahedrite for thermoelectrics via glass crystallization*. Journal of Alloys and Compounds **664** (2016). doi:10.1016/j.jallcom.2015.12.213

[96] D. P. Weller, D. T. Morelli: *Rapid synthesis of zinc and nickel co-doped tetrahedrite thermoelectrics by reactive spark plasma sintering and mechanical alloying*. Journal of Alloys and Compounds **710** (2017). doi:10.1016/j.jallcom.2017.03.272

[97] T. Barbier et al.: *Thermoelectric Materials: A New Rapid Synthesis Process for Nontoxic and High-Performance Tetrahedrite Compounds*. Journal of the American Ceramic Society **99**, 1 (2015). doi:10.1111/jace.13838

[98] P. Levinsky, C. Candolfi, A. Dauscher, J. Tobola, J. Hejtmanek, B. Lenoir: *Thermoelectric properties of the tetrahedrite-tennantite solid solution $Cu_{12}Sb_{4-x}As_xS_{13}$ ($0 \leq x \leq 4$)*. In preparation.

[99] A. Bansil, S. Kaprzyk, P. E. Mijnarends, J. Tobola: *Electronic structure and magnetism of $Fe_{3-x}V_xX$ (X = Si, Ga, and Al) alloys by the KKR.CPA method*. Physical Review B **60**, 13396 (1999). doi:10.1103/PhysRevB.60.13396

[100] T. Stopa, S. Kaprzyk, J. Tobola: *Linear aspects of the Korringa–Kohn–Rostoker formalism*. Journal of Physics: Condensed Matter **16**, 28 (2004). doi:10.1088/0953-8984/16/28/012

[101] J. P. Perdew, Y. Wang: *Accurate and simple analytic representation of the electron-gas correlation energy*. Physical Review B **45**, 13244 (1992). doi:10.1103/PhysRevB.45.13244

[102] S. Kaprzyk, A. Bansil: *Green's function and a generalized Lloyd formula for the density of states in disordered muffin-tin alloys*. Physical Review B **42**, 7358 (1990). doi:10.1103/PhysRevB.42.7358

[103] S. Jin et al.: *Thousandfold Change in Resistivity in Magnetoresistive La-Ca-Mn-O Films*. Science **264**, 5157, pp. 413-415 (1994). doi:10.1126/science.264.5157.413

[104] I. Terasaki, Y. Sasago, K. Uchinokura: *Large thermoelectric power in NaCo2O4 single crystals*. Phys. Rev. B **56**, R12685(R) (1997). doi:10.1103/PhysRevB.56.R12685

[105] K. Koumoto, I. Terasaki, R. Funahashi: *Complex Oxide Materials for Potential Thermoelectric Applications*. MRS Bulletin **31**, 3, pp. 206-210 (2006). doi:10.1557/mrs2006.46

[106] H. Wang, W. Su, J. Liu, C. Wang: *Recent development of n-type perovskite thermoelectrics*. Journal of Materiomics **2**, 3, pp. 225-236 (2016). doi:10.1016/j.jmat.2016.06.005

[107] S. Hébert, A. Maignan: *Thermoelectric Oxides*. In: Functional Oxides. John Wiley & Sons, pp. 203–255 (2010). ISBN: 978-0-470-99750-5.

[108] Y Tokura: *Critical features of colossal magnetoresistive manganites*. Reports on Progress in Physics **69** (2006). doi:10.1088/0034-4885/69/3/R06

[109] M. Baldini et al.: *Origin of colossal magnetoresistance in $LaMnO_3$ manganite*. Proceedings of the National Academy of Sciences **112**, 35 (2015). doi:10.1073/pnas.1424866112

[110] J. Hejtmanek et al.: *Oxide Thermoelectric Materials for High Temperature Waste Heat Recovery*. Czech Science Foundation project n. GA13-17538S report (2016)

[111] E. O. Wollan, W. C. Koehler: *Neutron Diffraction Study of the Magnetic Properties of the Series of Perovskite-Type Compounds $[(1-x)La,xCa]MnO_3$*. Phys. Rev. **100**, 545 (1955). doi:10.1103/PhysRev.100.545

[112] J. Hejtmánek, P. Levinský, C. Martin: *On the thermoelectric n-type manganites $Ca_{1-x}Yb_xMn_{1-y}W_yO_{3-\delta}$*. Poster presented at: European Conference on Thermoelectrics 2014. Madrid, Spain (2014).

[113] J. Hejtmánek et al.: *Interplay between transport, magnetic, and ordering phenomena in $Sm_{1-x}Ca_xMnO_3$*. Phys. Rev. B **60**, 14057 (1999). doi:10.1103/PhysRevB.60.14057

[114] Y. Wang et al.: *High Temperature Thermoelectric Response of Electron-Doped $CaMnO_3$*. Chem. Mater. **21**, 19 (2009). doi:10.1021/cm901766y

[115] Y. Wang et al.: *Thermal conductivity of electron-doped $CaMnO_3$ perovskites: Local lattice distortions and optical phonon thermal excitation*. Acta Materialia **58**, 19 (2010). doi:10.1016/j.actamat.2010.07.052

[116] E. Bakken et al.: *Entropy of oxidation and redox energetics of $CaMnO_{3-\delta}$*. Solid State Ionics **176**, 29 (2005). doi:10.1016/j.ssi.2005.06.009

[117] A. Srivastava, N. K. Gaur: *The role of lattice distortions in determining the thermal properties of electron doped $CaMnO_3$*. Journal of Physics: Condensed Matter **21**, 9 (2009). doi:10.1088/0953-8984/21/9/096001

[118] P. Thiel et al.: *Influence of tungsten substitution and oxygen deficiency on the thermoelectric properties of $CaMnO_{3-\delta}$*. Journal of Applied Physics **114**, 243707 (2013). doi:10.1063/1.4854475

[119] L. Jiang, M. Zhang, Q. Jiang: *Thermal transport by lattice excitations in hexagonal rare-earth manganites*. Journal of Applied Physics **104**, 8 (2008). doi:10.1063/1.3005875

[120] R. K. Zheng, C. F. Zhu, J. Q. Xie, X. G. Li: *Structural change and charge ordering correlated ultrasonic anomalies in $La_{1-x}Ca_xMnO_3$ ($x = 0.5$, 0.83) perovskite*. Phys. Rev. B **63** (2000). doi:10.1103/PhysRevB.63.024427

[121] E. V. Mostovshchikova et al.: *Magnetic and structural transitions in $CaMn_{0.96}Mo_{0.04}O_3$*. Journal of Alloys and Compounds **615** (2014). doi:10.1016/j.jallcom.2014.06.179

[122] Li Y.: *Conducting Polymers*. In: Organic Optoelectronic Materials. Springer (2015). doi:10.1007/978-3-319-16862-3_2

[123] H. Shirakawa, E. J. Louis, A. G. MacDiarmid, C. K. Chiang, A. J. Heeger: *Synthesis of electrically conducting organic polymers - halogen derivatives of polyacetylene, $(CH)_x$*. Journal of the Chemical Society, Chemical Communications **0**, 578-580 (1977). doi:10.1039/C39770000578

[124] M. Culebras, C. M. Gómez, A. Cantarero: *Review on Polymers for Thermoelectric Applications*. Materials **2014**, 7(9), pp. 6701-6732 (2014). doi:10.3390/ma7096701

[125] N. Dubey, M. Leclerc: *Conducting polymers: Efficient thermoelectric materials*. Journal of Polymer Science Part B: Polymer Physics **49**, 7 (2011). doi:10.1002/polb.22206

[126] Bubnova O., Crispin X.: *Towards polymer-based organic thermoelectric generators*. Energy & Environmental Science **5**, 9345 (2012). doi:10.1039/c2ee22777k

[127] H. Yao: *Recent Development of Thermoelectric Polymers and Composites*. Macromolecular Rapid Communications **39**, 6 (2018). doi:10.1002/marc.201700727

[128] B. Wunderlich: *Heat Capacities of Solid Polymers (The Advanced THermal Analysis System, ATHAS*. Web. As of 19th june 2018. https://www.osti.gov/servlets/purl/7021212-WabTRM/

[129] Asegun H.: *Thermal Transport In Polymers*. Annual Review Of Heat Transfer **17**, pp. 485–520 (2014). doi:10.1615/AnnualRevHeatTransfer.2013006949

[130] Mark J.E. - Physical Properties of Polymers Handbook 2nd ed.pdf J. E. Mark: *Physical Properties of Polymers Handbook*. 2nd ed. Springer, 2007. 1076 p. ISBN 978-0-387-69002-5.

[131] Wei Q et al.: *Recent Progress on PEDOT-Based Thermoelectric Materials*. Materials **2015**, 8(2) (2015). doi:10.3390/ma8020732

[132] Kim N. et al.: *Role of Interchain Coupling in the Metallic State of Conducting Polymers*. Phys. Rev. Lett. **109**, 10, 106405 (2012). doi:10.1103/PhysRevLett.109.106405

[133] Sun K. et al.: *Review on application of PEDOTs and PEDOT:PSS in energy conversion and storage devices*. Journal of Materials Science: Materials in Electronics **26**, 7 (2015). doi:10.1007/s10854-015-2895-5

[134] Bubnova O. et al.: *Optimization of the thermoelectric figure of merit in the conducting polymer poly(3,4-ethylenedioxythiophene)*. Nature Materials **10**, pp. 429-433 (2011). doi:10.1038/nmat3012

[135] I. Sapurina et al.: *Polypyrrole nanotubes: The tuning of morphology and conductivity*. Polymer **113**, 247–258 (2017). doi:10.1016/j.polymer.2017.02.064

[136] Y. Li, P. Bober, M. Trchová, J. Stejskal: *Polypyrrole prepared in the presence of methyl orange and ethyl orange: nanotubes versus globules in conductivity enhancement*. Journal of Materials Chemistry C **5**, 4236 (2017). doi:10.1039/c7tc00206h

[137] A. Rudajevová, M. Varga, J. Prokeš, J. Kopecký, J. Stejskal: *Thermal Properties of Conducting Polypyrrole Nanotubes*. Acta Physica Polonica A **128** (2015). doi:10.12693/APhysPolA.128.730

[138] B. A. Lunn, J. Unsworth, N. G. Booth, P. C. Innis: *Determination of the thermal conductivity of polypyrrole over the temperature range 280–335 K*. Journal of Materials Science **28**, 18 (1993). doi:10.1007/BF00361185

[139] D. S. Maddison, R. B. Roberts, J. Unsworth: *Thermoelectric power of polypyrrole*. Synthetic Metals **33**, 3 (1989). doi:10.1016/0379-6779(89)90474-8

[140] A. B. Kaiser et al.: *Comparison of electronic transport in polyaniline blends, polyaniline and polypyrrole*. Synthetic Metals **84**, 1–3 (1997). doi:10.1016/S0379-6779(96)04112-4

[141] N. T. Kemp et al.: *Thermoelectric power and conductivity of different types of polypyrrole*. Journal of Polymer Science: Part B: Polymer Physics **37** (1999). doi:10.1002/(SICI)1099-0488(19990501)37:9¡953::AID-POLB7¿3.0.CO;2-L

[142] M. Nechtschein, C. Santier, J. P. Travers, J. Chroboczek, A. Alix, M. Ripert: *Water effects in polyaniline: NMR and transport properties*. Synthetic Metals **18**, 1–3 (1987). doi:10.1016/0379-6779(87)90897-6

[143] Y. Wei, K. F. Hsueh: *Thermal analysis of chemically synthesized polyaniline and effects of thermal aging on conductivity*. Journal of Polymer Science: Part A Polymer Chemistry **27**, 13 (1989). doi:10.1002/pola.1989.080271312

[144] O. N. Timofeeva, B. Z. Lubentsov, Y. Z. Sudakova, D. N. Chernyshov, M. L. Khidekel': *Conducting polymer interaction with gaseous substances I. Water.* Synthetic Metals **40**, 1 (1991). doi:10.1016/0379-6779(91)91493-T

[145] B. Lubentsov et al.: *The study of conducting polymer interaction with gaseous substances IV. The water content influence on polyaniline crystal structure and conductivity.* Synthetic Metals **47**, 2 (1992). doi:10.1016/0379-6779(92)90386-W

[146] L. Tarachiwin, P. Kiattibutr, L. Ruangchuay, A. Sirivat, J.Schwank: *Electrical conductivity response of polyaniline films to ethanol–water mixtures.* Synthetic Metals **129**, 3 (2002). doi:10.1016/S0379-6779(02)00112-1

[147] Y. W. Park, Y. S. Lee, C. Park, L. W. Shacklette, R. H. Baughman: *Thermopower and conductivity of metallic polyaniline.* Solid State Communications **63**, 11 (1987). doi:10.1016/0038-1098(87)90662-4

[148] S. Sakkopoulos, E. Vitoratos, E. Dalas, G. Pandis, D, Tsamouras: *Thermopower sign reversal versus temperature and DC conductivity in polyaniline derivatives.* Journal of Physics: Condensed Matter **4**, 9 (1992). doi:10.1088/0953-8984/4/9/016

[149] C. O. Yoon et al.: *Hopping transport in doped conducting polymers in the insulating regime near the metal-insulator boundary: polypyrrole, polyaniline and polyalkylthiophenes.* Synthetic Metals **75**, 3 (1995). doi:10.1016/0379-6779(96)80013-0

[150] Y. Hu, O. Naonori, T. Naoki: *Low Thermal Conductivities of Undoped and Various Protonic Acid-Doped Polyaniline Films.* Chemistry Letters **29**, 4 (2000). doi:10.1246/cl.2000.392

[151] H. Yan, N. Sada, N. Toshima: *Thermal transporting properties of electrically conductive polyaniline films as organic thermoelectric materials.* Journal of Thermal Analysis and Calorimetry **69**, 3 (2002). doi:10.1023/A:1020612123826

[152] P. B. Kaul, K. A. Day, A. R. Abramson: *Application of the three omega method for the thermal conductivity measurement of polyaniline.* Journal of Applied Physics **101**, 083507 (2007). doi:10.1063/1.2714650

[153] C. Nath, A. Kumar, K.-Z. Syu, Y.-K. Kuo: *Heat conduction in conducting polyaniline nanofibers.* Applied Physics Letters **103**, 121905 (2013). doi:10.1063/1.4821656

[154] A. Famengo, S. Rossi, P. Bison, S. Boldrini: *Thermal conductivity characterization of polyaniline doped material for thermoelectric applications.* Proceedings of SPIE **10214** Thermosense: Thermal Infrared Applications XXXIX (2017). doi:10.1117/12.2262080

List of the Author's Publications

Z. Jirák, O. Kaman, K. Knížek, P. Levinsky, M. Míšek, P. Veverka, J. Hejtmánek: *High-field magnetoconductance in La-Sr manganites of FM and AFM ground states.* Journal of Magnetism and Magnetic Materials 456 (2018). doi:10.1016/j.jmmm.2018.02.026

P. Levinský, C. Candolfi, A. Dauscher, B. Lenoir, J. Hejtmánek: *Influence of As-Sb Substitution on $Cu_{12}Sb_4S_{13}$ Thermoelectric Properties.* In: Sborník příspěvků 7. studentské vědecké konference fyziky pevných látek a materiálů [Proceedings of the 7th Student Scientific Conference on Solid State Physics nd Materials]. Prague: Czech Technical University, 2017. ISBN 978-80-01-06374-3.

D. Ibrahim, J.-B. Vaney, S. Sassi, C. Candolfi, V. Ohorodniichuk, P. Levinsky, C. Semprimoschnig, A. Dauscher, B. Lenoir: *Reinvestigation of the thermal properties of single-crystalline SnSe.* Applied Physics Letters 110, 3 (2017). doi:10.1063/1.4974348

Z. Jirak, J. Hirschner, O. Kaman, K. Knizek, P. Levinsky, M. Marysko, J. Hejtmanek: *Structure and transport properties of the $La_{1-x}Sr_xMnO_3$ granular ceramics.* Journal of Physics D: Applied Physics 50, 7 (2017). doi:10.1088/1361-6463/aa54e7

P. Levinsky, J.-B. Vaney, C. Candolfi, A. Dauscher, B. Lenoir, J. Hejtmánek: *Electrical, Thermal, and Magnetic Characterization of Natural Tetrahedrites-Tennantites of Different Origin.* Journal of Electronic Materials 45, 3 (2016) pp. 1351-1357. doi:10.1007/s11664-015-4032-x

J. Buršík, M. Soroka, K. Knížek, J. Hirschner, P. Levinský, J. Hejtmánek: *Oriented thin films of $Na_{0.6}CoO_2$ and $Ca_3Co_4O_9$ deposited by spin-coating method on polycrystalline substrate.* Thin Solid Films 603 (2016) pp. 400-403. doi:10.1016/j.tsf.2016.02.056

P. Levinský, J. Hejtmánek, C. Candolfi, A. Dauscher, B. Lenoir: *Microstructure and thermoelectric properties of mixtures of natural and synthetic tetrahedrite.* In: Sborník příspěvků 6. studentské vědecké konference fyziky pevných látek [Proceedings of the 6th Student Scientific Conference on Solid State Physics]. Prague: Czech Technical University, 2016. ISBN 978-80-01-06072-8.

P. Levinsky, L. Kalvoda, J. Aubrecht, J. Fojtikova: *Diffusion of ammonia gas in PDMS characterized by ATR spectroscopy.* Proceedings of SPIE 9540 (2015). doi:10.1117/12.2070372

J. Aubrecht, L. Kalvoda, P. Levinsky: *The modification methods of polymer fiber cladding for sensing application.* Proceedings of SPIE 9450 (2015). doi:10.1117/12.2070462

V. Ryukhtin, P. Strunz, G. Kopitsa, K. Ezdakova, N. Gubanova, V. Ivanov, A. Baranchikov, B. Angelov, A. Feoktistov, V. Pipich, P. Levinsky: *Microstructure of Zirconia-Based Sol-Gel Glasses Studied by SANS.* Acta Physica Polonica A 128, 4 (2015) pp. 582-584. doi:10.12693/APhysPolA.128.582

P. Levinský, J. Hejtmánek, C. Candolfi, A. Dauscher.: *Thermoelectric Characterization of Natural Tetrahedrites-Tennantites of Various Origins.* In: Sborník příspěvků 5. studentské vědecké konference fyziky pevných látek [Proceedings of the 5th Student Scientific Conference on Solid State Physics]. Prague: Czech Technical University, 2015. ISBN 978-80-01-05842-8.

P. Levinský: *Investigating Ammonia Diffusion and Reaction in Dye-Sensitized Polydimethylsiloxane Using Attenuated Total Reflection.* In: Sborník příspěvků 4. studentské vědecké konference fyziky pevných látek [Proceedings of the 4th Student Scientific Conference on Solid State Physics]. Prague: Czech Technical University, 2014. ISBN 978-80-01-05565-6.

P. Levinský: *Příprava tenkých vlnovodných vrstev a jejich charakterizace metodou ATR [Fabrication of Thin Wave-Guiding Layers and Their Characterization Using the ATR Method].* In: Sborník příspěvků 3. studentské vědecké konference fyziky pevných látek [Proceedings of the 3rd Student Scientific Conference on Solid State Physics]. Prague: Czech Technical University, 2013. ISBN 978-80-01-05344-7.

L. Kalvoda, J. Aubrecht, P. Levinský: *Development of Distributed Fiber Optic Sensor of Ammonia Gas.* In Ammonia: Structure, Biosynthesis and Functions. Hauppauge, NY: Nova Science Publishers, 2012, pp. 33-60. ISBN: 978-1-62100-502-5.

P. Levinský: *Počítačové simulace distribuované detekce plynů pomocí optického vlákna [Computer Simulations of Distributed Gas Detection Using an Optical Fiber].* In: Sborník příspěvků 1. studentské vědecké konference fyziky pevných látek [Proceedings of the 1st Student Scientific Conference on Solid State Physics]. Prague: Czech Technical University, 2011. ISBN 978-80-01-04869-6.

Extended Résumé (in French)

Les dispositifs thermoélectriques (TE) permettent de convertir directement de l'énergie électrique en énergie thermique par effet Peltier ou de convertir de l'énergie thermique en énergie électrique par effet Seebeck. Ces dispositifs ne nécessitent ni gaz, ni turbine, ni alternateur pour la production d'électricité conventionnelle et ni compresseur pour le refroidissement conventionnel. De cette manière, il est possible de construire des dispositifs à l'état solide sans parties mobiles qui offrent une fiabilité supérieure, un fonctionnement silencieux et qui ne demandent pas d'entretien.

L'efficacité plutôt faible (de l'ordre de 5 %) de ces dispositifs, lié à leur coût élevé et à une certaine toxicité de leurs matériaux constitutifs a limité jusqu'à présent leur utilisation à des applications de niche. Ainsi, les dispositifs TE ont été et sont toujours principalement utilisés pour des applications spatiales pour fournir une source d'électricité stable, continue et autonome pendant des décennies. Ces générateurs TE utilisent un radio-isotope comme source de chaleur, celle-ci étant ensuite convertie en électricité grâce aux matériaux TE dont ils sont constitués. Une autre utilisation est le refroidissement simple et à petite échelle grâce aux modules Peltier. Au cours des vingt dernières années, deux impulsions ont stimulé la recherche sur la technologie TE : l'une est l'orientation de la société vers l'utilisation de procédés plus verts, ce qui conférait aux systèmes TE un nouveau rôle dans la récupération d'énergie à partir de la chaleur perdue, qui constitue une grande partie du budget énergétique de l'humanité, l'autre est liée au développement de nouveaux concepts et à la découverte de nouveaux matériaux TE plus performants, ouvrant de nouvelles voies d'investigation et élargissant le potentiel d'exploitation.

Améliorer les qualités et performances des matériaux traditionnels et identifier de nouveaux matériaux potentiels pour lever certains verrous de la technologie TE est cependant une tâche ardue et de nombreux efforts sont actuellement consacrés à cette recherche. Les principales conditions pour avoir un bon matériau thermoélectrique sont plutôt simples et se traduisent à produire un facteur de mérite adimensionnel ZT élevé, $ZT = \frac{S^2 T}{\rho\kappa}$, soit un coefficient Seebeck S élevé et, en même temps, de faibles résistivité électrique ρ et conductivité thermique κ, à la température absolue T. Ces paramètres étant toutefois interdépendants, la tâche de trouver et d'optimiser un bon matériau TE est délicate et nécessite l'utilisation de diverses approches, conduisant à une large variété de familles de matériaux. [1–10]

Cette thèse est intitulée : Synthèse, caractérisation et optimisation de nouveaux matériaux thermoélectriques. Comme le suggère le titre, une partie de la thèse est consacrée à la synthèse d'échantillons de matériaux TE, généralement à

partir d'éléments purs ou de composés précurseurs simples. Une autre partie est dédiée à la caractérisation des propriétés des échantillons, d'origine synthétique ou minérale. La caractérisation des propriétés thermoélectriques (coefficient Seebeck, résistivité électrique et conductivité thermique), mesurées dans une large gamme de température, est complétée par des caractérisations de la structure cristalline, de la microstructure et de la composition chimique. L'objectif est de tenter d'améliorer les performances thermoélectriques des matériaux étudiés et de mieux comprendre le lien entre les différentes propriétés physiques, en relation avec la micro-structure. En ce qui concerne les nouveaux matériaux étudiés, cette thèse porte principalement sur les tétraédrites, une famille de matériaux à base de minéraux sulfurés dont les propriétés TE prometteuses n'ont été découvertes qu'il y a seulement six ans. [11] Deux autres familles ont été étudiées: les oxydes et les polymères conducteurs.

Cette thèse a été faite en co-tutelle entre l'Université Technique Tchèque de Prague (République tchèque) et l'Université de Lorraine à Nancy (France). Les directeurs et co-directeurs de thèse sont pour la partie tchèque le Dr. Ladislav Kalvoda de l'Université Technique Tchèque de Prague et le Dr. Jiří Hejtmánek de l'Institut de Physique de l'Académie Tchèque des Sciences, respectivement et pour la partie française, le Dr. Anne Dauscher de l'Institut Jean Lamour et le Prof. Bertrand Lenoir de l'Université de Lorraine, respectivement.

Les tétraédrites existent sous forme de minéraux sulfurés naturels, ainsi appelées en raison de la forme tétraédrique de leurs cristaux. Elles sont caractérisées par une structure cristalline cubique et la composition chimique $Cu_{10}Me_2(Sb,As)_4S_{13}$, où Me représente un métal de transition tel que Cu, Zn, Fe ou Co. Quand le Me représente un atome dont la valence est supérieure à un, la tétraédrite est un sémi-conducteur avec une résistivité électrique élevée. Celle-ci peut être réduite en substituant cet atome par des atomes monovalents de Cu qui fournissent des trous qui agissent comme porteurs de charge. La chimie et la structure cristalline des tétraédrites ont été étudiées de manière approfondie depuis plusieurs décennies par des minéralogistes [55,59], mais ce n'est qu'en 2012 que leurs intéressantes propriétés thermoélectriques, comme leur conductivité thermique exceptionnellement basse, ont été découvertes. [11]

Une grande partie de ma thèse a été consacrée à l'étude des matériaux tétraédrites. Dans un premier temps, les propriétés électriques, thermiques et magnétiques de huit minéraux naturels de différentes origines géographiques ont été mesurées et leur comportement analysé en fonction de différents paramètres (température, champ magnétique, ...). Leur comportement TE, peu différent d'un minéral à l'autre, et relativement prévisible justifie leur utilisation partielle pour la fabrication de dispositifs thermoélectriques. Nous avons ensuite développé cette idée [13] plus profondément en étudiant les propriétés de mélanges de tétraédrites naturelles et synthétiques. L'arsenic étant un substituant usuel dans les minéraux naturels, nous avons aussi synthétisé et caractérisé plusieurs tétraédrites en substituant de l'antimoine par de l'arsenic. Nous avons montré que les propriétés TE ne sont que faiblement influencées par cette substitution. Finalement, l'influence de différentes substitutions sur des échantillons synthétiques a également été étudiée, comme par exemple des substitutions de Sn, Mg, Ag ou In sur le site de Cu.

Dans une première approche, nous avons donc caractérisé les compositions chimiques et les propriétés physiques de huit tétraédrites naturelles provenant de divers endroits du monde. Avant les caractérisations, les échantillons ont été broyés et densifiés par spark plasma sintering (SPS), les échantillons naturels étant trop fragiles. Les échantillons possèdent tous une très faible conductivité thermique κ (<0,5 $W.m^{-1}.K^{-1}$) sans la présence d'un pic diélectrique. À basse température, κ suit une loi en T^1, suggérant que le mécanisme de diffusion est différent d'un mécanisme de diffusion aux joints de grains. Les échantillons ne sont pas complètement isolants, mais la résistivité est néanmoins élevée. Elle varie d'un ordre de grandeur entre les échantillons les moins résistifs et les plus résistifs. Cette conductivité électrique résiduelle est en accord avec la présence de lacunes de métaux de transition qui fournissent des porteurs de charge. Nous n'avons trouvé aucune corrélation entre les propriétés thermoélectriques et la composition chimique (i.e. la teneur en métaux de transition, le rapport Sb/As, etc.). Par contre, tous les échantillons se sont comportés comme prévu par la théorie selon leur composition chimique. Il n'y a donc eu aucune surprise, malgré la variété de leur composition. Cette observation supporte l'idée d'utiliser des minéraux tétraédrites naturels dans la fabrication de dispositifs TE. Le meilleur ZT obtenu est de 0,13 à 720 K, une valeur relativement faible mais cependant non négligeable en considérant que ce n'est finalement que celle d'un caillou. Elle est entravée principalement par une résistivité électrique élevée. Les mesures magnétiques au-dessous de la température ambiante reflètent le paramagnétisme des ions de Fe, ainsi que le ferromagnétisme des impuretés de fer situées hors de la structure tétraédrique.

Ensuite, nous avons étudié en détail des mélanges de tétraédrites naturelles et de tétraédrites synthétiques $Cu_{12}Sb_4S_{13}$. Nous avons mélangé dans un broyeur planétaire à billes une des tétraédrites naturelles précédemment étudiées avec une tétraédrite $Cu_{12}Sb_4S_{13}$ synthétisée par nos soins, dans un rapport 50:50 massique. Nous avons soigneusement suivi le processus de broyage du mélange en analysant la structure cristallographique par diffraction des rayons X (DRX) et la morphologie par microscopie électronique à balayage (MEB) de la poudre formée, prélevée plusieurs fois au cours du broyage. Nous avons observé une diminution progressive de la taille des particules pour atteindre une taille inférieure à 100 nm. Nous avons mis en évidence que les deux phases sont conservées pendant toute la durée du broyage (90 min). L'évolution semble se stabiliser au bout de 60 min. Par contre, une solution solide est formée au cours du frittage par SPS. Néanmoins, la durée de frittage de quatre minutes semble légèrement insuffisante pour la formation complète d'une solution solide parfaite. A partir des mesures des propriétés électriques et thermiques, nous avons calculé le facteur ZT. Celui-ci est augmenté d'environ 15 % par rapport au matériau synthétique pur. Nos données sont comparables aux résultats publiés précédemment [13]. Il est cependant possible que nous surestimions la conductivité thermique des tétraédrites possédant les valeurs de κ les plus faibles, en raison de la surestimation probable de la capacité thermique.

Nous avons aussi effectué un simple broyage à la main dans un mortier du mélange 50:50. Dans le cas de ce processus faiblement énergétique, les particules produites ont une taille d'environ 10 µm et la présence des deux phases a été con-

servée même après le frittage. La résistivité électrique de ce système composite était deux fois plus importante que celle de la solution solide, conduisant à des valeurs de ZT inférieures à celles des échantillons 50:50 broyés mécaniquement et des échantillons synthétiques seuls. Un processus assez énergétique, comme le broyage à billes, est donc nécessaire pour obtenir un matériau avec des bonnes propriétés TE à partir des mélanges.

Les propriétés électriques et thermiques d'échantillons réalisés à partir de mélanges tétraédrites naturelles:tétraédrites synthétiques 25:75 et 75:25 broyés mécaniquement et frittés ont été étudiées. Celles-ci varient en fonction de la concentration des porteurs de charge qui dépend de la composition chimique. Du point de vue thermoélectrique, les échantillons 50:50 et 25:75 se comportent de manière optimale, les deux possédant des valeurs de ZT plus élevées d'environ 10 % par rapport à celles de l'échantillon 100% synthétique.

Dans la formule chimique d'une tétraédrite $Cu_{12}Sb_4S_{13}$, n'importe quel nombre d'atomes de Sb peut être substitué par des atomes d'As, les deux formes extrêmes, la tétraédrite (riche en Sb) et la tennantite (riche en As), constituant une solution solide parfaite. Dans les tétraédrites naturelles, des atomes d'As sont presque toujours présents. [56, 59] Lors de notre étude des minéraux naturels, nous n'avions observé aucune corrélation directe entre le nombre d'atomes d'As et les propriétés TE. Nous avons alors synthétisé et étudié trois séries de tétraédrite-tennantite, à savoir $Cu_{10}Me_2Sb_{4-x}As_xS_{13}$, $x = 0, 1, 2, 3, 4$, Me = Cu, Co, Zn.

Les séries au Cu et au Co ont été synthétisées avec succès. Par contre, pour la série au Zn, un dégazage de soufre a eu lieu lors du recuit des échantillons riches en As. Nous avons montré que les propriétés thermoélectriques ne sont que faiblement influencées par la substitution isovalente du Sb par de l'As. Ce résultat est en accord avec des calculs de structures de bande électronique. Dans la série au Cu, ρ varie de quelques pourcents selon le rapport Sb/As, S baisse de 3 % avec chaque atome d'As substitué et le ZT maximal de l'échantillon le plus riche en As est de 10 % moins élevé que pour l'échantillon le plus riche en Sb. Bien que S augmente fortement avec la transition métal–semi-conducteur dans $Cu_{12}Sb_4S_{13}$, la dépendance $S(T)$ de tous les échantillons contenant de l'As est quasiment inexistante.

Les séries au Co et au Zn ont été synthétisées dans le but de réduire la conductivité électrique. Ceci permet de réduire la partie électronique de la conductivité thermique et, par conséquent, d'obtenir une vue plus claire sur l'autre partie – cette du réseau. Les propriétés électriques des séries au Co et au Zn dépendent de la concentration d'atomes de Co et de Zn qui ont été incorporés avec succès dans la structure tétraédrite-tennantite. La concentration réelle de Co et Zn diminue dans les échantillons les plus riche en As. Par conséquent, la concentration de porteurs de charge est augmentée et le niveau de Fermi est situé plus bas dans ces échantillons. La dépendance de la conductivité thermique de réseau en fonction de la teneur en As a donné des résultats plutôt différents pour chacune des trois séries. La série au Cu présente une diminution pour les échantillons contenant à la fois Sb et As, indiquant un effet d'alliage ; la série au Co présente des valeurs plutôt constantes, indiquant l'absence d'effet de la substitution ; la série au Zn ne présente aucune dépendance évidente, indiquant encore une fois qu'il n'y a aucun effet de la substitution. Ces

résultats montrent donc que l'As ne semble pas influencer de manière significative la conductivité thermique de réseau de la tétraédrite, à l'exception d'un léger effet d'alliage.

Diverses substitutions sur le site de Cu ont elles-aussi été étudiées. A partir de prédictions théoriques, nous avons mis en évidence quelques nouveaux éléments qui pourraient rentrer dans la composition de la tétraédrite : Mg, Zr, Hf, Ga. Nous avons ensuite tenté de synthétiser des échantillons avec des substitutions d'In, Mg, Ca et Al sur le site du Cu. L'indium se substitue bien dans la tétraédrite et le ZT que nous avons mesuré pour une substitution de 0,5 atome par formule chimique est identique à celui d'une tétraédrite non substituée. Le calcium ne semble pas entrer dans la tétraédrite, les données sur l'aluminium ne sont pas concluantes, et le magnésium entre dans la tétraédrite, confirmant nos prédictions. L'effet du Mg est similaire à celui d'autres substituants à valence supérieure à un et son influence sur le ZT est très faible. A notre connaissance, c'est la première fois qu'un élément alcalino-terreux ou alcalin a été introduit dans une tétraédrite.

Concernant les matériaux oxydes, deux séries de manganites thermoélectriques dopées avec la formule générale $Ca_{1-x}Yb_xMn_{1-y}W_yO_3$ ont été étudiées. Le facteur de puissance $PF = S^2/\rho$ maximal obtenu à 1000 K est d'environ 400 µW.m^{-1}.K^{-2} pour ($x = 0,02$, $y = 0$), c'est-à-dire pour un échantillon faiblement dopé. Pour l'échantillon le plus dopé, la valeur a légèrement diminué à environ 260 µW.m^{-1}.K^{-2}.

Nous avons mené une analyse approfondie de la conductivité thermique à base des données expérimentales mesurées dans une large gamme de température entre 4 et 1000 K. Le dopage électronique forme des quasi-particules de type polaronique caractérisées par des octaèdres MnO_6 localement déformés du fait de l'effet Jahn-Teller. En raison du fort couplage électron-phonon, ces quasi-particules réduisent fortement la conductivité thermique pour atteindre un comportement semblable à celui d'un verre au-dessous de la température ambiante. Selon notre analyse, une partie de la conductivité thermique à haute température est associée à des phonons optiques. La conductivité thermique mesurée à haute température est proche de la valeur minimale théorique calculée avec le modèle de Cahill. On ne peut donc espérer qu'une amélioration très minime des performances en jouant sur la conductivité thermique, par exemple en nano-structurant les matériaux. Le ZT de nos meilleurs échantillons est de 0,16 à 1000 K.

Un avantage intéressant des matériaux thermoélectriques à base de $CaMnO_3$ est que le facteur de puissance et le facteur de compatibilité thermoélectrique ne changent pas beaucoup avec le niveau de dopage. Ce dernier ne varie que d'environ 25 % entre les manganites faiblement dopés et fortement dopés. Ceci présente une belle opportunité pour ajuster les propriétés thermoélectriques sans impact significatif sur sa compatibilité avec un matériau thermoélectrique approprié pour former la partie plus froide d'une jambe TE segmentée. Pour la fabrication d'un module, nous avons montré que la pâte d'argent convient aux contacts électriques, bien que sa faible adhérence mécanique sur un substrat en alumine doive être améliorée.

Nous avons étudié les propriétés électriques et thermiques de trois polymères : des films de PEDOT:PSS et des pastilles pressées à froid de polypyrrole (PPy) et de polyaniline (PANI). Nous avons acquis une première expérience avec des

polymères et montré que nous sommes capables de mesurer avec succès les propriétés thermoélectriques de cette famille de matériaux spécifiques. La sensibilité à l'humidité est un facteur crucial à prendre en considération quand on étudie des polymères.

Les échantillons PEDOT:PSS ont demandé une modification du porte-échantillon de mesure pour pouvoir monter des échantillons minces. La résistivité électrique et le coefficient Seebeck des échantillons sont en accord avec les valeurs de la littérature et correspondent à un mécanisme de conduction souvent observé dans des polymères – le « variable range hopping ». Le polypyrrole est un polymère intéressant avec un coefficient Seebeck typiquement métallique mais avec une résistivité semi-conductrice. Nos données correspondent à la littérature qui suggère une hétérogénéité du polymère pour expliquer ce comportement : des îlots métalliques, responsables de S, sont séparés par des barrières non métalliques, responsables de ρ. Le pressage à froid de la pastille de PPy a créé une anisotropie importante de la conductivité thermique d'un échantillon nanotubulaire. Autour de la température ambiante, les valeurs mesurées perpendiculairement sont d'environ 0,3 $\mathrm{W.m^{-1}.K^{-1}}$, tandis que les valeurs dans le plan étaient trois fois plus élevées.

Au-dessous de la température ambiante, la polyaniline présente un comportement en température de la résistivité de type semi-conducteur qui correspond, comme dans le cas de PEDOT:PSS, au « variable range hopping ». Au-dessus de la température ambiante, les mesures de cet échantillon étaient délicates à cause de sa sensibilité à l'humidité. Contrairement au PPy, sa conductivité thermique était isotrope avec une valeur de 0,4 $\mathrm{W.m^{-1}.K^{-1}}$ à température ambiante. Nous avons calculé le libre parcours moyen des phonons dans les pastilles de PPy et PANI à partir des données expérimentales. Au-dessus de la température ambiante, il a peu varié en fonction de la température et correspond à l'ordre de grandeur de l'espacement interatomique, c'est-à-dire la valeur raisonnable la plus basse. Il augmente avec la diminution de la température pour atteindre des valeurs supérieures à 10 nm en dessous de 10 K.

Abstract

Synthèse, caractérisation et optimisation de nouveaux matériaux thermoélectriques

Les matériaux thermoélectriques (TE) permettent de convertir directement de la chaleur en électricité et vice-versa. Les objectifs de cette thèse étaient de tenter d'améliorer les performances TE de trois familles de matériaux et de mieux comprendre le lien entre les propriétés physiques (électriques, thermiques, magnétiques) généralement mesurées dans une large gamme de température (5–700 K) et les microstructures/compositions chimiques observées. Généralement, les matériaux ont été synthétisés par des techniques de métallurgie des poudres et densifiés par spark plasma sintering.

La majeure partie de nos travaux a concerné la famille des matériaux tétraédrites, dérivés du minéral naturel $(Cu,Ag)_{10}(Zn,Fe)_2(Sb,As)_4S_{13}$, présentant des propriétés TE prometteuses, récemment mises en évidence. D'abord, les propriétés TE de huit tétraédrites naturelles de provenance différente ont été étudiées. Nous avons montré que leurs propriétés physiques sont plutôt prévisibles selon leur composition chimique et finalement peu différentes selon leur origine. Les propriétés TE de mélanges de tétraédrites naturelles et synthétiques obtenus par broyage mécanique ont ensuite été déterminées. Ce procédé fortement énergétique produit des particules de taille nanométrique des deux phases qui forment une solution solide pendant le frittage. Par contre, un broyage manuel conserve la présence des deux phases, ce qui conduit à de plus faibles performances TE. Ensuite, nous avons montré que la substitution Sb⇔As, usuelle dans les spécimens naturels, n'influence que faiblement les propriétés TE. Enfin, les propriétés TE de manganites de calcium et de polymères conducteurs ont également été étudiées.

Mots-clés

Matériaux thermoélectriques · Synthèse des matériaux · Mesures thermoélectriques · Tétraédrite · Manganite de calcium · Polymères conducteurs

Synthesis, Characterization and Optimization of New Thermoelectric Materials

Thermoelectric (TE) materials allow direct conversion between heat and electricity. The aim of this thesis was to try to improve the thermoelectric performance of three different families of materials and to better understand the link between the various physical properties (electrical, thermal, magnetic) generally measured in a broad temperature range (5–700 K) and the observed microstructure/chemical composition. In general, the materials were synthesized by powder metallurgy techniques and densified by spark plasma sintering (SPS).

The major part of our studies concerns the tetrahedrite family of materials, derived from the mineral tetrahedrite, $(Cu,Ag)_{10}(Zn,Fe)_2(Sb,As)_4S_{13}$, whose promising thermoelectric properties were only recently discovered. In a first approach, the TE properties of eight natural tetrahedrites of different geographic origin are studied. It is shown that they all behave rather predictably and uniformly. Next, the properties of ball milled mixtures of natural and synthetic tetrahedrites are investigated. This high-energy process yields nanoscale particles of the two phases, which form a solid solution during the sintering. Low-energy hand grinding preserves the two-phase nature and results in inferior TE performance. Because arsenic is a common substituent in natural specimens, several As-substituted tetrahedrites are synthesized and characterized. It is shown that the TE properties are only weakly influenced by the substitution of As for Sb. Besides tetrahedrites, calcium manganese oxides and conductive polymers are also studied.

Keywords

Thermoelectric materials · Material synthesis · Thermoelectric measurements · Tetrahedrite · Calcium manganite · Conductive polymers